Two-Photon Ionization and Dissociation Dynamics in Atoms and Molecules Studied Using Vacuum Ultraviolet Laser Harmonics and Coincidence Momentum Imaging

by

Kirk Anders Larsen

A dissertation submitted in partial satisfaction of the

requirements for the degree of

Doctor of Philosophy

in

Applied Science and Technology

in the

Graduate Division

of the

University of California, Berkeley

Committee in charge:

Professor Roger Falcone, Chair
Professor David Attwood
Professor Stephen Leone

Fall 2020

Two-Photon Ionization and Dissociation Dynamics in Atoms and Molecules Studied Using Vacuum Ultraviolet Laser Harmonics and Coincidence Momentum Imaging

Abstract

Two-Photon Ionization and Dissociation Dynamics in Atoms and Molecules Studied Using Vacuum Ultraviolet Laser Harmonics and Coincidence Momentum Imaging

by

Kirk Anders Larsen

Doctor of Philosophy in Applied Science and Technology

University of California, Berkeley

Professor Roger Falcone, Chair

The correlated motion of electrons within gas-phase atoms and molecules influences various fundamental physical and chemical processes. In molecular systems, these complex electron dynamics may become coupled to the motion of the nuclei, resulting in many-particle dynamics that drive chemical transformations, such as isomerization or fragmentation. The valence electrons and their dynamics within atoms and molecules can be probed using vacuum ultraviolet (VUV) light to photoionize or photodissociate the system. The charged particles generated in such an interaction encode information on the many-particle system and its properties, with different types of measurements extracting differing levels of this information content. In order to reach a more complete description of the system, including the many-electron dynamics and coupled electron-nuclear motion, higher information content measurements are necessary. This involves going beyond photoelectron or ion yield measurements, instead turning to combined energy- and angle-resolved experiments, while leveraging the power of coincidence methods, allowing the total wave function of the system to be interrogated accurately. In this thesis, the valence electron dynamics in atoms and diatomic molecules are investigated using an intense femtosecond VUV light source to drive two-photon absorption and a coincidence 3-D momentum imaging spectrometer to measure the generated charged particles. This enables energy- and angle-resolved measurements on electrons and ions to be performed in coincidence, providing a multi-modal measurement carrying increased information content, allowing the many-electron and non-adiabatic dynamics to be explored and understood.

The Ti:sapphire laser system used to generate ultrashort VUV pulses, the VUV beamline, and the experimental endstation, including the charged particle 3-D momentum imaging spectrometer, are discussed thoroughly in the following chapters. In the experiments presented in this thesis, the near-infrared laser pulses from the Ti:sapphire system are frequency doubled to create bright 400 nm femtosecond pulses that are then used to produce VUV radi-

ation via high harmonic generation (HHG). Going to the second harmonic of the fundamental frequency enables high-brightness 9.3 eV femtosecond pulses, the third harmonic, to be generated with pulse energies of roughly 50 nJ, i.e. greater than 10^{10} photons at 9.3 eV per pulse. Such pulse energies enable two-photon absorption to be efficiently driven in the VUV, both resonantly and non-resonantly. Techniques for selecting different harmonics from the VUV frequency comb and attenuating the driving field are covered. Energy- and angle-resolved measurements on photoelectrons and photoions are performed using a coincidence 3-D momentum imaging spectrometer, also known as a reaction microscope or COLTRIMS (Cold Target Recoil Ion Momentum Spectrometer), specifically designed for the characteristics of the HHG based VUV light source.

A detailed experimental investigation of the angle-resolved non-resonant one-color two-photon valence ionization dynamics of isolated argon atoms is presented. This study reports the first measurements of the photoelectron angular distribution from non-resonant two-photon ionization of argon, finding that the photoelectron angular distribution is shaped by the interference between different angular momentum components of the photoelectron scattering wave function, which exhibits maximum intensity perpendicular to the ionizing VUV field. By comparing these results with a previous set of theoretical calculations, which have remained unverified for more than a few decades, this work reveals that electron-electron correlation significantly influences the photoionization dynamics. A thorough experimental and theoretical investigation of the energy- and angle-resolved resonant one-color two-photon absorption and dissociation dynamics of single O_2 molecules is also provided. This study reports the observation of two narrow and nearly degenerate autoionizing states of different symmetry that are dipole-forbidden, which both can decay through internal conversion to ion-pair states of the same total symmetry. This decay process competes with and interrupts autoionization. These experimental measurements are compared with a set of theoretical calculations, which indicate that these two resonances are excited by parallel-parallel and parallel-perpendicular two-photon transitions, and that the autoionizing states are directly accessed, without intensity borrowing. The calculations also reveal the electronic states participating in the two-photon transitions and Fano line shapes of the involved resonances. Finally, a comprehensive experimental and theoretical study of the energy- and angle-resolved non-resonant one-color two-photon valence ionization dynamics of isolated nitrogen molecules is presented. This investigation represents the first measurements of the photoelectron angular distribution from non-resonant two-photon valence ionization of N_2. It is found that the photoelectron angular distributions associated with the $X^2\Sigma_g^+$ and $A^2\Pi_u$ ionic states both vary with changes in photoelectron kinetic energy of only a few hundred meV. The rapid evolution in the photoelectron angular distributions can be attributed to the excitation and decay of dipole-forbidden autoionizing resonances, which belong to series of different symmetries, all of which are members of the famous Hopfield series.

Contents

List of Figures

List of Tables

Acknowledgments

I would like to thank all the individuals who have helped support and encourage me along the journey through my graduate studies and research. Since beginning my voyage through graduate school in the Fall of 2015, various people acted as guides, helping lead this work towards success. Many obstacles were encountered, often stifling progress, but the wisdom and expertise of many contributing scientists allowed these barriers to be overcome. I will never forget when I first arrived in Berkeley, in my first walk-through of the Advanced Light Source, I saw more experimental science than I had ever seen in my entire life up to that point. The amount of scientific thought and research I have had the opportunity to be exposed to in my time at Berkeley has truly been indescribably wonderful and transformative.

First, I would like to acknowledge my research advisor, Professor Roger Falcone, who gave me the opportunity to come to UC Berkeley as a graduate student. Roger has always provided me with excellent support and advice, and allowed me to freely explore many research opportunities during my graduate studies. I am truly indebted to him for all the guidance, mentorship, independence and help he has given me across these years. Roger's generosity and dedication to shaping students into the next generation of scientists is profoundly inspiring and I feel extremely fortunate to have been a member of his research group. I would also like to acknowledge Dr. Daniel Slaughter, who took me on as a graduate student researcher in the AMOS group at Lawrence Berkeley National Laboratory, facilitating the connection to the UC Berkeley campus and funding my graduate studies. Dan has offered me countless scientific opportunities, helping me thrive and I am genuinely grateful for everything he has done to help my work and career. Dan has always been sincere, patient and kind with me, and I can not thank him enough for his mentorship and support. I also want to acknowledge Dr. Thorsten Weber, who taught me much of what I know about COLTRIMS and who has always supported me through the thick and thin. Thorsten allowed and entrusted me to work with the MISTERS endstation, while also giving me the opportunity to participate in the COLTRIMS beamtimes at the Advanced Light Source. Thorsten is always willing to help me learn and grow scientifically, and I am extremely grateful for his wise advice and mentorship he has provided me with through all these years. I would also like to sincerely thank the other members of my dissertation committee, Professor David Attwood and Professor Stephen Leone. I am also grateful for all the help I received in navigating through the administrative labyrinth of graduate school from Ariana Castro and Yeen Mankin.

I also would like to thank all the graduate students and postdoctoral researchers who have assisted me along the way, while making the experience genuinely fun: Tyler Troy, Saijoscha Heck, Felix Sturm, Elio Champenois, James Cryan, Niranjan Shivaram, Richard Thurston, Travis Wright, Wael Iskandar, Said Bakhti, Maya Fabrikant, Dipanwita Ray, Brandon Griffin, Averell Gatton, Kasra Nowrouzi, Ashley Fidler, Catherine Saladrigas, Johannes Mahl, and Felix Brausse. So much of what I learned in graduate school was through these students and postdocs. I also want to thank the AMOS theory team at Lawrence Berkeley National Laboratory: Bill McCurdy, Robert Lucchese, Tom Rescigno, Cynthia Trevisan, Loren Greenman, Roger Bello, and Zachary Streeter. The theorists were always willing to

explain the physics to me and help me understand things, even when I needed things spelled out repeatedly before they would stick!

Finally, I would like to acknowledge my family, friends and loved ones, for all the support and encouragement they have given me outside of lab through these years. I would like to specifically thank my parents, who have given me unconditional love, care and support through my entire life. I would not be where I am today without their love and guidance. I would also like to thank Margaret Doyle for her endless support and for helping establish the famous rock climbing and eating Flacos routine, Tyler Troy for all the entertaining evenings passed at his apartment and all the programming knowledge and baked goods shared with me, Saijoscha Heck for all the amazing times we shared at the Berkeley Student Cooporatives, Huda Qureshi for the reliable stream of thought provoking discussions at the tea house, Ali Catena for consistently having the scoop on all the good upcoming concerts and always getting me a ticket, Daniel Martinez for all those memorable backyard conversations and outings to Viks and Urban Ore, Miles Sorce for all the innumerable good times we have had in both the Easy Bay and now in San Francisco (and of course back in Oregon too), and Lucas Pinelli for surviving an undisputedly ludicrous living situation with me during my first months in Berkeley. I also want to thank my fellow graduate students Satcher Hsieh, Pratik Sachdeva, and Jonah Haber, for enduring all those extremely long hours working on homework together in the dense jungle that is the first year of graduate school. Last I want to thank all my friends back in Portland, far too many to name, who have always supported and encouraged me every time I find my way back up north to the other side of the Oregon California border, as well as those who have made the trek down to the Bay Area to visit: Lucas Pinelli, Hope Pinelli, David Millen, Sam Connell, Jason Weiss, John Bonoff and Demetre Kazaras.

Chapter 1

Photoionization and Photodissociation Dynamics In Atoms and Molecules

In this chapter, the background and motivation for investigating photoionization and photodissociation dynamics in atoms and molecules is provided. This begins first with a brief discussion of our ability to control electron motion on atomic scales, and the influence that this has had in our modern society and experience. The connection between spatial and temporal scales for electron dynamics and energy is examined. A quick journey through history is then taken, with a review of the various vacuum ultraviolet (VUV) and x-ray light sources in modern science that are efficacious in the study of photoionization and photodissociation in atomic and molecular systems, as well as breakthroughs in laser technologies that enabled these VUV and x-ray photons to migrate from large-scale accelerator facilities to table-top laboratory settings.

Following this introductory section, we then turn to the theoretical framework necessary to understand and study many-electron systems like atoms and molecules, and their photoionization and photodissociation dynamics. This begins with descriptions of various forms of electron dynamics that can arise in many-electron systems, specifically electron-electron correlation effects, as well as autoionizing and shape resonances. This is followed by a discussion of the wave functions used to describe the quantum states of molecules and how they can be approximately solved for via the Born-Oppenheimer approximation. The limitations of this approximation are also explored. Next, a theoretical description of various observables in photoionization and photodissociation is provided, including an in-depth discussion on the amount of information content encoded within them. Finally, this section closes with a review of time-dependent perturbation theory, an indispensable tool used to describe light-matter interaction and photon driven electronic dipole transitions in atomic and molecular systems. A brief analysis of the spectroscopic selection rules that emerge from time-dependent perturbation theory are also presented.

In the last section, we assemble these pieces, introducing the generic experimental design

used in the measurements presented in this thesis. This involves a high-information content observable used in conjunction with an intense VUV light source in order to drive and study two-photon ionization and dissociation dynamics in atoms and molecules. An energy- and angle-resolved coincidence measurement on the electrons and ions produced in photoionization and photofragmentation serves as the high-information content observable, which allows subtle quantum dynamics and many-electron effects in atoms and molecules to be resolved, and the wave function of the total system to be probed.

1.1 A Broad and Historical Perspective

A large number of scientific and technological advancements in the modern era rely on electrons and controlling or exploiting their dynamics in some way. For example, the crucial technologies of transistors and lasers involve controlling the atomic-scale motion of electrons. These devices have had far-reaching applications that have influenced and shaped our modern experience. Consider the advent of transistors, which revolutionized the field of electronics and are now fundamental building blocks of all modern electronic devices. Advancements in transistor technology and manufacturing have driven breakthroughs towards more compact computing devices, which has lead to the smartphones, computers and laptops of today, with the MOSFET (metal–oxide–semiconductor field-effect transistor) being the most widely manufactured device in history. With the discovery of lasers and their following technological revolution, these devices now play a central role in science, industry and medicine. Some of their critical applications include photolithography (manufacturing chips and dense integrated circuits of transistors), information transmission (fiber-optics carrying telephone and internet traffic), information storage and readout (optical disk drives, barcode scanners), laser surgery, cancer treatment, DNA sequencing, materials processing and manufacturing, and imaging. Our ability to control electrons on the atomic scale has allowed us to shape the world around us and our experience in unexpected ways, forming a bridge between the arena of quantum mechanics and the domain of our everyday experiences. As our insight and ability to control electrons on atomic scales undergoes further development, new and exciting technologies will continue to emerge and revolutionize our society.

Within the fields of physics, chemistry and biology, electron motion lies at the core of many fundamental processes. Electron dynamics within atoms can lead to the emission of photons spanning a wide range of the spectral domain, from radio to x-rays. Within molecules, chemical bonds are formed and cleaved (initiating chemical transformation) by electron motion, with electron dynamics driving charge and energy redistribution within the system. In biological systems, molecular scale electron dynamics are crucial in triggering structural and chemical changes in biomolecules, as well as in the transport of bioinformation, charge, and energy. The intrinsic time scales for the electron dynamics depends on the nature of the system, but often lies in the attosecond to femtosecond regime ($10^{-18} - 10^{-15}$ sec).

Fig. 1.1 shows the natural spatial and temporal scales of structure and dynamics within quantum mechanical systems. Energy is canonically related to length and time through the

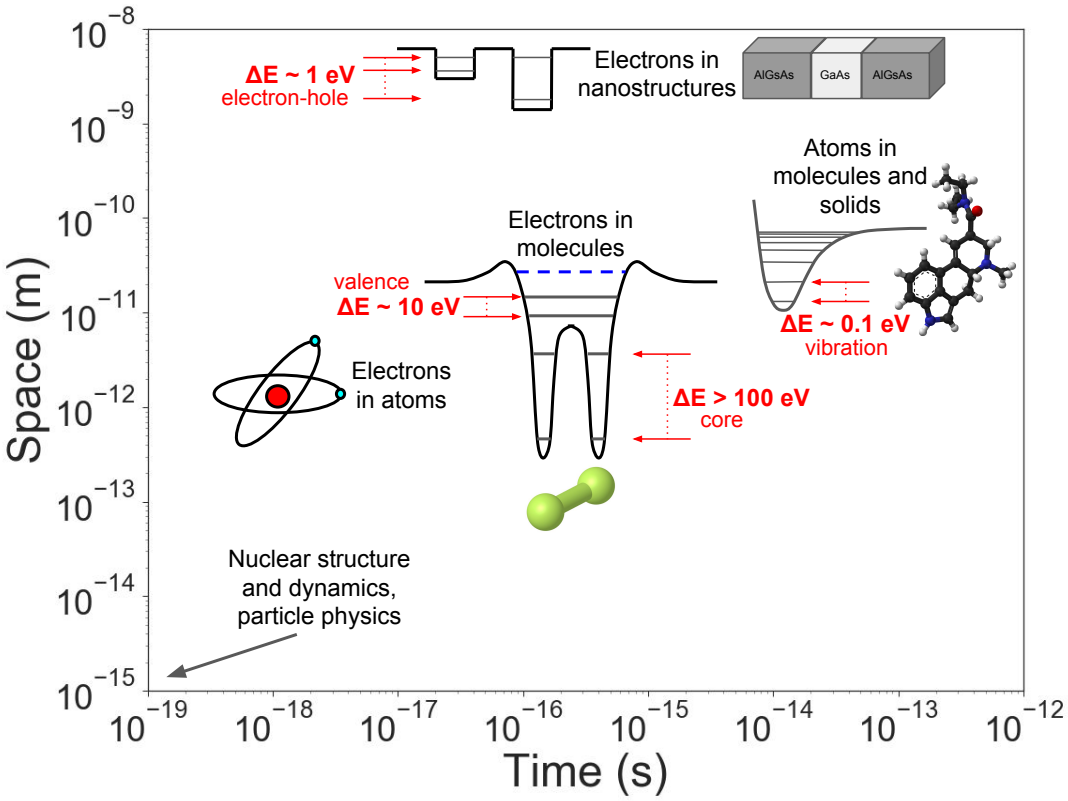

Figure 1.1: The characteristic length and time scales for spatial structure and temporal dynamics in the quantum world. Energy is intrinsically connected to spatial and temporal scales through the principles of quantum mechanics. Greater energy separation between eigenstates results in dynamics on shorter length and time scales involving those states. The ∼100 meV spacing of the vibrational energy levels in molecules and solids results in atomic motion on time scales ranging from tens to hundreds of femtoseconds and at the angstrom level. The motion of electrons in semiconductor nanostructures, molecular orbitals and atomic orbitals occur on increasingly shorter time scales with increasing energy separation between states. Core and inner shell eigenstates in atoms and molecules have separations on the order of 100–1000 eV (dynamics on time scales of tens of attoseconds, or less), while outer shell and valence stationary states are spaced on the order of 10 eV (dynamics on time scales of hundreds of attoseconds to few-femtoseconds), and valence and conduction bands in solids are separated on the 1 eV-scale (dynamics on time scales of tens to hundreds of femtoseconds). Figure inspired by Ref. [86].

framework of quantum mechanics, which is also illustrated in Fig. 1.1. This relationship arises due to the fact that the energy separation between states in a quantum system is both related to the spatial extent of the confining potential, and the time scales for the

dynamics involving a superposition of those states. This results in a connection between the time scales of dynamics and the spatial extent of a quantum system. On the right, we see that the spacing between vibrational energy levels in molecules and solids is on the order of 100 meV, resulting in temporal dynamics ranging from tens to hundreds of femtoseconds and at spatial scales on the order of an angstrom. This corresponds with the characteristic length and time scales for atomic motion within molecules and solids. Above and to the left, we encounter the regime of electron motion within semiconductor nanostructures. These dynamics occur on spatial scales on the order of a nanometer and on time scales ranging from tens to hundreds of femtoseconds, corresponding with the ∼1 eV energy spacing between valence and conduction bands. Below and to the left, we next find electrons in atomic and molecular orbitals. For core and inner shell electrons in atoms and molecules, the spatial and temporal scales for dynamics are generally in the range of tens to hundreds of picometers and few to tens of attoseconds in atoms, in accordance with the ∼100-1000 eV energy spacing between eigenstates. In outer shell and valence eigenstates, the spatial scales are typically within hundreds of picometers to angstroms, while the time scales for dynamics lie in the range of hundreds of attoseconds to a few femtoseconds. This naturally corresponds with the approximate 10 eV energy spacing between such stationary states. In the far bottom left corner, continuing beyond the scale of both the time and space axes, we find length and time scales corresponding with the dynamics that occur within nuclei and processes that transpire within the realm of high energy particle physics.

We can see in Fig. 1.1 that in order to access and probe electrons within atomic and molecular systems to gain insight into their motion and the physical processes that they drive, we need access to some source of energy that is capable of depositing ∼10 eV of energy or greater into the system (∼10 eV or more in the case of addressing valence states and >100 eV in the case of addressing core levels). On particularly convenient and useful form of energy is electromagnetic radiation, i.e. light. At energies of ∼10 eV or greater, this corresponds with photons that lie within the vacuum ultraviolet (VUV) and X-ray regions of the electromagnetic spectrum. Fig. 1.2 shows the historical progression of the peak brightness (in essence a metric for scientific usefulness and ability to produce discoveries) of VUV and X-ray light sources, which has exhibited remarkable growth since Roentgen's initial discovery of X-rays in 1895. X-ray tubes served as the earliest sources (and are still used in hospitals in radiography), which were supplanted by the various generations of synchrotrons which emerged as electron storage ring and undulator technologies developed. The first and second generation synchrotrons utilized light that was generated as a by-product in electron ring accelerators, while third generation synchrotrons, with their characterisitic electron storage rings, where designed with the specific purpose of bright VUV and x-ray generation using various forms of insertion devices. Fourth generation synchrotrons show an increase in brightness through the use of diffraction limited storage rings, which can be achieved using what is known as a multi-bend achromat focusing lattice. High current electron linear accelerators drive free-electron lasers (FELs), which show an enormous increase in peak brightness over synchrotron technologies. This breakthrough technology can be realized by suitably guiding a relativistic electron beam through a long array of undulators to achieve what is

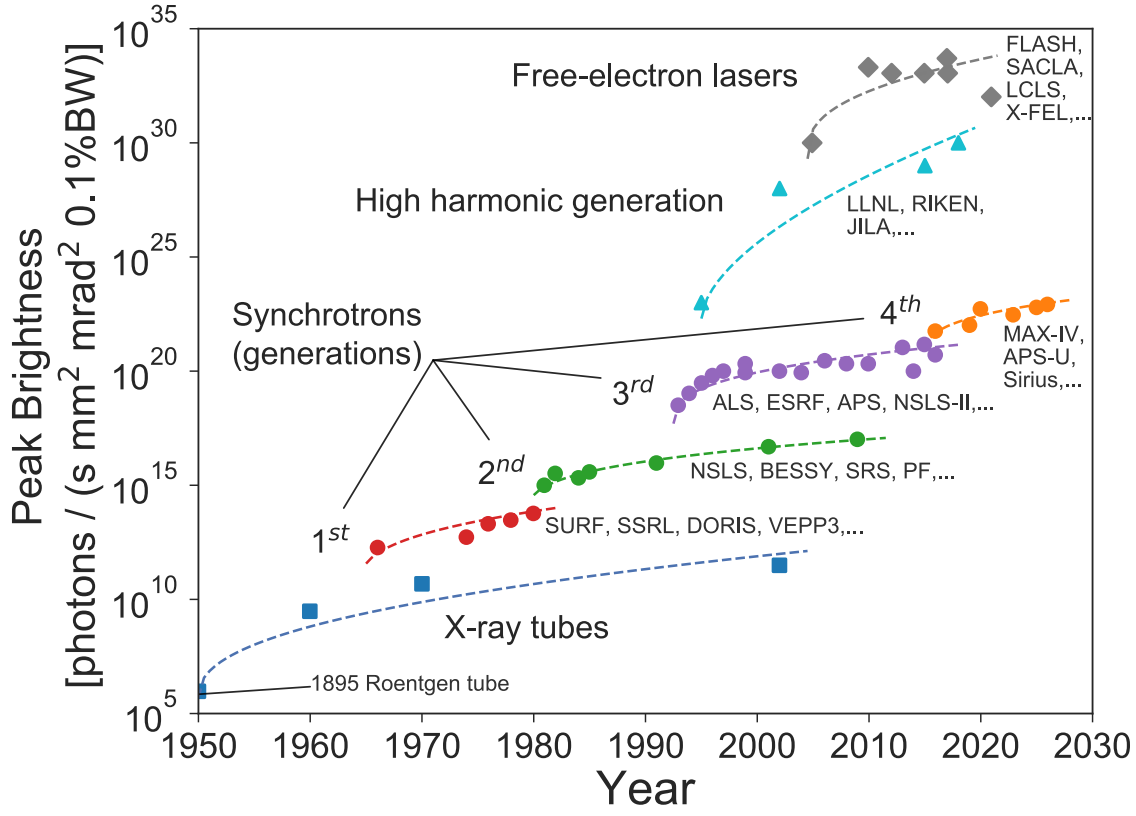

Figure 1.2: The peak brightness of VUV and X-ray light sources, showing remarkable growth since Roentgen's discovery of X-rays in 1895. X-ray tubes provided early sources, while the development of electron storage rings gave rise to the different generations of synchrotrons that followed. High current electron linear accelerators drive free-electron lasers (FELs). The enormous gap in peak brightness between synchrotrons and FELs is bridged by high harmonic generation based light sources. Figure inspired by Ref. [144].

known as self-amplified spontaneous emission (SASE). The rift in peak brightness between synchrotrons and FELs is bridged by high harmonic generation (HHG) based light sources. This method of VUV and X-ray generation relies on up-converting the frequency of an extremely intense laser pulse through nonlinear interactions with a medium. The substantial boost in peak brightness observed in HHG and FELs compared with synchrotrons is due to an extreme reduction in pulse length (by roughly four orders of magnitude or greater), with HHG and FELs capable of producing pulses lying in the tens to hundreds of attoseconds and are thus able to probe electron dynamics in atomic and molecular systems on their natural time scales. Since these light sources are capable of addressing the valence, inner-shell, and core-level electrons in atomic and molecular systems, their proliferation and advancement

has driven substantial scientific progress in experimental physics, chemistry and biology, as well as in industry and medicine. The acceleration in peak brightness of VUV and X-ray sources across the years is truly striking, exhibiting an increase of approximately 30 orders of magnitude since the mid-1960s. This has produced an abundance of scientific discoveries and resulted in the ability to drive and probe new and unfamiliar physical processes and mechanisms, as previously unexplored regimes in peak brightness are charted. Drawing a parallel with Moore's law, the peak brightness of VUV and X-ray light sources displays a doubling time of ∼0.5 years, which is four times faster than the growth seen in Moore's law for transistors.

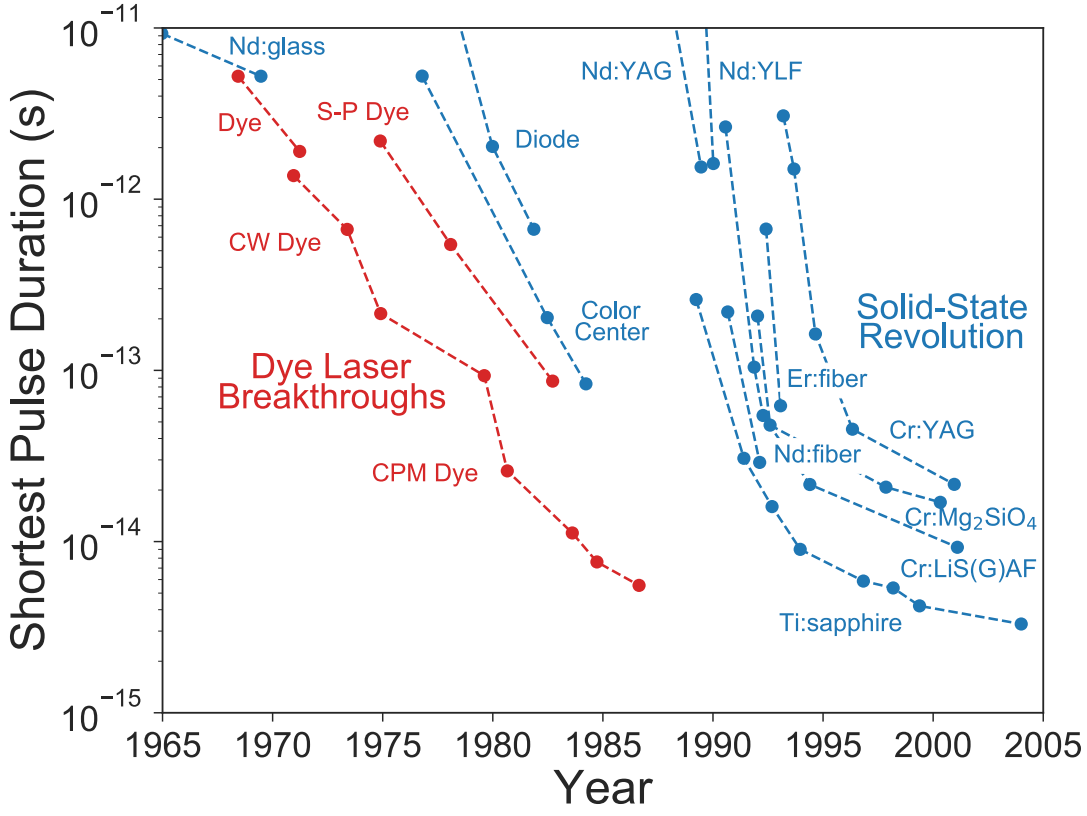

Figure 1.3: The historical progression of ultrashort optical pulse duration. Developments in dye laser technologies were supplanted by solid-state lasers, due to their rapid advancement in the early 1990s with the discovery of Kerr-lens mode locking (KLM). Optical pulses containing less than two cycles have been produced via KLM in Ti:sapphire, where sub-ten fs pulses are now routinely available. These developments in ultrashort pulse solid-state laser technologies enabled progress in high-brightness high harmonic generation. Figure inspired by Ref. [77].

While the prodigious scaling in peak brightness of synchrotrons and FELs has been driven by breakthroughs in accelerator physics and technologies, the discovery and subsequent advancements in HHG have been driven by revolutions within laser technology. Fig. 1.3 shows the shortest pulse lengths generated by lasers as a function of year, illustrating the noteworthy historical progression of ultrashort optical pulse duration. The steady developments in dye laser technologies across the 1970s and 1980s were supplanted by solid-state laser technologies, which rapidly advanced in the early 1990s with the discovery of Kerr-lens mode locking (KLM). This technology is the basis for femtosecond pulse production in a wide range of solid-state laser systems, where Ti:sapphire lasers quickly became the de facto standard of ultrafast femtosecond laser systems. Sub-ten femtosecond pulses can now be routinely generated and come standard in many commercially available Ti:sapphire laser systems. Optical pulses containing fewer than two cycles with octave-spanning spectra have been produced using KLM in Ti:sapphire. These advancements in ultrashort laser pulse technologies, combined with the development of chirped pulse amplification in the mid-1980s, lead to the discovery of HHG and the ensuing revolution that transformed it into a serious competitor with accelerator-based VUV and X-ray light sources, with respect to peak brightness. Additionally, since HHG is a laser-based method, it enables the dynamics electrons within atoms and molecules to be probed on ultrashort timescales in a laboratory setting, without need for a billion dollar accelerator facility.

1.2 Many-Electron Systems and Dynamics

Quantum systems composed of many interacting particles play a central role in various fields of physics and chemistry, where an accurate description and understanding of the complex quantum dynamics poses a significantly challenging problem. For example, the electrons within multi-electron atomic and molecular systems undergo repeated interactions with one another, resulting in highly correlated motion. This results in an enormous amount of information becoming encoded in the total wave function of the system. In these circumstances, exact or analytic calculations characterizing the dynamics of the system are not possible. Thus understanding these types of physical systems from a theoretical perspective often involves making various levels of approximations and significant supercomputing resources. Further, experimental measurements that provide a view on the complex total wave function and the information encoded within it, characterizing the electron dynamics and many-electron effects through the subtle details encoded in some observable, represents a great challenge in modern quantum mechanics. In the next two subsections, a few important examples of electron dynamics in many-electron quantum systems, such as atoms and molecules, are provided. As will be described in the later sections of this chapter, these electron dynamics can often be probed using photons to fragment the system, removing electrons (photoionization) and/or cleaving bonds (photodissociation), and then measuring the charged particles that are generated, as the photoionization and photodissociation dynamics can be shaped by many-electron effects.

1.2.1 Electron-Electron Correlation

The motion of electrons within multi-electron atomic and molecular systems is highly correlated in nature. The electrons in the system interact and do not evolve independently of one another, where the electron dynamics are greatly influenced by the presence of the other electrons in the system. Consider a simple two-electron system. Mathematically, if the dynamics of the two electrons are completely independent of one another, we can express the total wave function Ψ as

$$\Psi(\mathbf{x}_a, \mathbf{x}_b) = \psi_1(\mathbf{x}_a)\psi_2(\mathbf{x}_b) \tag{1.1}$$

Here, the probability of simultaneously observing an electron at $\mathbf{x}_a$ and another at $\mathbf{x}_b$ is given by

$$|\Psi(\mathbf{x}_a, \mathbf{x}_b)|^2 d\mathbf{x}_a d\mathbf{x}_b = |\psi_1(\mathbf{x}_a)|^2 d\mathbf{x}_a |\psi_2(\mathbf{x}_b)|^2 d\mathbf{x}_b \tag{1.2}$$

which is the product of two independent probabilities, the probability of finding one electron at $\mathbf{x}_a$ times the probability of finding one electron at $\mathbf{x}_b$. In this independent particle model, the electron motion is uncorrelated since they move independently of one another.

In reality, the two electrons interact through their Coulomb fields, repelling each other, and therefore their motion is highly correlated. The instantaneous Coulomb repulsion energy goes as the inverse of the distance between the two electrons, r_{ab}^{-1}. Because of this, the probability of finding an electron at $\mathbf{x}_a$ depends on the position of the second electron $\mathbf{x}_b$, and the total wave function can not be simply expressed as the product shown in Eq. 1.1 (a product of independent wave functions does not describe reality), which is known as the Hartree product. For instance, applying Eq. 1.1 for uncorrelated electron pairs at small distances results in an incorrect electron density that is too high, while at large electron pair distances the electron density is too low.

The Hartree-Fock method is typically used to approximate the wave functions and energies of the stationary states of a quantum many-body system, e.g. atoms and molecules, by approximately solving the Schrödinger equation. In this approach, the N-body wave function for the system is approximated as a single Slater determinant of N spin-orbitals (named after John C. Slater, who introduced the concept in 1929 [145]). Slater determinants are used in quantum mechanics to describe the wave function of multi-fermionic systems, where exchange of two identical fermions results in a sign change of the wave function, making it anti-symmetric and therefore satisfying the Pauli exclusion principle. For a collection of N electrons, each with a wave function given by spin-orbitals $\chi_1(\mathbf{x}), \chi_2(\mathbf{x}), \ldots, \chi_N(\mathbf{x})$, the Slater determinant describing the N-electron wave function of the total system is given by

$$\Psi(\mathbf{x}_1, \mathbf{x}_2, \ldots, \mathbf{x}_N) = \frac{1}{\sqrt{N!}} \det \begin{pmatrix} \chi_1(\mathbf{x}_1) & \chi_2(\mathbf{x}_1) & \cdots & \chi_N(\mathbf{x}_1) \\ \chi_1(\mathbf{x}_2) & \chi_2(\mathbf{x}_2) & \cdots & \chi_N(\mathbf{x}_2) \\ \vdots & \vdots & \ddots & \vdots \\ \chi_1(\mathbf{x}_N) & \chi_2(\mathbf{x}_N) & \cdots & \chi_N(\mathbf{x}_N) \end{pmatrix} \tag{1.3}$$

However, this approximation does not adequately capture reality, since the real wave function can not be written as one Slater determinant. Using a single Slater determinant to approximate an antisymmetric N-electron wave function replaces the instantaneous electron-electron interactions with an interaction with an average field, and because of this, the Coulomb correlation is lost in this approach (the electrons each interact with one another, an electron does not interact with an average charge distribution due to the other electrons, a mean field). This introduces an error in the wave function and its energy, which differs from the exact solution to the nonrelativistic Schrödinger equation within the Born-Oppenheimer approximation. The Hartree-Fock limit (i.e. the best possible solution within the Hartree-Fock method, the limit of the Hartree-Fock energy as the basis set approaches completeness) lies above the true energy of the system, as illustated in Fig. 1.4. The difference in energy between the Hartree-Fock limit and the exact solution to the nonrelativistic Schrödinger equation is known as the correlation energy, a term first coined by Löwdin in 1955 [100]. This provides a measure on the extent to which the dynamics of one electron is influenced by the other electrons in the system, i.e. the level at which the electronic structure of a quantum system is shaped by interaction between electrons (a measure of many-particle effects).

Since a Slater determinant is used to construct the wave function for the system, some electron correlation is intrinsically built into the Hartree-Fock approach, as the wave function automatically respects the electron exchange symmetry by construction. This basic level of correlation between interacting fermions is called Pauli repulsion, or Fermi correlation, preventing parallel-spin electrons from occupying the same spatial state, and is related to the Pauli exclusion principle. The Coulomb correlation that arises is due to the mutual Coulomb repulsion between the electrons in the system, which is dependent on the electron positions. Such Coulomb correlation is important for describing various chemical effects, such as London dispersion forces (van der Waals forces, e.g. long-range attraction between atomic and molecular dimers, which arise due to instantaneous fluctuations in the electron distribution in an atom or molecule that induce electron redistribution in a near-by atom or molecule, an instantaneous dipole-induced dipole force, giving rise to correlated electron motion), in addition to accurately determining the eigenstates and energies of the system, i.e. the electronic structure.

The electron correlation can be split into two categories, dynamical and static correlation, which are crucial in accurately describing correlated electron motion and ground state wave functions that are not well approximated by a single Slater determinant, respectively. These two different types of electron correlation can be handled using post-Hartree-Fock methods, such as in the configuration interaction (CI) or multi-configuration self-consistent field (MCSCF) methods, respectively. Various other techniques, in addition to the two just

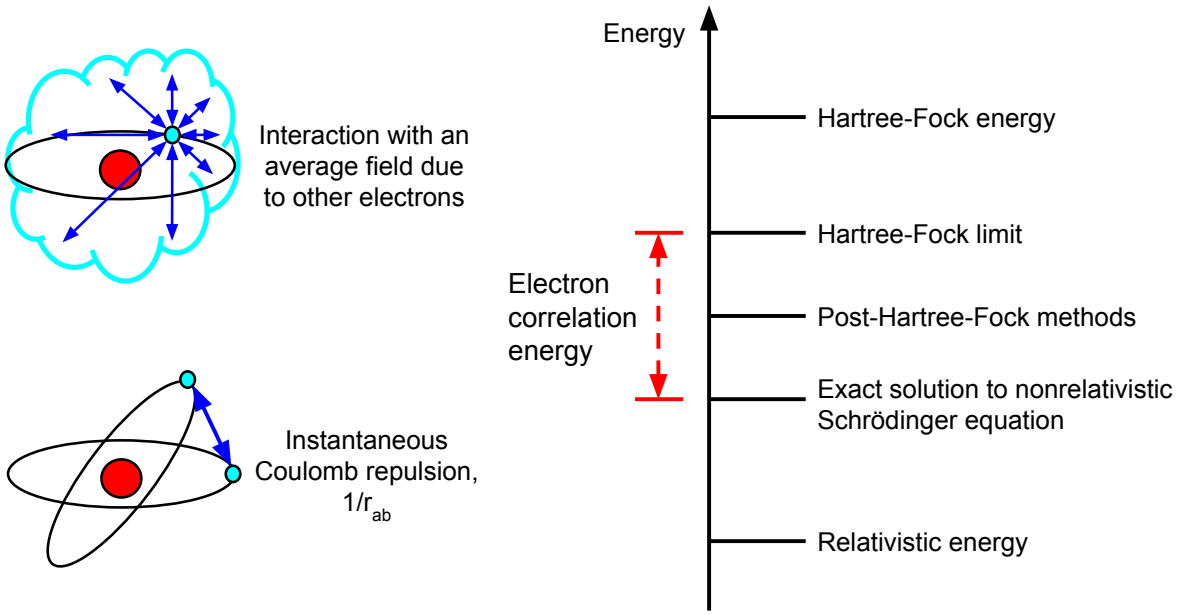

Figure 1.4: An energy ladder depicting solutions to the Schrödinger equation using different levels of theory, which overestimate the energy of the system. The electron correlation energy is the difference in energy between the exact solution to the nonrelativistic Schrödinger equation and the Hartree-Fock limit. On the left is a simple depiction of a helium atom, illustrating how the instantaneous Coulomb repulsion between the two electrons is replaced with an electron interacting with an average charge distribution due to the other electron in the Hartree-Fock method, which introduces error into the wave function and its energy.

mentioned, also allow electron correlation to be handled, improving the accuracy of the approximation and converging towards the exact solution to the nonrelativistic Schrödinger equation and the true electronic structure, seen in Fig. 1.4. Determining the role of electron correlation in different physical processes and the number of active electrons needed for their accurate description, such as in photoionization and photodissociation, is a great challenge both theoretically and experimentally.

1.2.2 Continuum Electronic Structure

The quantum mechanical description of the state of motion of electrons in the fields produced by stationary nuclei in a quantum system (the wave functions and corresponding energies for the ground and excited states) is known as the electronic structure of the system. The electronic structure of a quantum system can be obtained by solving the nonrelativistic

Schrödinger equation using fixed nuclei, i.e. within the Born-Oppenheimer approximation. Characterizing the electronic structure of the neutral system, as well as higher charge states, represents both an experimental and theoretical challenge, with different physics appearing depending on if the system is neutral, singly charged, or multiply charged.

Discrete electronic states that lie in the continuum above the first ionization threshold are energetically degenerate with states that belong to a continuous spectrum. Such continuum-embedded discrete states were postulated early in the development of quantum mechanics, for example in 1929 by von Neumann and Wigner [118], and later described in detail by Fano in a seminal and celebrated paper in the *Physical Review* in 1961 [56] (which is one of the most cited papers to ever appear in the journal). Due to the configuration interaction between the discrete and continuous spectra, such continuum-embedded discrete states are quasi-bound (meta-stable) and decay with a finite lifetime. Characterizing the coupling between discrete resonances and the continuum is a challenge for both experimental and theoretical understanding and descriptions of the physics. Such continuum electronic structure resulting from an electron scattering from an ion can in some instances result in many-electron dynamics, in the form of multi-electron rearrangement, due to the decay of the aforementioned resonances. Various continuum resonances can classified as either one- or two-electron resonances, i.e. shape resonances and autoionizing states. These continuum states can greatly influence the photoionization and dissociation dynamics, e.g. how photoelectrons are ejected from the system. Below we discuss both these types of resonances and provide details on their underlying physical mechanisms.

Autoionization is a process in which a quantum system (e.g. an atom or molecule) in an excited state relaxes by spontaneously emitting an electron and going from a state with charge Z to $Z+1$. Since these continuum-embedded discrete states are generally short lived, they are not well described by typical bound states, and can result in interference effects, a paradigmatic example being the Fano resonance, where the scattering amplitudes of a resonant (discrete) and background (continuum) process interfere to give rise to the famous asymmetric line shape [56]. For example, in photoionization, continuum states that decay via autoionization can provide an indirect channel to target states that can interfere with the direct ionization channel to the same target states [16, 47, 75, 137, 172]. Transitions via autoionization can in many cases be described quantum mechanically using a two-electron matrix element, with the instantaneous electron-electron Coulomb repulsion acting as the perturbation

$$\langle \psi_\gamma, \phi_{\mathbf{k}} | V_{ee} | \psi_\alpha, \psi_\beta \rangle \tag{1.4}$$

where $V_{ee} = \frac{1}{4\pi\epsilon_0} \frac{e^2}{|\mathbf{r}_1 - \mathbf{r}_2|}$, ψ_α and ψ_β are the initial states of the two electrons that participate in the decay of the autoionizing resonance (often one bound and one quasi-bound), while ψ_γ and $\phi_{\mathbf{k}}$ are the final states of those two electrons (one bound and one in the continuum). Here, the likelihood of undergoing an autoionizing transition depends on the magnitude squared of this matrix element, which depends on the overlap between the perturbed initial and final state wave functions of the system.

In the neighborhood of the resonant energy, the background scattering amplitude varies slowly with energy, while the resonant scattering amplitude varies rapidly in magnitude and phase. Far off resonance, the background scattering amplitude dominates. Near the resonance, the phase of the resonant scattering amplitude undergoes a π phase shift, and the interference between the slowly and rapidly varying phases of the background and resonant scattering processes generates an asymmetric line-shape. The Fano line-shape of an autoionizing resonance can be described using the equation Fano derived in 1961 for the total scattering cross section σ

$$\sigma(\omega) \sim \frac{(q + \epsilon(\omega))^2}{1 + \epsilon(\omega)^2} \tag{1.5}$$

where $\epsilon(\omega) = (\omega - \omega_0)/(\Gamma/2)$, Γ is the resonance width, ω_0 is the resonant frequency, and q is the Fano q parameter (a measure of the ratio of resonant to background scattering amplitudes). The energy width of the state Γ carries information on the resonance lifetime through the time-energy uncertainty principle, $\Delta E \Delta t \geq \hbar/2$, while the q parameter can indicate if the resonance is excited directly via dipole coupling ($q^2 \gg 1$) or indirectly via intensity borrowing ($q \sim 0$). Note that when the background scattering amplitude vanishes, so does q, and the above equation reduces to the famous Breit-Wigner formula for a Lorentzian distribution. The scattering cross section as a function of $\epsilon(\omega)$ is shown for different values of the Fano q parameter in Fig. 1.5. Here we can see the line-shape progress from a symmetric Lorentzian when $q = 0$ to an asymmetric distribution as q increases.

These electron-ion resonances can generate complex continuum electronic structure and possess different decay mechanisms that may compete. Some of these relaxation processes may involve ionization, e.g. autoionization, while others can involve mechanisms where all electrons remain bound, e.g. neutral dissociation or ion-pair formation (predissociation). The different decay mechanisms of these resonances can involve multi-electron dynamics in the form of electron rearrangement, where two or more electrons can be shuffled between different molecular orbitals during relaxation. This is depicted schematically in Fig. 1.6, on the left. Furthest to the left, the neutral ground state absorbs two photons, either undergoing direct ionization to the ground state of the cation (shown as the lower long purple arrow) or exciting an inner-valence electron to a continuum-embedded discrete state (shown as the short upper purple arrow). This continuum resonance decays to the ground state of the cation via autoionization (shown as the short black arrow), where an outer-valence electron fills the inner-valence vacancy and the quasi-bound electron is released into the continuum. These direct and indirect paths both connecting to the ground state of the cation can interfere, with the electron scattering wave function accumulating different phase depending on the path taken. A depiction of two competing decay mechanisms for an autoionizing state is shown in Fig. 1.6, on the right. Here, the neutral ground state undergoes two-photon absorption (purple arrows), which may populate a Rydberg state belonging to a series converging to the second single ionization threshold (indicated by the bottom of the green region). This two-photon energy lies above the first single ionization threshold (indicated by the bottom of the blue region), and the Rydberg state is degenerate with a continuum level that can

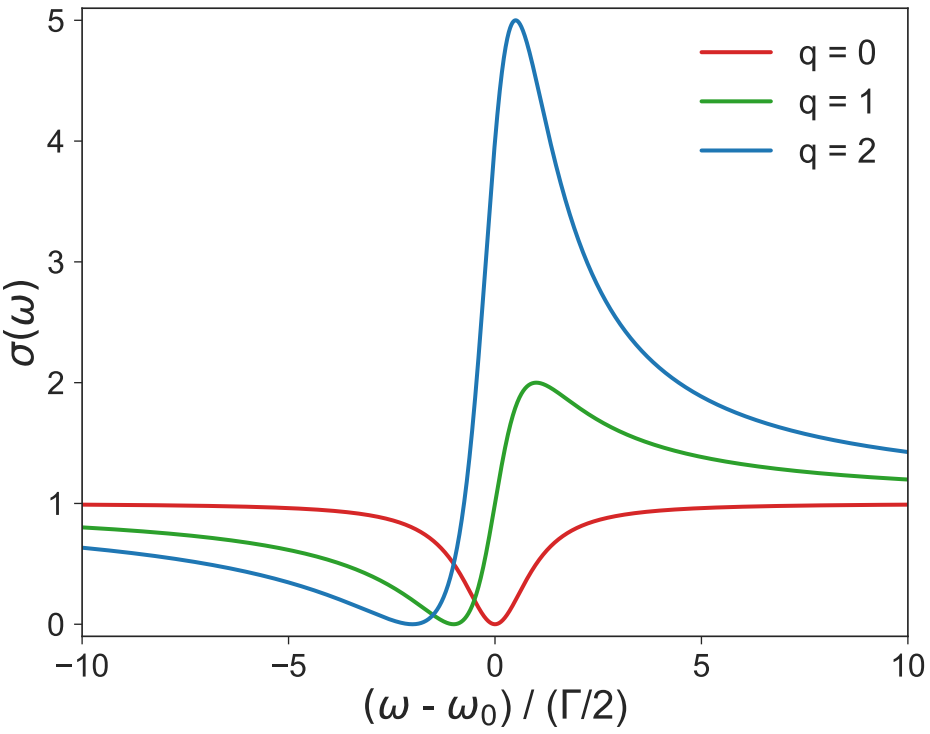

Figure 1.5: The scattering cross section as a function of the shifted and normalized frequency (resonance shifted to zero and normalized to the width parameter $\Gamma/2$), for various Fano q parameters. Here the evolution from a Lorentzian to an asymmetric Fano line-shape can be seen as the value of q increases from zero. For negative values of q, the line-shapes are simply reflected across the zero of the abscissa.

also be populated (dashed black line). Configuration interaction between these two states can result in autoionization (shown as the red arrow). Here, the autoionizing state can also dissociate (shown as the blue arrow), which provides an alternative pathway for the resonance to decay through. Such a situation may arise when the autoionizing state is predissociated and internal conversion between the resonance and dissociative state is can take place. As mentioned earlier, such fragmentation can involve ion-pair creation or neutral dissociation.

Another type of resonance that can occur in the continuum electron structure of atoms and molecules is known as a shape resonance, which is a one-electron resonance (predominantly). Shape resonances are quasi-bound states that arise due to an angular momentum potential barrier that can temporarily trap the escaping photoelectron, depending on if the excitation energy is on resonance. Here the "shape" of the potential momentarily captures the electron, before it escapes by tunneling through the barrier. Shape resonances were first observed in the late 1940s and early 1950s in nuclear scattering experiments, where broad

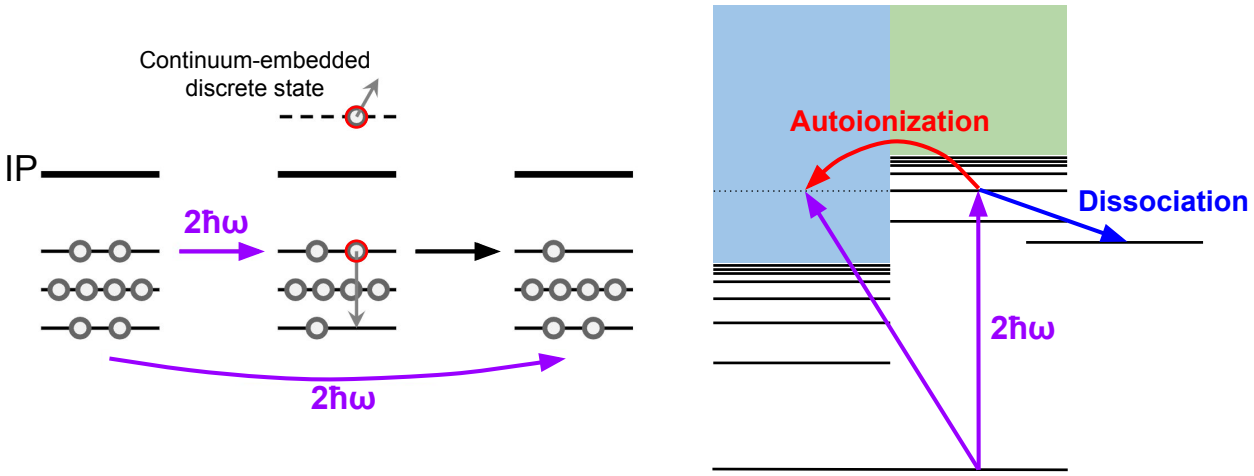

Figure 1.6: Depicted on the left, the decay of a molecular autoionizing state through a two-electron resonance. The neutral ground state absorbs two photons, either undergoing direct ionization to the ground state of the cation by removing the outer-valence electron (lower purple arrow), or by a two-photon transition to a continuum-embedded discrete state by exciting an inner-valence electron (upper purple arrow). This continuum resonance decays via autoionization (black arrow), where the inner-valence vacancy is filled by the outer-valence electron and weakly bound electron released into the continuum, producing the ground state of the cation. Depicted on the right, a schematic showing two different relaxation pathways of a continuum-embedded discrete state. The neutral ground state absorbs two photons, with energy exceeding the first single ionization threshold. The two-photon energy is resonant with a continuum-embedded Rydberg state (solid black line) converging to the second single ionization threshold, as well as a continuum level (dashed black line). Coupling between these two degenerate states can lead to autoionization (red arrow). Here the continuum-embedded Rydberg state can also undergo relaxation via fragmentation (blue arrow). This can occur when the autoionizing state is predissociated, leading to relaxation by coupling to the dissociative state through internal conversion.

asymmetric peaks were observed in neutron and proton scattering cross sections from nuclei. The name "shape resonance" emerged because it was observed that the shape of the nucleus influenced the resonance characteristics. However, these resonances were subsequently observed to appear in the photoionization of atoms and molecules, originating from electron-ion scattering (the escaping photoelectron scatters from the potential of the atomic or molecular ion). Such resonances have been observed in both valence and core ionization [34]. Similar to autoionizing resonances, shape resonances emerge due to quantum interference between closed and open scattering channels. On resonance, the meta-stable continuum state is degenerate with states belonging to a continuous spectrum, and configuration interaction between these states can lead to relaxation and interference. This can be measured with

different physical observables and contrasts strongly with the non-resonant behavior alone and can amplify subtle electron and structural dynamics in the excited system.

Shape resonances have been studied in depth in molecular systems, and have been observed in a wide collection of molecules [34]. The centrifugal barrier through which the electron tunnels originates from the molecular fields, and can inhibit the motion of otherwise free electrons along certain spatial dimensions. The centrifugal barrier term is seen in the Hamiltonian for a particle in a spherically symmetric system. Consider eigenstates of the Schrödinger equation, which we can express in spherical coordinates as $\psi(r, \theta, \phi) = R(r)Y_{lm}(\theta, \phi)$, where Y_{lm} is a spherical harmonic. The radial component of the Schrödinger equation is given by

$$\frac{1}{r^2}\frac{d}{dr}r^2\frac{d}{dr}R(r) - \frac{l(l+1)}{r^2}R(r) + \frac{2m_e}{\hbar^2}(E - V(r))R(r) = 0 \tag{1.6}$$

In the above equation, the $-l(l+1)/r^2$ term is known as the centrifugal barrier term, which effectively behaves as a repulsive force due to its negative sign. Thus when the angular momentum l is large, the centrifugal term contributes significantly and introduces a greater effect in scattering processes. This barrier term can result in escaping electrons becoming temporarily trapped in a spatial region near and on the perimeter of the molecular ion. Thus these resonances are quite localized, showing higher electron density closer to the core, hence they are largely decoupled from the external environment (they can be observed in both free molecules and those adsorbed onto surfaces). Further, scattering from a resonance originating from an angular momentum barrier can impart a well-defined angular momentum character on the electron, which can be observed in angle-resolved measurements. Certain studies have measured trapping of angular momentum components of the continuum molecular wave function ranging from $l = 1$ to $l = 5$ [34].

A diagram showing the central concept behind the shape resonance is shown in Fig. 1.7. On the left, a depiction of a flat continuum is juxtaposed with a structured continuum possessing a shape resonance. On the right, the scattering behavior is shown for the shape resonance, which varies depending on the excitation energy. The mechanism of relaxation is that of the familiar single-channel barrier-penetration model of quantum mechanics, with the resonance behavior emerging from the shape of the potential barrier (the inner and outer wells of the potential). In this simplified illustration, we see that the effective potential an escaping electron experiences possesses an inner well at small electron-ion separations, a potential barrier at intermediate separations, and an outer repulsive region at large distances. The inner well is formed by the partially screened nuclei of the molecular core, while the barrier originates from the competing repulsive (centrifugal) and attractive (Coulombic) forces within the molecule and on its perimeter (where these forces are more closely balanced). The outer repulsive region lies further away from the molecular core, where the centrifugal and Coulombic terms are no longer balanced.

A depiction of the wave function for the escaping electron is also shown in Fig. 1.7 for different excitation energies, which illustrates the effect of the potential barrier on the electron scattering wave function. For excitation energies below resonance ($E < E_{res}$, bottom

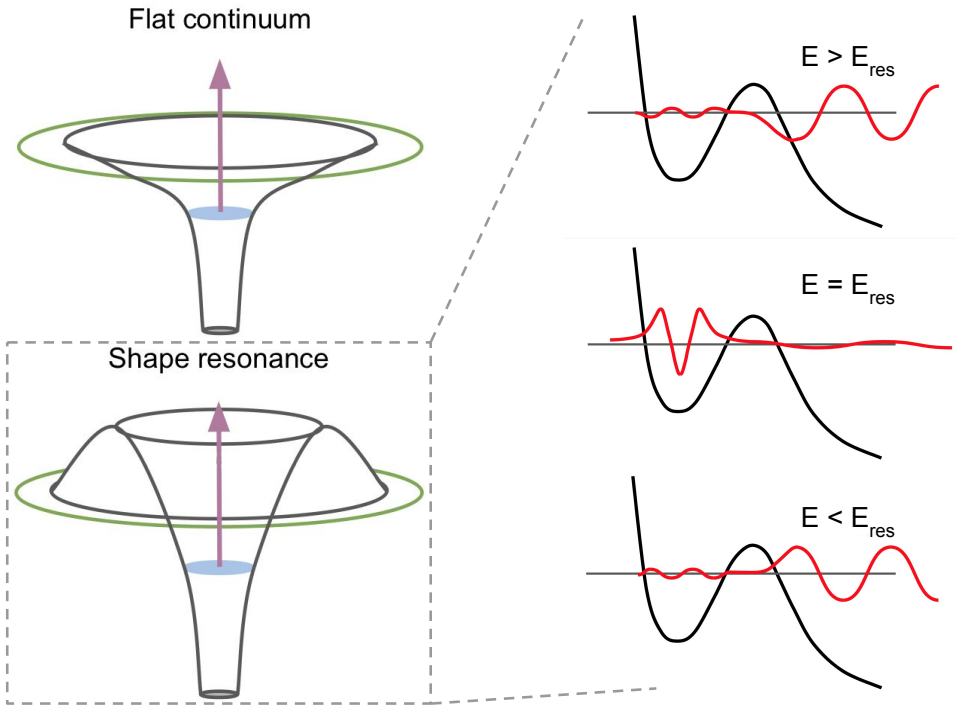

Figure 1.7: On the left, a flat continuum compared with a structured continuum containing a shape resonance. On the right, the resonant scattering behavior involved in the shape resonance, illustrating the resonant trapping mechanism, i.e. the effect of the potential barrier on the unbound electron wave function in the neighborhood of the resonant energy. On the right, the horizontal axis represents the distance between the escaping electron and the core.

right), the inner potential well does not support excitation of the quasi-bound state, but rather shows extremely low amplitude in the inner region and significantly larger amplitude in the outer region (these are essentially eigenstates of the outer region, i.e. typical continuum states). On resonance ($E = E_{res}$, middle right), the inner potential well supports the quasi-bound state, with the electron exhibiting a largely localized wave function. This wave function undergoes exponential decay in the classically forbidden region and since the potential barrier is finite, a this is not a true bound state. Thus the wave function penetrates barrier, possessing greatly diminished but non-zero amplitude in the outer region, where most of the amplitude is concentrated in the inner well (making it essentially an eigenstate of the inner well, with a small fraction leaking through the barrier and into the outer region). Like autoionizing resonances, the lifetime of the shape resonance is related to its energy width via the time-energy uncertainty principle. Last, for excitation energies above resonance ($E > E_{res}$, top right), the scenario is similar to that of $E < E_{res}$, where the scattering wave function reverts back to what is essentially an eigenstate of the outer region.

If various resonances with non-negligible scattering amplitude appear in the same energetic neighborhood, i.e. near-by one another, the scattering amplitude will be highly dependent on the excitation energy. Such continuum states can interact, depending on the relative positions and widths of adjacent resonances. For example, two adjacent resonances may overlap if they are broad, as seen in the case of shape resonances. When such shape resonances possess different symmetries, but when combined with the core produce final states of the same total symmetry, the resonances can show strong intra-channel coupling and thus interference, leading to rapid variations in the photoelectron emission pattern [90]. Careful experimental and theoretical characterization of the continuum electronic structure (identifying both the autoionizing and shape resonances) allows the role of many-electron and interference effects to be explored and illuminated in various physical processes, e.g. photoionization and photodissociation in atoms and molecules.

1.3 Theoretical Framework

In this section, we introduce the theoretical framework necessary to understand and study the properties of many-electron quantum systems, such as atoms and molecules, and their dynamics, including the correlation and resonance effects discussed in the previous section.

We first begin with a discussion of how the wave functions and their energies for a many-electron system can be solved for, specifically for the case of a molecule, using what is known as the Born-Oppenheimer approximation. This enables the extremely difficult problem of solving the non-relativistic time-independent Schrödinger equation to become more manageable. These wave functions provide an approximate description of the electron motion in the different states of the system in question. Conditions under which the Born-Oppenheimer approximation breaks down and no longer applies are also discussed.

Next, we turn to a description of quantum mechanical observables within the context of photoionization and photodissociation. Here, we provide a theoretical description of the final states that are measured in photoionization (photoelectron scattering wave functions), as well as a discussion of observables and the varying levels of information content encoded within them, while describing methods for increasing the amount of information content that a measurement carries.

Following this, we finish with a theoretical treatment of light-matter interaction, which can be described quantum mechanically using time-dependent perturbation theory. The concepts and equations presented in this section allow electronic transitions between the initial, intermediate and final states described in the previous two sections to be described and calculated. We discuss both first and second order processes and how these relate to one- and two-photon absorption. Last, a discussion of spectroscopic selection rules and their origin are provided, which allows one to determine if a dipole transition between electronic states of a quantum system is allowed or forbidden.

1.3.1 Wave Functions, The Born-Oppenheimer Approximation, and Its Limitations

Determining the wave functions and the corresponding energies of a quantum system, such as an atom or molecule, is known as the electronic structure problem, which was mentioned in the previous section. This involves quantum mechanically describing the motion of the electrons of the system in its ground and excited states, which is achieved by solving the non-relativistic time-independent Schrödinger equation. This allows the eigenstates of the neutral system, as well as the singly ionized system and beyond, to be determined. Below, we provide a discussion of this problem in the case of molecules, as the atomic case can be treated similarly and is less complex.

The state of the molecule is described by a wave function that depends on the positions of the n electrons, $\{\mathbf{r}_i\}$, and m nuclei of the system, $\{\mathbf{R}_j\}$,

$$\Psi(t) = \Psi(\mathbf{r}_1, \mathbf{r}_2, \ldots, \mathbf{r}_n, \mathbf{R}_1, \mathbf{R}_2, \ldots, \mathbf{R}_m; t) \tag{1.7}$$

which satisfies the time-independent Schrödinger equation

$$H_{mol}\Psi = E\Psi \tag{1.8}$$

for the molecular Hamiltonian H_{mol} given by

$$\begin{aligned} H_{mol} = &-\sum_{i=0}^{n} \frac{\hbar^2}{2m_e}\nabla_i^2 - \sum_{j=0}^{m} \frac{\hbar^2}{2M_j}\nabla_j^2 - \sum_{j=0}^{m}\sum_{i=0}^{n} \frac{Z_j e^2}{4\pi\epsilon_0 |\mathbf{R}_j - \mathbf{r}_i|} \\ &+ \sum_{j=0}^{m}\sum_{k>j} \frac{Z_j Z_k e^2}{4\pi\epsilon_0 |\mathbf{R}_j - \mathbf{R}_k|} + \sum_{i=0}^{n}\sum_{k>i} \frac{e^2}{4\pi\epsilon_0 |\mathbf{r}_i - \mathbf{r}_k|} \\ &= T_e + T_N + V_{eN} + V_{NN} + V_{ee} \end{aligned} \tag{1.9}$$

where M_j is the mass of nucleus j, Z_j is the atomic number of nucleus j, with m_e and e equal to the electron mass and charge, respectively, while ∇_i^2 is the Laplace operator of particle i (the Laplacian with respect to either the electron or nuclear coordinates). Here we see that the molecular Hamiltonian is a sum of five terms, the electron and nuclei kinetic energy operators T_e and T_N, the potential energy between the electrons and nuclei V_{eN}, and the potential energy associated with electron-electron and nuclei-nuclei Coulomb repulsion V_{ee} and V_{NN}.

Solving the time-independent Schrödinger equation for this Hamiltonian exactly (or even numerically) is extremely challenging, even for small systems with few nuclei and electrons, and thus approximations need to be invoked. An extremely useful approximation can be made by assuming that the motion of the atomic nuclei and electrons within a molecule can be treated separately, since the nuclei are much more massive than electrons and thus their time-scales of motion should be correspondingly much longer. This approximation was introduced in the early days of quantum mechanics by Born and Oppenheimer in 1927

[19]. Mathematically, this means separating the wave function into a product of two wave functions, one that depends exclusively on the nuclear coordinates, and another that depends on the electron coordinates and parametrically on the nuclear coordinates. This product of a nuclear and electronic wave function can be written as

$$\Psi(\mathbf{r}, \mathbf{R}) = \chi(\mathbf{R})\psi(\mathbf{r}; \mathbf{R}) \tag{1.10}$$

where $\mathbf{r}$ and $\mathbf{R}$ represent the combined coordinates of the electrons and nuclei, respectively. Factoring the wave function in this fashion is known as the Born-Oppenheimer approximation, and is justified under the adiabatic theorem of quantum mechanics, which states that gradually changing conditions allow a quantum system to adapt to its configuration, meaning if it starts in an eigenstate of the initial Hamiltonian, it will end in the corresponding eigenstate of the final Hamiltonian. Changes in the nuclear geometry of the molecule are adiabatic processes with respect to the electron dynamics. The electrons experience the same forces as the nuclei within the molecule, however they are three orders of magnitude (or more) less massive than the nuclei, hence they are able to quickly adapt in their configuration to the comparatively slow changes in the molecular structure, remaining in the corresponding instantaneous eigenstate as the molecular structure varies. Under this approximation, the Hamiltonian can be separated into electronic and nuclear terms, decoupling the system into two simpler and smaller ones that can be more readily handled. This allows the electronic eigenstates $\{\psi_n\}$ and corresponding energies $\{E_n\}$ (the electronic spectrum) to be solved for at a given clamped nuclear geometry $\mathbf{R}$ using the electronic Hamiltonian and wave function

$$H_e\psi_n(\mathbf{r}; \mathbf{R}) = (T_e + V_{ee} + V_{eN})\psi_n(\mathbf{r}; \mathbf{R}) = E_n(\mathbf{R})\psi_n(\mathbf{r}; \mathbf{R}) \tag{1.11}$$

Solving this simpler equation is still extremely challenging even for few-electron systems, with the difficulty scaling exponentially with each added electron, since a Slater determinant is involved in producing an asymmetric wave function. With the electronic spectrum solved for at each geometry $\{E_n(\mathbf{R})\}$, the nuclear part of the problem can be treated. The total potential energy of the system as a function of the nuclear geometry $\mathbf{R}$ can be computed by adding the nuclei-nuclei Coulomb repulsion term to the electronic eigenstate energies $\{E_n(\mathbf{R})\}$

$$V_n^{tot}(\mathbf{R}) = E_n(\mathbf{R}) + V_{NN}(\mathbf{R}) \tag{1.12}$$

The term $V_n^{tot}(\mathbf{R})$ is associated with the potential energy surface (PES) of the electronic state $\psi_n(\mathbf{r}; \mathbf{R})$ of the molecule. Since a molecule containing N nuclei possesses $3N-6$ internal coordinates, this hypersurface often exists in a high dimensional space, making visualization challenging and requiring projections or cuts to be made through the PES in order to produce a visual representation of the hypersurface where the nuclear part of the problem is solved. The Schrödinger equation for the total molecular Hamiltonian (including the nuclear terms) can be written as

$$H_{mol}\chi_m(\mathbf{R})\psi_n(\mathbf{r}; \mathbf{R}) = (T_N + V_n^{tot}(\mathbf{R}))\chi_m(\mathbf{R})\psi_n(\mathbf{r}; \mathbf{R}) \tag{1.13}$$

In order to solve this equation, another approximation is made, again invoking adiabaticity, by assuming that the electron wave function varies slowly with changes in nuclear geometry. Under this adiabatic approximation, the nuclear kinetic energy operator T_N does not act on the electronic wave function $\psi_n(\mathbf{r};\mathbf{R})$, i.e.

$$T_N\chi_m(\mathbf{R})\psi_n(\mathbf{r};\mathbf{R}) \approx \psi_n(\mathbf{r};\mathbf{R})T_N\chi_m(\mathbf{R}) \tag{1.14}$$

With this approximation, we can write the Schrödinger equation for the nuclear wave function

$$H_N\chi_m(\mathbf{R}) = (T_N + V_n^{tot}(\mathbf{R}))\chi_m(\mathbf{R}) = E_{nm}\chi_m(\mathbf{R}) \tag{1.15}$$

Like in the electronic case, solving this equation can again be challenging, and produces eigenstates of the nuclear wave function $\{\chi_m\}$ and the corresponding energies $\{E_m\}$. These eigenstates are quantized in the case of vibrational levels of a bound potential $V_n^{tot}(\mathbf{R})$ or are members of a continuous spectrum in the case of dissociative levels or an unbound potential. For bound potentials, in the neighborhood of the minimum of the PES for a given electronic state, the potential can be approximated as a multi-dimensional harmonic oscillator, where the normal modes (which form a basis set to describe internal motion) are decoupled. Far away from the minimum of the PES, the normal modes begin to couple and the value of the basis set is eroded. The methods described above thus allow the electronic structure problem in molecules to be treated more readily and provides significant insight into problems of spectroscopic nature.

The Born-Oppenheimer approximation, which separates the electronic and nuclear motion, relies fundamentally on the adiabatic theorem. The nuclei are massive and move slowly, relative to the electrons, which produces a gradually varying Hamiltonian, to which the electrons are able to instantaneously adapt to, remaining in the same eigenstate as nuclear geometry evolves. Within the framework of quantum mechanics, the electronic and nuclear motion can be described by characteristic frequencies $\omega \sim \Delta E/\hbar$, where ΔE is the energy difference between the involved eigenstates. Inspecting the frequency ratio between the electrons and nuclei, $\omega_e/\omega_N \sim \Delta E_e/\Delta E_N$, we find a ratio to be on the order of 100 or greater (the spacing between electron states is rougly 10 eV, while the spacing between vibrational levels is roughly 100 meV). However, there may exist molecular geometries where the splitting between electronic eigenstates becomes comparable (or less than) to the spacing between vibrational levels. In such cases, the time-scales for electron and nuclear motion become similar and the adiabatic approximation no longer holds, leading to non-Born-Oppenheimer effects. Here, the electron and nuclear motion can become concerted, where the rapidly changing conditions cause the electron wave function to no longer be able to instantaneously adapt to the varying nuclear configuration (known as a diabatic process), and thus the electrons do not remain in the same eigenstate, instead ending up in some linear combination of states (that reproduce the initial instantaneous probability density).

When the adiabatic approximation was invoked by assuming the nuclear kinetic energy operator does not operate on the electron wave function, the terms that are dropped corre-

spond with derivatives of the electronic wave function with respect to the nuclear coordinates. Properly applying the product rule to $T_N\chi_m(\mathbf{R})\psi_n(\mathbf{r};\mathbf{R})$, we arrive at the expression

$$\begin{aligned} T_N\chi_m(\mathbf{R})\psi_n(\mathbf{r};\mathbf{R}) = -\sum_{j=0}^{m}\frac{\hbar^2}{2M_j}\Big(&\nabla_j^2\chi_m(\mathbf{R})\psi_n(\mathbf{r};\mathbf{R}) \\ &+2\nabla_j\chi_m(\mathbf{R})\cdot\nabla_j\psi_n(\mathbf{r};\mathbf{R}) + \chi_m(\mathbf{R})\nabla_j^2\psi_n(\mathbf{r};\mathbf{R})\Big) \end{aligned} \tag{1.16}$$

When the last two terms (involving derivatives of the electron wave function with respect to R) can not be ignored as before, they can instead be re-inserted into the molecular Hamiltonian as a perturbation. This perturbation can result in coupling between different molecular electronic eigenstates, leading to non-radiative transitions between electronic states (internal conversion) and non-adiabatic dynamics that proceed via the interaction between the electronic and nuclear degrees of freedom that are decoupled and neglected within the Born-Oppenheimer approximation. Here, non-adiabatic coupling arises from the nuclear kinetic energy operator acting on adiabatic electronic states.

Let us consider the simplest case, where two electronic states approach one another energetically, enabling non-adiabatic coupling between the two eigenstates that can result in efficient radiationless population transfer. In such a scenario, we can express the total wave function as a linear combination of the two electronic states

$$\Psi(\mathbf{r},\mathbf{R}) = \chi_1(\mathbf{R})\psi_1(\mathbf{r};\mathbf{R}) + \chi_2(\mathbf{R})\psi_2(\mathbf{r};\mathbf{R}) \tag{1.17}$$

where this wave function solves the time-independent Schrödinger equation

$$H_{mol}\Psi(\mathbf{r},\mathbf{R}) = E(\mathbf{R})\Psi(\mathbf{r},\mathbf{R}) \tag{1.18}$$

Projecting left with the electronic state $\langle\psi_j|$, we can re-express this in matrix form as

$$\left[\begin{pmatrix} T_N^{11}(\mathbf{R})+E_1(\mathbf{R}) & T_N^{12}(\mathbf{R}) \\ T_N^{21}(\mathbf{R}) & T_N^{22}(\mathbf{R})+E_2(\mathbf{R}) \end{pmatrix} - \begin{pmatrix} E(\mathbf{R}) & 0 \\ 0 & E(\mathbf{R}) \end{pmatrix}\right]\begin{pmatrix}\chi_1(\mathbf{R})\\ \chi_2(\mathbf{R})\end{pmatrix} = 0 \tag{1.19}$$

where $E_1(\mathbf{R})$ and $E_2(\mathbf{R})$ are the energies of the two electronic states of the linear combination and $T_N^{ij}(\mathbf{R})$ is given by

$$T_N^{ij}(\mathbf{R}) = \langle\psi_i(\mathbf{r};\mathbf{R})|T_N(\mathbf{R})|\psi_j(\mathbf{r};\mathbf{R})\rangle \tag{1.20}$$

where the integration in the above matrix element is preformed over the electronic coordinates only. It is possible to find a basis in which these off-diagonal coupling matrix elements vanish, which involve first and second derivatives of the wave function with respect to R (by use of the product rule with the Laplacian, see Eq. 1.16), i.e.

$$\langle\psi_i(\mathbf{r};\mathbf{R})|\frac{\partial}{\partial R}|\psi_j(\mathbf{r};\mathbf{R})\rangle = \langle\psi_i(\mathbf{r};\mathbf{R})|\frac{\partial^2}{\partial R^2}|\psi_j(\mathbf{r};\mathbf{R})\rangle = 0 \tag{1.21}$$

This can be achieved through a coordinate transformation, by performing a rotation of the original adiabatic electronic states $\{\psi_n\}$ (those found under the adiabatic approximation) to what are known as the diabatic electronic states $\{\phi_n\}$,

$$\begin{pmatrix}\phi_1\\ \phi_2\end{pmatrix} = \begin{pmatrix}\cos\theta(\mathbf{R}) & \sin\theta(\mathbf{R})\\ -\sin\theta(\mathbf{R}) & \cos\theta(\mathbf{R})\end{pmatrix}\begin{pmatrix}\psi_1\\ \psi_2\end{pmatrix} \tag{1.22}$$

Following this coordinate transformation, the coupling between diabatic electronic states now emerges due to matrix elements of the form $\langle\phi_i|H_e|\phi_j\rangle$, where H_e is the electronic Hamiltonian. In the case of diatomic molecules (i.e. the case where the PES is one-dimensional, meaning a potential energy curve), the diabatic electronic states can cross one another (becoming degenerate), whereas the adiabatic electronic states possess avoided crossings (not reaching degeneracy). These avoided crossings arise as the two eigenvalues of a Hermitian matrix (representing an observable) can not cross one another in energy. If the corresponding electronic state wave functions for the diabatic and adiabatic states are examined, it is found that the diabatic states retain their electronic character in the energetically degenerate region, while the adiabatic states rapidly change in electronic character in the neighborhood of the avoided crossing. The probability of undergoing a non-adiabatic transition between different electronic states in the avoided crossing region was famously explored by Landau and Zener in 1932 (as well as Stueckelberg and Majorana) [88, 171]. Here, an analytic equation (known as the Landau-Zener formula) for the probability of undergoing a non-adiabatic transition in a two-state quantum system was derived using the adiabatic and diabatic representations of the electronic states, given by

$$P = e^{-2\pi\Gamma} \tag{1.23}$$

where Γ is given by

$$\Gamma = \frac{a^2}{\hbar|\alpha|} \tag{1.24}$$

where a is the off-diagonal matrix element in the Hamiltonian of the system that couples the two states and $\alpha = \frac{\partial}{\partial t}(E_2 - E_1) = v\frac{\partial}{\partial R}(E_2 - E_1)$, where $v = \frac{\partial R}{\partial t}$ is a measure of the classical velocity of the nuclei, i.e. the rate of change of the internuclear distance or bond length. Under this formulation, at very low velocities, the adiabatic theorem approximately holds (and thus the Born-Oppenheimer approximation) and the likelihood of undergoing a non-adiabatic transition between different electronic states is vanishing. As the velocities of the nuclei increase, the adiabatic theorem begins to lose validity and the probability of the wave function undergoing a non-adiabatic transition between electronic states, propagating from one adiabatic PES onto another, increases.

A simple cartoon depiction of an avoided crossing in the diatomic LiF molecule is shown in Fig. 1.8, which shows the potential energy of two electronic states as a function of the bond length. Here, the potential energy curves for the $X^1\Sigma^+$ and $B^1\Sigma^+$ electronic states exhibit an avoided crossing when the bond length is stretched to internuclear separations

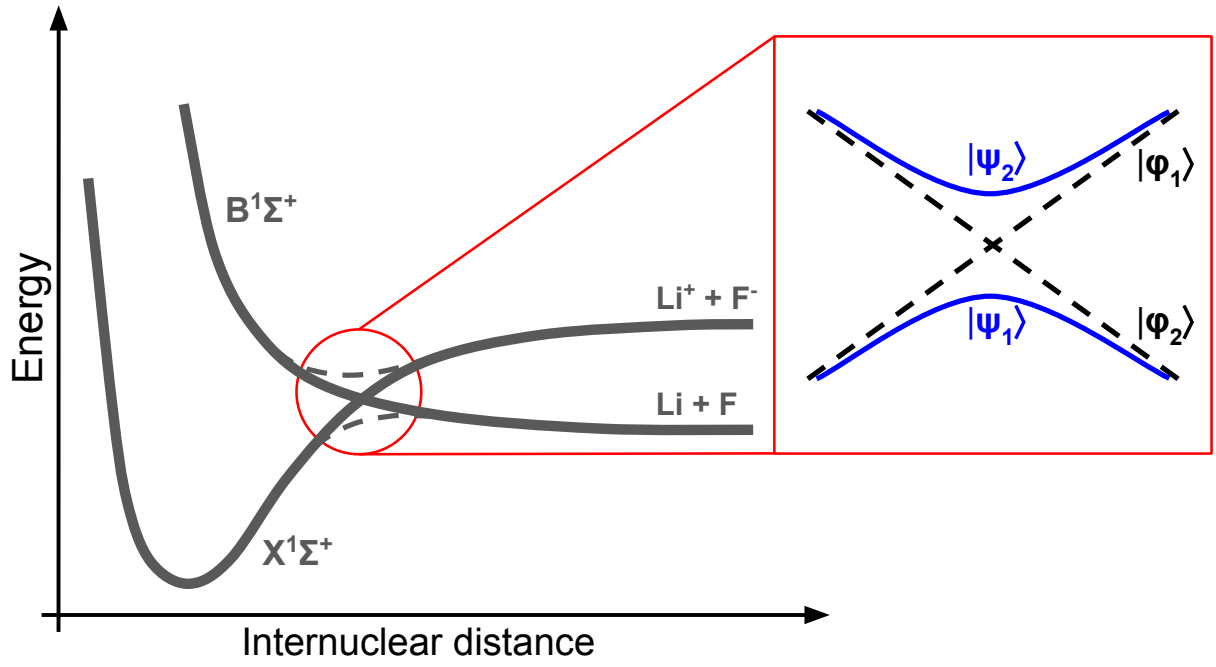

Figure 1.8: An avoided crossing exhibited by potential energy curves in the diatomic molecule LiF, showing the potential energy of two electronic states as a function of bond length. The difference between the two adiabatic limits of the $X^1\Sigma^+$ and $B^1\Sigma^+$ is given by the ionization potential of Li minus the electron affinity of F. In the inset on the right, the diabatic electronic states $\{\phi_i\}$ are shown as black dashed curves, while the adiabatic electronic states $\{\psi_i\}$ are shown as solid blue curves. In the neighborhood of the coupling region, the diabatic states cross one another and can be locally approximated as linear, while the adiabatic states avoid one another. Far away from the coupling region, the two representations are equivalent, where the Born-Oppenheimer approximation holds.

greater than that of the neutral ground state ($X^1\Sigma^+$). The non-adiabatic coupling region is shown in the inset on the right, with the adiabatic and diabatic representations of the electronic states shown as solid blue and dashed black curves, respectively. Here the adiabatic states are seen to avoid each other, while the diabatic states cross, becoming degenerate at a critical geometry, where they are locally approximated as linear. It can be seen that further away from the coupling region, the adiabatic and diabatic representations converge to one another, becoming identical (where the states are well separated and hence the Born-Oppenheimer approximation is once again valid at these geometries). This is a famous example of an avoided crossing that can lead to a "haproon" mechanism of charge transfer and LiF formation. Here a fluorine anion approaches a lithium cation on the upper potential energy curve from large separations. As the atomic separation converges to the coupling

region, the anion "harpoons" the cation and charge is exchanged between the Li and F atoms, resulting in an abrupt increase in electron density on the Li atom and leading to LiF formation in its ground state. This process can occur with some non-zero probability, while the anion and cation can also forward- or back-scatter from each other, without charge exchange and bond formation (or with charge exchange and without bond formation).

In polyatomic molecules possessing greater than two nuclei, i.e. beyond the one dimensional case, the adiabatic PESs can still energetically approach one another at various geometries. At and in the neighborhood of these geometries where two or more electronic states become degenerate, the non-adiabatic coupling can be non-vanishing and non-Born-Oppenheimer dynamics can ensure (coupled electron-nuclear motion). These locations on the PESs are known as conical intersections, and have gained widespread appreciation in recent decades in physics and chemistry for their role in governing various non-adiabatic phenomena, e.g. certain reaction mechanisms in photochemistry. Like in the one-dimensional case, the character of the electronic states in the adiabatic representation vary rapidly near these conical intersections, and the off-diagonal coupling matrix elements involving derivatives of the electronic wave function with respect to the nuclear coordinates can become non-negligible. In such cases, the Born-Oppenheimer approximation completely loses validity. These conical intersections often play a significant role in electronic relaxation of a molecular system following photoexcitation to an excited electronic state, where the non-adiabatic processes can out-compete other processes such as fluorescence and dissociation by many orders of magnitude. Examples of non-adiabatic dynamics proceeding through conical intersections range from the photostability of DNA and RNA bases, to the photoisomerization of rhodopsin (a light-sensitive receptor protein present within the rods and retina of biological organisms) required in the first step of vision [140, 76, 158, 33].

Studying these critical non-adiabatic effects in diatomic and polyatomic molecules, which can have significant influence in steering photon-driven molecular processes and dynamics, is challenging for various reasons. In particular, this is because the photon energies required to access such regions of the PESs often lie in the VUV and the time-scales of these dynamics lie in the femtoseconds (in general, the excited wavepacket only briefly traverses these coupling regions, making the dynamics difficult to capture and resolve). Thus probing this concerted electronic and nuclear motion and unraveling the many-particle quantum dynamics involved typically requires femtosecond VUV pulses and sensitive spectroscopic techniques, which poses significant experimental challenges.

1.3.2 Observables and Their Information Content

In order to accurately characterize and interrogate the many-electron and non-adiabatic effects that can occur in atoms and molecules described in the previous sections, we can turn to the methods and techniques of quantum metrology, which broadly encapsulates experimental measurements that provide information on the quantum mechanical properties of the system (e.g. the populations, relative phases, correlation and entanglement etc). As we shall see in this section, extracting information on the quantum state of the system possesses

significant and inherent challenges associated with the nature of quantum mechanics (we can only measure what corresponds with a wave function squared, measurement involves projecting the wave function to some experimentally observable quantity, while integrating over unobserved variables of the wave function, etc), and often measurements provide only a general view of the underlying dynamics, without detailed insight. This is because the extremely high dimensional quantum system is in essence projected down into one or a few dimensions that are measured, which will intrinsically result in the loss of information content. To extract a more complete and resolved picture of the dynamics of a quantum system and its subtleties, higher dimensional, higher information content measurements and techniques of quantum metrology need to be relied on. Although such high information content measurements are generally more challenging and involved, they display increased sensitivity to the quantum mechanical properties and details of the system.

One particularly efficacious manner of probing and studying a quantum system is through photoionization and/or photodissociation, i.e. using photons to remove electrons and/or cleave bonds in the system. Here, the charged particles that emerge from the interaction of the quantum system with an electromagnetic field can be carefully measured using different charged particle detection and imaging schemes, which have undergone immense advancement in the past few decades. These charged particles can encode information on the properties of the quantum system, where suitably designed measurements can extract this information content, often by projecting the charged particles onto position- and/or time-sensitive detectors in the far field. These strides in charged particle detection paired with the advances in ultrafast VUV and X-ray light sources described in the first section have in recent years enabled breakthroughs in perturbative spectroscopic measurements carrying high information content. Since the innate photoionization and photodissociation dynamics of scattering systems like atoms and molecules can be shaped by many-electron and non-adiabatic effects, we seek an observable that will be highly sensitive to these quantum effects.

In quantum mechanics, an observable corresponds with some measurable physical quantity that somehow depends on the final quantum state of the system, i.e. the final state wave function, which corresponds with some Hermitian linear operator. Within the context of photoionization, final states for photoelectrons are continuum electron wave functions, or free particle wave functions (eigenstates of the ionization continuum). Performing a measurement on the photoelectron wave function involves projecting this continuum state onto some observable corresponding with the measurement. In atomic and molecular photoionization, the continuum states in question amount to scattering solutions of the local ionic scattering potential $V(\mathbf{r})$, formed by the charged core from which the photoelectron scatters. The exact form of the localized scattering potential $V(\mathbf{r})$ depends on the geometry of the scattering system. Using the framework of scattering theory, a photoelectron scattering wave function $\Psi(\mathbf{r})$ can be expressed in what is known as partial wave expansion, which involves decomposing the scattering solution into its constituent angular momentum components, i.e.

$$\Psi(\mathbf{r}) = \sum_l \sum_m \psi_{lm}(\mathbf{r}) = \sum_l \sum_m c_l \Phi_l(r) Y_{lm}(\theta, \phi) \tag{1.25}$$

where c_l and $\Phi_l(r)$ are an angular momentum dependent coefficient and radial wave function, respectively, and $Y_{lm}(\theta, \phi)$ are the angular basis set of spherical harmonics. Here, the exact form of c_l and $\Phi_l(r)$ depends on the nature of the scattering potential $V(\mathbf{r})$. This partial wave expansion provides an exact description of the asymptotic wave function in the far-field, with each component carrying a relative phase. The exact relationship between the phases of the different angular momentum components can strongly shape the form of this far-field scattering wave function. Thus performing a measurement on the scattering wave function can provide phase sensitivity that is self-referenced.

As mentioned earlier, we can not directly measure this scattering wave function and any general observable corresponds with the modulus of the wave function squared, i.e.

$$I(\mathbf{r}) = \Psi^*(\mathbf{r})\Psi(\mathbf{r}) = |\Psi(\mathbf{r})|^2 \tag{1.26}$$

where I is the intensity of some observable quantity (e.g. particle flux, particle energy, etc). This operation of squaring the wave function results in a loss of access to the absolute phase of the wave function. However, as we can see from Eq. 1.25, taking the conjugate of this summation and multiplying it with the summation itself will result in a large number of cross terms between different angular momentum components (terms of the form $\psi^*_{l'm'}(\mathbf{r})\psi_{lm}(\mathbf{r})$). These cross terms can result in interference, which is shaped by the relative phases between the different angular momentum components and their amplitudes. Thus, it is possible to retrieve information on the relative phases the wave function, even though the global phase of the wave function is inaccessible and can not be observed. This is illustrated in Fig. 1.9, which depicts a simplified view of a photoelectron scattering wave function (two different spherical harmonics possessing equal weight) and the angular interference pattern that it generates. Here it is seen that the interference pattern evolves drastically as the relative phase between the two angular momentum components of the scattering wave function varies between 0 to π.

To derive a more useful functional form for the generic observable given in Eq. 1.26, we first can rewrite this expression as

$$I(E, r, \theta, \phi) = \sum_{l'm'} \sum_{lm} \psi^*_{lm}(E, r, \theta, \phi)\psi_{lm}(E, r, \theta, \phi) \tag{1.27}$$

where we have simply expanded out the coordinate dependence of the wave function explicitly (i.e. $\mathbf{r} \rightarrow (E, r, \theta, \phi)$), where E is the photoelectron kinetic energy and (r, θ, ϕ) are the usual spherical coordinates. This observable generally corresponds with the observed particle yield at a particular coordinate in space, (r, θ, ϕ), at a given kinetic energy, E. Here we see that the coherent summation runs over both pairs of angular momentum quantum numbers (l, m) and (l', m'). The interference that arises between cross terms of different angular momentum mentioned in the last paragraph is made explicit in this equation. For a given

$$|\Psi_{e^-}\rangle = Y_{20}(\theta,\phi) + Y_{40}(\theta,\phi)e^{-i\theta'}$$

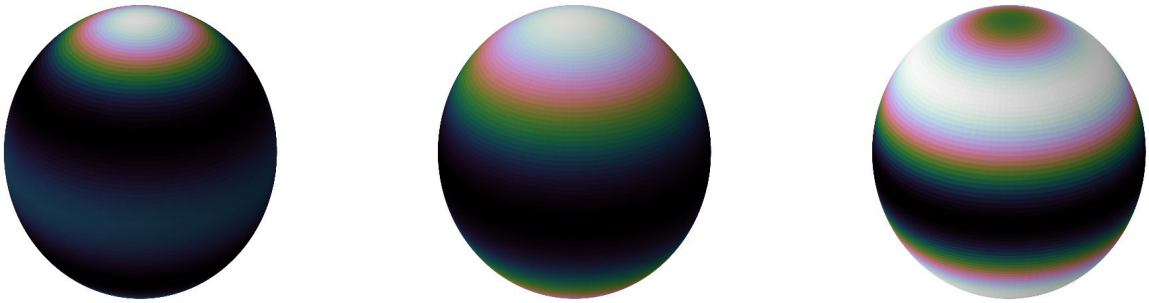

$\theta' = 0$ $\theta' = \frac{\pi}{2}$ $\theta' = \pi$

Figure 1.9: A simple depiction of an angular interference pattern generated by a photoelectron scattering wave function, exhibiting relative phase sensitivity. Here, the scattering wave function is composed of a linear combination of two different and equally weighted spherical harmonics ($Y_{20}(\theta,\phi)$ and $Y_{40}(\theta,\phi)$). As the relative phase between the two different angular momentum components varies between $\theta' = 0$ to π, the observed angular flux correspondingly varies.

observable, any unobserved coordinates of the scattering wave function are integrated over. Thus for measurements that involve projecting the photoelectron scattering wave function to some position- and time-sensitive detector in the far-field (i.e. measuring the asymptotic form of the scattering wave function), as in many energy- and angle-resolved photoelectron measurements, the radial coordinate of the scattering wave function is integrated over and the observable takes the form

$$I(E,\theta,\phi) = \int \left(\sum_{l'm'} \sum_{lm} \psi^*_{lm}(E,r,\theta,\phi)\psi_{lm}(E,r,\theta,\phi) \right) r^2 dr \tag{1.28}$$

Photoelectron measurements that are energy- and angle-resolved can exhibit great sensitivity to the aforementioned interference effects between the different angular momentum components due to their relative phase differences, which manifest as energy-dependent angular interference patterns. For energy-resolved observables, such as the photoelectron energy spectrum, the unobserved angular coordinates of the scattering wave function are also intergated over, with the observable taking the form

$$I(E) = \int\int\int \left(\sum_{l'm'} \sum_{lm} \psi^*_{lm}(E, r, \theta, \phi) \psi_{lm}(E, r, \theta, \phi) \right) r^2 \sin(\theta) dr d\theta d\phi \tag{1.29}$$

while for measurements of the photoelectron yield alone, all coordinates of the scattering wave function are integrated out and the observable is given by

$$I = \int\int\int\int \left(\sum_{l'm'} \sum_{lm} \psi^*_{lm}(E, r, \theta, \phi) \psi_{lm}(E, r, \theta, \phi) \right) r^2 \sin(\theta) dr d\theta d\phi dE \tag{1.30}$$

Here it is apparent that as more coordinates of the scattering wave function are integrated over, the information content that is encoded in those coordinates of the wave function is also integrated over and lost. Thus as the dimensionality of the observable undergoes reduction, the information content that is carried by the measurement is also reduced and sensitivity to the subtle quantum dynamics and interference effects becomes compromised. Energy- and angle-resolved measurements thus carry the highest amount of information content on the scattering wave function and allow the photoionization dynamics to be probed with a higher degree of sensitivity when compared with other lower dimensional observables.

Equation 1.28 for an energy- and angle-resolved observable can be re-expressed in terms of a spherical harmonic basis, with energy-dependent expansion coefficients

$$I(E, \theta, \phi) = \sum_{l=0}^{2n} \sum_{m=-1}^{l} \beta_{lm}(E) Y_{lm}(\theta, \phi) \tag{1.31}$$

where $Y_{lm}(\theta, \phi)$ are the spherical harmonics and the coefficients $\beta_{lm}(E)$ are the energy-dependent anisotropy parameters, also known as the energy-dependent β parameters. These energy-dependent β parameters fully characterize the form of the observed energy-resolved photoelectron angular distribution and encode all the information content. The summation over l involves a maximum index of $2n$, where the exact value of n depends on the nature of the measurement. For example, in photoelectron angular distributions that are measured in the molecular frame, $n = l_{max}$, where l_{max} is the maximum allowed value of the photoelectron orbital angular momentum component (which is determined via molecular symmetry). Molecular frame measurements can be achieved, for instance by aligning the molecules within the lab frame preceding photoionization, or through dissociative photoionization combined with coincidence techniques, where a recoiling fragment ion can be used to establish the orientation of the molecule at the instant of photoionization and thus the electron emission pattern can be rotated into this frame. For photoelectron distributions measured in the laboratory frame, n simply corresponds with the number of photons absorbed by the system during ionization. For laboratory frame measurements using a linearly polarized ionizing field, Eq. 1.31 simplifies significantly due to geometry and symmetry considerations. In this case, for an n-photon process, by reflection symmetry it follows that l must be even

($Y_{lm}(\theta,\phi)$ for odd l does not possess reflection symmetry), and by cylindrical symmetry it follows that only $m = 0$ terms can contribute ($Y_{lm}(\theta,\phi)$ for non-zero m does not possess cylindrical symmetry). Accordingly, we can be re-express Eq. 1.31 for an n-photon process using a linearly polarized field and in the laboratory frame as

$$I(E,\theta) = \frac{\sigma_0(E)}{4\pi}[1 + \sum_{l=1}^{n} \beta_{2n}(E) P_{2n}(\cos(\theta))] \tag{1.32}$$

where $\sigma_0(E)$ is the total photoionization cross section at photoelectron kinetic energy E, and $P_{2n}(\cos(\theta))$ are the Legendre polynomials in variable $\cos(\theta)$.

Molecular frame measurements carry a higher degree of information content than laboratory frame measurements, although measurements made in the molecular frame are significantly more challenging than those made in laboratory frame. Molecular frame measurements generally display finer structures and more features, when compared with laboratory frame measurements, since there are fewer restrictions on the angular momentum components of Eq. 1.31.

Since the energy-dependent anisotropy parameters carry all the information content of the scattering wave function, performing measurements that project the electrons to scattering states containing a larger set of angular momentum components (l, m) can encode a higher degree of information content than those that occur in lower dimensions of the complete angular space. Measurements that occur over a larger subspace, i.e. a larger range of (l, m) values, of the total angular space populate more partial wave components, which exhibit enhanced sensitivity to the angular interference patterns when compared with measurements that access a smaller subspace with fewer angular momentum components. Since the number of contributing β parameters in the sum in Eq. 1.32 depends on the number of photons interacting with the system, energy- and angle-resolved measurements corresponding with one-photon ionization will naturally carry less information content than a similar energy- and angle-resolved measurement corresponding with two-photon ionization, which can show more anisotropy and structure. Thus one method of gaining increased sensitivity to the photoionization dynamics is by simply increasing the amount of information encoded in the scattering wave function by performing two-photon ionization, rather than a more conventional and simple one-photon ionization measurement.

Although the entire above discussion surrounded photoelectron wave functions and corresponding observables, the above concepts and equations map equivalently to charged fragment ions produced in photodissociation, applying to both photoion yield measurements, as well as energy and/or angle-resolved measurements. The fragment ions produced in photodissociation can carry different and complementary information content on the properties of the quantum system when compared with the photoelectrons, where energy- and angle-resolved photoion measurements can for instance be sensitive to non-adiabatic dynamics, the symmetries of continuum resonances and can be used to distinguish different photoionization pathways by the symmetries of the involved states. Performing a multi-modal measurement, where two high information content observables are measured together, such as in an energy-

and angle-resolved measurements on both photoelectrons and photoions simultaneously, enables a complicated and high dimensional quantum system to be more directly mapped out and its properties more accurately characterized. In particular, if photoelectrons and photoions, either bound cations or fragment ions, originating from the same photoionization event can be measured in coincidence in an energy- and angle-resolved scheme, this provides the opportunity to probe the total wave function of the system in a detailed manner. Taking as an example the case of photoionization to a bound state of the cation, the total final wave function can be generically written as

$$|\Psi_f\rangle = |\chi_i \psi_j, \Psi_{e^-}\rangle \tag{1.33}$$

where $\chi_i \psi_j$ is the wave function of a state of the bound cation (given by the Born-Oppenheimer approximation, as described in the previous section), while Ψ_{e^-} is the photoelectron scattering wave function (given by a partial wave expansion). In a coincidence measurement, observables correspond with measurement of this total wave function, which enables kinematically complete experiments that carry close to the maximal information content possible within the framework of quantum mechanics, whereas measurements on the electrons or ions alone only probes one of these two respective pieces of the entire wave function of the quantum system.

1.3.3 Light-Matter Interaction

Electronic transitions between the eigenstates (initial, intermediate and final) described in the previous subsections can be induced via light-matter interaction, e.g. photoabsorption, which can be treated quantum mechanically within the framework of time-dependent perturbation theory. This allows the effect of introducing some time-dependent perturbing potential $V(t)$ to a time-independent Hamiltonian H_0 of the quantum system to be characterized. The perturbed Hamiltonian for the system thus becomes time-dependent, and hence so do its eigenstates and energies. Time-dependent perturbation theory allows the time-dependent occupancy of the eigenstates of the system to be characterized, which is particularly useful when considering problems in atomic and molecular spectroscopy.

As in the description above, consider a time-independent Hamiltonian H_0 to which a time-dependent perturbation $V(t)$ is applied. The total Hamiltonian of the system becomes

$$H = H_0 + V(t) \tag{1.34}$$

Next consider the set of eigenstates of the unperturbed Hamiltonian $\{|\psi_n\rangle\}$ with corresponding energies $\{E_n\}$, which satisfy the time-independent Schrödinger equation

$$H_0|\psi_n\rangle \ = E_n|\psi_n\rangle \tag{1.35}$$

Letting $|\Psi(t)\rangle$ denote the state of the perturbed quantum system at time t, this wave function obeys the time-dependent Schrödinger equation

$$H|\Psi(t)\rangle = i\hbar\frac{\partial}{\partial t}|\Psi(t)\rangle \tag{1.36}$$

Since the eigenstates of the unperturbed Hamiltonian form a complete basis, the wave function at any instant in time can be expressed as a linear combination of those eigenstates

$$|\Psi(t)\rangle = \sum_n c_n(t)e^{-iE_nt/\hbar}|\psi_n\rangle \tag{1.37}$$

where the time-dependent coefficients $c_n(t)$, often referred to as the amplitudes, are complex values that vary in time and are to be determined. These coefficients are closely related to the populations in the corresponding eigenstates. In particular, the modulus square of the amplitude $c_n(t)$ corresponds with the probability of finding the system in the state $|\psi_n\rangle$ at time t, as

$$|c_n(t)|^2 = |\langle\psi_n|\Psi(t)\rangle|^2 \tag{1.38}$$

and thus the sum of the squares of the coefficients is unity, $\sum_n |c_n(t)|^2 = 1$. Plugging this wave function into the time-dependent Schrödinger equation, we can write

$$\sum_n \left(i\hbar\frac{dc_n}{dt} - c_n(t)V(t)\right)e^{-iE_nt/\hbar}|\psi_n\rangle = 0 \tag{1.39}$$

Inserting a resolution of the identity in front of $V(t)$ and projecting left with the state $\langle\psi_k|$ (including its usual time-dependence $e^{-iE_kt/\hbar}$), the above equation reduces to a set of coupled differential equations for the time-dependent amplitudes

$$\frac{dc_k}{dt} = \frac{-i}{\hbar}\sum_n \langle\psi_k|V(t)|\psi_n\rangle c_n(t)e^{i\omega_{kn}t} \tag{1.40}$$

where $\omega_{kn} = (E_k - E_n)/\hbar$. Here, the matrix elements of V corresponds with the rate at which amplitudes are transferred between the eigenstates, where the direction of transfer is modified by the time-dependent exponential phase factor. This can cause amplitudes to oscillate over time-scales that are greater than the corresponding energy difference between levels. In order to arrive at perturbative solutions to the above differential equation, we can re-express it first in integral form

$$c_k(t) = c_k(0) + \frac{-i}{\hbar}\sum_n \int_{t_0}^{t} \langle\psi_k|V(t')|\psi_n\rangle c_n(t')e^{i\omega_{kn}t'}dt' \tag{1.41}$$

which results in an iterative solution that can be truncated at a given order, by repeatedly substituting in the expression for the basis coefficients c_k into the right side of the above equation for the coefficient c_n any desired number of times, i.e.

$$c_n(t) = c_n^{(0)} + c_n^{(1)}(t) + c_n^{(2)}(t) + \cdots \tag{1.42}$$

with $c_n^{(0)}$ being the time-independent initial state and $c_n^{(m)} \sim O(V^m)$. For example, the first order term for the amplitudes is given by

$$c_k^{(1)}(t) = \frac{-i}{\hbar} \sum_n \int_{t_0}^{t} \langle \psi_k | V(t') | \psi_n \rangle c_n^{(0)} e^{i\omega_{kn} t'} dt' \tag{1.43}$$

If the system is initialized in some state $|\psi_i\rangle$, then $c_n^{(0)} = \delta_{ni}$ and the above equation can be rewritten as

$$c_k^{(1)}(t) = \frac{-i}{\hbar} \int_{t_0}^{t} \langle \psi_k | V(t') | \psi_i \rangle e^{i\omega_{ki} t'} dt' \tag{1.44}$$

Various results follow from this first order approximation, including Fermi's golden rule, a famous equation relating the transition rate between quantum states in a system to the density of states at a particular excitation energy. In certain instances, the first order term is identically zero (the first order matrix elements of V are vanishing due to selection rules or symmetry considerations), or higher order terms can be non-negligible and significantly contribute. In such cases, first order perturbation theory provides an inadequate description and transitions can be enabled via intermediate states. Here the transition probability can be handled using second order perturbation theory, with the second order basis coefficients given by

$$c_k^{(2)}(t) = -\frac{1}{\hbar^2} \sum_m \int_{t_0}^{t} \int_{t_0}^{t'} \langle \psi_k | V(t') | \psi_m \rangle \langle \psi_m | V(t'') | \psi_i \rangle e^{i\omega_{km} t' + i\omega_{mi} t''} dt' dt'' \tag{1.45}$$

Thus the probability of making a transition between from some state $|\psi_i\rangle$ to some state $|\psi_n\rangle$ (for $i \neq n$) is given by $P_{i\to n}(t) = |c_n(t)|^2 = |c_n^{(1)}(t) + c_n^{(2)}(t) + \cdots|^2$.

If the perturbing potential is a weak electromagnetic field, as in the case of electric dipole transitions in light-matter interaction, then taking the field to be polarized along z, we can express this as

$$V(t) = -qE_0 z \cos(\omega t) \tag{1.46}$$

where E_0 is the field amplitude and ω is the frequency. From equations 1.44 and 1.45, it follows that for first order processes, the electric dipole transition probability goes as

$$P_{i\to f}(t) \sim |E_0|^2 |\langle \psi_f | z | \psi_i \rangle|^2 \tag{1.47}$$

i.e. it is proportional to the field intensity and the matrix element squared, while for second order processes, the transition probability goes as

$$P_{i\to f}(t) \sim |E_0|^4 |\langle \psi_f | z | \psi_m \rangle \langle \psi_m | z | \psi_i \rangle|^2 \tag{1.48}$$

i.e. it is proportional to the field intensity squared and the product of the two matrix elements squared. For the sake of simplicity, in the above expression for the second order transition probability, we have neglected the summation over intermediate states and taken a single state $|\psi_m\rangle$ to be actively participating. This is typical of resonant second order processes, where the excitation energy of the light is on resonance with a single intermediate state. In non-resonant second order processes (where the frequency of light does not lie on resonance with any intermediate states), the summation over intermediate levels can not be neglected in order to achieve an accurate description of the transition probability. In such cases, a single state no longer dominates as the intermediate level and many need to be invoked.

From the above, we see that first order processes correspond with interacting with the field once, i.e. absorption of a single photon, while second order processes correspond with interacting with the field twice, i.e. absorption of two photons. In the case of two-photon absorption, the excitation proceeds through an intermediate state and in non-resonant cases, the intermediate levels may not be well defined in energy (they can be both real states and virtual states). Here, conservation of energy is enforced between the initial and final states, but the virtual transitions to the intermediate levels do not have the same conservation requirements (since they are not necessarily well defined in energy).

From the above derivations, constraints immediately follow on the possible transitions between quantum states, which are known as selection rules. These rules arise due to conservation laws (momentum, parity, etc) and symmetry considerations. Spectroscopic selection rules are primarily related to what is known as the transition moment integral

$$\langle \psi_f | z | \psi_i \rangle = \int\int\int \psi_f^* z \psi_i \; dxdydz \tag{1.49}$$

As we saw above, this quantity is related to the probability of making a transition between states ψ_i and ψ_f. Thus if the above integral (matrix element) is equal to zero, the probability of making a transition between the two states is zero, i.e. the transition is forbidden. In practice, it is not necessary to explicitly evaluate the transition moment integral in order to determine if it is vanishing, as this can be determined using simple symmetry considerations. The symmetry of the transition moment function $\psi_f^* z \psi_i$ provides sufficient information to determine if the transition is forbidden. In particular, the symmetry of the transition moment function must span the totally symmetric representation of the point group of the atom or molecule in order for a transition to be allowed. Further, if the transition moment function $\psi_f^* z \psi_i$ is an odd function, the transition between states is forbidden. This function must be even in order for the transition to be allowed. Since z is an odd function, this requires ψ_f to be an even function and ψ_i to be odd, or vice versa, in order for the product $\psi_f^* z \psi_i$ to be of even symmetry. This rule applies to both the parity as well as the orbital angular momentum of the wave functions of the two states, meaning that ψ_i and ψ_f must be of opposite parity and differ in orbital angular momentum in order for a dipole transition between the two to be allowed.

In the case of parity, this is known as the Laporte rule, which applies to atoms and centrosymmetric molecules, stating that dipole transitions that conserve parity are forbidden ($g \to g$ and $u \to u$ are forbidden, where g and u correspond with gerade, i.e. even, and ungerade, i.e. odd, parity wave functions). This means that dipole-allowed transitions must involve a change in the parity of the wave function ($g \to u$ or $u \to g$).

Since the total wave function is a product of a spatial component and a spin component, the above constrains also exist on the spin wave function in addition to the spatial wave function. Since spin is directional and has odd parity, it follows that the spin quantum number, or spin multiplicity, of the system can not change (transitions where the spin direction changes are forbidden), when taken together with the change in parity of the spatial wave function. Thus, spin-allowed transitions must conserve the total spin quantum number.

Further, since a photon carries intrinsic angular momentum of one ($1\hbar\omega$), the orbital angular momentum (azimuthal quantum number L) must also change by one in dipole transitions by momentum conservation. The situation is slightly more complicated in molecules, since the transition momentum can lie either parallel or perpendicular to a molecular symmetry axis. The symmetry of the transition momentum function involves a direct product of three separate components, where the symmetry properties of each component can be determined using standard character tables and the rules for establishing the symmetry of the direct product can be found in various textbooks [9].

All of the above spectroscopic selection rules for single photon dipole transitions naturally generalize to n-photon transitions. For one-photon transitions, the spectroscopic selection rules are summarized in the table below, for atoms and homonuclear diatomic molecules ($D_{\infty h}$ symmetry). In atoms, the electronic selection rules are described by the principle quantum number n, the orbital angular momentum quantum number L (or azimuthal quantum number), the spin quantum number S, and the total angular momentum quantum number J. Under the Russell-Saunders electron coupling scheme, the atomic eigenstates are described by the atomic term symbol ${}^{2S+1}L_J$. In homonuclear diatomic molecules, the selection rules are described by the principle quantum number n, the quantum number Λ (the projection of the orbital angular momentum quantum number onto the symmetry axis), the spin quantum number S, the quantum number Ω (the projection of the total angular momentum quantum number onto the symmetry axis), the parity g/u (reflection symmetry through the inversion center), and the reflection symmetry along an arbitrary plane containing the internuclear axis $+/-$. Here, the molecular eigenstates are described by the molecular term symbol ${}^{2S+1}\Lambda^{(+/-)}_{\Omega,(g/u)}$, a group representation of the angular momenta describing the state of the molecule that is similar to the atomic term symbol. For heteronuclear diatomic molecules ($C_{\infty v}$ symmetry), the molecular term symbol is the same, however the g/u component is removed as the eigenstates no longer possess this form of inversion symmetry.

Atoms	Homonuclear diatomic molecules
$\Delta L = \pm 1$	$\Delta\Lambda = 0, \pm 1$
$\Delta S = 0$	$\Delta S = 0$
$g \leftrightarrow u$	$g \leftrightarrow u$
	$+/- \leftrightarrow +/-$

A simple depiction of dipole-allowed one- and two-photon transitions in an atom and homonuclear diatomic molecule is shown in Fig. 1.10. The atomic case is shown on the left, with the system initially in an S state, while the molecular case is shown on the right, with the system intially in a Σ state. One-photon transitions are shown in red, while two-photon transitions are shown in purple. In the molecular case, parallel transitions, i.e. those where the transition moment lies along the molecular symmetry axis, are indicated by solid lines, while perpendicular transitions, i.e. those where the transition moment lies orthogonal to the molecular symmetry axis, are indicated by dashed lines. These transition diagrams can be viewed as generic multi-path interferometers. For example, in the molecular transition diagram, there are two different two-photon transitions that both connect to the Σ and Π final states (in addition to the one-photon transitions). Differences in accumulated phase along these various paths can result in interference effects observed in the final state where the paths are summed over.

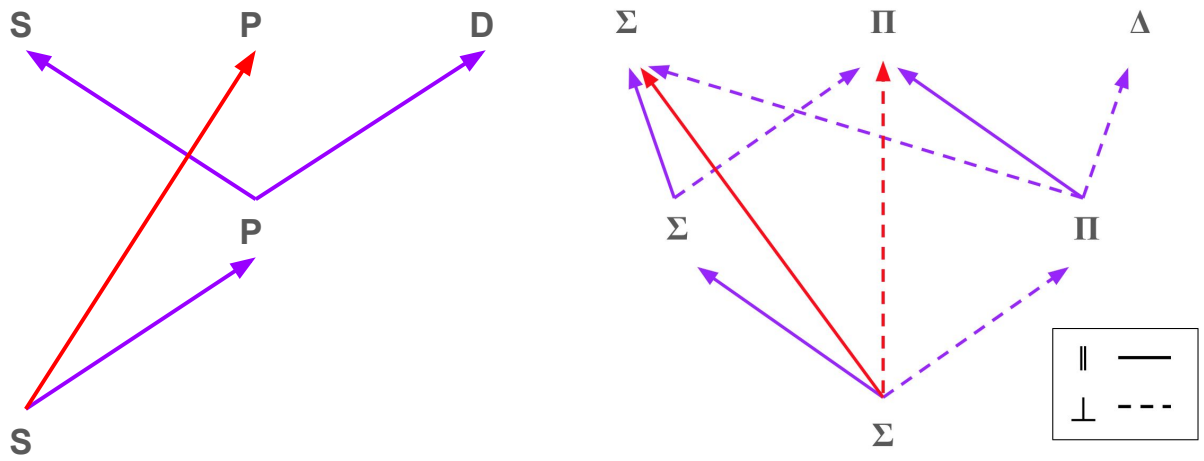

Figure 1.10: Diagrams indicating dipole-allowed transitions under spectroscopic selection rules for one- and two-photon absorption, shown in red and purple, respectively, with the case of an atomic system shown on the left (initialized in an S state), and the case of a homonuclear diatomic molecule shown on the right (initialized in an Σ state). In the molecular case, parallel transitions are indicated as solid lines, while perpendicular transitions are indicated as dashed lines. These transition diagrams are analogous to a generic multi-path interferometer, which can result in interference effects.

1.4 Assembling the Pieces

In the previous sections, various fundamental forms of quantum dynamics in many-electron systems were introduced. This included electron-electron correlation effects, electron dynamics due to continuum electronic structure (both autoionizing and shape resonances), as well as non-adiabatic dynamics involving coupled electron-nuclear motion. Additionally, various forms of observables in photoionization and photodissociation in atomic and molecular systems were introduced, together with time-dependent perturbation theory describing photoabsorption and electronic dipole transitions within the context of quantum mechanics. In this section, these pieces are assembled in order to form a complete picture that is a high information content experimental scheme for probing VUV driven two-photon ionization and dissociation dynamics in gas phase atomic and molecular systems, elucidating subtle many-particle effects.

As previously explained, increasing the information content encoded within a measurement can be achieved in various ways. One such method is to integrate over fewer coordinates of the wave function by performing a higher dimensional measurement, as in energy- and angle-resolved observables. Another approach is to perform a multi-modal measurement, where both electrons and ions are measured together, potentially in coincidence. Yet another way is to generate scattering state wave functions containing more angular momentum components, which can encode more information, by increasing the number of photons involved in the ionization or fragmentation. In the experiments presented in this thesis, these concepts are combined, making use of energy- and angle-resolved coincidence measurements on the electron-ion pair, together with an ultrafast intense VUV pulse to drive the two-photon ionization, while in the case of photodissociation (ion-pair formation, all electrons remain bound), an energy- and angle-resolved measurement is performed on the cation.

Fig. 1.11 shows a cartoon illustration of a few potential energy curves (PECs) for a generic diatomic molecule of the form AB, depicting a general experimental scheme. The molecule, in its neutral ground state shown as the gray PEC, undergoes two-photon absorption. The energy of the first photon lies near the orange PEC. In this general scheme, this state can either correspond with a dipole-allowed transition or a dipole-forbidden transition. In the case of a dipole-allowed transition, the two-photon absorption is resonant, while if the transition is dipole-forbidden, the two-photon absorption is non-resonant. As previously described, resonant and non-resonant second order process are described differently using time-dependent perturbation theory (either invoking a single intermediate state or a collection of many), and thus the photoionization and fragmentation dynamics are influenced by these details. Here, the two-photon energy (indicated by the dashed horizontal black line) lies above the green PEC corresonding with the ground state of the cation, and hence can be reached via direct ionization, producing $AB^+ + e^-$, with the photoelectron kinetic energy E_{e^-} dependent on the final vibrational level of the cation that is populated in the ionization process.

$$AB + 2\hbar\omega \rightarrow AB^+ + e^-$$

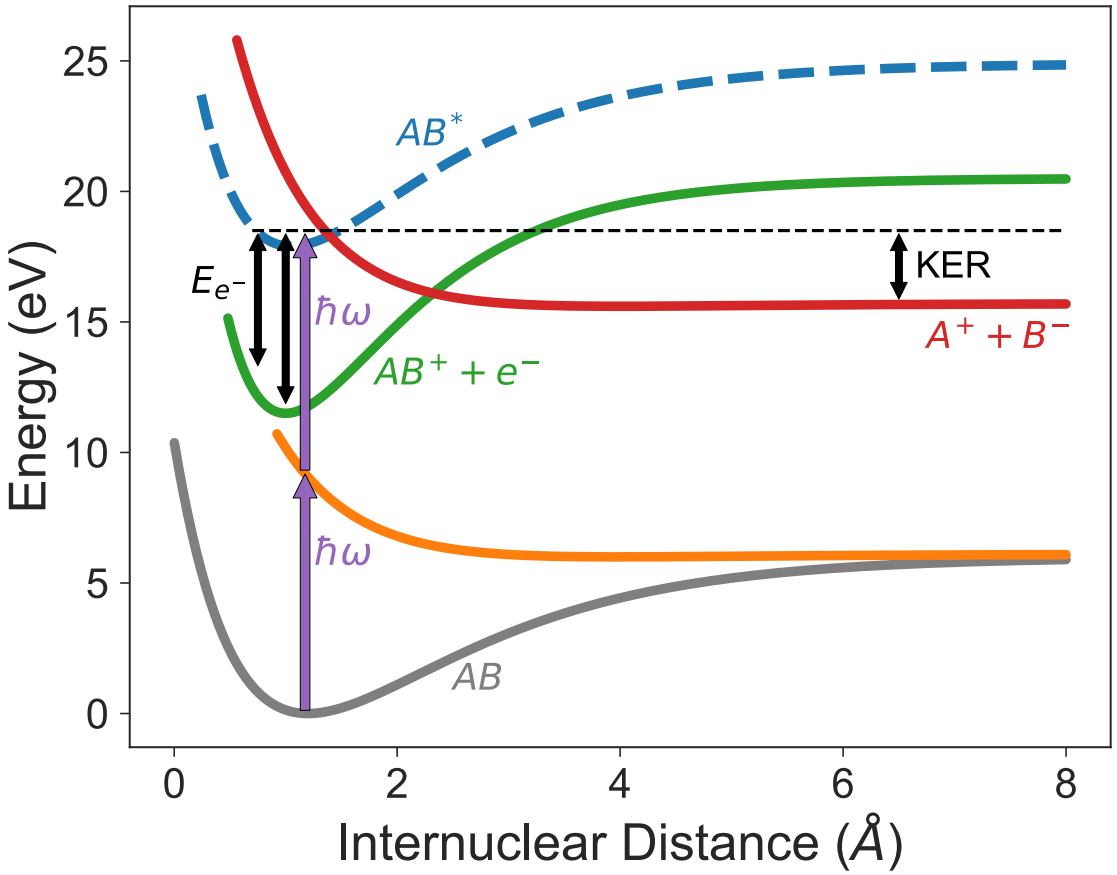

Figure 1.11: A cartoon depicting potential energy curves (PECs) for some generic diatomic molecule AB and a general experimental scheme. Two VUV photons are used to ionize or fragment the molecule. The orange PEC can represent a state that can be accessed in a dipole-allowed or forbidden transition, corresponding with resonant or non-resonant two-photon absorption, respectively. The green PEC of the cation can be reached via direct ionization, producing $AB^+ + e^-$, or via autoionization, where the dashed blue PEC associated with some continuum-embedded discrete state AB^* is first populated, with this resonance then decaying to the green PEC by emitting an electron, producing $AB^+ + e^-$. Here, the continuum resonance AB^* can also relax through a nonadiabatic transition to a dissociative state, shown as the red PEC, resulting in ion pair creation, $A^+ + B^-$. By performing an energy- and angle-resolved coincidence measurement on the electron-ion pair $AB^+ + e^-$ or an energy- and angle-resolved measurement on fragment ion A^+, the many-electron effects, nonadiabatic dynamics and continuum electronic structure can be investigated and unraveled.

Above the green PEC lying in the ionization continuum, there is a discrete state shown as the dashed blue PEC. This continuum-embedded discrete state AB^* can be populated by a two-photon transition. The resonance can then decay to the ground state of the cation (the green PEC) through autoionization, producing $AB^+ + e^-$, where the photoelectron kinetic energy E_{e^-} depends on the final vibrational level of the cation that is populated in the relaxation process (indicated by the two black double sided arrows of different lengths).

$$AB + 2\hbar\omega \rightarrow AB^* \rightarrow AB^+ + e^-$$

Performing an energy- and angle-resolved coincidence measurement on the electron-ion pair allows the many-electron dynamics and interference effects to be detected and reveals their role in shaping the photoionization process. It can also be seen that the autoionizing resonance is predissociated by a ion-pair formation state, shown as the red PEC. Here the continuum-embedded discrete state AB^* can undergo a nonadiabatic transition to the dissociative state in the neighborhood of their crossing, resulting in fragmentation with a given kinetic energy release (KER). This involves correlated electron-nuclear motion and many-electron rearrangement, with an electron and a hole localizing to opposite sites producing $A^+ + B^-$.

$$AB + 2\hbar\omega \rightarrow AB^* \rightarrow A^+ + B^-$$

In this case, performing an energy- and angle-resolved measurement on the cation enables the non-Born-Oppenheimer dynamics and resonance properties to be sensed and can indicate their influence on the fragmentation. This generic experimental scheme can be applied to a host of atomic and molecular systems in order to explore the role or many-electron and non-adiabatic effects in the dynamics of these fundamental quantum systems, using high harmonic generation as an intense VUV light source in conjunction with a coincidence charged particle momentum imaging spectrometer.

Chapter 2

Ultrafast High-Fluence Vacuum Ultraviolet Light Source

In this chapter, we will introduce the theory behind generating useful ultrafast vacuum ultraviolet pulses of light to perform measurements on two-photon ionization dynamics, which requires photons of suitable energy and pulse duration to enable two-photon ionization. We first provide a review of nonlinear frequency up-conversion in the perturbative and strong field regimes, before providing an overview of the ultrafast NIR laser system used to generate ultrafast vacuum ultraviolet pulses that are used in the experiments presented in this thesis.

At low intensities, the nonlinear optical response of a system can be treated perturbatively. However, as the field intensity rises and transitions into the strong field regime, this description breaks down. In the strong field regime, a different type of frequency conversion process emerges, known as high harmonic generation, with properties that differ from harmonics generated in the perturbative regime. High harmonic generation provides a path to generating ultrafast vacuum ultraviolet and soft x-ray photons in a table-top setting and has become a valuable tool in physics and chemistry since its discovery a few decades ago. The high harmonic generation process can be described at a single atom level using a simple semi-classical 3-step model. Both the spectral and temporal characteristics of high harmonic generation are presented in this chapter. Macroscopic effects such as phase matching and reabsorption in high harmonic generation are also considered, going beyond the single atom picture. The relationship between the driving wavelength and high harmonic generation efficiency is also discussed, which illustrates the benefits of going to shorter driving wavelengths. Finally, the experimental realization of the high-fluence ultrafast vacuum ultraviolet light source is described in detail. By using a Ti:sapphire laser system that is frequency doubled to drive high harmonic generation, sufficient pulse energies for two-photon absorption can be achieved.

2.1 Nonlinear Optics

2.1.1 Linear and Nonlinear Material Response

When a dielectric material is exposed to an electromagnetic field, it can become polarized, with an induced electric dipole moment in the atoms or molecules composing the matter. The response of the system is typically linear in the applied electric field $\vec{E}$, where the polarization (or electric dipole moment per unit volume) takes the form

$$\vec{P} = \chi \epsilon_0 \vec{E} \tag{2.1}$$

where ϵ_0 is the vacuum permittivity, and χ is the electric susceptibility of the medium. At low field strengths, the polarization is typically linearly proportional to the applied field in most materials, and as such, obeys the principle of superposition. Thus given two applied fields $\vec{E}_1$ and $\vec{E}_2$, the induced polarization can be written as the sum of the polarizations induced by each field alone

$$\vec{P}_{1+2} = \vec{P}_1 + \vec{P}_2 = \chi \epsilon_0 \vec{E}_1 + \chi \epsilon_0 \vec{E}_2$$

As the applied field strength is increased, materials can begin to exhibit a nonlinear response, where the polarization density can depend nonlinearly on the electric field, and as such, the principle of superposition is no longer valid. At moderate field intensities, a perturbative approach may be taken, where the polarization at time t, $\vec{P}(t)$, can be expanded in a Taylor series in $\vec{E}(t)$, where the coefficients are the n^{th}-order susceptibilities of the medium

$$\vec{P}(t) = \epsilon_0(\chi^{(1)}\vec{E}(t) + \chi^{(2)}\vec{E}^2(t) + \chi^{(3)}\vec{E}^3(t) + \cdots) \tag{2.2}$$

$$= \vec{P}^{(1)}(t) + \vec{P}^{(2)}(t) + \vec{P}^{(3)}(t) + \cdots$$

where $\chi^{(n)}$ is a rank $(n+1)$ tensor. From a historical perspective, the first nonlinear optical phenomena that was theoretically predicted was two-photon absorption, which was outlined in the seminal PhD work of Nobel laureate Maria Goeppert Mayer in 1931 [62]. As such, the unit of the two-photon absorption cross section is appropriately named the Goeppert Mayer (GM) unit, where 1 GM is equivalent to 10^{-50} cm^{4}s/photon. It took 30 years and the development of the first lasers before field intensities sufficient to enable such processes were achieved, and in 1961 both two-photon absorption and second-harmonic generation were observed [58, 74].

In a simple order-of-magnitude estimate, one may expect that the second-order nonlinear polarization, $\vec{P}^{(2)}$, to be comparable to the linear response, $\vec{P}^{(1)}$, when the applied field strength is on the order of the characteristic internal field strength holding together the atoms composing the material

$$E_{atom} = \frac{e}{4\pi\epsilon_0 a_0^2} \approx 5.1 \times 10^{11}\ V/m$$

where e is the electron charge and $a_0 = 4\pi\epsilon_0\hbar^2/m_e e^2$ is the Bohr radius of the hydrogen atom, where m_e is the electron mass. From this, one expects $\chi^{(2)}$ to be on the order of $\chi^{(1)}/E_{atom}$ in non-resonant conditions, and more generally, for $\chi^{(n)}$ to be on the order of $\chi^{(1)}/E_{atom}^{n-1}$, limiting frequency up-conversion processes in most materials to low-orders within this perturbative limit.

Below we introduce the simple example of second harmonic generation, providing a qualitative description. We then briefly introduce some principles from strong-field physics, before providing an overview of high harmonic generation, an extreme nonlinear optical process, the discovery of which opened the door to attosecond science.

2.1.2 An Example: Second Harmonic Generation

Second-harmonic generation, or frequency doubling, is a second order ($\chi^{(2)}$) nonlinear optical process in which two photons at the same frequency interact with a material, where the two are destroyed and a single photon at twice the frequency of the driving field is simultaneously generated. This is a single-step quantum mechanical process, not a sequential process, and is illustrated schematically in Fig. 2.1. In Fig. 2.1(a), the solid line represents the ground state of the system, while the dashed lines represent virtual levels. These virtual levels are not eigenstates of the free system and are instead associated with combined eigenstates of the system with one or more photons of the radiation field.

In second-harmonic generation, an electric field at frequency ω, which we write as

$$E(t) = Ee^{-i\omega t} + c.c.$$

interacts with a material that possesses nonzero $\chi^{(2)}$ (i.e. a medium that does not possess inversion symmetry). A nonlinear polarization $P^{(2)}(t)$ is generated in the medium, given by

$$\begin{aligned} P^{(2)}(t) &= \epsilon_0\chi^{(2)}E^2(t) \\ &= 2\epsilon_0\chi^{(2)}EE^* + (\epsilon_0\chi^{(2)}E^2e^{-i2\omega t} + c.c.) \end{aligned}$$

From the above equation, we see that the second-order nonlinear polarization $P^{(2)}(t)$ consists of a zero-frequency component (the first term) and a component oscillating at twice the driving frequency 2ω (the second term). This second term can result in the generation of light at the second-harmonic of the driving frequency, whereas the first term results in optical rectification (a DC electric field is generated across the material). It is worth mentioning that second-harmonic generation is a specific case of the more general nonlinear process known as sum-frequency generation.

Second-harmonic generation was first demonstrated at the University of Michigan in 1961 by Peter Franken and his coworkers [58], where they focused a ruby laser (lasing at 694 nm)

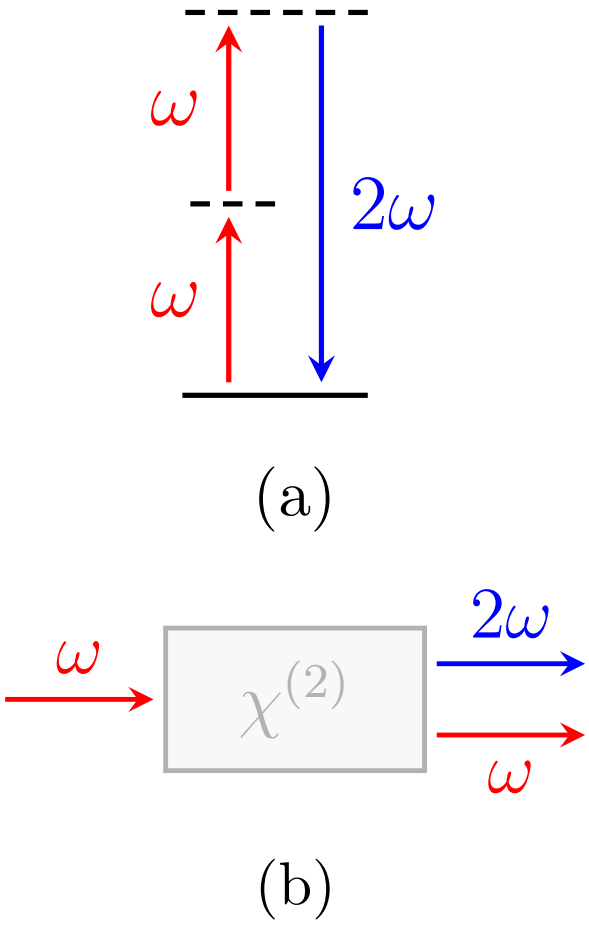

Figure 2.1: A schematic depicting (a) an energy level diagram illustrating second-harmonic generation, and the (b) geometry of second harmonic generation.

into a quartz crystal and recorded the output light using a spectrometer and photographic paper. A small signal was observed at 347 nm, indicating that the driving field had been frequency-doubled upon interacting with the quartz. However, when the results were published in the *Physical Review Letters*, the copy editor mistook the small signal at 347 nm in the image as "schmutz" and erased it prior to publication, rendering the second-harmonic signal invisible in the manuscript's primary figure. This story is well-known among the nonlinear optics community and demonstrates the technological breakthroughs achieved in this field since these early discoveries, where now in some cases nearly 100% of an applied field can be frequency converted using modern methods [21], compared with the extremely weak signal in the seminal 1961 paper [58] that was erroneously removed.

Second-harmonic generation is now a commonly used experimental technique for fre-

quency up-conversion of laser light, as well as for ultrashort pulse characterization (e.g. FROG). One such routine application is frequency doubling the NIR output of a Nd:YAG laser (which operates around 1064 nm) to a visible green frequency (around 532 nm), which can then be used to optically pump a Ti:Sapphire laser system. Another common application of second-harmonic generation is frequency doubling the NIR output of a Ti:sapphire laser system (near 800 nm) in order to generate blue light (near 400 nm). Two commonly used nonlinear materials are β-BBO (β-BaB_2O_4) and LBO (LiB_3O_5) crystals, both of which do not possess inversion symmetry, as required for nonzero $\chi^{(2)}$.

2.1.3 Strong Field Physics

The expression shown in Eq. 2.2 was derived in the perturbative limit (i.e. the weak field regime), which is characterized by a rapidly decreasing yield with increasing harmonic order, meaning successive terms in Eq. 2.2 decrease in their contribution with increasing order. At high field strengths (strong field regime), this perturbative approach breaks down, as the electric field strengths become strong enough to substantially distort the Coulomb potential of the constituent atoms. The transition into the strong field regime occurs at intensities around 10^{14} W/cm^2. At these field strengths, different nonlinear optical processes involving harmonic generation can emerge, which will be discussed in the following section.

The rapid development of ultrafast lasers has enabled electric field strengths on the order of, or exceeding, atomic field strengths to be routinely achieved at UV/Vis/IR wavelengths, where a perturbative treatment of the physics no longer holds. Instead, the light field needs to be included in the Hamiltonian of the system and new eigenstates need to be found. As such, when an atomic system is photoionized by a low-frequency field (UV/Vis/IR), the mechanism of ionizaton depends on the field strength, or intensity regime.

In the perturbative regime, photoionization ensues via multi-photon ionization, where multiple photons are absorbed, overcoming the ionization potential of the system. In the strong field regime, the electric field strength can be comparable to the internal field strength of the atom, distorting the Coulomb potential and forming a barrier that the electron can tunnel through to reach the continuum. This mechanism is known as tunneling ionization. At even higher intensities, the applied field strength can exceed the internal field strength of the atom, suppressing the barrier to the point where the electron is no longer bound. This mechanism is known as barrier suppression ionization, or over-the-barrier ionization. All three of these regimes are depicted in Fig. 2.2.

Strong field ionization can be theoretically described using the framework derived by Ammosov, Delone, and Krainov in 1986 [5], which is known as ADK theory and will be briefly discussed in a later section.

In 1965, Keldysh introduced a simple yet useful parameter which serves to distinguish between the weak (perturbative) and strong field regimes [80], named the Keldysh parameter γ. This parameter characterizes the ratio of multi-photon ionization to tunneling ionization in terms of the ionization potential of the system, I_p, and the pondermotive energy of the applied light field, U_p

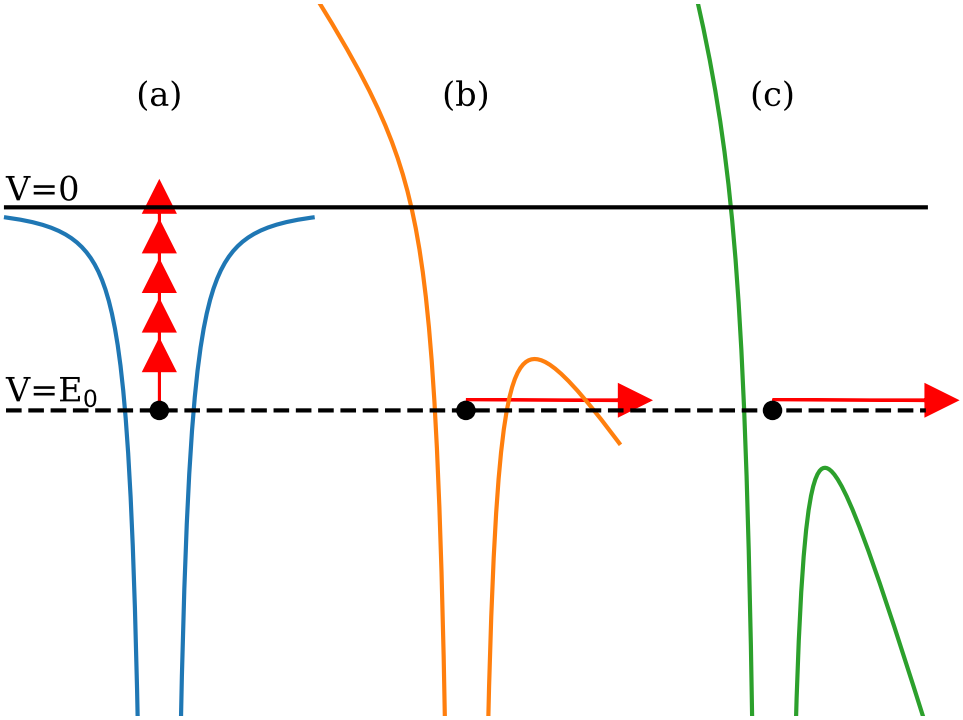

Figure 2.2: The three regimes for ionization by low-frequency fields. (a) In the perturbative limit (weak field regime), photoionization occurs via the absorption of multiple photons whose combined energy exceed the ionization potential. (b) At field strengths on the order of the atomic potential (strong field regime), the perturbative approximation is no longer valid and the applied field can distort the Coulomb potential to form a barrier, leading to tunneling ionization. (c) At field strengths exceeding the atomic potential, the barrier is suppressed such that the electron is no longer bound, resulting in barrier suppression ionization. Figure adapted from [24].

$$\gamma = \sqrt{\frac{I_p}{2U_p}} \tag{2.3}$$

where the pondermotive energy is given by

$$U_p = \frac{e^2 E^2}{4 m_e \omega^2} = 9.33 \text{ eV} \times (\lambda[\mu\text{m}])^2 \times I[10^{14} \text{ W/cm}^2] \tag{2.4}$$

where e and m_e are the charge and mass of the electron, E and ω are the amplitude and frequency of the applied field, and I and λ is corresponding intensity and wavelength.

The pondermotive energy describes the cycle-averaged kinetic energy of a free electron in an oscillating electric field, sometimes referred to as the quiver energy. For a Keldysh parameter $\gamma \gg 1$ (perturbative limit), ionization mainly ensues via multi-photon absorption, whereas for $\gamma \ll 1$ (strong field regime), tunneling is the dominant ionization mechanism. It is worth mentioning that due to the dependence of γ on U_p, the intensities required to reach the strong field regime increase with increasing frequency.

2.2 High Harmonic Generation

In 1987 at the University of Illinois at Chicago, using a KrF ultraviolet excimer laser at 248 nm, McPherson and his coworkers irradiated various rare gases and observed the generation of harmonic radiation [109]. In the case of neon, harmonics extending to the 17^{th}-order were observed. The following year, Ferray and coworkers focused an Nd:YAG laser at 1064 nm into different noble gases and observed harmonic light extending to the 33^{rd}-order in the case of argon [57]. These results came as a surprise to the physics community, as the generated harmonic light had properties which were not observed from harmonics generated in the perturbative limit. While the low-order harmonics fell off in intensity with increasing order, a "plateau" region of harmonics was observed towards higher orders, where the intensity of adjacent harmonic orders were of comparable intensity and similar across many orders, rather than exhibiting the expected rapidly decreasing yield. The plateau region was then observed to exhibit a rapid cut off in yield at very high orders. These pioneering experiments marked the first observations of a new type of nonlinear optical process, known as high harmonic generation. This nonlinear frequency up-conversion process occurs in the strong field regime, rather than the perturbative limit, and hence the properties of the radiation deviate from what had been seen in perturbative harmonic generation, due to the different mechanisms in which the radiation is generated. Below we first introduce a simple model for high harmonic generation, which is then followed by a more quantitative treatment.

2.2.1 The Three Step Model

In contrast to harmonics generated in the perturbative regime, ionization plays a central role in the high harmonic generation mechanism, which is inherently a strong field process. A semi-classical theory for the high harmonic generation process was introduced in 1993 by Schafer and coworkers [139], and Corkum and coworkers [32, 93], which treated the light generation mechanism in terms of the single atom response using a 3-step model. This intuitive description for the high-order frequency up-conversion process in the strong field is separated into three stages occurring in sequence

1. Tunneling: The strong laser field distorts the Coulomb potential of the atom, creating a potential barrier and leading to bound electrons undergoing tunneling ionization. These electrons are born in the continuum with zero (or low) velocity.

2. Acceleration: Once in the continuum, the electron undergoes classical acceleration away from its parent ion in the field of the laser (where the Coulomb potential of the core is considered to be negligible), gaining kinetic energy along its classical trajectory (which depends on the phase of the field at the instant of ionization). As the field alternates in direction, some electrons are decelerated and then driven back towards the core.

3. Recombination: A fraction of the continuum trajectories that are driven back towards the core will re-encounter the parent ion. With low probability, some of these electrons will recombine with the core, leading to the emission of a single high energy photon with energy equal to the kinetic energy of the electron plus the ionization potential of the ground state of the system. This recombination step can be thought of as the conjugate, or time-reversal, of single-photon ionization.

The 3-step model for high harmonic generation is depicted in Fig. 2.3. Since a monatomic gas possesses inversion symmetry, all even order nonlinearities vanish and only odd harmonics can be produced. It should be mentioned that the 3-step model is for a linearly polarized field, as a rotating electric field drives the electron trajectories away such that none return near the core to permit recombination. As the ellipticity of the driving field is increased, the efficiency of the high harmonic generation process rapidly decreases, first verified in 1994 by Corkum [36]. It is also worth pointing out that although high harmonic generation is inherently a strong field process, the Lorentz force places an intrinsic limit on the intensities that can be used to drive the nonlinear up-conversion. At intensities near 10^{17} W/cm^2, the magnetic component of the laser field can become significant enough to deflect electron trajectories away from the core via the Lorentz force ($q\vec{v} \times \vec{B}$) which inhibits recombination [160].

2.2.2 The Cut Off Law

The energy of the photon that is emitted in the recombination step is equal to the sum of the ionization potential of the ground state of the system and the kinetic energy of the electron, $\hbar\omega = I_p + E_{KE}$. The kinetic energy of the electron is determined by its trajectory, which depends on the phase of the field at the instant of ionization. Thus the emitted photon energy depends on the phase of the field at the time of birth of the free electron. The recombination step occurs at low field strength, where the trajectories that recombine are those of emission near the peak of the field. There are in general two such trajectories in the continuum that will result in the emission of a photon of the same energy, i.e. two trajectories that result in the same electron velocities at the instant of recombination, and these two trajectories may interfere. These are known as the short and long trajectories and are illustrated in Fig. 2.4, which depicts the relationship between the electron trajectory (determined by the phase of the field at the instant of ionization) and the recombination energy. Since different short and long trajectories recombine at different times, the emitted radiation is chirped, which

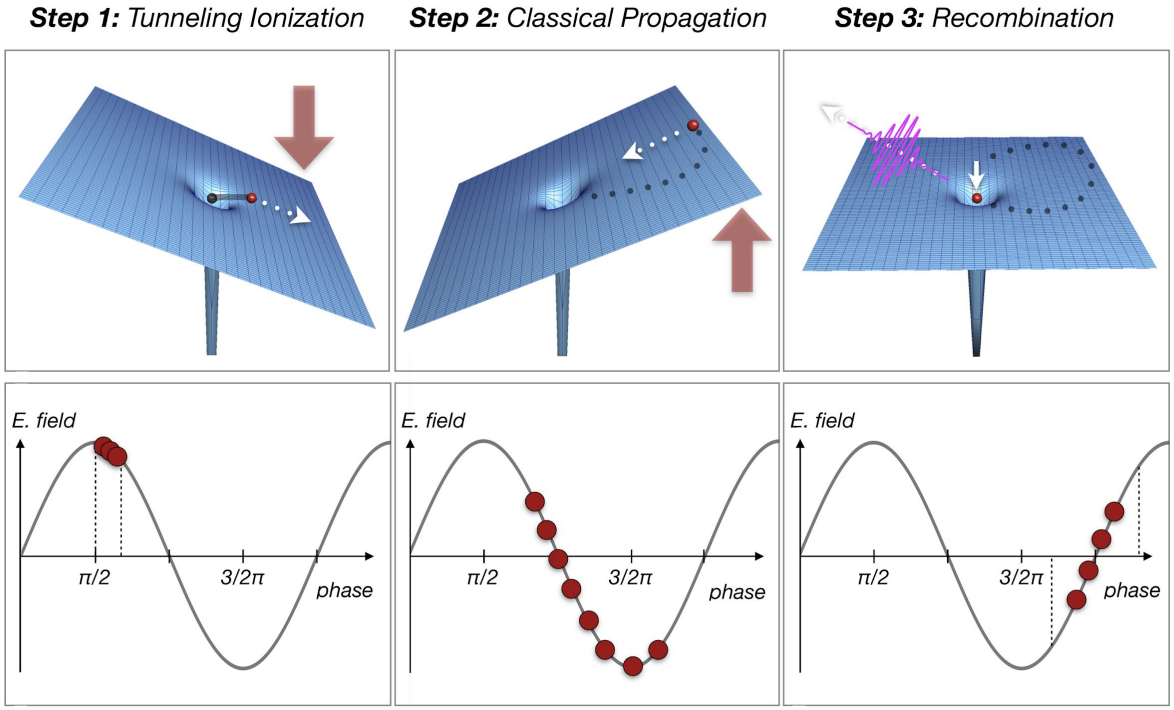

Figure 2.3: An illustration of the 3-step model of high harmonic generation. (1) Near the peak intensity of the laser field, the Coulomb potential of the atom is warped, generating a barrier. Here electrons are released into the continuum with near zero velocity via tunneling ionization. (2) Free electrons propagate along classical trajectories (that are determined by the phase at the instant of ionization), gaining kinetic energy in the laser field. As the field changes sign, some electrons are driven back towards the core. (3) A small fraction of electrons recombine with their parent ion to form the atomic ground state, resulting in the emission of a single high energy photon. This 3-step process repeats every half-cycle of the laser field, resulting in an attosecond pulse train of XUV radiation and thus forming a frequency comb in the spectral domain composed of odd harmonics of the driving frequency. Figure adapted from [154].

is known as attochirp. Electrons that are emitted at a phase of $\sim 18°$ result in the highest recombination energy, with a kinetic energy at the time of recombination of approximately $3.17U_p$ [10]. Thus the maximum photon energy emitted under this mechanism, known as the cut off energy, is given by

$$E_{max} = I_p + 3.17U_p \tag{2.5}$$

Using Eq. 2.4, we can rewrite the above expression as $E_{max} = I_p + \kappa\lambda^2 I$, where λ is

the wavelength and I is the intensity, and where all prefactors have been absorbed into the constant κ. This expression illustrates how the cut off energy depends quadratically on the driving wavelength and linearly on the intensity. Thus, the cut off energy can be pushed out to higher energies by using longer wavelengths to drive the high harmonic generation process (qualitatively, at longer driving wavelengths, the free electron spends more time in the continuum gaining kinetic energy before recombination), or by turning the field strength up, which itself is constrained by the Lorentz force from the magnetic component of the field, as well as by dispersion issues (phase matching, discussed in the following section) introduced by the generation of plasma. The cut off energy can also be extended by using a medium with a higher ionization potential. Harmonics with energies extending out to 1.6 keV have been observed using a 3.9 μm mid-IR driving field and a high pressure (tens of atm) helium gas filled waveguide [132].

2.2.3 Spectral and Temporal Properties

Each recombination event falls into a short time window of the laser cycle, resulting in an attosecond burst of radiation. A single attosecond burst has a continuous and broad spectrum. However, since the electric field of a laser oscillates many times over the duration of the pulse, the 3-step process resulting in an attosecond burst of high energy radiation is repeated every half-cycle, $T/2$, of the field. In the temporal domain, this results in an attosecond pulse train, with each attosecond burst temporally spaced by $T/2$ (i.e. at twice the driving field frequency). In the spectral domain, a frequency comb forms, whose teeth are spaced at odd integers of the driving field $\omega_n = n\omega_0$, where n is an odd integer. Due to the symmetry of the atomic medium, emission from neighboring half-cycles destructively interfere for even order harmonics of the driving field and constructively interfere for odd orders. As the driving pulse duration is decreased, the 3-step model occurs over a fewer number of half-cycles, and thus the interference process may not reach saturation, which can result in a quasi-continuum, lying in between a discrete frequency comb and continuous spectrum. Using various gating techniques (e.g. attosecond lighthouse, or amplitude, ionization and polarization gating), it is possible to limit emission to a single half-cycle of a driving pulse [27], in which case a broad and continuous spectrum is recovered. In 2017, the group of Wörner at ETH Zurich used a two-cycle CEP-stable mid-IR driver to produce soft x-rays with the shortest measured pulse duration, with a pulse length of 43 attoseconds [60], which at the time of this writing is the shortest pulse measured.

The connection between the temporal and spectral domains is equivalently captured through Fourier analysis, where the Fourier transform of an attosecond pulse train results in a frequency comb with peaks separated at odd integer harmonics of the driving field ω_0, while the Fourier transform of an isolated attosecond burst results in a broad continuous spectrum. This is depicted in Fig. 2.5. In high harmonic generation, the coherence properties of the driving field (both spatial and temporal) are imprinted onto the emitted high energy radiation [10], since recombination and emission is locked to the phase of the coherent driving field. Both even and odd harmonic orders can be generated by breaking spatial or temporal

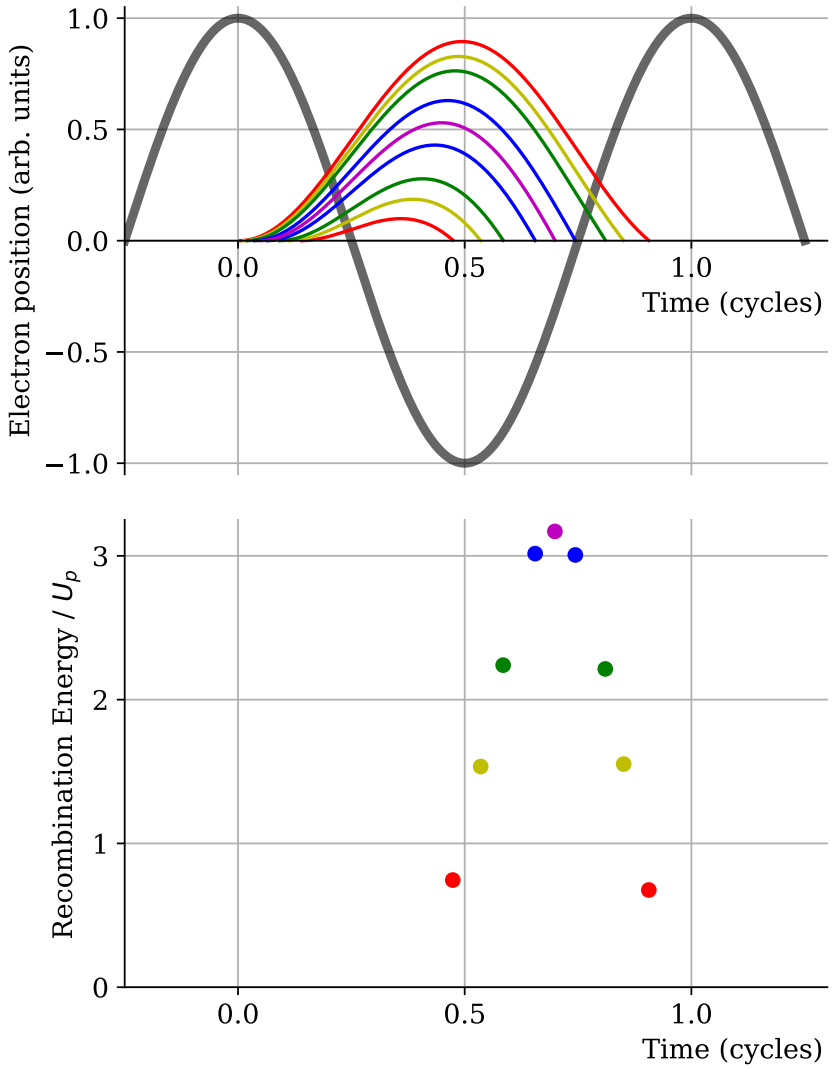

Figure 2.4: The classical trajectories taken by free electrons that emerge from tunneling ionization and their corresponding recombination energies. For a given recombination energy, there are two corresponding trajectories (short and long), shown in the same color. The phase of the field at the instant of ionization determines the trajectory and thus the recombination energy. Since different trajectories recombine with the core at different times, the emitted radiation is chirped (known as attochirp). The recombination energy scales linearly with the pondermotive potential, meaning it has quadratic dependence on the wavelength and linear dependence on the intensity. Figure from [24].

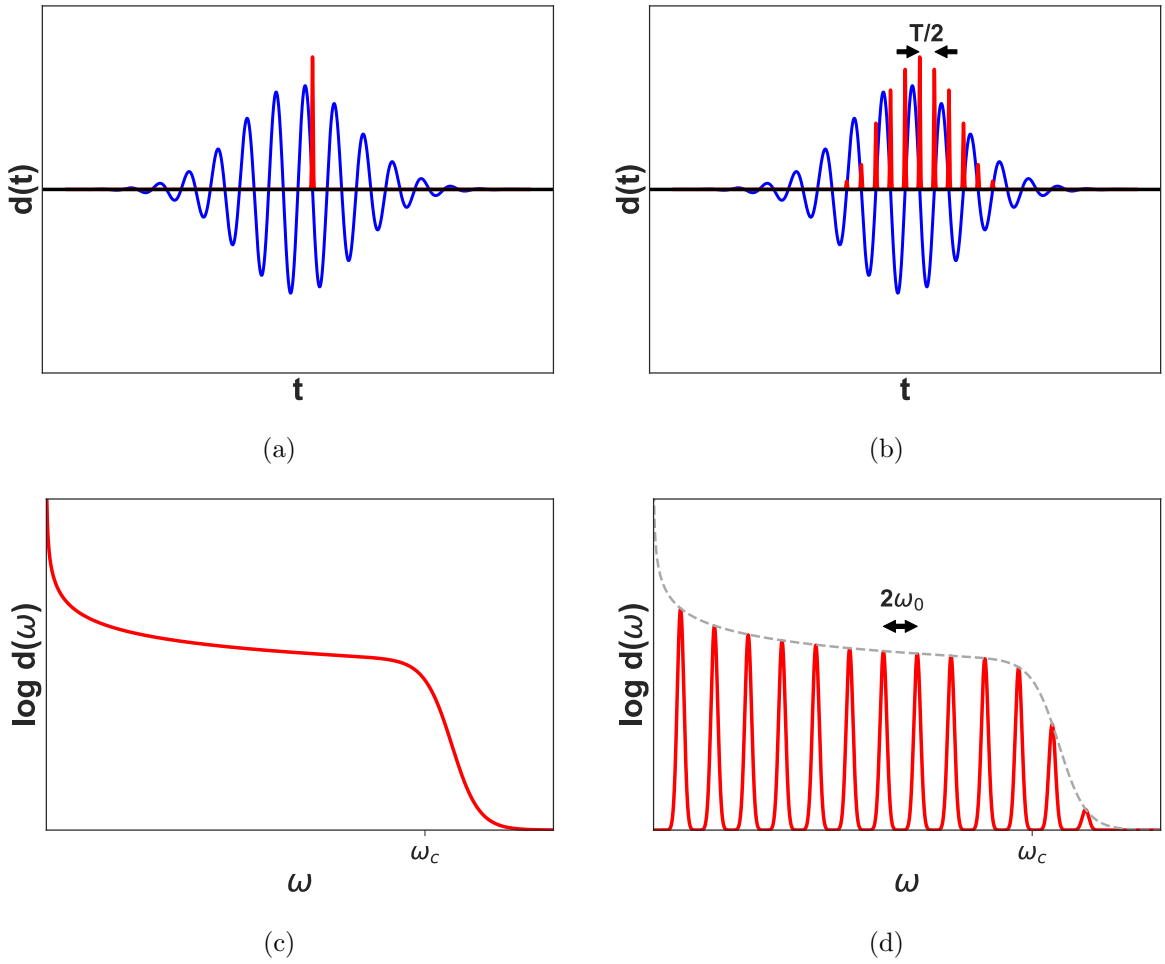

Figure 2.5: An illustration of the relationship between the temporal and spectral domains for an isolated attosecond pulse and an attosecond pulse train. The time-dependent atomic dipole moment, $d(t)$, induced by the alternating laser field is shown in the top row, and the logarithm of the corresponding frequency spectrum, $d(\omega)$, of the emitted photons is shown in the bottom row. Here, $d(t)$ and $d(\omega)$ (the temporal and spectral domain) are connected via the Fourier transform. (a) An isolated attosecond burst and (b) an attosecond pulse train (with bursts separated by half an optical cycle, T/2), shown in the temporal domain. (c) The Fourier transform of an isolated attosecond burst has a broad and continuous spectrum. (d) The Fourier transform of an attosecond pulse train forms a frequency comb, with teeth spaced at twice the driving frequency.

symmetry, either by mixing a second color with the driving field thus breaking the temporal symmetry and resulting in emission only once per cycle, or by breaking the spatial inversion symmetry of the generating medium (achieved for example using an aligned heteronuclear

diatomic molecular target as the generating medium).

The semi-classical 3-step model accurately describes the qualitative physics involved in the high harmonic generation process at the single atom level, however, an analytic and fully quantum mechanical description was presented in 1994 by Lewenstein [93]. In this theory, the time-dependent dipole moment of the target is expressed as a product of the ionization transition probability to the continuum, the wavepacket propagation in the field-dressed continuum, and the recombination transition probability with the ground state (the complex conjugate of the ionization transition probability). The Fourier transform of this time-dependent dipole moment is the emitted spectrum. An additional feature of the quantum mechanical description is that it describes how the recombination probability scales with the driving wavelength λ. As longer driving wavelengths are used, the free electron wavepacket spends more time in the continuum before returning to the parent ion (i.e. time along a trajectory scales with λ). Free electron wavepackets are initially relatively localized when born in the continuum, but naturally spread during propagation. Thus the recombination probability with the localized core reduces with increased time spent in the continuum, since the returning wavepacket becomes more diffuse and its wavefunction shares less overlap with the localized core. Both the semi-classical 3-step model and the fully quantum mechanical description only describe the mechanism for harmonics generated with energy above the ionization potential of the generating medium, while low order harmonics with energy below the ionization potential of the medium (below-threshold harmonics) require more complex descriptions involving bound states, as well as the effects of the Coulomb potential of the core on the electron trajectories in the field-dressed continuum [69, 167].

2.2.4 The Phase Mismatch Form Factor

In the previous section, high harmonic generation was described at the single atom level in terms of both the time-dependent atomic dipole moment and the 3-step model. To produce measurable vacuum ultraviolet flux, coherent emission from many atoms within a macroscopic volume is necessary. However, photons emitted by atoms that are macroscopic distances away from one another within the generating medium do not have a random distribution of phases, but rather have a fixed relationship that is locked to the phase of the driving field. Constructive interference between emitters at different locations within the focal volume leads to high flux emission, a condition known as phase matching (amounting to conservation of momentum). Below, a simple theoretical description is provided, connecting weak emission from a single atom to high-fluence coherent emission across many atoms within a macroscopic volume.

The wave equation for electromagnetic radiation propagating through a nonlinear optical medium is given by

$$-\nabla^2 \vec{E}(\vec{r},t) + \frac{1}{c^2}\frac{\partial^2}{\partial t^2}\vec{E}(\vec{r},t) = \frac{-4\pi}{c^2}\frac{\partial^2}{\partial t^2}\vec{P}(\vec{r},t) \tag{2.6}$$

where $\vec{P}$ is the polarization density of the material (given by the product of the single atomic dipole moment, d, with the medium density, ρ) [21]. In the above equation, it is apparent how a time-varying nonlinear polarization drives an electric field and can give rise to new components in the electromagnetic field. If we consider writing both the field and polarization as a superposition of waves at the driving frequency and its odd harmonics

$$\{\vec{E},\vec{P}\}(\vec{r},t) = \sum_{q \text{ odd}} \{\vec{E}_q,\vec{P}_q\}(\vec{r})e^{-i\omega_q t} + c.c.$$

then equation (2.6) admits a coupled set of driven wave equations for each harmonic q,

$$-\nabla^2\vec{E}_q(\vec{r})e^{-i\omega_q t} + \frac{1}{c^2}\frac{\partial^2}{\partial t^2}\vec{E}_q(\vec{r})e^{-i\omega_q t} = \frac{-4\pi}{c^2}\frac{\partial^2}{\partial t^2}\vec{P}_q(\vec{r})e^{-i\omega_q t}$$

$$\implies \quad \nabla^2\vec{E}_q(\vec{r},t) + \frac{\omega_q^2}{c^2}\vec{E}_q(\vec{r},t) = -\frac{-4\pi\omega_q^2}{c^2}\vec{P}_q(\vec{r},t)$$

Due to the nonlinearity of the material response, the atoms composing the medium each develop an oscillating dipole moment, which contains frequency content at ω_q. The atoms in the material oscillate with a phase determined by the applied field and in certain conditions, a phase relationship between different atoms in the material can be established, resulting in constructive interference of the emitted radiation in the forward direction. Adjusting the parameters of the driving field and the generating medium allows conditions to be found where there is maximal coherent emission across the focal volume, which is known as phase matching. In these phase matching conditions, the nonlinear material acts as a phased array of oscillating dipoles that add coherently, resulting in the field $\vec{E}_q$.

Now, let us consider a linearly polarized electric field of the form

$$\vec{E}(\vec{r},t) = \sum_{q \text{ odd}} \vec{E}_q(z,t) = \sum_{q \text{ odd}} A_q(z)e^{i(k_q z-\omega_q t)}e^{-\kappa_q z}\hat{x} + c.c.$$

where κ_q accounts for attenuation of the q^{th} harmonic along the propagation direction and satisfies the relationships $(ik_q-\kappa_q)^2 = \epsilon^1(\omega_q)\frac{\omega_q^2}{c^2}$ and $2\kappa_q = \rho\sigma$, where σ is the photoabsorption cross section at the q^{th} harmonic and ρ is the target density [21, 59]. If we split the polarization into linear and nonlinear components

$$\vec{P}(z,t) = \sum_{q \text{ odd}} \vec{P}_q^1(z,t) + \vec{P}_q^{NL}(z,t) = \sum_{q \text{ odd}} (P_q^1(z) + P_q^{NL}(z))e^{-i\omega_q t}\hat{x} + c.c.$$

then (1) reduces to a coupled set of wave equations [21]

$$\nabla^2\vec{E}_q(z,t) - \frac{\epsilon^{(1)}(\omega_q)}{c^2}\frac{\partial^2}{\partial t^2}\vec{E}_q(z,t) = \frac{4\pi}{c^2}\frac{\partial^2}{\partial t^2}\vec{P}_q^{NL}(z,t)$$

from which it follows that

$$\frac{\partial^2}{\partial z^2}(A_q(z)e^{i(k_q z-\omega_q t)}e^{-\kappa_q z}) - \frac{\epsilon^{(1)}(\omega_q)}{c^2}\frac{\partial^2}{\partial t^2}(A_q(z)e^{i(k_q z-\omega_q t)}e^{-\kappa_q z})$$

$$= \frac{4\pi}{c^2}\frac{\partial^2}{\partial t^2}(P_q^{NL}(z)e^{-i\omega_q t})$$

$$\implies \quad ((\frac{\partial^2}{\partial z^2}A_q(z))e^{i(k_q z-\omega_q t)}e^{-\kappa_q z}) + 2(\frac{\partial}{\partial z}A_q(z))(\frac{\partial}{\partial z}e^{i(k_q z-\omega_q t)}e^{-\kappa_q z})$$

$$+A_q(z)(\frac{\partial^2}{\partial z^2}e^{i(k_q z-\omega_q t)}e^{-\kappa_q z})) - \frac{\epsilon^{(1)}(\omega_q)\omega_q^2}{c^2}(A_q(z)e^{i(k_q z-\omega_q t)}e^{-\kappa_q z})$$

$$= \frac{4\pi\omega_q^2}{c^2}(P_q^{NL}(z)e^{-i\omega_q t})$$

Since $(ik_q - \kappa_q)^2 = \epsilon^1(\omega_q)\frac{\omega_q^2}{c^2}$, it follows that the last two terms on the left side of the equation above cancel, which yields

$$\big(\frac{d^2}{dz^2}A_q(z) + 2(ik_q - \kappa_q)\frac{d}{dz}A_q(z)\big)e^{(ik_q-\kappa_q)z} = -4\pi k_q^2 P_q^{NL}(z)$$

Under the slowly varying envelope approximation [21], the first term on the left side of the equation above vanishes, and we are left with

$$\frac{d}{dz}A_q(z) = -\frac{2\pi k_q^2}{ik_q - \kappa_q}P_q^{NL}(z)e^{(-ik_q+\kappa_q)z} \tag{2.7}$$

In the Lewenstein model of HHG, the phase of the nonlinear polarization P_q^{NL} with respect to the driving field is given by

$$\Phi_q = q\omega_0 t_f - S/\hbar$$

where S is the semiclassical action in momentum space for the electron born in the oscillating field and t_f is the time of recombination of the electron with respect to a reference phase of the driving period [13]. Here, the phase is determined by two components: the phase due to the time delay t_f and the phase acquired by the electron wavepacket in the continuum. In the strong field regime, i.e. $\gamma \ll 1$, where $\gamma = \sqrt{I_p/2U_p}$ is the Keldysh parameter, I_p is the ionization potential of the medium and $U_p = \frac{e^2E^2}{4m_e\omega_0^2}$ is the pondermotive energy, the semiclassical action can be approximated by $S \approx -U_p\tau$ for each quantum path, where τ is the time the between the birth and recombination of the electron wavepacket [13]. The phase evolution along z can be expanded as

$$\Phi(z) \approx \Phi_0 + \frac{d\Phi}{dz}z = \Phi_0 + z\frac{d}{dz}(q\omega_0 t_f + \frac{U_p\tau}{\hbar})$$

Now, $\omega_0 t_f$ is a phase offset with respect to the driving field, hence it evolves along z like the driving field, i.e. $\frac{d}{dz}\omega_0 t_f = k_0$. Next, we know that the intensity dependent phase is approximately linear and thus we can write $\frac{1}{\hbar}\frac{d}{dz}U_p\tau = -\alpha_q\frac{dI}{dz}$, where the phase coefficient for the q^{th} harmonic, α_q, is representative of the quantum path taken by the electron wavepacket in the continuum. This coefficient depends on if the harmonic it corresponds with is in the below-threshold, plateau or cutoff region, and whether it is a short or long trajectory in the continuum. For harmonics in the plateau, $\alpha_q \sim 10^{-14}$ cm^2/W for the short trajectory and $\sim 25 \times 10^{-14}$ cm^2/W for the long trajectory [59]. The expression for the z dependent phase then reduces to

$$\Phi(z) \approx \Phi_0 + z(qk_0 - \alpha_q\frac{dI}{dz})$$

Since we can write the polarization of the generating medium as a product of the target density and the induced single atom dipole moment, $\vec{P} = \rho\vec{d}$, we have that

$$P^{NL}(z)e^{(-ik_q+\kappa_q)z} = \rho|d(\omega_q)|e^{i\Phi(z)}e^{(-ik_q+\kappa_q)z} = \rho|d(\omega_q)|e^{(i\Delta k+\kappa_q)z}$$

where we have defined $\Delta k = (qk_0 - k_q) - \alpha_q\frac{dI}{dz}$ and neglected the constant phase offset. Here we see the phase mismatch has two components: the common phase (wavevector) mismatch caused by the difference in phase velocity between the harmonic and driving field, and the intensity dependent dipole phase. The product Δkz describes the phase slip between the q^{th} harmonic field generated at two different points along the propagation direction, separated by a distance z. The separation between two points along the propagation direction in which harmonics emitted at these locations would destructively interfere is known as the coherence length, $L_c = \pi/\Delta k$. Similarly, the separation between two points along the propagation direction in which harmonic intensity has been attenuated by a factor of $1/e$ is known as the absorption length, $L_{abs} = 1/\rho\sigma = 1/2\alpha_q$. We can write equation (2.7) as

$$\frac{d}{dz}A_q(z) = -\frac{2\pi k_q^2}{ik_q - \kappa_q}\rho|d(\omega_q)|e^{(i\Delta k+\kappa_q)z}$$

Integrating this equation, we find that the amplitude of the electric field for the q^{th} harmonic at the exit of the generating medium of length L is given by

$$E_q(L) = A_q(L)e^{-\kappa_q L} = -\frac{2\pi k_q^2}{ik_q - \kappa_q}\rho|d(\omega_q)|e^{-\kappa_q L}\int_0^L e^{(i\Delta k+\kappa_q)z}dz$$

$$= -\frac{2\pi k_q^2}{\kappa_q(ik_q - \kappa_q)}\rho|d(\omega_q)|g(\Delta k, L)$$

where $g(\Delta k, L)$ is known as the phase mismatch form factor [52, 54], or the time dependent phase matching factor, expressed as

$$g(\Delta k, L) = \frac{e^{i\Delta kL} - e^{-\kappa_q L}}{1 + i\Delta k/\kappa_q} \tag{2.8}$$

The phase mismatch form factor can be used as a metric for phase matching quality for the q^{th} harmonic. Since $|E_q|^2 \propto (|d(\omega_q)||g(\Delta k, L)|)^2$, we see that the intensity of the q^{th} harmonic field at the exit of the generating medium is proportional to the square of the product of the atomic dipole moment at ω_q and the phase mismatch form factor. In HHG, the atomic dipole at ω_q is induced through tunnel ionization, hence we can make the approximation that $|d(\omega_q)|$ is proportional to the time dependent tunnel ionization rate. Following the next section, it will be shown that the primary source of phase mismatch originates from the difference in phase velocity between the fundamental and harmonic fields, $qk_0 - k_q$.

2.2.5 Reabsorption

An important consideration in high harmonic generation in a macroscopic volume is the reabsorption of the emitted harmonic radiation by the generating medium, since the generating medium will have nonzero linear absorption across the spectral range of the harmonics. As defined in the previous section, the absorption length is given by $L_{abs} = 1/\rho\sigma = 1/2\alpha_q$, corresponding with the distance along the propagation direction in which the harmonic intensity is attenuated by a factor of $1/e$. High harmonic generation differs from typical laser amplification, as the presence of more harmonic light does not stimulate addition emission of harmonic radiation within the medium (harmonic radiation is solely generated by the driving field). The gain in harmonic emission across a length L is at best linear, unlike the nonlinear amplification seen in lasers. Thus, the generated harmonic flux can saturate, where any additional harmonic emission is balanced by harmonic absorption.

By assuming that the amplitude of the driving field remains constant across the generating volume L, which is a good assumption in loose focusing conditions or in thin targets, we can integrate our expression for $E_q(L)$ over the generating length in order to determine the intensity of the q^{th} harmonic, $I_q = |E_q|^2$, at the output of the medium

$$I_q \propto \frac{L_a^2}{1 + 4\pi^2(L_a/L_c)^2}[1 + e^{-L_m/L_a} - 2\cos(\pi L_m/L_c)e^{-L_m/2L_a}] \tag{2.9}$$

where L_c is the coherence length introduced in the previous section and L_m is the medium length. Fig. 2.6 shows the harmonic flux plotted as a function of the generating medium length for different values of coherence and absorption lengths. For short coherence lengths, oscillations are observed in the harmonic intensity along the medium length, which are the result of interference. At longer coherence lengths, saturation is reached within a small number of absorption lengths. In near perfect phase matching conditions ($L_c \gg L_a$), harmonic flux is still limited by reabsorption and is seen to saturate. When the harmonic emission and absorption rates balance and saturation is reached, the high harmonic generation is called absorption limited. It is worth mentioning that the lower order below-threshold harmonics do not in general suffer greatly from reabsorption effects, since they lie below the ionization threshold of the medium (provided the generating atomic medium does not possess any bound state resonances that coincide in energy with a low order harmonic). This can lead to low order harmonics that are significantly more bright than the higher orders.

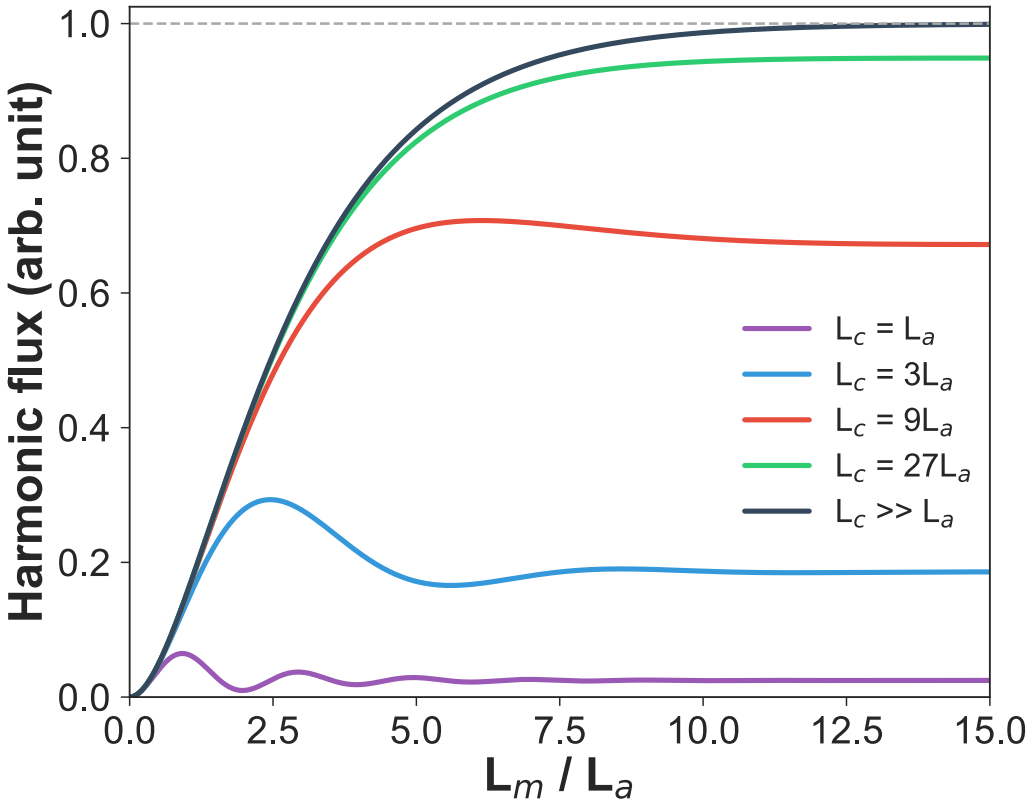

Figure 2.6: The harmonic yield, with reabsorption, as a function of the generating medium length, for different coherence and absorption length conditions. As the coherence length increases relative to the absorption length, the harmonic yield increases until reaching saturation. Phase mismatch and harmonic reabsorption limits attainable harmonic flux, leading to the saturation effect.

2.2.6 The Phase Mismatch for a Gaussian Beam

If we now consider a focused Gaussian beam, the electric field can be written as [21]

$$E(r,z,t) = E_0 \frac{w_0}{w(z)} e^{-(r/w(z))^2} e^{i(k_0 z + k_0 r^2/2R(z) + \Phi_{\text{Gouy}}(z))} e^{-i\omega_0 t}\hat{x}$$

where $w(z) = w_0\sqrt{1+(z/z_R)^2}$ is the beam width, w_0 is the beam waist, $z_R = \pi\omega_0^2/\lambda_0$ is the Rayleigh length, $R(z) = z(1+(z/z_R)^2)$ is the radius of curvature of the wavefronts, and $\Phi_{\text{Gouy}}(z) = -\arctan(z/z_R)$ is the Gouy phase. Here, the phase evolution on axis along z is given by

$$\Phi(z) \approx \Phi_0 + \frac{d\Phi}{dz}z = \Phi_0 + z\frac{d}{dz}\big(q\omega_0 t_f + \frac{U_p\tau}{\hbar} + \Phi_{\text{Gouy}}(z)\big)$$

Treating the first two terms in the parenthesis as before, and noting that $\frac{d}{dz}\Phi_{\text{Gouy}} = -1/(z_R(1+(z/z_R)^2))$, we can write

$$\Phi(z) \approx \Phi_0 + z(qk_0 - \alpha_q\frac{dI}{dz} - \frac{1}{z_R}\frac{1}{1+(z/z_R)^2})$$

Since the on axis intensity distribution for a Gaussian beam is given by $I(z) = I_{\max}(w_0/w(z))^2 = I_{\max}/(1+z/(z_R)^2)$, we have that

$$\frac{dI}{dz} = \frac{-2I_{\max}}{z_R^2}\frac{z}{1+(z/z_R)^2}$$

Evaluating the phase at the cell position $z = z_c$, the new expression for Δk reads

$$\Delta k = (qk_0 - k_q) + \alpha_q\frac{2I_{\max}}{z_R^2}\frac{z_c}{1+(z_c/z_R)^2} - \frac{q}{z_R}\frac{1}{1+(z_c/z_R)^2}$$

Next, since $k_q = \omega_q n(\omega_q)/c = q\omega_0 n(\omega_q)/c$, we can write

$$\Delta k = \frac{q\omega_0}{c}\big(n(\omega_0) - n(\omega_q)\big) + \alpha_q\frac{2I_{\max}}{z_R^2}\frac{z_c}{1+(z_c/z_R)^2} - \frac{q}{z_R}\frac{1}{1+(z_c/z_R)^2}$$

Let us split the first of the three phase matching terms into its neutral atomic and plasma components

$$\Delta k_{\text{atomic}} + \Delta k_{\text{plasma}} = \frac{q\omega_0}{c}\Big(\big(n(\omega_0) - n(\omega_q)\big)_{\text{atomic}} + \big(n(\omega_0) - n(\omega_q)\big)_{\text{plasma}}\Big)$$

Since we can write the index of refraction for the target atoms in terms of the atomic form factors [59], $n(\omega) = 1 - \frac{\rho r_0\lambda^2}{2\pi}(f_1^0 - if_2^0)$, where r_0 is the classical electron radius, then since only the real component of $n(\omega)$ contributes to the phase mismatch and $\lambda_q = \lambda_0/q$, we see that

$$\Delta k_{\text{atomic}} = q\rho r_0\lambda_0\big(f_1^0(\omega_q)/q^2 - f_1^0(\omega_0)\big)$$

Now, since the driving field ionizes the generating medium, a free electron plasma is formed in the irradiated volume. The index of refraction of the plasma is given by $n(\omega) = \sqrt{1-(\omega_p/\omega)^2}$, where $w_p(t) = \sqrt{\eta(t)\frac{4\pi\rho e^2}{m_e}}$ is the plasma frequency and $\eta(t)$ is the ionized fraction [59]. For $\omega_p \ll \omega$, a good approximation for driving and harmonic frequencies and densities encountered in HHG, we can expand $n(\omega)$ as $n(\omega) \approx 1 - \frac{2\pi\rho e^2}{m_e\omega^2}\eta$, hence

$$\Delta k_{\text{plasma}} = \frac{-q\omega_0}{c}\frac{2\pi\rho e^2}{m_e}\frac{q^2+1}{q^2\omega_0^2}\eta(t) \approx \frac{-q\omega_0}{c}\frac{2\pi\rho e^2}{m_e\omega_0^2}\eta(t) = -q\rho r_0\lambda_0\eta(t)$$

where we have approximated $(q^2+1)/q^2$ as unity. It follows that we can write, $\Delta k = \Delta k_{\text{atomic}} + \Delta k_{\text{plasma}} + \Delta k_{\text{dipole}} + \Delta k_{\text{Gouy}}$, where

$$\Delta k_{\text{atomic}} = q\rho r_0 \lambda_0 \big(f_1^0(\omega_q)/q^2 - f_1^0(\omega_0)\big) \tag{2.10}$$

$$\Delta k_{\text{plasma}} = -q\rho r_0 \lambda_0 \eta(t) \tag{2.11}$$

$$\Delta k_{\text{dipole}} = \alpha_q \frac{2I_{\max}}{z_R^2} \frac{z_c}{1+(z_c/z_R)^2} \tag{2.12}$$

$$\Delta k_{\text{Gouy}} = -\frac{q}{z_R} \frac{1}{1+(z_c/z_R)^2} \tag{2.13}$$

When the phase mismatch from these four terms in the sum balance one another such that $\Delta k \approx 0$, phase matching for the q^{th} harmonic is satisfied. Phase matching is achieved in practice by adjusting the pressure of the generating gas medium, as well as the position of the driving field focus, as well as the field intensity and pulse duration.

2.2.7 The ADK Rate

In order to determine $\eta(t)$, as well as an approximate expression for $|d(\omega_q)|$, the ADK model can be used to calculate the tunnel ionization rate of target atoms in the driving field [5]. For a linearly polarized field, the probability of ionization per unit time from a state with energy E, angular quantum number l, and magnetic quantum number m_l is given by

$$w_{\text{ADK}} = C^2_{n^*l^*} \sqrt{\frac{3\mathcal{E}}{\pi\mathcal{E}_0}} E \frac{(2l+1)(l+|m_l|)!}{2^{|m_l|}|m_l|!(l-|m_l|)!} \Big(\frac{2\mathcal{E}_0}{\mathcal{E}}\Big)^{2n^*-|m_l|-1} e^{-2\mathcal{E}_0/3\mathcal{E}}$$

with

$$C^2_{n^*l^*} = \frac{2^{2n^*}}{n^*\Gamma(n^*+l^*+1)\Gamma(n^*-l^*)}$$

where $\mathcal{E}$ is the electric field amplitude, $n^* = Z/\sqrt{2E}$, Z being the charge of the atomic residue, and $\mathcal{E}_0 = \sqrt{2E}$. The expression for the effective angular quantum number l^* is given by

$$l^* = \begin{cases} 0 & \text{for } l \ll n \\ n^* - 1 & \text{otherwise} \end{cases}$$

These preceding expressions all assume atomic units, i.e. $\hbar = m_e = e = 1$. Using this time dependent tunnel ionization rate, we can make the approximation that $|d(\omega_q)| \propto w_{\text{ADK}}$. Treating photoionization as a Poissonian process and using the tunnel ionization rate w_{ADK}, the ionized fraction as a function of time is given by [15]

$$\eta(t) = 1 - \exp\Big(- \int_{-\infty}^{t} w_{\mathrm{ADK}}(\mathcal{E}(t'))dt' \Big) \tag{2.14}$$

which completes the expression for $\Delta k_{\mathrm{plasma}}$.

2.2.8 The Atomic Form Factor

Since the atomic form factors are only well documented for photon energies between $\sim$ 30 - 30,000 eV[67], these need to be calculated at lower energies, such as the driving frequency. The index of refraction for noble gases in the UV/Vis/IR can be accurately described using a Sellmeier equation of the form

$$n(\lambda, p, T) = \sqrt{1 + \frac{p}{p_0}\frac{T_0}{T}\Big(\frac{B_1\lambda^2}{\lambda^2 - C_1} + \frac{B_2\lambda^2}{\lambda^2 - C_2}\Big)}$$

where λ is measured in μm [20]. The set of coefficients B_1, B_2, C_1, C_2, which vary between atomic targets, have been calculated at $p_0 = 1000$ mbars and $T_0 = 273$ K and can be found in [20]. To retrieve the atomic form factor from the calculated index of refraction, recall the expression used earlier for the index of refraction, $n(\omega) = 1 - \frac{\rho r_0 \lambda^2}{2\pi}(f_1^0 - i f_2^0)$. Noting that f_2^0 is vanishing for noble gases in the UV/Vis/IR, we can write

$$f_1^0(\lambda) = -\frac{2\pi\big(n(\lambda, p, T) - 1\big)}{\rho r_0 \lambda^2}$$

which allows $\Delta k_{\mathrm{atomic}}$ to be determined. Figure 2.7 shows $f_1^0(\lambda)$ for $\lambda = 0.130 - 1.000$ μm for room temperature Ar at a pressure of 1 Torr.

2.2.9 Harmonic Yield and Driving Wavelength Scaling

With complete expressions for all the phase mismatch components (2.10)-(2.13), the phase mismatch form factor (2.8) can be calculated as a function of time and since $|E_q(t)|^2$ scales as $(|d(\omega_q)||g(\Delta k(t), L)|)^2$, we now have an approximate expression proportional to the q^{th} harmonic flux. Below we compare the harmonic yield at similar energies, using the same driving field but at different wavelengths. As mentioned in the subsection covering the 3-step model, using shorter driving wavelengths provides less time for the free electron wavepacket to spread before recombination. This results in an increase in the recombination probability, due to the increased overlap between the free electron wavepacket and the wavefunction of the localized core. We also see from equations (2.10) and (2.11) that the phase mismatch due to neutral atomic and plasma dispersion scales linearly with the driving wavelength. Thus the benefit of going to shorter driving wavelengths is two-fold: the recombination probability is increased, and the phase mismatch is reduced. This can result in a significant increase in the harmonic generation efficiency by two of three orders of magnitude [53, 161, 107]. It is worth mentioning that while there is a benefit in an increased conversion efficiency by going to

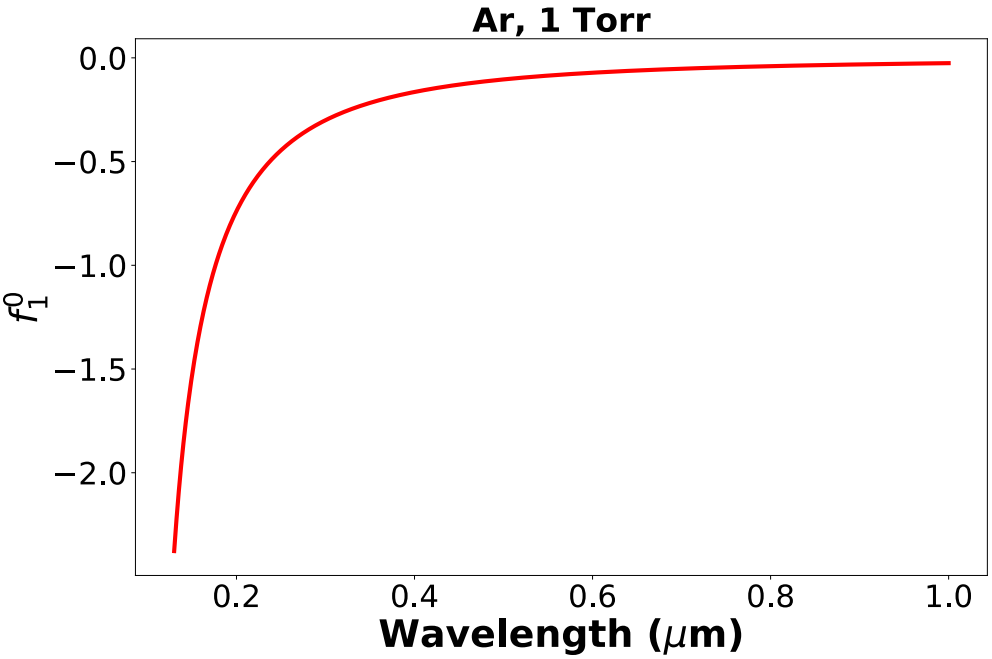

Figure 2.7: $f_1^0(\lambda)$ for 1 Torr of room temperature Ar for $\lambda = 0.130 - 1.000$ μm.

shorter driving wavelengths, there is a trade-off in that the cut off energy is reduced and thus higher energy photons can not be generated. Hence shorter driving wavelengths can provide a high-flux source of vacuum ultraviolet photons, while longer driving wavelengths can provide photons extending out into the soft x-rays, although with limited fluence. Another feature of using a shorter driving wavelength is that the spacing between the teeth of the frequency comb is increased, which can make spectral filtering or isolation of a single harmonic of the vacuum ultraviolet frequency comb more readily achievable.

In Fig. 2.8 and 2.9, $\eta(t)$ is presented for a 50 femtosecond, 5×10^{14} W/cm^2 Gaussian pulse. Using the conditions of a 6 meter focusing geometry, with a generating medium 10 cm in length and at a pressure of 1 Torr, $(|d(\omega_q)||g(\Delta k(t), L)|)^2$ is computed for the 9$^{\text{th}}$ harmonic of $\lambda = 400$ nm (44.44 nm = 27.9eV) and the 19$^{\text{th}}$ harmonic of $\lambda = 800$ nm (42.1 nm = 29.5eV). The position of the generating medium is 20 cm upstream from the focus. The results for both Ar and Kr are shown below in Fig. 2.8 and 2.9. The product $(|d(\omega_q)||g(\Delta k(t), L)|)^2$ for both driving fields is normalized to the same peak value for better visualization.

In both generating media, three things are immediately apparent. First, the 400 nm driving field's peak harmonic flux is roughly 10 times that of the 800 nm driving field's. Second, the two different driving wavelengths phase match at different parts of the temporal profile of the driving field. In the case of the blue driving wavelength, good phase matching occurs near the peak intensity of the pulse, while the NIR wavelength phase matches earlier in

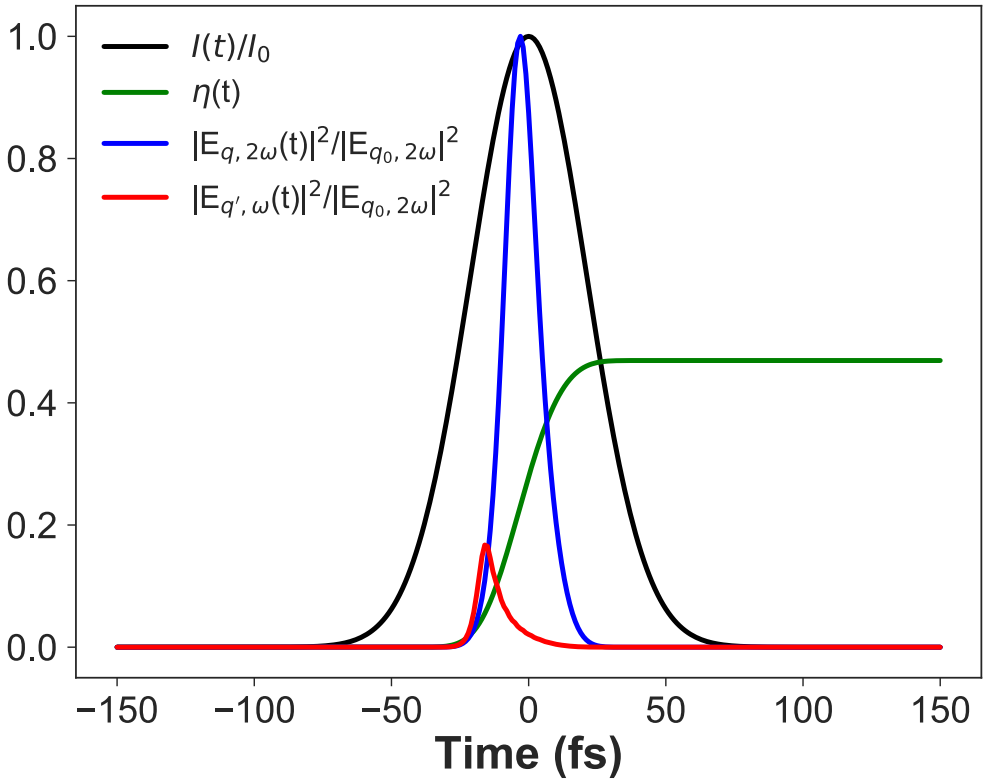

Figure 2.8: A 50 fs, 5×14 W/cm^2 pulse, the ionized fraction $\eta(t)$, and the square of the phase mismatch form factor times the atomic dipole in Ar for the 9th harmonic of 400 nm ($2\omega_o$) and the 19th harmonic of 800 nm (ω_o). Here, ∼45% of the target atoms have been ionized by the end of the pulse. Phase matching is mostly satisfied on the leading edge of the pulse, before too much plasma density has built up. The 400 nm driven harmonics tolerate high plasma densities and thus satisfy phase matching near peak intensity and over a longer duration of time, resulting in significantly increased yield when compared with 800 nm driven harmonics.

the pulse at lower field intensities. Third, the two different driving wavelengths phase match for different lengths of time. In both cases, the blue driving wavelength phase matches for more than twice as long as the NIR wavelength (i.e. it possess a wider ionization gate).

Evidently, using a 400 nm driving wavelength results in higher fluence per harmonic when compared to an 800 nm driving wavelength, due to the benefit of yielding phase matching at preferable field intensities where $|d(\omega_q)|$ is larger, and for a longer portion of time within the driving pulse profile.

As mentioned above, this is achieved due to the wavelength dependence of the neutral atomic and plasma phase mismatch. These two components of the total phase mismatch have

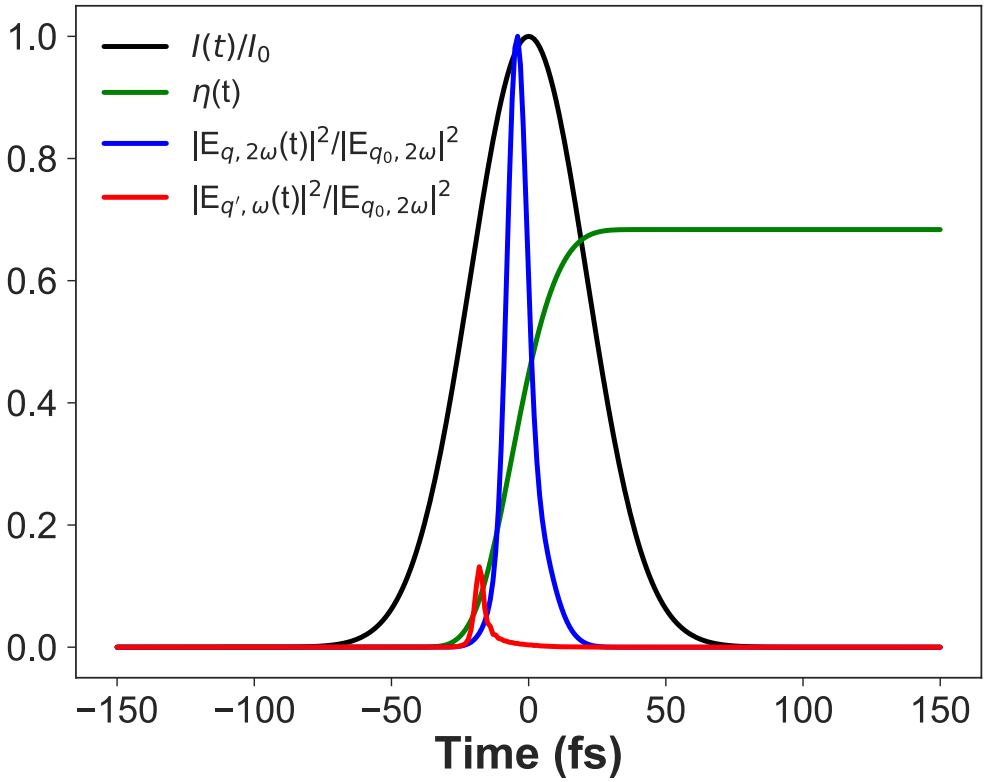

Figure 2.9: A 50 fs, 5×14W/cm^2 pulse, the ionized fraction $\eta(t)$, and the square of the phase mismatch form factor times the atomic dipole in Kr for the 9th harmonic of 400 nm ($2\omega_o$) and the 19th harmonic of 800 nm (ω_o). Here, ∼70% of the target atoms have been ionized by the end of the pulse. Phase matching is mostly satisfied on the leading edge of the pulse, before too much plasma density has built up. The 400 nm driven harmonics tolerate high plasma densities and thus satisfy phase matching near peak intensity and over a longer duration of time, resulting in significantly increased yield when compared with 800 nm driven harmonics.

opposite sign and balance each other over different ranges of the ionized fraction, depending on the driving wavelength. For a NIR driving field, we see that the neutral atomic and plasma dispersion balance one another over a short range of ionized fraction around just a few percent, while for a blue driving field, the neutral atomic and plasma dispersion balance one another over a wider and higher range of ionized fraction, where there is greater contribution from $|d(\omega_q)|$. In both cases, good phase matching is mostly confined to the leading edge of the pulse.

To roughly quantify the difference in the harmonic flux generated, we define

$$\Omega = \frac{\int_{-\infty}^{\infty} (|d(\omega_q)||g(\Delta k_{400\text{nm}}(t), L)|)^2 dt}{\int_{-\infty}^{\infty} (|d(\omega_{\tilde{q}})||g(\Delta k_{800\text{nm}}(t), L)|)^2 dt}$$

which approximately gives the ratio of integrated intensities of the q^{th} and $\tilde{q}^{th}$ harmonic field produced by the driving pulse at 400 nm and 800 nm, respectively. Under the parameters shown in Figs. 2.8 and 2.9, in the case of Ar we find that $\Omega = 8.55$, i.e. the 400 nm driving field produces ~ 9 times more harmonic photons than the 800 nm driving field, while in the case of Kr we find that $\Omega = 15.3$, i.e. the 400 nm driving field produces ~ 15 times more harmonic photons than 800 nm.

2.3 High-Fluence High Harmonic Generation Light Source

Since their invention at the MIT Lincoln Laboratory in 1982 [117], titanium-doped sapphire lasers have served as a workhorse for the ultrafast laser community, capable of producing tunable ultrashort red and NIR pulses [147]. In these transition-metal-doped lasers, the gain medium is an Al_2O_3 (sapphire) crystal, doped with Ti^{3+} ions. Since Ti:sapphire has high thermal conductivity (minimizing thermal effects), a very broad gain bandwidth (capable of supporting sub-two-cycle pulses [156, 115]), and a wide range of usable pump wavelengths, it rapidly supplanted the use of most dye lasers and quickly gained wide use in various fields of science. Such systems are generally pumped at green wavelengths and lase at NIR wavelengths.

2.3.1 The 50 Hz Ti:sapphire Laser System

The laser system used in the present work is based on chirped pulse amplification [153, 106] (CPA) in titanium-doped sapphire (Ti:sapphire), producing ∼30 mJ, 45 femtosecond pulses at a repetition rate of 50 Hz, with a central wavelength of ∼800 nm. CPA was developed in the mid-1980s by Donna Strickland and Gèrard Mourou who were awarded the Nobel Prize in Physics in 2018 for their work. The laser system is comprised of a Kerr-lens mode-locked oscillator, an Offner stretcher, a regenerative amplifier (operating at 50 Hz), a 4-pass amplifier, and a grating compressor.

The oscillator was constructed from a kit produced by Kapteyn-Murnane Laboratories (KMLabs Dragon kit), similar to the system described in [7]. A schematic of the oscillator layout is shown in Fig. 2.10. Here, the intracavity dispersion is controlled via a Brewster-cut prism pair (labeled as P1 and P2 in Fig. 2.10). The Ti:sapphire crystal is pumped by 4.35 W of 532 nm green CW light produced by a frequency-doubled Nd:YVO_4 laser (Coherent

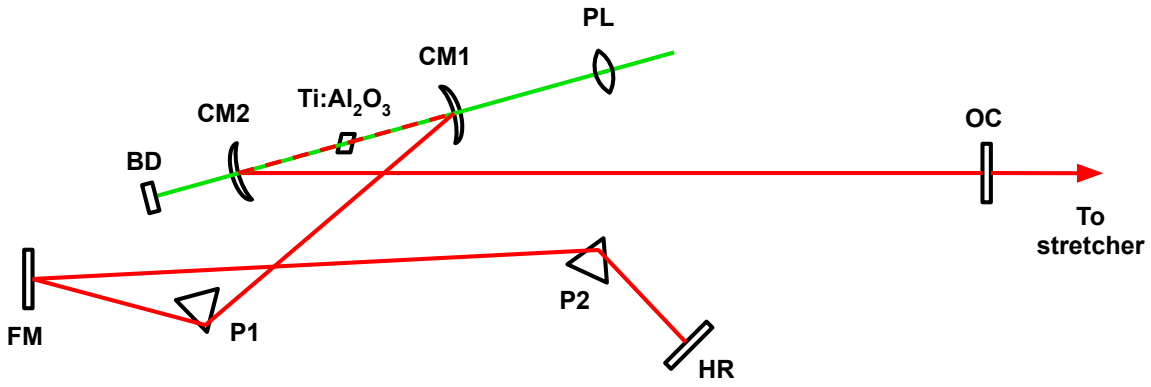

Figure 2.10: A schematic of the Kerr-lens mode-locked Ti:sapphire oscillator. PL and BD mark the pump lens and beam dump, respectively. The cavity output coupler is marked by OC, the high reflector by HR, the fold mirror by FM, the Brewster cut prisms by P1 and P2, and the curved dichroic mirrors by CM1 and CM2.

Verdi V6). The laser mode-locks via the nonlinear optical Kerr effect, a third order $\chi^{(3)}$ effect resulting in an intensity dependent index of refraction

$$n = n_0 + n_2 I \tag{2.15}$$

where n_0 is the linear index of refraction, n_2 is the nonlinear index of refraction, and I the intensity [21]. The nonlinear index of refraction can be written as

$$n_2 = \frac{3}{4\epsilon_0 c n_0^2} \mathrm{Re}(\chi^{(3)}) \tag{2.16}$$

Since the beam mode is Gaussian, the intensity profile is spatially varying, with highest field strengths near the center of the beam mode that decrease radially. This can establish an effective lens within the material and lead to self-focusing. When operating in CW mode, if one of the Brewster-cut prisms is jogged to modify the intracavity dispersion, a pulse may begin to build up within the cavity. This pulse has significantly higher instantaneous field strengths than the CW field, and begins to induce a Kerr-lens within the Ti:sapphire crystal. This causes the pulsed mode to shrink due to self-focusing, relative to the CW mode. The cavity is designed such that there is greater overlap between the pump and pulsed mode, leading to higher gain at the peak of the pulse with each round trip. These intensity changes are then even further amplified by Kerr-lensing, which further decreases the pulse length. This leads to the pulsed field to outcompeting the CW field, with any available gain in the pumped Ti:sapphire going into the pulse, pushing the laser into mode-locked operation and overcoming the CW mode. In mode-locked operation, the laser oscillator produces ∼6 nJ

pulses at a repetition rate of ∼88 MHz, with a ∼25 nm FWHM bandwidth centered at 805 nm. The typical output power in mode-locked operation is ∼525 mW, while the typical output power in CW operation is ∼400 mW.

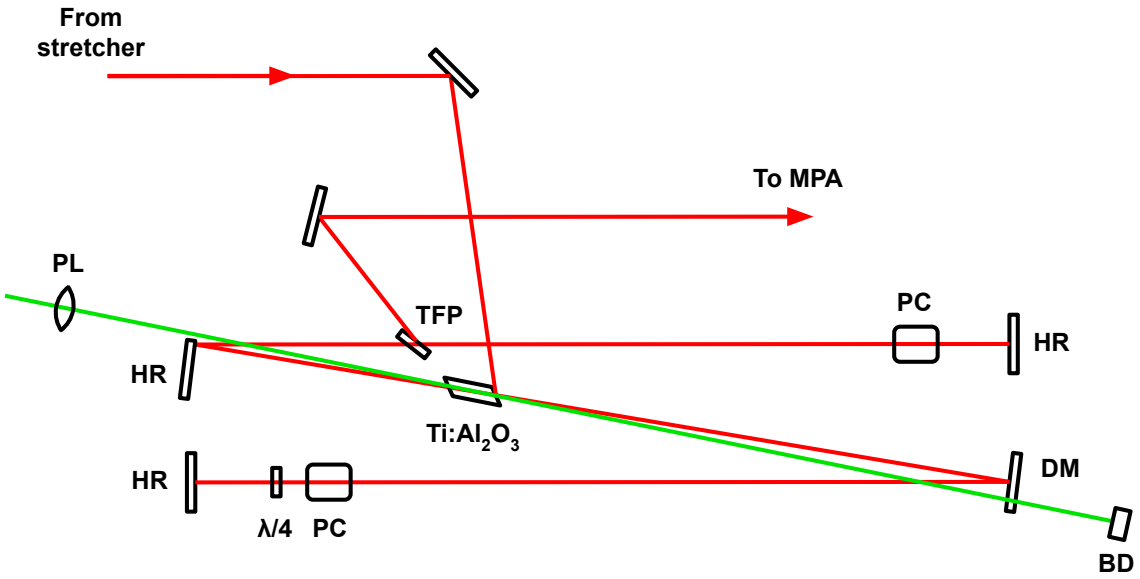

Figure 2.11: A schematic of the regenerative amplifier z-fold cavity. PL and BD mark the pump lens and beam dump, respectively. The cavity high reflectors are marked by HR, the dichroic mirror by DM, the quarter-wave plate by $\lambda/4$, the Pockels cells by PC, and the thin film polarizer by TFP.

The pulses are stretched in an Offner-type stretcher [124] to a pulse duration of ∼200 ps, using a 1200 lines/mm NIR holographic Au grating (Spectrogon), which then undergo regenerative amplification at 50 Hz. The stretcher and regenerative amplifier (Positive Light Legend USP) were produced by Positive Light Inc. A schematic of the regenerative amplifier is shown in Fig. 2.11. Here, pulses are selected and amplified to ∼1.2 mJ from the oscillator pulse train at a repetition rate of 50 Hz. Pulses are switched in and out of the z-fold cavity until gain saturation is reached using a pair of Pockels cells, a quarter-wave plate, and a thin-film polarizer. The amplifier itself is pumped at 527 nm and at 1 kHz by ∼9 mJ, 220 ns pulses from an intracavity frequency doubled Q-switched diode-pumped Nd:YLF laser (Coherent Revolution 20).

The 50 Hz pulse train propagates out of the regenerative amplifier and enters a home-built multi-pass amplification state, depicted schematically in Fig. 2.12. This is a 4-pass amplifier in a "bow tie" geometry, which is pumped by ∼400 mJ, 5 ns, 532 nm pulses from a flashlamp pumped frequency doubled Nd:YAG laser (Continuum Powerlite DLS 9050).

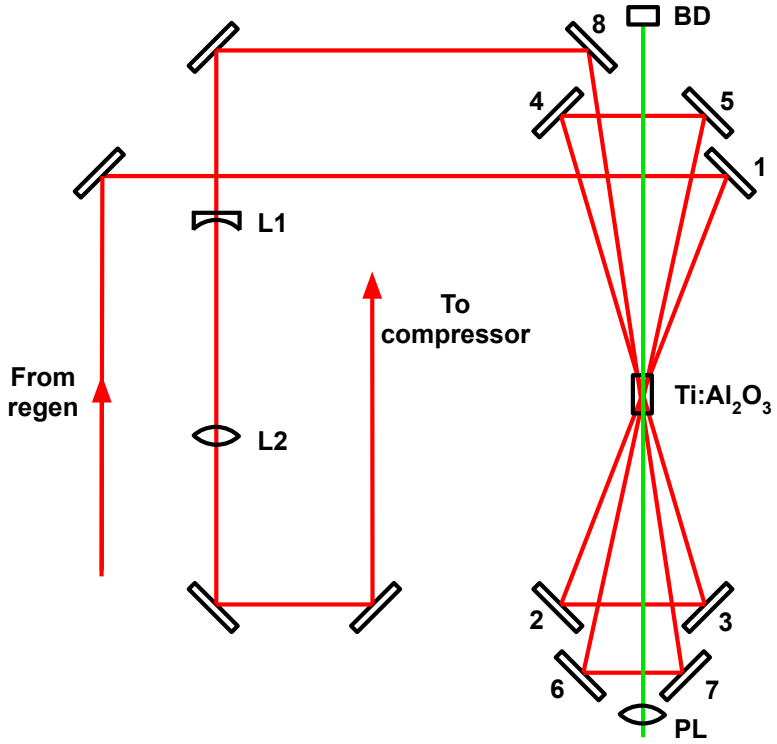

Figure 2.12: A schematic of the 4-pass amplifier. PL and BD mark the pump lens and beam dump, respectively. Each mirror of the bow tie is numbered, with mirrors 1 and 2 indicating the first pass, mirrors 3 and 4 indicating the second pass, mirrors 5 and 6 indicating the third pass, and mirrors 7 and 8 indicating the fourth and final pass. The beam then propagates through an expanding telescope, with lenses marked by L1 and L2.

The output power of the pump laser is attenuated using a waveplate in conjunction with a thin-film polarizer, where ∼10 W of pump power (200 mJ) is used in typical operation. The pump beam is relay-imaged to the crystal, which helps preserve the flat-top mode and beam quality during propagation. After amplification, the beam mode is expanded through a Galilean telescope, which magnifies the beam diameter by a factor of ∼3. The output power of the amplifier is adjusted by varying the pump power and is capable of amplifying up to a NIR pulse energy of 60 mJ, however, experiments were typically performed using pulse energies between 10-15 mJ (measured just before compression, after the last reflection shown in Fig. 2.12). The negative lens of the telescope is mounted on a rotatable stage, which allows the lens to be rotated off normal incidence to compensate for any astigmatism of the amplifier.

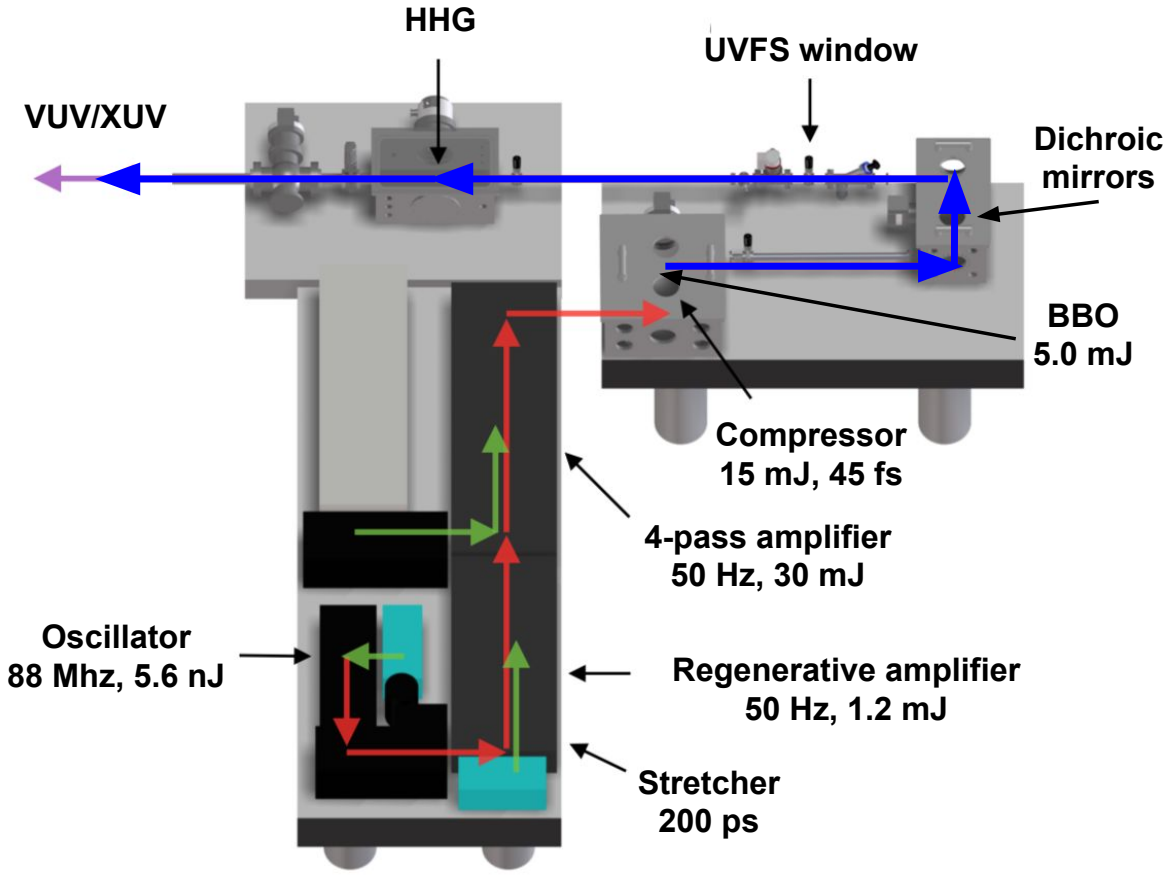

Figure 2.13: A schematic of the laser system used to drive high harmonic generation. The output from a Ti:sapphire oscillator undergoes chirped pulse amplification and is then compressed and frequency doubled in a low pressure helium environment. The 400 nm photons are then reflected and propagate into the vacuum beamline through a 0.25 mm thick UVFS window, where they are then used to drive high harmonic generation within a gas cell a few meters downstream. Figure adapted from [154].

2.3.2 Compression and Frequency Doubling

The amplified pulse train enters a series of vacuum chambers connected to a beamline, shown in Fig. 2.13. First, the uncompressed NIR laser pulses are coupled into the compression chamber through a standard viewport, where they undergo compression using a home-built grating pulse compressor, comprised of two 1500 line/mm NIR holographic Au gratings (Spectrogon) and a 4" roof reflector. The overall efficiency of the compressor has been measured to be ∼65%. This compressor is housed within a helium environment at a pressure

of roughly 100 Torr. Compression is performed in a low-pressure helium environment in order to minimize the third order $\chi^{(3)}$ nonlinear effects of self-focusing and self-phase modulation, which can be significant at these high field strengths when propagating at atmosphere. These effects are due to the intensity dependent refractive index (see discussion of the nonlinear optical Kerr effect above), shown in equation 2.15. In addition to arising in the spatial domain, nonlinear temporal effects can occur due to the rapidly changing gradients of the field within the pulse, where the high intensity leading edge of the pulse can modify the refractive index seen by the trailing edge of the pulse. This can cause a phase shift in the pulse or the creation of new frequencies and is known as self-phase modulation. The phase shift experienced by the pulse due to nonlinear effects is given by

$$\phi_{NL} = \frac{2\pi}{\lambda_0} n_2 I L \tag{2.17}$$

where L is the propagation distance and λ_0 is the carrier wavelength of the pulse. For propagation at atmosphere, a phase shift of π is picked up after a distance of only 0.7 m at NIR wavelengths and intensities of $\sim 10^{12}$ W/cm^2 [24]. Helium possesses a nonlinear refractive index that is two orders of magnitude lower than air per unit pressure [119], thus self-focusing and self-phase modulation issues are largely circumvented through propagating in 100 Torr of helium. Additionally, helium possesses exceptionally high thermal conductivity [29] when compared with other gases (roughly 5 times greater than that of N_2). This aids in dissipating thermal energy deposited on the grating from the average power of the laser. We have also found that the helium environment mitigates the deposition of laser-ablated hydrocarbon films on the gratings [155], which greatly extends their lifetime.

The spectral and temporal profile of the compressed beam was characterized using a single-shot FROG measurement (GRENOUILLE) [122], with the spectral and temporal traces shown in Fig. 2.14 and the measured and retrieved full GRENOUILLE traces shown in Fig. 2.15. The pulse duration is 46 femtoseconds, with a central wavelength of 800 nm and a 21 nm FWHM bandwidth. GRENOUILLE also allows the spatial profile of the pulse to be characterized and is sensitive to spatial chirp, depecited in the measured and retrieved GRENOUILLE traces shown in Fig. 2.16(a). Here, as a spatially chirped mode propagates through the Fresnel biprism, the two spatially separated components are overlapped at an angle in a nonlinear crystal. The autocorrelation signal encodes the spatial components of the pulse into the time domain. This results in a variation in trace wavelength vs position, appearing as a shear in the trace. The lineouts of the GRENOUILLE spectrum at different delays are shown in Fig. 2.16(b). Here we see that the central wavelength does not shift with delay, indicating the GRENOUILLE trace does not possess any sheer and the mode is free of spatial chirp.

Following compression, the beam is focused using a curved mirror ($f = 6$ m). Just after focusing, the beam propagates through a fifth order 0.4 mm quartz half-wave plate, which provides control over the NIR beam polarization. The beam diameter just after propagating through this waveplate was measured using a knife-edge scan, shown in Fig. 2.17, and is found to be $\sim$12.2 mm. After transmission through the half-wave plate, the beam is then

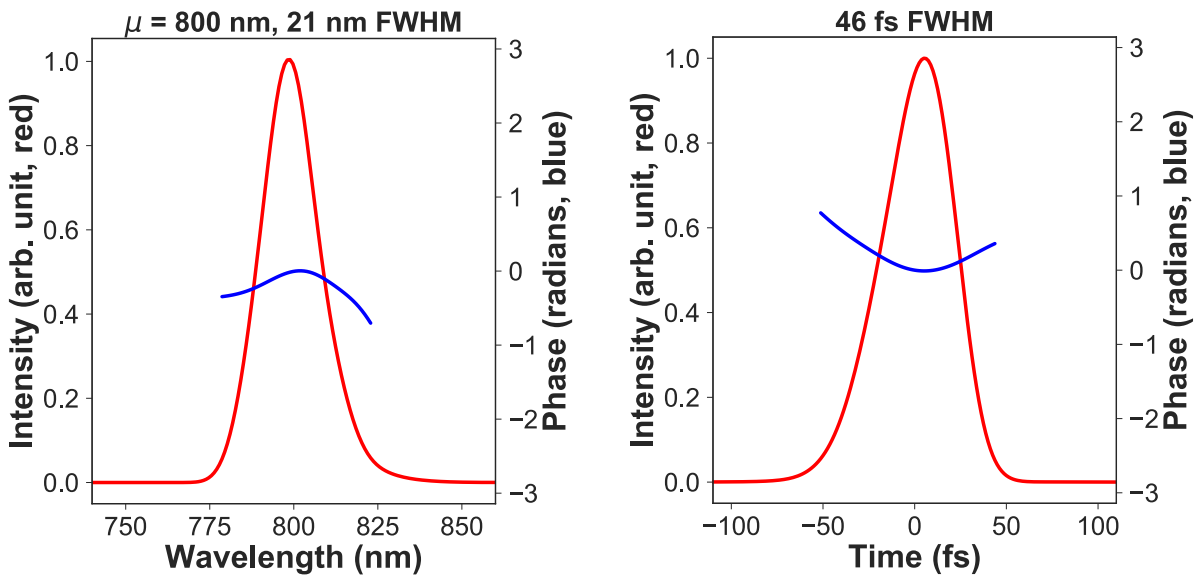

(a) (b)

Figure 2.14: (a) The spectrum of the compressed NIR pulse - the spectrum is centered at 800 nm with a FWHM of 21 nm. (b) The temporal intensity profile of the compressed NIR pulse - the pulse width has a FWHM of 46 fs. The spectral and temporal characteristics are retrieved via single-shot FROG (GRENOUILLE) [122].

frequency doubled using a 0.250 mm thick β-barium borate (BBO) crystal. The spectrum of the frequency doubled pulse is shown in Fig. 2.18, which exhibits a central wavelength of 401 nm and a FWHM of 8 nm. This crystal is mounted on a pair of motorized rotation stages which provides control over the phase-matching angle of the BBO, as well as the roll angle, which are optimized daily. We achieve doubling efficiencies near 30-35% in typical operation, where the 800 nm and 400 nm pulse energies, as well as the doubling efficiency, are shown as a function of amplifier pump power in Fig. 2.18. The copropagating 800 nm and 400 nm fields then exit the compression chamber through a beam-tube and enter the folding chamber, which houses two dichroic mirrors that transmit the NIR pulses, while reflecting the 400 nm pulses. The reflected 400 nm beam then exits the folding chamber and enters the VUV beamline through a window gate valve, which serves to separate the helium environment from the beamline that is under vacuum. These two sections are connected with a 0.250 mm UV fused silica window, which is AR coated for 400 nm on both window surfaces.

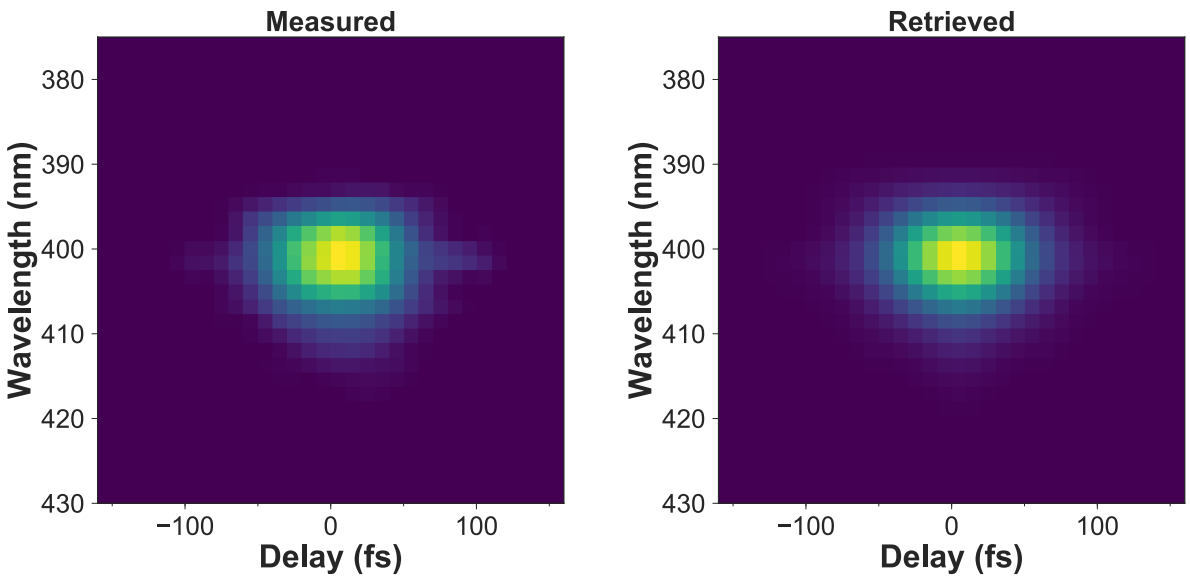

(a) (b)

Figure 2.15: The (a) measured and (b) retrieved single-shot FROG (GRENOUILLE) traces [122].

2.3.3 High-Fluence High Harmonic Generation

Once in vacuum, the 400 nm beam continues to focus towards the chamber containing a gas cell, where high-order harmonics of the blue field are generated. Here, the beam is loosely focused through a 10 cm long gas cell. This gas cell is placed on a translation stage, which has 50 cm of travel, allowing the cell position to be adjusted relative to the focus of the 400 nm beam. This gas cell is connected to a Swagelok 0.25" fitting and gas-line via a vacuum feedthrough, which is then connected to a gas delivery system, allowing the cell to be filled with different rare gases. The gas-line pressure backing the gas cell is monitored using a capacitance manometer coupled to an electronic needle valve (MKS Instruments), which is generally operated between 1-10 Torr. The gas cell is sealed off at both ends using 0.05 mm thick stainless steel shims which are each compressed against a viton O-ring. The entrance and exit apertures of the cell are then drilled by the laser itself, once the 400 nm beam has been properly aligned through the VUV beamline. These entrance and exit holes are roughly 1 mm in diameter and are drilled within a few seconds, however, they continue to increase in size with time, as the beam pointing is not actively stabilized. Thus new shims are replaced on the cell regularly, and between different measurements. The gas cell, together with an example of a pair of laser drilled shims, is shown in Fig. 2.19. The chamber containing the gas cell is pumped by a pair of 790 l/s turbomolecular pumps (Pfeiffer HiPace 800).

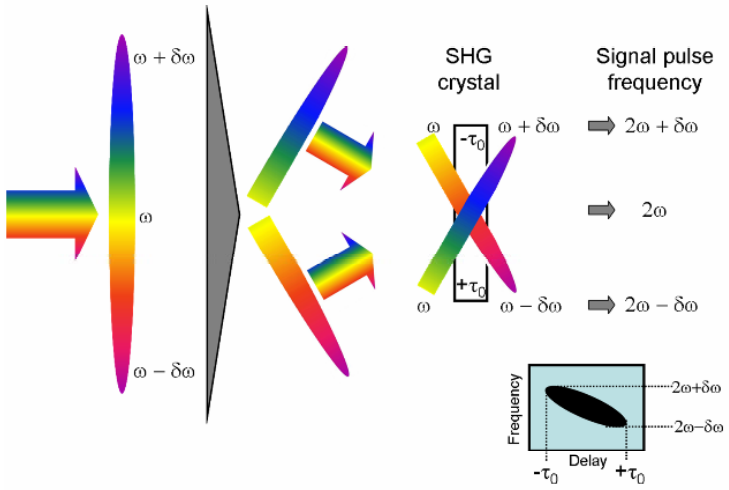

(a)

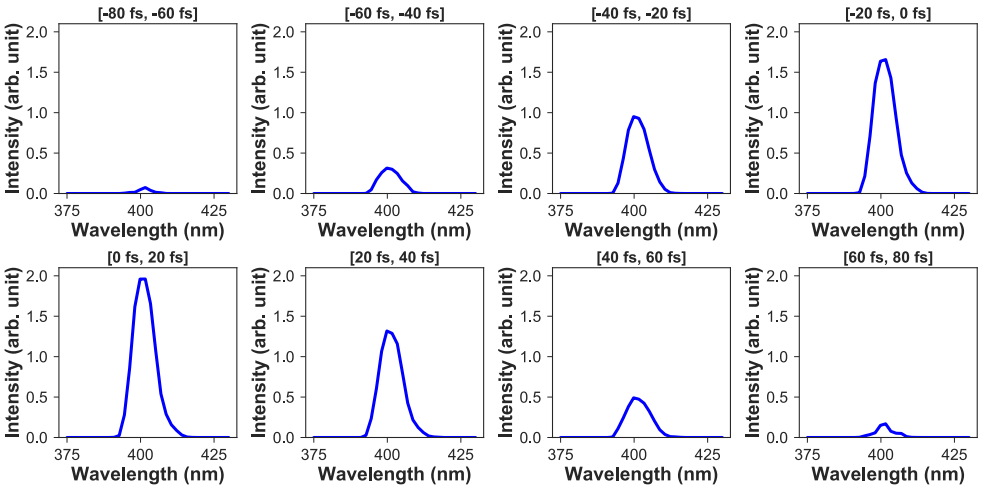

(b)

Figure 2.16: (a) A diagram from [1] showing the relationship between spatial chirp and a measured GRENOUILLE trace [122]. When a spatially chirped pulse passes through the Fresnel biprism, the pulse is split into two spatial components and overlapped at an angle in the nonlinear crystal. This autocorrelation signal encodes spatial components of the pulse into time, where spatial chirp results in a variation in the trace wavelength vs position, producing a shear in the GRENOUILLE trace. (b) Lineouts taken in 20 fs steps from the measured GRENOUILLE trace. We see that the pulse is not spatially chirped, as the wavelength does not shift with delay.

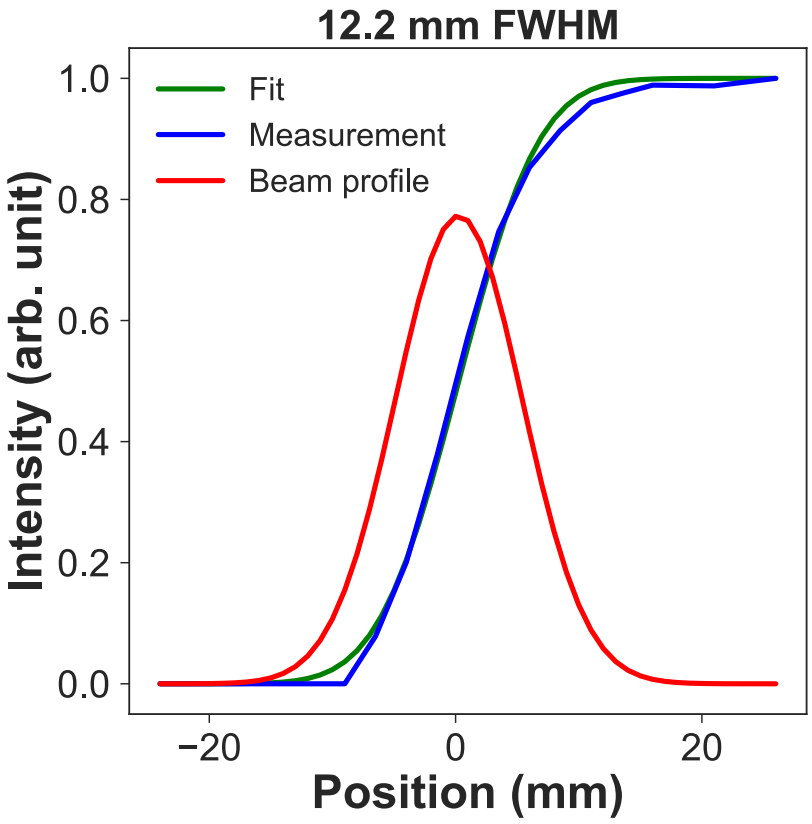

Figure 2.17: A knife edge scan of the compressed NIR beam before propagating through the BBO. The retrieved beam mode diameter possesses a FWHM of 12.2 mm.

The fluence of the harmonics are optimizing by varying different experimental parameters, such as the gas cell position relative to the focus, the driving pulse length and energy, and the gas pressure in the cell. Varying these parameters allows conditions where phase-matching across a large interaction volume of atoms can be achieved, resulting in a large number of in-phase emitters and thus high flux. These parameters are varied while the signal on either an Al coated XUV photodiode (Opto Diode AXUV100TF400) is monitored for optimizing the high orders, or the signal on a calibrated XUV photodiode (Opto Diode AXUV100G) in conjunction with two bandpass VUV filters (Acton Optics FB130-B-1D.3) is used to optimize the third harmonic. In optimized conditions, the focus is usually placed roughly 50 cm downstream from the gas cell, and can be varied using the translation stage on which the cell is mounted, as previously mentioned. The pulse duration is varied by adjusting the separation between the two gating in the compressor using a motorized stage, where in optimized conditions, the pulses are nearly transform-limited. As highlighted in the previous paragraph, the pressure inside the gas cell is controlled via a needle valve in feedback with

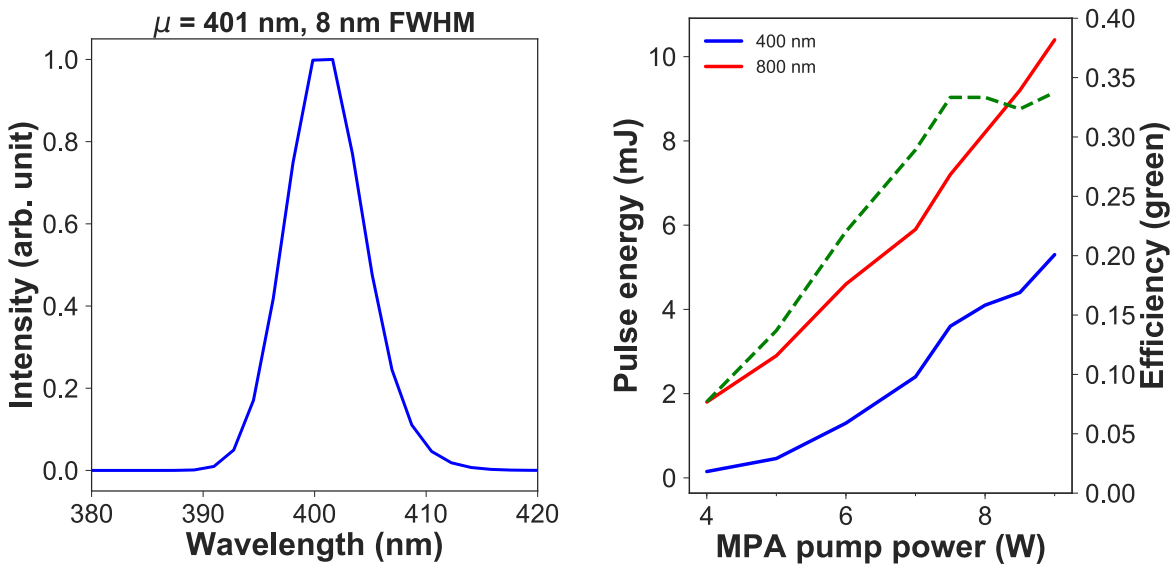

(a) (b)

Figure 2.18: (a) The measured BBO spectrum, with a central wavelength of 401 nm and a FWHM of 8 nm. (b) A comparison between the 532 nm MPA pump power and the compressed NIR 800 nm pulse energy (red curve) as well as the frequency doubled 400 nm pulse energy (blue curve). The dashed green curve indicates the BBO conversion efficiency, which saturates just under 35%.

a capacitance manometer. The optimal gas pressure varies significantly depending on which harmonic order in the frequency comb is being optimized. The optimum conditions for low order harmonics are achieved at higher gas pressures (∼3-4 Torr). As the pressure is increased, the number of emitters in the focal volume increases, but the plasma density also increases. This results in greater plasma dispersion and thus phase-mismatch. Since the high order harmonics are very intolerant of plasma dispersion, they do not phase-match well at high pressures. In contrast, the low order harmonics can tolerate a greater amount of plasma dispersion while still maintaining phase-matching. Thus higher pressure results in more emitters, where phase-matching is more easily maintained for the lower orders. Additionally, higher gas pressure results in greater neutral dispersion, resulting in another form of phase-mismatch that is similarly less tolerated at higher orders. For these reasons, lower gas pressures (∼1 Torr) are used to achieve maximum flux for the higher order harmonics.

The pulse energy of the third and seventh harmonic as a function of krypton pressure inside the gas cell is shown in Fig. 2.20. The pulse energies were measured using a calibrated XUV photodiode (Opto Diode AXUV100G) in conjunction with two bandpass VUV filters (Acton Optics FB130-B-1D.3) in the case of the 3rd harmonic, and a calibrated Al coated XUV photodiode (Opto Diode AXUV100TF400) in the case of the 7th harmonic. These

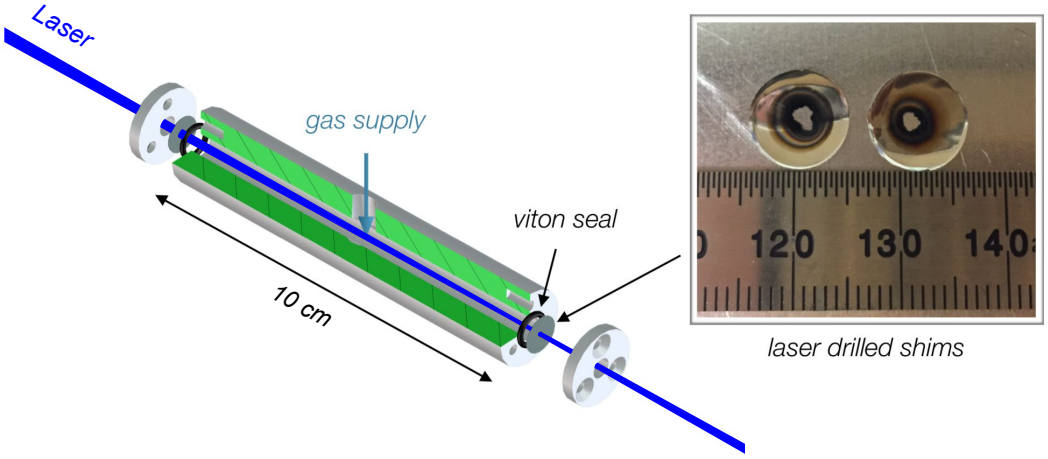

Figure 2.19: The 10 cm long finite gas cell used for HHG. The gas cell is sealed off at the entrance and exit using 0.05 mm stainless steel shims, which are compressed against viton O-rings. The inset depicts a pair of laser drilled shims (mm scale for reference). Figure adapted from [154].

pulse energies indicate a conversion efficiency of 7e-6 for the 3rd harmonic and 8e-8 for the 7th harmonic, suggesting that the 5th is likely near 1e-6. The spectra of these two harmonics are shown in Fig. 2.20, with their central wavelength and FWHM indicated above each plot. The spectrum of the 3rd was determined using a measured photoelectron spectrum resulting from non-resonant two-photon ionization of argon atoms using the 3rd harmonic, while the spectrum of the 7th was determined using a measured photoelectron spectrum resulting from photoionization of argon atoms using the 7th harmonic. The complete VUV frequency comb is shown in Fig. 2.21.

The pulse duration of the 5th harmonic of the NIR field has been measured to be 16 fs for a 50 fs NIR driving pulse ([3]) and is between 10-20 fs for higher orders ([154]). Since the pulse duration of the 400 nm field is similar and the spectral bandwidth of the 3rd harmonic of the 400 nm field (200 meV) is comparable to the high orders (300 meV) and larger than the 5th harmonic of the NIR field (150 meV), we estimate the pulse duration of the 3rd harmonic to be somewhere between 15 - 30 fs. The spectral bandwidth of the 3rd harmonic is capable of supporting transform limited pulses between 6-7 fs, using a Gaussian time-bandwidth product. We point out that the ionization gate set in the HHG process does not limit the pulse durations as significantly as it does in the NIR case, thus it is likely that the pulse duration of the 3rd harmonic is slightly greater than that of the NIR driven harmonics. However, the plasma effect is not as serious at longer wavelength harmonics (low orders), so the pulse durations are expected to be similar.

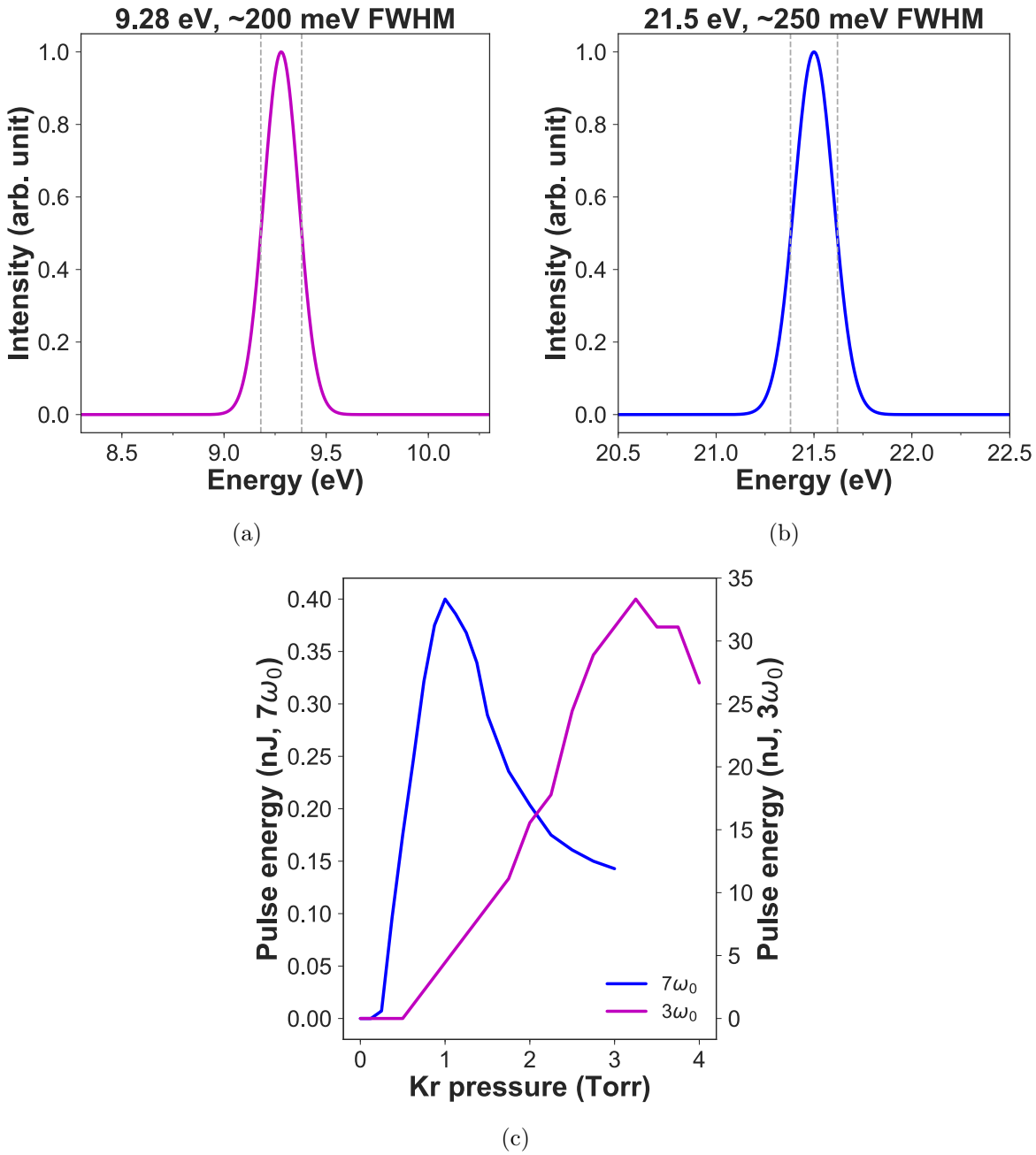

(a) (b)

(c)

Figure 2.20: (a) The spectrum of the 3rd harmonic of the 400 nm driving field, centered at 9.28 eV with a FWHM of ∼200 meV, and (b) the spectrum of the 7th harmonic of the 400 nm driving field, centered at 21.5 eV with a FWHM of ∼250 meV. (c) The pulse energy of the 3rd harmonic (magenta, right y-axis) and 7th harmonic (blue, left y-axis) as a function of Kr pressure inside the HHG cell.

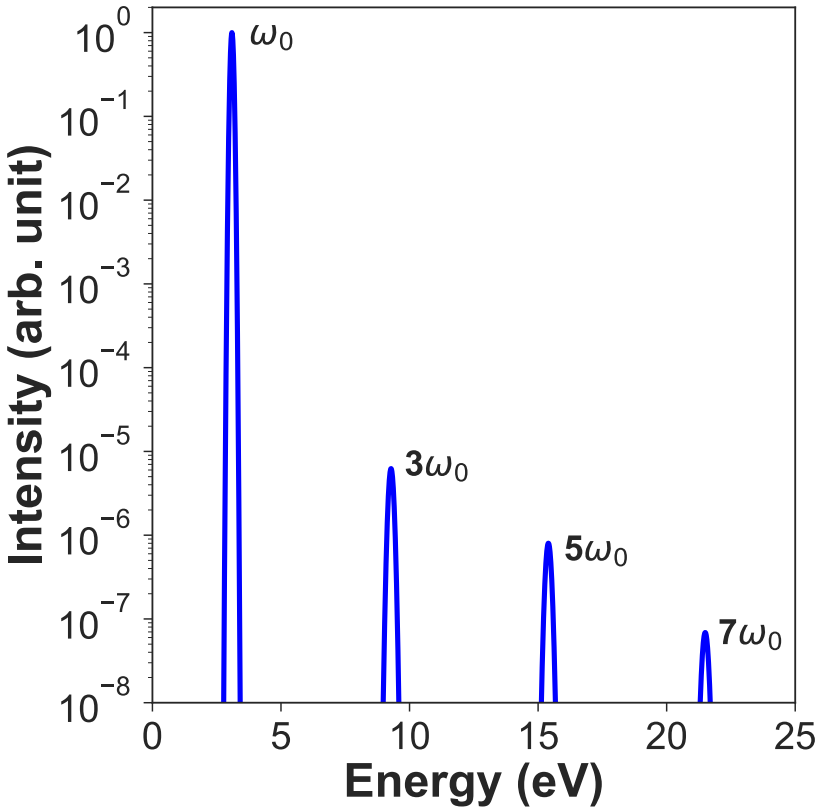

Figure 2.21: The VUV frequency comb produced in the present HHG set-up. The intensity of the $3\omega_0$ and $7\omega_0$ peaks are determined from the measured pulse energy of these two harmonics at optimal driving pulse energy and Kr pressure, while the intensity of the $5\omega_0$ peak is inferred from the two adjacent harmonics. The position of $3\omega_0$ (9.28 eV) was determined from the measured photoelectron spectrum from non-resonant two-photon ionization of Ar with the third harmonic, while the position of $7\omega_0$ (21.5 eV) was determined from the measured photoelectron spectrum from photoionization of Ar with the seventh harmonic. The position of the $5\omega_0$ (15.4 eV) peak is then inferred from the two adjacent harmonics.

Chapter 3

Vacuum Ultraviolet Beamline

In this chapter, we will discuss the vacuum ultraviolet beamline and its instruments that are used in the measurements presented in this thesis. The beamline itself contains various components which enable beam-transport, surveillance and spectral tailoring, which are all discussed in detail.

Since the photon energies created in high harmonic generation lie in the VUV, the beam needs to be transported in a beamline under vacuum, with various components housed in vacuum chambers connected to the beamline. This presents technical challenges in terms of beam transport, heat transport, material choice, beam viewing, spatial constrains and actuation of mechanical devices in vacuum. Further, experiments may require a single or multiple VUV photon frequencies that excite either resonant or non-resonant transitions and processes, hence spectral selectivity become a necessary capability. Various methods are implemented to select specific harmonics from the VUV frequency comb. These all involve transmission of the VUV photon beam through either gas-phase or condensed-phase media. The fundamental frequency used to generate the VUV photons also needs to be attenuated, to minimize any unwanted effects from the driving field. This is achieved using reflections near Brewster's angle for the fundamental frequency. One of these reflections is from a custom in-vacuum split-mirror interferometer (developed in collaboration with the Center for X-Ray Optics at Lawrence Berkeley National Laboratory), which allows a time-delay to be introduced for pump-probe experiments. The beamline components, as well as the methods for overcoming specific technical challenges, are described in the following chapter.

3.1 Beamline Instruments

Immediately following high harmonic generation, the photon beam propagates downstream into the VUV beamline. Various beamline instruments enable the spectral and temporal properties of the VUV field to be shaped, and the fundamental frequency to be attenuated. A rendering and partial layout of the beamline and its instruments are shown in Fig. 3.1 and 3.2, where the various components are labeled, which are discussed in the following

subsections. Two-photon transitions in atomic and molecular systems driven in the VUV can lead to photoionization and photodissociation. In order to understand the underlying dynamics involved in these processes, it is necessary to know the photon energies being used to drive the dynamics in the system. Thus having selectivity in the VUV spectrum is crucial in reducing the degree of complexity in measurements, and providing more interpretable and understandable experiments.

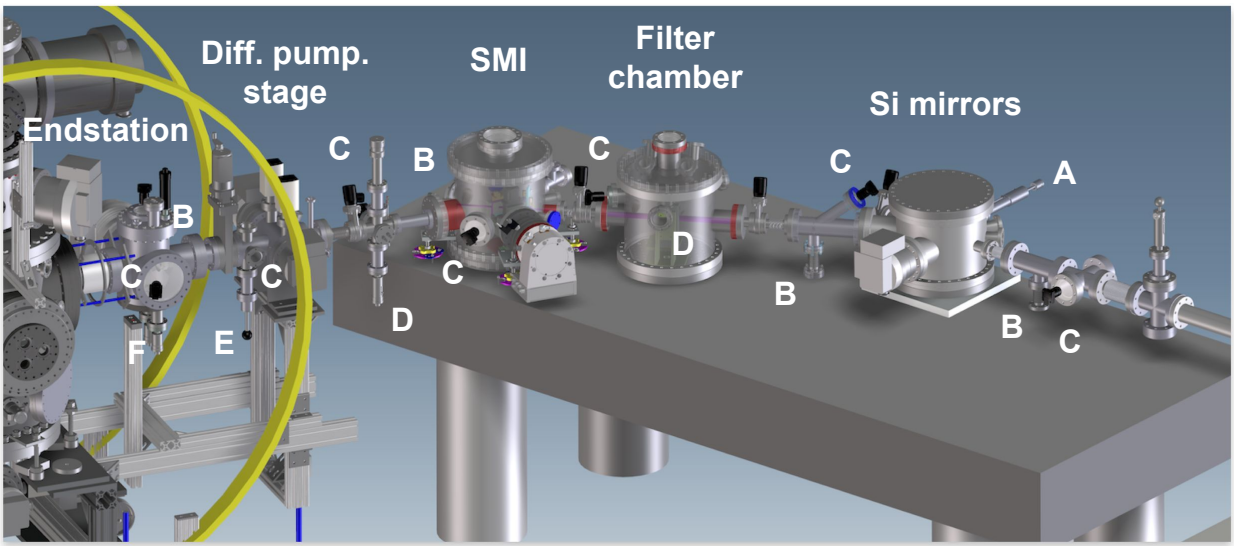

Figure 3.1: A rendering of the partial layout of the VUV beamline and its various instruments, with labeled components: (A) The actuator for the Si mirror pair, (B) beamline irises, (C) beamline cameras, (D) beamline photodiodes, (E) phosphor screen, (F) Cu plate. Figure adapted from [154].

Spectral selectivity is often achieved using a monochromator, which are often encountered at synchrotron radiation light sources, as well as free electron lasers. However, designing time-preserving monochromators that do not significantly stretch the pulse duration is a technical challenge. This is a non-issue for synchrotrons, since the pulse durations are already on the order of 100 ps, but for free electron lasers and high harmonic generation based light sources, this can greatly influence the physics and dynamics that can be probed, since the ultrashort pulses are greatly stretched. In the case of time-preserving monochromators, this technical challenge is compounded by a significant reduction in VUV fluence, since this geometry requires reflection from a second grating, which recompresses the pulse in time. Due to the reflection from two gratings, as well as additional mirrors in the monochromator, the photon flux can be attenuated by a factor of 10 or greater. This creates limitations in terms of the types of experiments that can be performed, since two-photon absorption in the VUV requires high flux. Since state-of-the-art time-preserving monochromators exhibit such low transmission, other methods for spectral selectivity were implemented. These methods

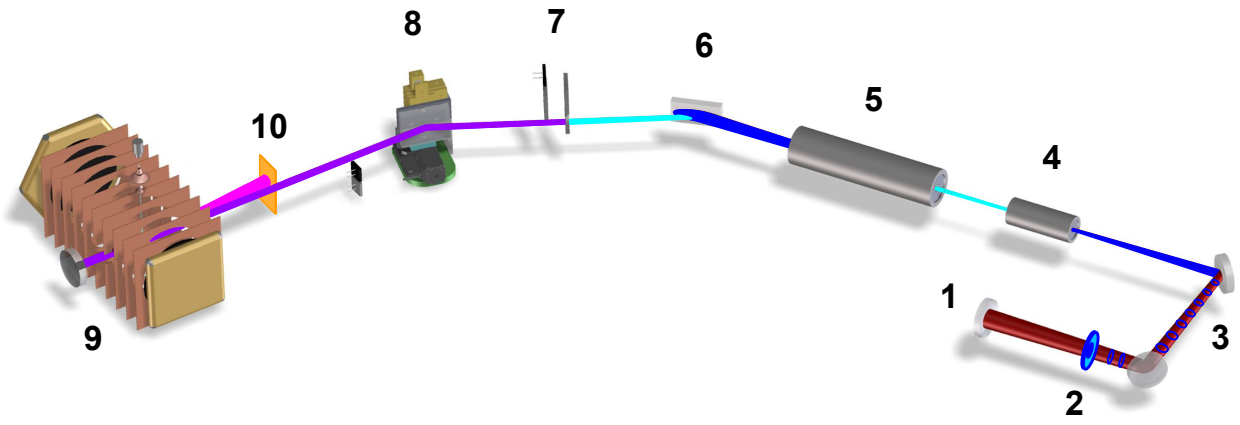

Figure 3.2: A schematic overview of the VUV beamline and its various instruments, with labeled components: (1) Curved mirror (f = 6 m), (2) BBO, (3) dichoric mirrors, (4) HHG cell, (5) gas filter, (6) Si mirror pair, (7) solid transmissive filters, (8) split-mirror interferometer, (9) 3-D momentum imaging spectrometer, (10) Cu plate. Figure adapted from [154].

involve transmitting the beam through an absorbing medium, which can be in the gas or condensed phase. In order to suppress the fundamental frequency, the beam undergoes a series of reflections from silicon mirrors at or near Brewster's angle for the driving field. One of these reflections is from a split-mirror that forms an interferometer, allowing a time-delay to be introduced for pump-probe studies. These details are all discussed in the following subsections.

3.1.1 Gas Filter

When light propagates through a material, the electromagnetic wave can be attenuated. The amount of attenuation depends on the properties of the medium through which the light is traveling. The field intensity as a function of penetration depth into the material can often be conveniently expressed in terms of the famous Beer-Lambert law. Taking the beam propagation direction to be along the z-axis, the field attenuation can be modeled using the ordinary differential equation

$$\frac{dI(z)}{dz} = -\mu(z)I(z) \tag{3.1}$$

where $I(z)$ is the z-dependent field intensity and $\mu(z)$ is the z-dependent attenuation coefficient of the medium (related to the number density and cross section of the species).

Solving this differential equation for a material with an attenuation coefficient that does not vary with z, the field intensity along the propagation direction can be simply expressed as

$$I(z) = I_0 e^{-\mu z} \tag{3.2}$$

Here the intensity falls off exponentially along the beam propagation direction. As such, the spectral properties of the VUV beam can be manipulated via transmission through a volume of gas. Depending on the photoabsorption spectrum of the species used, different photon energies can be filtered out of the beam. Both photoexcitation and photoionization contribute to attenuation at specific photon energies. Gas filter cells are used at synchrotron and FEL facilities, however their use in HHG beamlines is less widespread. Such gas cells enable the simple exchange of filter medium, where the transmission can be varied with the gas pressure.

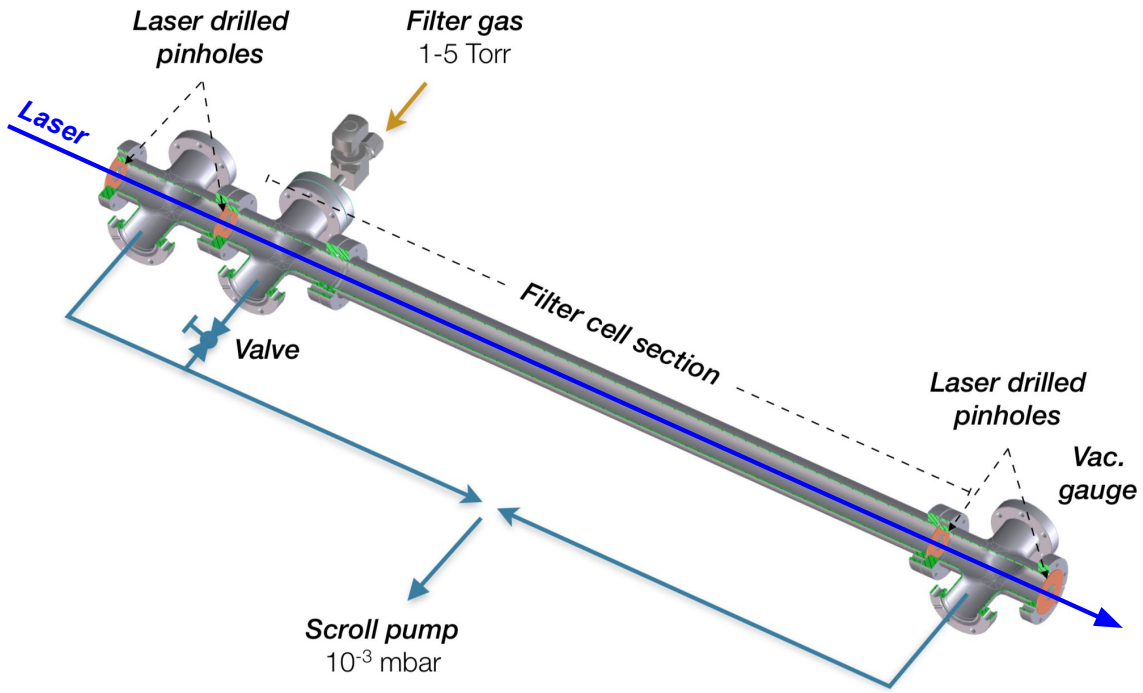

Figure 3.3: A diagram of the section of the VUV beamline containing the gas filter cell. Certain photon energies are attenuated upon transmission through the gas medium. The beam tube separating the laser drilled pinholes is 32" in length. A few Torr of gas can be introduced into this section of the beamline, which is differentially pumped from both sides, maintaining high vacuum in the rest of the beamline. Figure adapted from [154].

The gas filter cell is composed of a section of the VUV beam tube itself and is depicted in Fig. 3.3. The section of the beamline containing the filter cell is immediately upstream from the HHG chamber and downstream from the chamber containing the first silicon mirror. Gas from a cylinder can be introduced into the filter cell via a manifold and by varying the vacuum pump configuration. The section of beamline that forms the filter cell consists of three DN38 ConFlat Tees that are connected with a long beam tube. The Tees serve as differential pumping stages that separate the gas filter section of the beamline from the high vacuum sections of the beamline. These sections are separated using solid copper plates containing roughly 1" holes, which themselves are covered with 0.1 mm thick stainless steel foil. The pre-aligned laser was used to drill holes through the steel foils with a diameter of a few mm, similar to the procedure performed in drilling through the steel shims on the HHG gas cell. This enables low gas conductivity to be achieved between the high and low pressure sections of the beamline.

The pressure inside of the gas filter cell can be controlled using a capacitance manometer coupled to an electronic needle valve (MKS Instruments), identical to that used in the HHG gas delivery and pressure monitoring system. Gas pressures of a few Torr are typically used for beam attenuation. Both the upstream and downstream differential pumping stages of the gas filter are pumped using a scroll pump (Varian TriScroll 600). It has been previously measured that using 3 Torr of gas pressure in the filter cell results in a measured vacuum in the silicon mirror chamber directly downstream of the cell of roughly $7\times\ 10^{-4}$ mbar, and is less than 10^{-6} mbar in the SMI chamber.

3.1.2 Si Mirror Chamber

Downstream from the HHG gas cell, the generated VUV field and the 400 nm driving field copropagate. Due to the conversion efficiency of the HHG process, the driving field may be several orders of magnitude more intense than the VUV field. The driving field can be separated from the generated VUV harmonics using a reflection from a silicon mirror at Brewster's angle for the driving field, serving as a dichroic beam splitter [55]. Brewster's angle is defined as the angle of incidence in which light of a particular polarization is totally transmitted at a dielectric interface, without any reflection. For p-polarized light, one can derive Brewster's angle from the Fresnel equation

$$R_p = \left| \frac{n_1 \cos\theta_t - n_2 \cos\theta_i}{n_1 \cos\theta_t + n_2 \cos\theta_i} \right|^2 \tag{3.3}$$

with Brewster's angle given by

$$\theta_B = \arctan\left(\frac{n_2}{n_1}\right) \tag{3.4}$$

where n_1 and n_2 is the refractive index of the two media composing the interface, while θ_i and θ_t are the angle of incidence and transmission, respectively. Reflection at Brewster's angle enables the fundamental frequency to be significantly attenuated, minimizing effects

from the driving field in experiments, while preserving a suitable level of the VUV flux to perform two-photon absorption. Further, silicon has a high laser induced damage threshold, which makes it a suitable material choice when the fundamental field intensities are high.

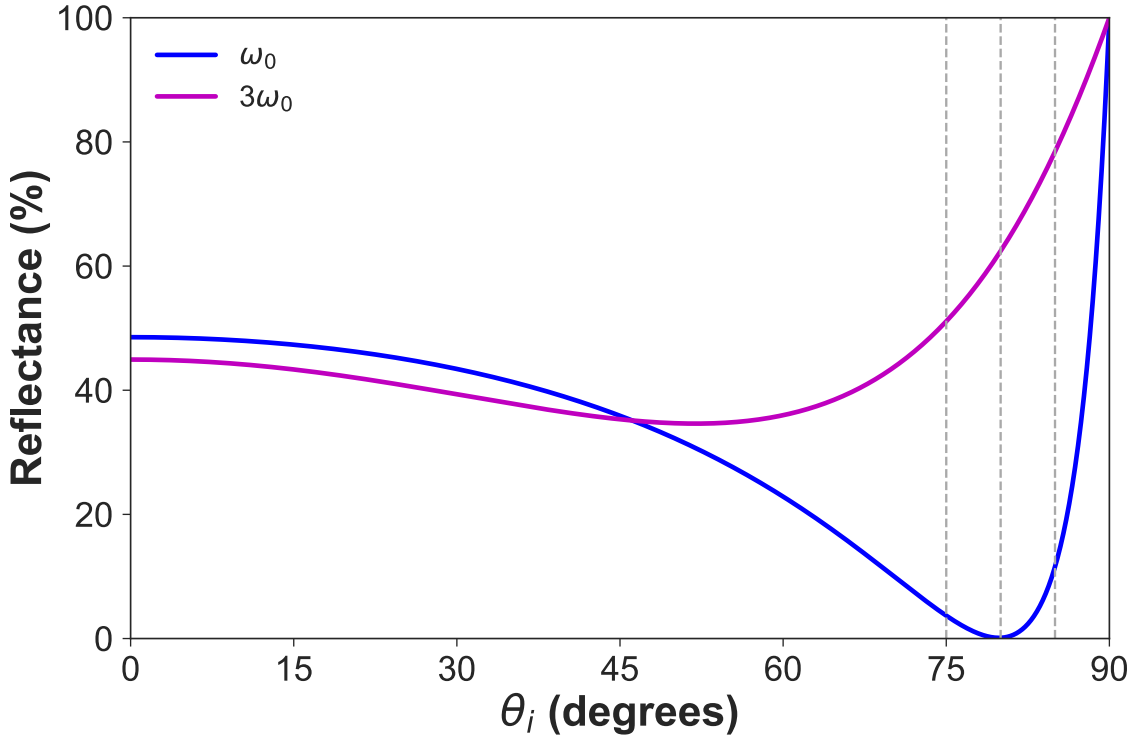

Figure 3.4: The reflectance of Si as a function of the angle of incidence θ_i for p-polarization for both the 400 nm driving field and the 3$^{\text{rd}}$ harmonic. The angle of incidence for the three reflections that are undergone are indicated by the dashed vertical gray lines. The result is that the driving field is suppressed by approximately 10^{-6}, while 25% of the 3$^{\text{rd}}$ harmonic is reflected. The curves are calculated from the Fresnel equations, where the refractive index properties of Si at 400 nm and the 3$^{\text{rd}}$ harmonic were obtained from Refs. [8, 127].

The reflectance of crystalline silicon as a function of the angle of incidence is calculated for the fundamental frequency ω_0 and third harmonic $3\omega_0$, and is shown in Fig. 3.4. At Brewster's angle for a p-polarized 400 nm field, which is 79.9°, the reflectance should in theory be zero. Slight deviations from this angle results in a measurable reflectivity. However, the reflectance curve exhibits a relatively broad minimum, meaning small departures from Brewster's angle will still result in significant driving field attenuation. It can be seen that at Brewster's angle for fundamental frequency, the reflectance of the Si mirror at the third harmonic $3\omega_0$ is approximately 62%. At angles of incidence in the neighborhood of Brewster's angle, the VUV reflectivity is rather high, remaining above 50% at an angle of incidence of 74.9°. At

these steep angles of incidence, the silicon mirrors must be several inches long, in order to provide adequate surface area to accommodate the entire beam profile on the mirror.

The fundamental field is suppressed using three silicon mirror reflections, which are indicated in Fig. 3.4 as the dashed vertical gray lines. One reflection is at Brewster's angle for the fundamental frequency, while the other two reflections are at $\pm 5^\circ$ from Brewster's angle. The first two silicon mirrors are contained in one vacuum chamber, while the third silicon mirror is contained in its own downstream vacuum chamber. The third silicon mirror is a split-mirror interferometer, which will be discussed in detail in a following subsection. The first reflection is at Brewster's angle of approximately an 80° angle of incidence, the second reflection is near an 85° angle of incidence, and the third reflection is near a 75° angle of incidence. In this configuration using three reflections, approximately 25% of the third harmonic $3\omega_0$ is reflected, while the fundamental frequency ω_0 is attenuated by roughly a factor of 10^{-6}.

The amount of attenuation of the fundamental varies, depending on the exact beam alignment, since the reflectance varies with the angle of incidence, as well as the beam ellipticity, since any s-polarization component is highly reflected (roughly 88% reflectance at Brewster's angle). The suppression of the fundamental field is optimized before performing a measurement. This is achieved by finding the optimal beam alignment using the motorized mirrors upstream in the beamline, and by minimizing the s-component of the polarization of the field by varying the roll angle of the BBO with respect to the NIR input polarization using its motorized stage. Minimizing the signal on a photodiode downstream from the three silicon mirrors provides a procedure that ensures that near-optimal driving field attenuation can be achieved in the actual experiments.

3.1.3 Solid Filter Chamber

As the beam propagates downstream from the first silicon mirror chamber, it enters a vacuum chamber containing various types of solid filters. Similar to the gas filter, transmission of the VUV beam through a thin solid material will result in attenuation of the spectral power density at certain frequencies that depend on the photoabsorption properties of the solid material. Transmission through a different solid materials can thus filter out different components of the VUV frequency comb, where the transmitted frequencies lie off resonance with the states and band structure of the material. Since most materials possess most of their oscillator strength in the VUV, this leaves very few materials that are of any practical use. Further, these materials must be fabricated to be extremely thin, due to the high number densities in condensed matter that result in significant attenuation and/or dispersion, which can create technical challenges.

One common type of VUV solid filter comes in the form of thin fluoride crystal windows, e.g. CaF_2, MgF_2 and LiF. These crystals are capable of transmitting certain VUV wavelengths, in particular the third harmonic $3\omega_0$ of the 400 nm driving field, while suppressing the fifth harmonic and above. The VUV transmission curve for a 2 mm thick MgF_2 window is shown in Fig. 3.5(b), where the wavelength of the third harmonic is shown as a dashed

vertical gray line, indicating an achieved transmission of above 60%. In the filter chamber itself, a 0.25 mm thick MgF_2 window is used, which will exhibit higher transmission at $3\omega_0$ than what is shown in Fig. 3.5(b). These windows can also be optically coated using a dielectric material, which can be highly reflective to the fundamental frequency. This can serve to further improve the suppression of the driving field. The transmission curve for a 0.30 mm thick dielectric coated MgF_2 window used in our experiments (Acton Optics FB130-B-1D.3) is shown in Fig. 3.5(a), where we see the transmission at 400 nm is near zero while still showing transmission above 30% at $3\omega_0$. Since MgF_2 is birefringent, it is important that windows are fabricated from a c-cut crystal, i.e. cut along the optical axis, in order to minimize the birefringence.

Thin metallic filters also offer a way to select certain spectral components or regions of the VUV spectrum. These are free-standing metal foils, typically on the order of 100 nm thick. Transmission curves for 150 nm thick Al, In and Sn metal filters are shown in Fig. 3.5(c). While fluoride windows are capable of transmitting the low-order VUV harmonics, in particular the third harmonic $3\omega_0$, the metal foils are capable of transmitting the higher-order VUV harmonics, including the fifth harmonic $5\omega_0$ and above. In Fig. 3.5(c), we can see that the In filter transmits the fifth harmonic $5\omega_0$, while the Al and Sn filters transmit the seventh harmonic $7\omega_0$, indicated as the dashed vertical gray lines. Due to oxidization, the actual transmission curves for metal foils used in experiments will be significantly lower than the calculated transmission indicated by the curves in Fig. 3.5(c). This is because the oxidized layer that builds up on the metal surface can be highly absorbing and lead to increased attenuation. The foils themselves oxidize immediately upon exposure to atmosphere, which makes handling and installation challenging. This oxidization can be minimized by keeping the foils in an Ar gas environment during transport and installation, which reduces contact between the foil and any oxygen in the air. Since these foils are free-standing and on the order of 100 nm thick, they are extremely delicate and need to be handled with care in order to not damage or tear the foils during installation. Caution must also be exercised when bringing the filter chamber down to vacuum, where air currents and pressure gradients introduced by the vacuum pump can rip the foils. Gate valves on the upstream and downstream sides of the filter chamber allow this volume to be isolated from the rest of the beamline and pumped down separately.

Transmission through the aforementioned fluoride windows will also introduce a temporal delay between the driving pulse and the third harmonic pulse, due to the dispersion of the material. The temporal separation between the ω_0 and $3\omega_0$ pulses depends on the thickness of the window. The delay that is introduced between the driving and harmonic pulse can be captured by the difference in the group velocity of the fundamental frequency ω_0 and third harmonic $3\omega_0$ in the material, where the group velocity is given by

$$v_g = \frac{c}{n_g(\omega)} = \frac{c}{n(\omega) + \omega \frac{dn(\omega)}{d\omega}} \tag{3.5}$$

where n_g is the group index of the material, defined as the ratio of the velocity of light in vacuum to the group velocity in the material. The group velocity of the light in the

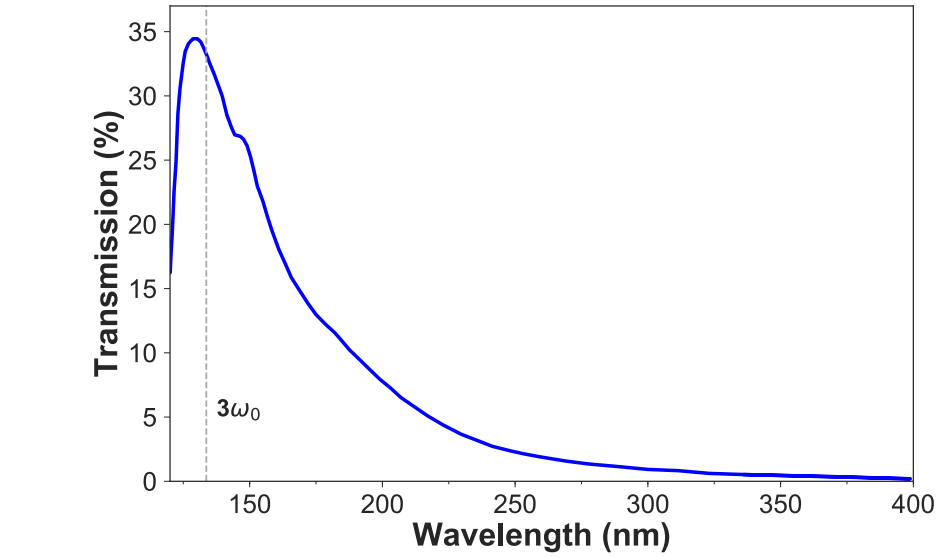

(a)

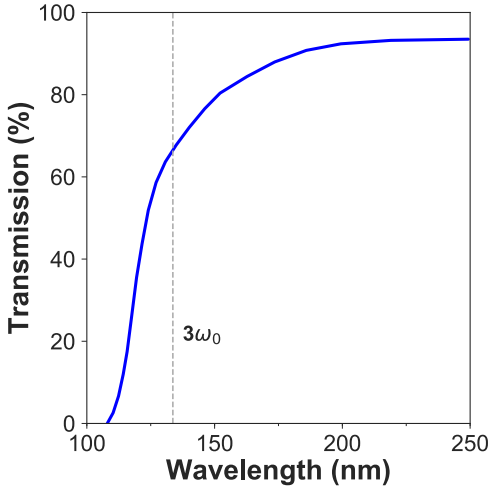

(b)

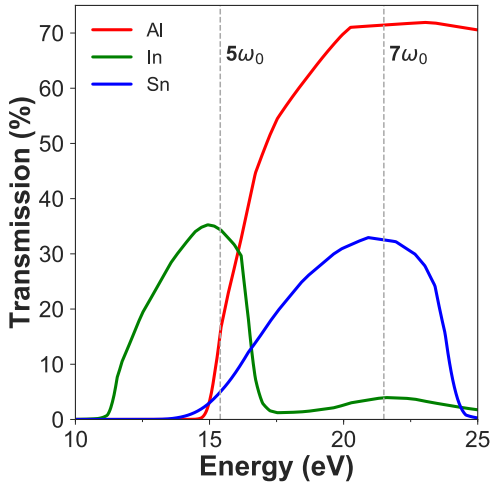

(c)

Figure 3.5: (a) The transmission as a function of wavelength for the 0.30 mm thick dielectric coated MgF_2 window. The 3rd harmonic wavelength is indicated by the vertical dashed gray line. (b) The transmission as a function of wavelength for a 2 mm thick MgF_2 window (data from [51]). The experiments make use of a 0.25 mm thick MgF_2 window, which will show higher transmission at the 3rd harmonic, indicated by the vertical dashed gray line. (c) The transmission as a function of wavelength for 150 nm thick Al, In and Sn filters. The 5th and 7th harmonic are indicated by the vertical dashed gray lines (data from [67]).

material is equivalent to the inverse of the group delay per unit length, where the group delay corresponds with the time delay experienced by a pulse when propagating through the medium. Hence the group delay per unit length T_d can be expressed as

$$T_d = \frac{1}{c}\left(n(\omega) + \omega\frac{dn(\omega)}{d\omega}\right) \tag{3.6}$$

From this expression, we can calculate the temporal separation Δt introduced between the driving pulse and third harmonic pulse upon transmission through a fluoride window of thickness L, which is given by

$$\Delta t = L\left(T_d(3\omega_0) - T_d(\omega_0)\right) \tag{3.7}$$

The temporal delay between the driving and third harmonic fields as a function of MgF_2 window thickness is shown in Fig. 3.6(a). The two MgF_2 filters mounted in the filter chamber are 0.25 mm and 0.30 mm thick (indicated as vertical dashed gray lines in Fig. 3.6(a)), which introduce a delay of roughly 710 fs and 850 fs (indicated as horizontal dashed gray lines in Fig. 3.6(a)), respectively. These temporal separations introduced between the fundamental and the third harmonic pulse can be useful in minimizing unwanted two-color effects in the experiments.

The pulse duration is also influenced via transmission through a material, which is known as dispersive pulse broadening. Since the group velocity in a medium is frequency dependent, different spectral components of an initially transform limited pulse will disperse in time when propagating through a material. This will chirp the pulse, increasing its duration. However, depending on the initial chirp of the pulse, the dispersion of the material can compress the pulse to shorter durations. The pulse length after propagation through a filter of thickness L is given by

$$\tau(L) = \tau_0\sqrt{\left(1 + 2\frac{1}{c}\frac{dn_g}{d\omega}L\beta\right)^2 + \left(\frac{4\ln(2)\frac{1}{c}\frac{dn_g}{d\omega}L}{\tau_0^2}\right)^2} \tag{3.8}$$

where τ_0 is the initial temporal FWHM width of the pulse and β is the initial chirp of the pulse. Harmonics that are generated in the strong field regime carry an intrinsic negative chirp acquired from the intensity dependent dipole phase, measured to be roughly $\beta = 3 \times 10^{27}$ rad/s^2 for NIR driven HHG [2]. Transmission of negatively chirped pulses, as in the case of harmonics generated in HHG, through sufficiently thin materials with positive dispersion can result in pulse compression.

The output pulse duration as a function of the input pulse duration for a 0.25 mm and 0.30 mm thick MgF_2 window is shown in Fig. 3.6(b) and (c). In both figures, the dashed diagonal black line indicates where the input pulse duration is equal to the output pulse duration. Thus when the red curve lies below this dashed line, the pulse is compressed via transmission through the material, whereas when the red curve lies above this dashed line, the pulse is stretched. The pulse duration of the third harmonic is estimated to lie within

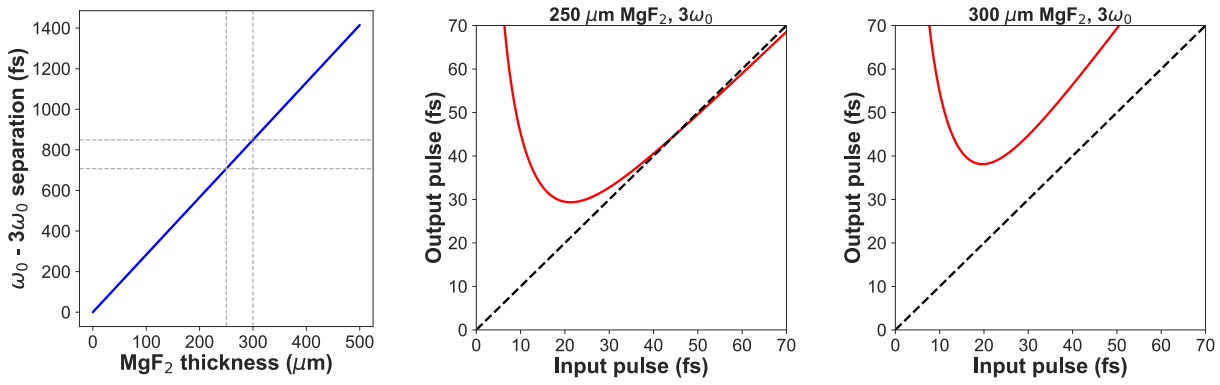

(a) (b) (c)

Figure 3.6: (a) The separation between the fundamental and 3$^{\text{rd}}$ harmonic as a function of MgF_2 filter thickness. The two filters used in the experiments are 250 μm and 300 μm, which results in a temporal separation of 710 fs and 850 fs, respectively, indicated as dashed gray lines. This curve is calculated from the Sellmeier equations for MgF_2 derived in [95]. The output pulse duration for a given input pulse duration for MgF_2 filter thicknesses of (a) 250 μm and (b) 300 μm. The diagonal dashed black line shows where an input pulse length is equal to the output pulse length. When the curve lies below this dashed line, the pulse is compressed when propagating through the material. For pulse durations between 15 - 30 fs (the estimated pulse duration of the 3$^{\text{rd}}$ harmonic), the 250 μm filter outputs pulses in the range of 29 - 32 fs, while the 300 μm filter outputs in the range of 38 - 44 fs. These curves are calculated from the same Sellmeier equations for MgF_2 derived in [95].

the range of 15–30 fs, and can be roughly approximated as the driving pulse duration times $1/\sqrt{3}$, i.e. $\sim$ 25 fs [61]. However, the actual pulse duration is estimated to be shorter than this value, since the $1/\sqrt{q}$ approximation is expected to be inadequate at our field intensities. For pulse durations lying in the range of 15–30 fs, the transmission through the 0.25 mm thick MgF_2 window results in pulse durations in the range of 29–32 fs, while transmission through the 0.30 mm thick MgF_2 window results in pulse durations in the range of 38–44 fs.

Fig. 3.7 depicts the motorized linear stages used for bringing the filters in and out of the beam path. The two stages can hold numerous filters, with mounts for both fluoride windows and free-standing metallic filters. The design enables both full 1" circular windows and metal foils to be mounted, as well as D-shaped windows and foils, which can spatially cover half of the beam mode. This allows one type of filter to be introduced into one half of the beam and a different type to be introduced into the second half of the beam. By spectrally filtering different spatial parts the beam mode, a pump and probe arm at different photon energies can be created. One of the motorized stages also contains an Al coated photodiode (Opto Diode AXUV100TF400), which permits VUV photon flux measurements after the first two silicon mirror reflections. These two stages allow for a total of two windows and three filters

to be mounted. In the case of D-shaped filters, this enables six different filter combinations.

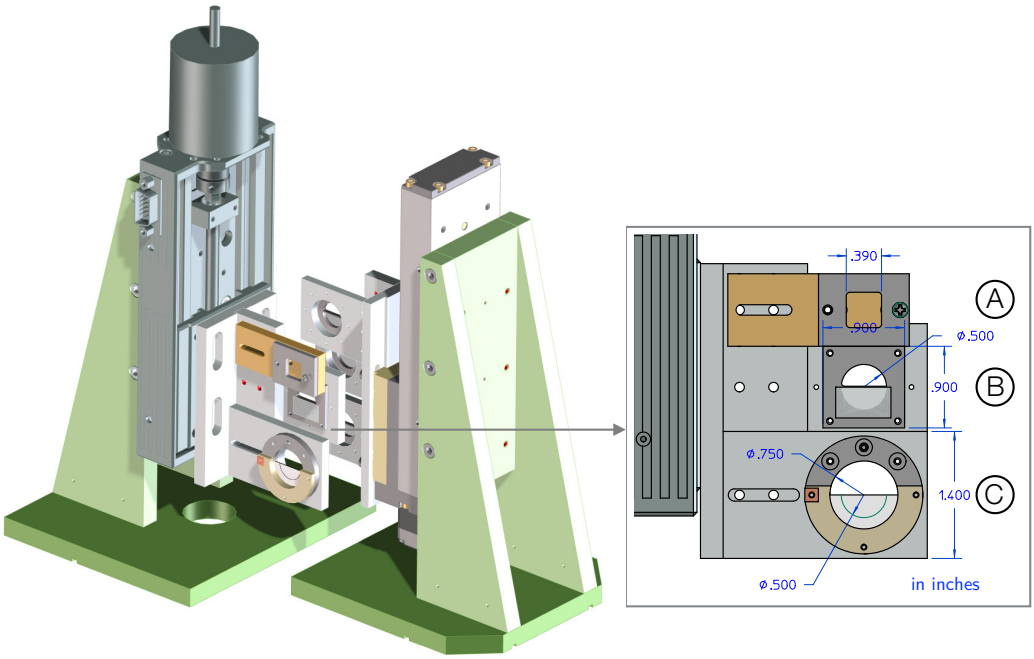

Figure 3.7: A diagram of the VUV beamline solid filter stages, comprised of two motorized linear stages. The stage motion is perpendicular to the beam propagation direction, which enables different filters to be introduced in and out of the beam path. An enlarged image of one of the mounts is shown on the right, which is equipped with a: (A) photodiode, (B) metal filter, and (C) window. Figure adapted from [154].

3.1.4 Split-Mirror Interferometer

Downstream from the filter chamber, the beam propagates into a chamber containing the third and final silicon mirror, where this reflection further suppressed the 400 nm driving field. This silicon mirror itself is split into two halves that can be individually controlled, vertically separated by less than 1 mm, where the bottom surface can translate relative to the top surface. This creates an interferometer, where the path length in one half of the beam can be varied relative to the other half, introducing a time-delay between the two halves of the split beam. The split beam creates a pump and probe arm, where the time-delay between the two arms of the interferometer can be varied by translating the bottom mirror surface relative to the top surface. By performing a series of measurements at different time-delays, dynamics initiated by the pump arm can be resolved in time.

The design of the split-mirror interferometer, which is upstream and independent of the focusing optic, is unique. It offers various advantages over the approach of a split back-focusing mirror, where the pump and probe overlap is very sensitive to the initial beam alignment and stability, and maximum time-delays are limited by the Rayleigh range. The interferometer is configured to hold two polished silicon substrates (Gooch and Housego, wavefront error of $\lambda/20$ at 630 nm, roughness <1), which split and reflect the beam.

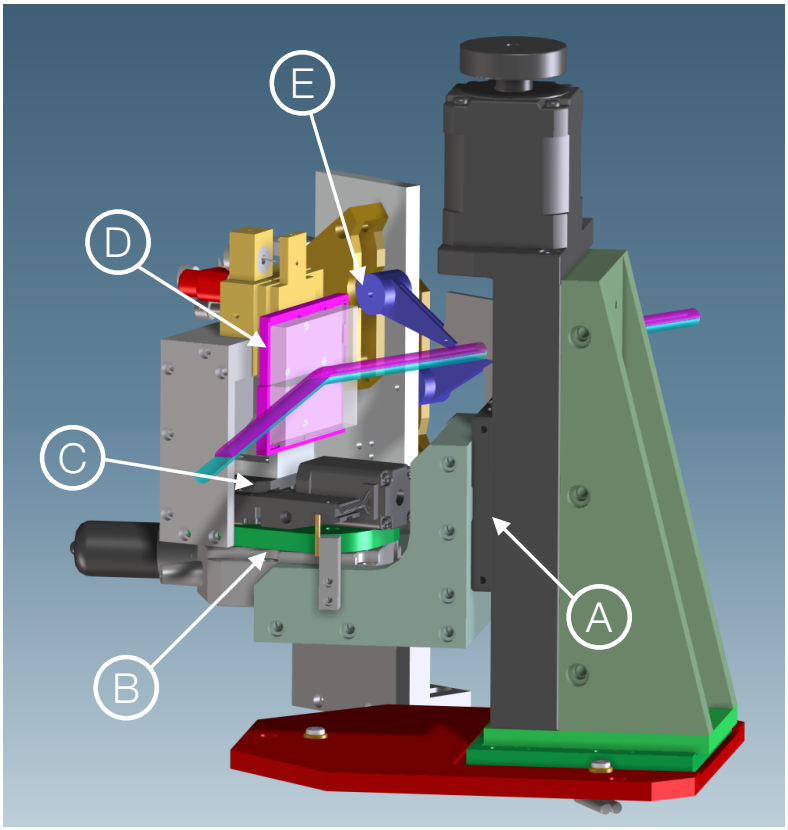

Figure 3.8: The in-vacuum split mirror interferometer (SMI) - figure adapted from [154]. The incident beam is reflected from a pair of vertically separated silicon mirrors, with labeled components: (A) vertical translation stage, (B), rotation stage, (C) bottom mirror translation stage, (D) silicon mirrors, (E) motorized beam blocks for occluding the top or bottom half.

A rendering of the split-mirror interferometer and the beam path is shown in Fig. 3.8. The two silicon substrates are vertically spaced less than 1 mm apart, which allows each surface to be independently controlled without obstructed motion. The upper substrate is driven by two picomotors that actuate the tip and tilt of the mirror. This enables the overlap of the two arms of the interferometer to be controlled. The lower substrate is mounted on a precision

encoded in-vacuum stepper motor translation stage, with closed loop position readout (Micos VT-21 with Corvus Eco encoder). The stage has a travel range of 10 mm, which corresponds with a maximum time-delay of 17.2 ps, with a minimum step size of 100 nm, corresponding with a minimum time-delay of 170 as. The two substrates can be rotated and translated together, using a rotational stage and vertical translational stage, allowing both the beam alignment and relative brightness in the pump and probe arms to be adjusted. There are also two additional aluminium plates, driven by electrically actuated rotating flappers, that serve as beam stops for the pump and probe arms of the interferometer. A picomotor drives the beam stops, which allows them to be precisely positioned to occlude different regions of the two mirrors.

A split-mirror interferometer implemented in a back-focusing geometry will provide a 6.68 fs delay for every 1 μm of travel. At a grazing incidence angle of 75°, the same 1 μm of travel will result in a 1.73 fs delay. Generally, for an angle of incidence θ, the time-delay Δt introduced by translation by distance D is given by

$$\Delta t = \frac{D}{c}\left(\frac{1-\cos(2\theta)}{\sin(\theta)}\right) \tag{3.9}$$

This grazing incidence geometry provides an increase in temporal resolution by roughly a factor of four, relative to the back-focusing geometry. In previous tests, the split-mirror interferometer has demonstrated a stability beyond 200 as, which is approaching the temporal resolution that the stage can provide (170 as). To minimize coupling vibrations from the vacuum system to the interferometer, the backing pumps are decoupled from the turbomolecular pumps using weights and passing forelines through volumes of sand, damping vibrations in the forelines. The chamber that contains the split-mirror interferometer is pumped using a turbomolecular pump with magnetic bearings. This chamber is connected to the upstream and downstream beamline using soft edge welded bellows, further decoupling this chamber from other vibrations in the beamline.

The small gap between the two mirrors of the interferometer results in a small loss of photons. Since the generated harmonics are slightly diverging after the HHG cell, the reduction in photon flux increases the closer the interferometer is placed to the HHG cell. It is therefore favorable to place the split-mirror interferometer far downstream from the HHG cell. For a Gaussian beam mode with a full width at half maximum (FWHM) of w, the reduction in photon flux due to the gap d between the mirrors can be estimated using the error function

$$L(d,w) = \frac{2}{\sqrt{\pi}}\int_0^{\frac{d\sqrt{\ln(2)}}{w}} e^{-t^2}dt = \mathrm{erf}(\frac{d\sqrt{\ln(2)}}{w}) \tag{3.10}$$

For a beam with a 6 mm FWHM and a 0.9 mm gap between the mirrors, this corresponds with a 14% reduction in flux. In the experiments presented in this thesis, the delay capabilities of the split-mirror interferometer were not necessary, and thus the beam was aligned to lie entirely on the top silicon mirror, with no beam loss in the gap of the interferometer.

3.1.5 Differential-Pumping Stage

After exiting the split-mirror interferometer, the beam propagates downstream and through a differential pumping stage, which separates the beamline from the experimental endstation. This differential pumping stage bridges the lower quality vacuum of roughly 10^{-6} mbar in beamline from the higher quality vacuum of roughly 10^{-9} mbar in endstation. By attaching a pair of turbomolecular pumps to a stage in the beamline, an increased pumping speed can be achieved on that volume, and thus higher vacuum can be reached.

When pressures dip below 10^{-6} mbar, the mean free path of atoms and molecules can become larger than the dimensions of the volume that is under vacuum. Here the gas is under what is known as free molecular flow, where atoms and molecules have linear trajectories, undergoing collisions and reflections from the chamber walls, and infrequent collisions with each other. In this regime, the flow of atoms and molecules between the two vacuum stages can be restricted by reducing the open area connecting the two volumes.

The flow resistance of the vacuum system can be quantified by its conductance. The flow of gas particles in the molecular flow regime can be expressed as

$$Q = C\Delta P \tag{3.11}$$

where the parameter C is the conductivity per unit time of the system and ΔP is the pressure difference between the two vacuum stages. The conductivity parameter for an orifice of area A is given by $C_{or} = A\bar{c}/4$, where $\bar{c}$ is the mean thermal velocity (a function of both temperature and mass). For a tube of diameter d and length l, the conductivity parameter is given by $C_{tube} = \bar{c}\pi d^3/12l$. Both small open area orifices and small diameter long tubes reduce the gas conductance of the vacuum system. When multiple conductance limiting elements are places in series, the sum of the reciprocals of the individual conductivities forms the total conductance

$$\frac{1}{C_{tot}} = \frac{1}{C_1} + \frac{1}{C_2} + \frac{1}{C_3} + \cdots \tag{3.12}$$

A diagram of the compact differential pumping stage is shown in Fig. 3.9, which consists of a pinhole and two low conductivity tubes, which are 0.5" in diameter, separating the two vacuum stages. Each stage is pumped by its own turbomolecular pump mounted to a DN100 ConFlat flange. Both turbomolecular pumps are mounted orthogonal to the beam propagation direction and on opposite sides of the DN100 ConFlat cross. A custom inset with a viton rubber seal divides the volume into two stages, where each side of the inset is pumped by its own turbomolecular pump through a D-shaped vent on opposite sides of the inset (which slightly reduces the pumping speed). The two vacuum stages are connected via a long tube lying along the beam propagation direction, which limits the conductance. A pinhole is placed at the entrance to the differential pumping stage, in addition to a second long tube at the downstream end of the vacuum stages, which enables a pressure differential of $\sim 10^4$ to be achieved in a distance of 58 cm.

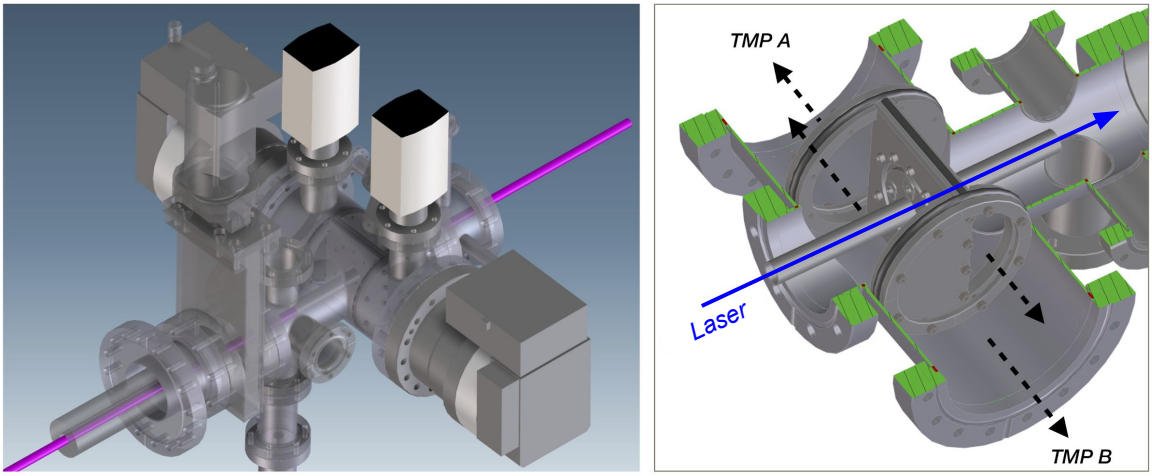

Figure 3.9: The VUV beamline compact differential pumping stage. A pinhole and two long 0.5" diameter tubes limit the gas conductance between the different stages. A custom inset separates the two sections and D-shaped vents allow a pair of turbomolecular pumps to individually pump each region. Figure adapted from [154].

3.1.6 In-Vacuum Alignment and Beam Surveillance

Since the photon beam needs to be transported in vacuum, there are challenges involved in beam alignment. Typically, manually actuated irises are used to bring the beam to alignment. Here, the irises need to be placed in the beamline under vacuum, where they can be actuated externally. Two different iris designs are implemented, a compact manually actuated magnetic iris and a spring-loaded non-magnetic iris.

The custom DN63 ConFlat Tee that houses the magnetically actuated iris is depicted in Fig. 3.10, where the iris itself has a 12 mm open aperture. The iris is mounted on a standard 0.5" optical post that is fixed to a base plate, which is then clamped onto the optical table. A DN38 ConFlat bellow is used to decouple the mounted iris from the beamline, which provides consistent alignment both at atmosphere and under vacuum. This mounting approach is taken with all pre-aligned in-vacuum optics, where both the compressor and folding chambers are decoupled from the beamline. The angled viewport is situated above the iris, such that the iris lies in the center of the viewing tube and a camera can be used to view the iris. A strong rare earth magnet is affixed to the manual actuator of the iris. This enables the iris opening to be controlled from outside the beamline, by sliding another magnet around the external surface of the beamline.

The use of magnetic materials near the experimental endstation needs to be avoided, since the magnetic fields can steer photoelectron trajectories in the spectrometer and therefore influence the reconstructed momenta, compromising measurements. Because of this

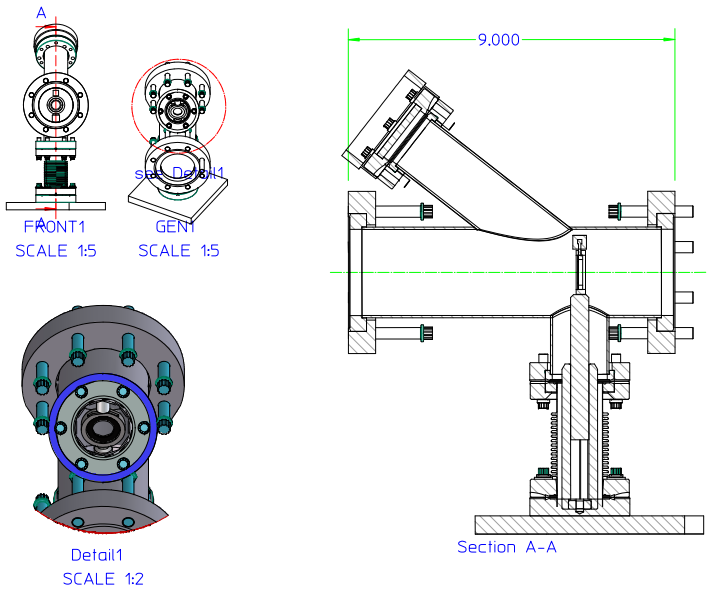

Figure 3.10: A schematic of a magnetic beamline iris. The iris is centered in a DN63 ConFlat tube, where the iris opening is actuated by sliding a magnet along the tube surface. The iris is mounted directly to the optical table and decoupled from the beamline with a DN38 ConFlat bellow. Figure adapted from [154].

limitation, the iris closest to the experimental endstation is designed without any magnetic components. A rendering of this non-magnetic iris is shown in Fig. 3.11. The iris is actuated using a linear feedthrough, which pulls on a metal wire that is connected to the iris actuating pin. This iris is spring-loaded, so that the iris closes when tension in the wire is lost.

Beam surveillance is performed using various cameras equipped with zoom lenses that lie at several locations along the beamline. This enables the beam alignment and positioning to be performed safely, allowing beam viewing without risk of direct exposure. The beam surveillance system is composed of analogue closed-circuit video cameras equipped with c-mount zoom lenses. The analogue video signal from each camera is digitized using an analogue to digital converter, and displayed on a computer monitor. This provides a reliable and cost effective beam surveillance system, where more than 10 of these camera systems are used throughout the lab, each lying at different points along the beamline and facilitating alignment and beamline operation.

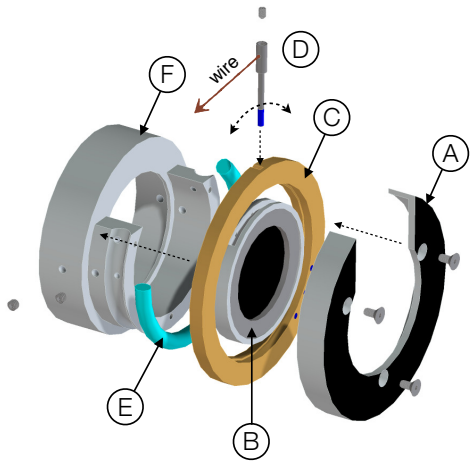

Figure 3.11: The spring-loaded non-magnetic mechanical iris, with labeled components: (A) carbon coated retaining shield, (B) iris actuated via a linear feedthrough, (C) PEEK ring, (D) iris actuating lever, (E) spring, (F) spring holder. Figure adapted from [154].

Chapter 4

Experimental Endstation and Coincidence 3-D Momentum Imaging Spectrometer

Numerous techniques exist for measuring the energy, angle of emission, or full 3-dimensional momentum vector of a charged particle produced in a photoionization event, where these various observables encode different information on the system from which they emerge. These different techniques each have their own strengths and limitations, where they generally involve overlapping a photon beam and an atomic or molecular beam in a spectrometer, and then projecting the charged particles to two-dimensional position- and time-sensitive detectors. These methods have advanced greatly since its initial demonstration in 1987 to study the photodissociation dynamics of methyl iodide (CH_3I) [26].

One commonly used approach, developed in 1997, is known as Velocity Map Imaging (VMI), which makes use of an electrostatic lens to accelerate charged particles towards a detector and allows the two-dimensional momentum in the detector plane to be reconstructed [50]. This method focuses charged particles with a particular velocity to the same point on the detector (velocity imaging), regardless of where the charged particle is created within the interaction region, greatly reducing blurring effects caused by the finite spatial overlap of the photon beam and the atomic or molecular beam. In this technique, photoproducts are extracted using high fields ($\sim$ 1000 V/cm) and projected onto a micro-channel plate (MCP) stack with a phosphor screen, where the 2-dimensional images are recorded using a charge-coupled device (CCD). By assuming the angular distributions possess cylindrical symmetry about the polarization axis of the ionizing field, the 3-dimensional momentum vector of the charged particle can be reconstructed.

Generally in VMI, either the photoelectrons or the photoions are detected. However, separate measurements can be conducted on the photoelectrons and photoions in the same experimental conditions, or a pair of detectors can be used simultaneously (one for electron imaging and one for ion imaging), and the photoelectron and photoion measurements can be correlated. In certain cases, electron-ion coincidence measurements can be done with a

single detector, or a detector pair, but the event rate must be kept below 1 event per photon pulse, to ensure unambiguous assignment between photoelectrons and photoions. This is challenging in VMI set-ups, since this method is more tailored towards recording multihit events (the fluorescence enables many hits to be captured in a single image) and the image capture rate of CCDs can limit the experiments.

A different method for measuring the 3-dimensional momentum of photoelectrons and photoions is known as Cold Target Recoil Ion Momentum Spectroscopy (COLTRIMS) or Reaction Microscopy [40, 157], which is the approach taken in the experiments presented in this thesis. This technique was developed through the 1980s and 1990s, with important early demonstrations in 1994 [116, 41], and incorporates an atomic or cold molecular beam, a photon beam, and a spectrometer designed for recording the 3-dimensional momentum of photoelectrons and photoions in coincidence. This is achieved using position- and time-sensitive detectors, and low extraction fields, which allow the full 3-dimensional momentum to be reconstructed without making any assumptions on symmetry. Rather than using a MCP-phosphor detector with a CCD, this approach uses an MCP stack with a delay-line anode read-out. This allows multiple electrons and ions to be recorded in a single event in coincidence, however the delay-line anode detectors themselves have multi-hit limitations.

This technique allows kinematically complete experiment to be preformed, i.e. experiments where the kinematic parameters of all final state products can be determined, enabling highly differential measurements, and photoionization and dissocation dynamics to be investigated in great detail. In the case of dissociative photoionization, this includes the ability to perform measurements in the molecular frame, as well as the laboratory frame, or any fixed-body frame of interest, without the need for prior alignment of the target. However, using fragmentation to establish the molecular orientation is predicated on what is known as the axial recoil approximation, which is the assumption that the dissociation axis of the molecule does not rotate during fragmentation, such that the fragment ion momentum vector corresponds with the molecular orientation. This implies that the timescale for fragmentation must be short relative to the rotational period of the molecule, so no significant rotation can occur between the instant of photoionization and dissociation, and orientation can be determined from the product ion momenta. This approximation can break down in the case of highly rotationally excited small molecules, as well as near regions of non-adiabatic coupling between different electronic states.

4.1 The MISTERS Endstation

The experimental endstation housing the coincidence 3-dimensional momentum imaging spectrometer (COLTRIMS) used in this work is named MISTERS, an abbreviation for Momentum Imaging Spectroscopy for Time Resolved Studies. This experimental apparatus consists of an atomic or cold molecular beam, produced from a skimmed supersonic expansion, the momentum imaging spectrometer itself, and an adjustable back-focusing mirror, which are all housed within a specially designed large ultrahigh vacuum chamber.

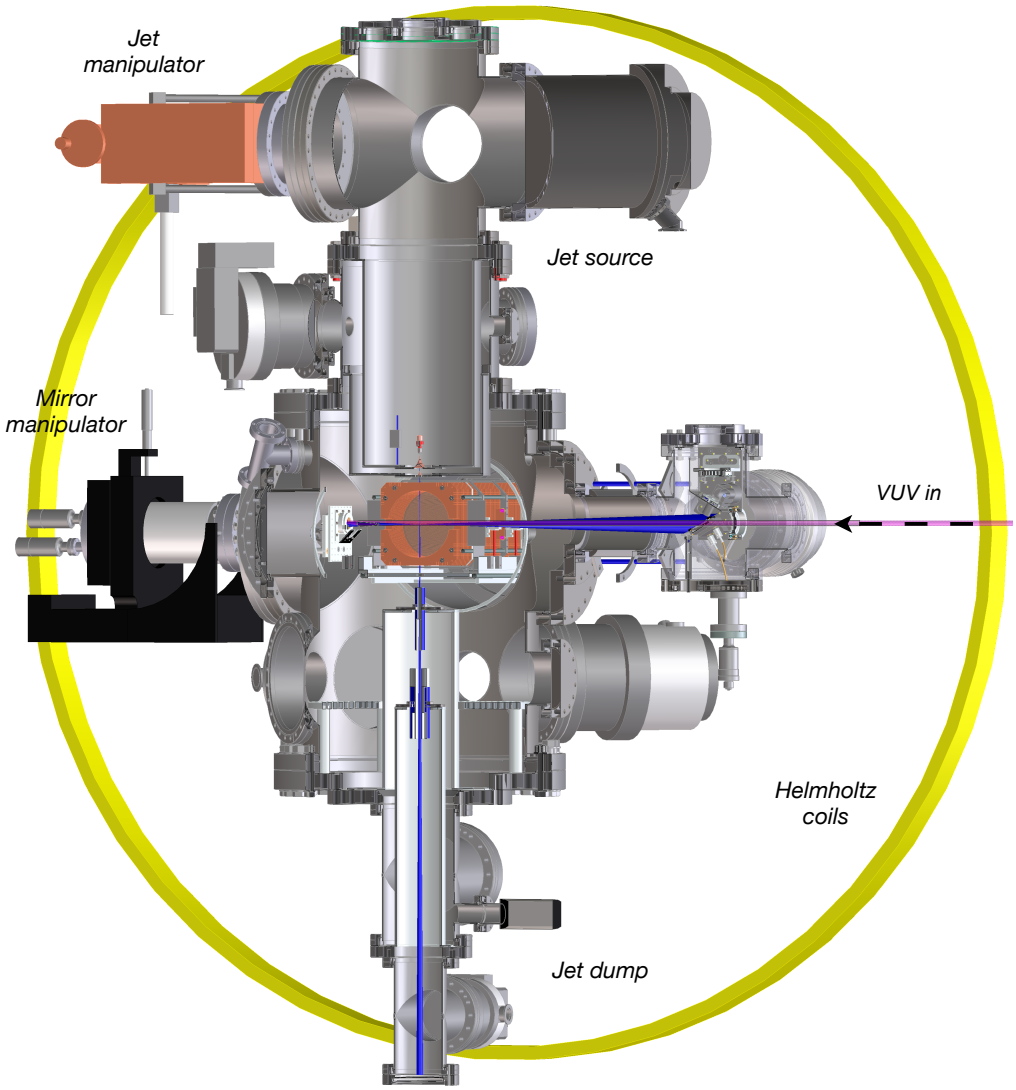

Figure 4.1: A cross section of the MISTERS experimental endstation. Expanded views of the spectrometer, as well as the beam path, are shown in Fig. 4.2. In the jet source chamber, the arm which holds the jet nozzle, as well as the nozzle cooling connection and gas lines, are not depicted here. Figure adapted from [154].

A cross section of the experimental endstation is depicted in Fig. 4.1, while a cross section of the spectrometer itself is shown in Fig. 4.2. This apparatus has a footprint of roughly ~ 1 m$\times 1.2$ m, and is roughly 2 m tall, excluding the Helmholtz coils. The VUV beam enters the endstation and propagates into the spectrometer, offset $\sim 2-4$ mm from the supersonic

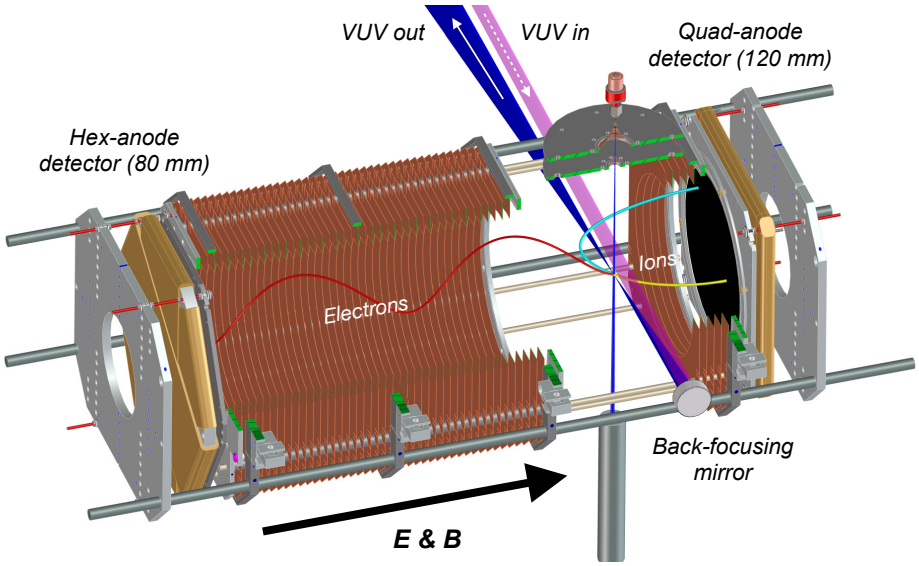

(a)

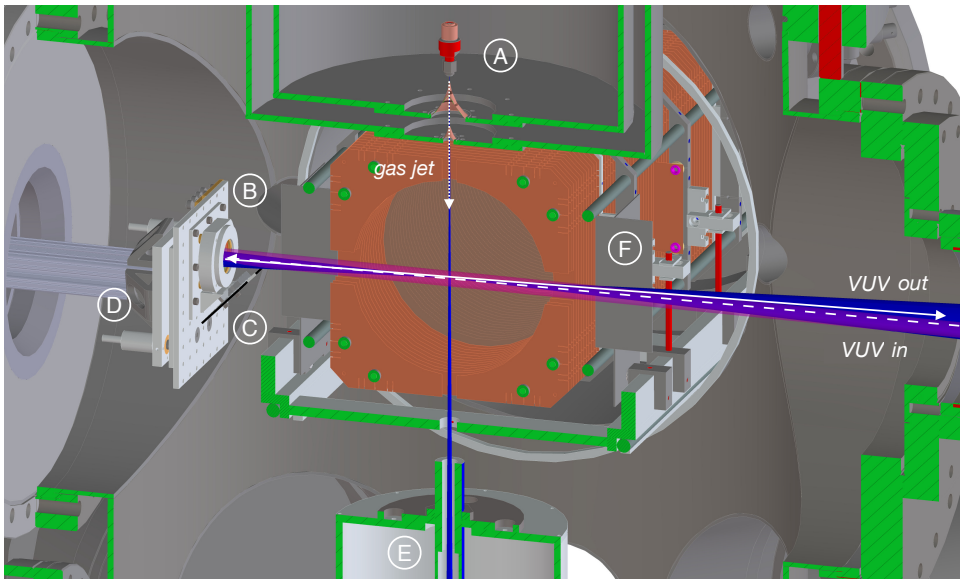

(b)

Figure 4.2: (a) A rendering of the MISTERS coincidence 3-D momentum imaging spectrometer. (b) The cross section and beam path of the 3-D momentum imaging spectrometer, with labeled components: (A) supersonic gas jet, (B) back-focusing mirror, (C) 45° downward reflecting mirror, (D) XYZ manipulator, (E) two-stage jet dump. The incoming VUV beam enters the spectrometer and passes the supersonic gas beam with a $\sim 2-4$ mm offset, and is back-focused at a small angle into the supersonic jet. Figures adapted from [154].

gas jet in the direction of the quad-anode detector. The photon beam is then back-focused into the gas jet using a curved mirror ($f = 15$ cm). The beam of target gas is formed from a skimmed supersonic expansion above the spectrometer that propagates vertically downward through the spectrometer and into a two-stage jet dump at the bottom of the chamber. The coincidence 3-D momentum imaging spectrometer itself is comprised of an aligned array of copper plates in which the direction of stacking lies perpendicular to both the photon beam and supersonic gas jet propagation directions. At each end of the aligned array of copper plates lie position- and time-sensitive detectors, composed of a micro-channel plate (MCP) stack in chevron with a delay-line anode readout, allowing photoelectrons and ions to both be measured in coincidence. The details of the different instruments and components of the MISTERS endstation will be discussed in detail in the following subsections.

4.1.1 Back-Focusing Mirror

From time-dependent perturbation theory, the probability for an atom or molecule to undergo an electric dipole transition from an initial state ψ_i to a final state ψ_f upon exposure to a weakly perturbing electromagnetic field is given by

$$P_{\psi_i \to \psi_f} = \frac{2\pi}{\hbar} |E_0|^2 |\langle \psi_f | \hat{\mu} | \psi_i \rangle|^2 \tag{4.1}$$

where E_0 is the amplitude of the field and $\hat{\mu} = q\hat{r}$ is the electric dipole operator. In the above expression, we see that the probability of undergoing a transition is proportional to the field intensity $I = |E_0|^2$. Two-photon absorption is a second-order process that involves interaction with the field twice. From time-dependent perturbation theory, the probability of undergoing a two-photon transition therefore involves a product of the square of two transition moments and intensities. This means the probability of undergoing a two-photon transition scales as the intensity squared, i.e. $P_{\psi_i \to \psi_f} \propto I^2$. Therefore, in order to drive two-photon absorption, high field strengths are crucial. Given a fixed photon fluence, high fields can be achieved by going to tighter focusing geometries, as the field intensity exhibits quadratic growth with the inverse of the beam diameter. Hence in experiments, achieving a small focal spot size will result in an increased two-photon transition probability.

In order to reach smaller focal volumes to drive two-photon processes, a back-focusing geometry was chosen over using a toroidal mirror at a shallow angle of incidence. Although the shallow angle geometry offers increased reflectance to the VUV field, there are two inherent disadvantages. First, toroidal mirrors are very sensitive to alignment, where small changes in beam pointing can result in significant instability downstream, such as a varying focal volume and position. Second, the achievable focal spot size with a shallow angle toroidal mirror compares poorly with a near normal incidence geometry, since the size of the source is approximately relayed to the focus by the toroidal mirror in a 1:1 fashion. Since the VUV photons generated via HHG are created using a loose focusing geometry in the present set-up, the initial extent of the VUV source is relatively large (approximately 200 μm), meaning the focal spot size at the target will be on the same order. This results in insufficient intensities

for driving two-photon processes. As such, a spherical 1" back-focusing mirror ($f = 15$ cm) was used in a near normal incidence geometry, resulting in a significantly smaller focal spot size and reduced sensitivity to beam pointing instabilities.

If a Gaussian beam shape is assumed, and the M^2 factor is taken to be roughly 2 (based off previous measurements [3]), the focal spot size can be roughly estimated. The divergence of the driving field θ_0 is estimated from the beam size at the $f = 6$ m focusing optic, while the divergence of the harmonics are estimated as $\theta_q = \theta_0/\sqrt{q}$. Since the split-mirror interferometer modifies the beam profile (when the beam is aligned onto both mirrors), the beam is modulated along the y-direction with a central gap missing, which deteriorates the mode further upon propagation and focusing. As a result, the focal spot size along the y-axis is elongated relative to the x-axis by roughly a factor of 2, yielding an oval shaped focal spot. The focal spot size is also dependent on the wavelength and divergence of the harmonic, resulting in focal spot sizes that vary with harmonic order. The focal volume for the 3$^{\text{rd}}$ harmonic is estimated to be roughly $5 \times 10 \times 220$ μm when the beam is divided across the two mirrors of the split-mirror interferometer, and roughly $5 \times 5 \times 220$ μm when the beam is aligned to lie entirely on a single mirror of the split-mirror interferometer.

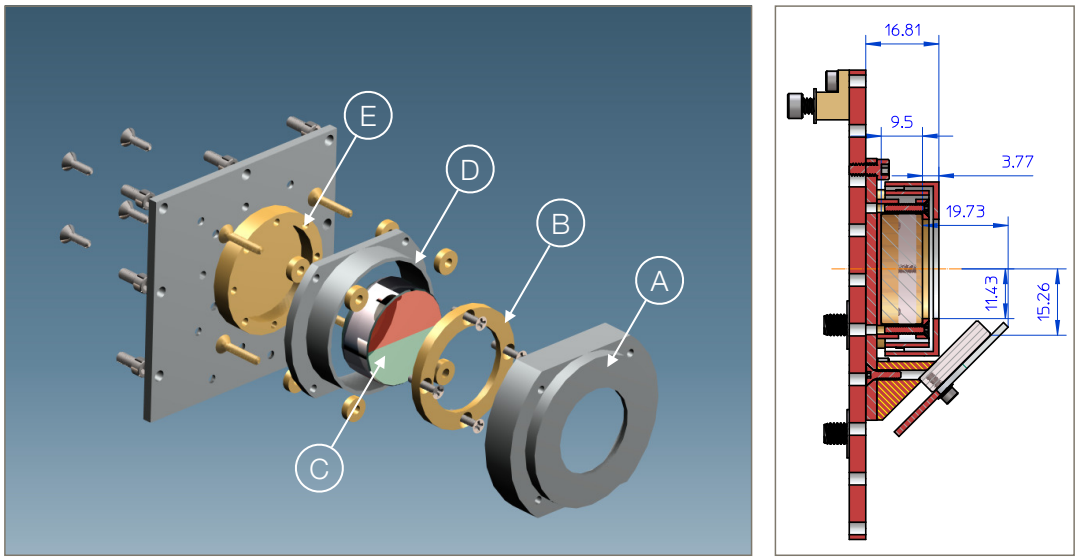

Figure 4.3: A rendering of the back-focusing mirror mount assembly used in the MISTERS experimental endstation, with labeled components: (A) Outer mirror shield that can be biased to minimize field distortion in the spectrometer, (B) an electrically isolating PEEK ring, (C) mirror substrate, (D) ring that can be biased to trap electrons generated on the surface of the mirror, (E) base plate of the mirror assembly. Figure adapted from [154].

The photon beam enters the spectrometer slightly offset ($\sim 2 - 4$ mm) from the gas target and passes by this jet, in order to reduce single ionization by the incoming beam.

The back-focusing mirror is therefore $\sim 1-2^{\circ}$ tilted away from normal incidence. Since the photon energies of the harmonics are above the work function of most mirror materials, a significant amount of photoemission can occur at the mirror interface. These electrons that are generated on the mirror surface can enter the spectrometer and create a background of low energy hits on the electron detector. This can create serious issues for successfully carrying out coincidence experiments. To help mitigate this effect, the mirror is mounted to an assembly that contains two electrically insulated shields that hold the substrate. A rendering of this assembly is shown in Fig. 4.3. The inner shield can be electrically biased in order to trap the low energy electrons created through photoemission, while the outer shield can be biased to reduce the field distortion within the spectrometer that is caused by the gap in the spectrometer plates that accommodates the mirror assembly. The entire spectrometer itself can also be negatively biased, which further limits the low energy electron background, in addition to the magnetic field provided by the Helmholtz coils.

Another significant problem originates from photoemission from the copper plates of the spectrometer itself, since the photon energies of the harmonics are all above the work function of copper. Diffuse reflections of the VUV beam from the mirror substrate can result in these high energy photons striking the spectrometer plates and creating electrons within the spectrometer. Since nearly every VUV photon that encounters a copper surface will result in photoemission, then even a few diffusely scattered photons can create problems, as these electrons will be guided towards the electron detector and also create a low energy background that makes coincidence very challenging to establish. These issues have yet to be overcome, however there are several potential solutions that can be implemented that could aid in reducing this effect. One possibility is using a substrate material with a higher work function, or coating the plates that are most likely to see scattered light with a suitable absorbing material. A second possibility is to increase the size of the gap in the spectrometer plates, both where the photon beam enters and where the mirror intrudes. This could reduce any electrons generated from a "halo" of scattered VUV light around the primary beam mode. Another possible solution is to reduce the solid angle for diffusely scattered photons to enter the spectrometer, by increasing the distance from the mirror to the spectrometer. This, of course, also influences the intensities achievable at the target, and so there are limitations to this approach.

The position of the back-focusing mirror is adjusted using a 3-axis manipulator that the mirror assembly is mounted to. This manipulator is attached to the rear flange of the endstation, and the mirror assembly is attached to the manipulator using a long aluminium arm that allows the mirror to be positioned near the gap in the spectrometer plates. The tip and tilt angle of the mirror surface is actuated using a pair of micrometer screws that are coupled to a pair of rotational vacuum feedthroughs on the rear flange of the manipulator by means of flexible cables. This tip and tilt actuation mechanism exhibits appreciable backlash, however both the tip and tilt positions are precisely measured using an encoder that measures the position of each micrometer screw. This high precision capacitive distance sensor was developed in-house by Paul Denham at CXRO and is a variation of the linear variable differential transformer (LVDT) design used in the split-mirror interferometer. Details on

its design can be found in [154].

In order to ensure that the photon beam is suitably aligned to the mirror, a small 45° mirror is mounted to the back-focusing mirror assembly, that allows the beam to be out-coupled through a viewport on the endstation. The small 45° mirror is mounted directly below the back-focusing mirror itself, sharing the full functionality of the assembly, and can be seen in Fig. 4.3 in the technical drawing on the right. This directs the beam downward and onto a second mirror at 45°, creating a periscope. This second mirror is a large silicon wafer and reflects the beam out of a DN100 ConFlat viewport. The window of the viewport is composed of UV grade sapphire, which shows high transmission of the fundamental. The beam is then imaged using a CMOS compact camera (ThorLabs) equipped with a telephoto lens. A cross is etched into the center of the surface small 45° mirror, which serves as a reference. This allows the beam to be aligned to the center of this cross, since the pattern is imprinted on the mode and can be clearly seen on the camera.

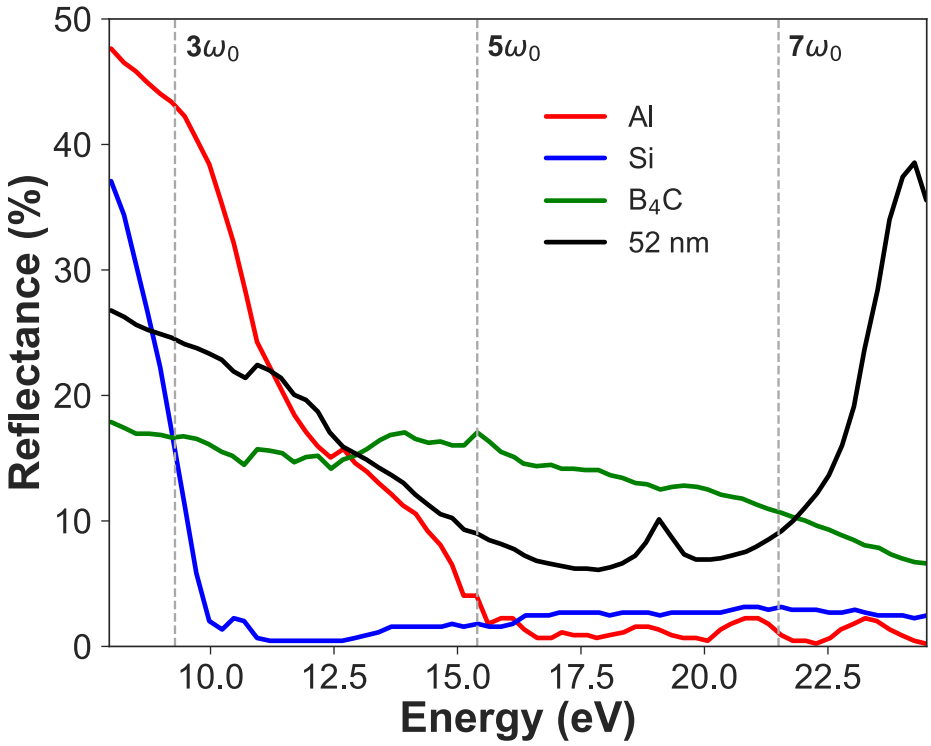

Figure 4.4: The reflectance of various back-focusing mirrors (Al, Si, B_4C, and a 52 nm multilayer) as a function of photon energy. The 3rd, 5th and 7th harmonic are indicated as vertical dashed gray lines. The data is extracted from the measurements in [89]

Additional spectral selectivity can be achieved using specific back-focusing mirrors, where ranges of photon energies can be selected through reflection. The back-focusing mirrors can

either be a simple uncoated substrate, a substrate with a single optical coating, or a substrate with a multilayer optical coating. Suitably chosen materials can result in appreciable reflectance in the VUV, despite the host of electronic resonances in materials that strongly absorb radiation at these short wavelengths. The measured reflectance of various back-focusing mirrors is shown in Fig. 4.4.

In the case of multilayer coated mirrors, high reflectance is achieved by alternating thin layers of materials with different indices of refraction, satisfying a Bragg reflection condition that results in constructive interference across a range of wavelengths. Some examples of materials used in multilayer mirrors are SiC, Al, B_4C, and MgF_2. These materials are deposited onto a substrate in layers that are tens of nanometers thick, forming a nanostructure where reflections from different layers of the stack produce constructive and destructive interference. By taking great care in design and fabrication of such mirrors, high reflectance in certain ranges of the VUV can be achieved. Custom multilayer mirrors can be fabricated in-house, taking advantage of the expertise of the scientists at the Center for X-Ray Optics (CXRO) at Lawrence Berkeley National Laboratory, where the 52 nm multilayer coating shown in Fig. 4.4 was fabricated by CXRO (supplied by Eric Gullikson).

In Fig. 4.4, it is apparent that the protected Al back-focusing mirror exhibits the highest reflectance at the third harmonic $3\omega_0$, near 45%. Additionally, this mirror does not reflect the higher order harmonics, and hence is suitable for experiments that only require the third harmonic $3\omega_0$. The B_4C mirror shows relatively constant reflectance across a broad range of VUV photon energies, and is hence suitable for a measurement that requires $5\omega_0$ or $7\omega_0$. For the experiments presented in this thesis, the protected Al mirror was chosen, since these measurements made use of the third harmonic $3\omega_0$.

4.1.2 Supersonic Gas Jet

Within the kinetic theory of gases, an atom or molecule carries momentum, or thermal speed, that is proportional to its thermal energy. This results in a velocity distribution for the gas particles at room temperature, which is captured by the famous Maxwell-Boltzmann distribution

$$f(v)dv = \left(\frac{m}{2\pi k_B T}\right)^{3/2} 4\pi v^2 e^{-\frac{mv^2}{2k_B T}} dv \tag{4.2}$$

where m is the particle mass, k_B is the Boltzmann constant, T the thermodynamic temperature, and v is the magnitude of the particle's velocity vector. In an ideal gas, according to the equipartition theorem, energy is distributed equally across each degree of freedom of the system as $\frac{1}{2}k_B T$. This results in an inherent momentum spread caused by the thermal energy and limits the resolution that can be achieved in a measurement, providing a clear benefit to performing experiments on a cold target.

Supersonic beams are capable of converting thermal energy into translational motion along a particular direction, cooling the target and resulting in a narrower momentum spread.

When a gas undergoes adiabatic free expansion from a high-pressure region into vacuum through a nozzle, the energy that is distributed among the different degrees of freedom of the gas atoms or molecules is converted into kinetic energy in the direction of propagation. This energy redistribution from the various degrees of freedom into a translational degree of freedom occurs through collisions between particles. In the region just outside the nozzle, the gas particles are supersonic and no more collisions between particles occur, forming what is known as the zone of silence, the size of which is a function of the nozzle geometry and backing pressure, and vacuum pressure. By placing a skimmer into the zone of silence, a directed supersonic beam can be created.

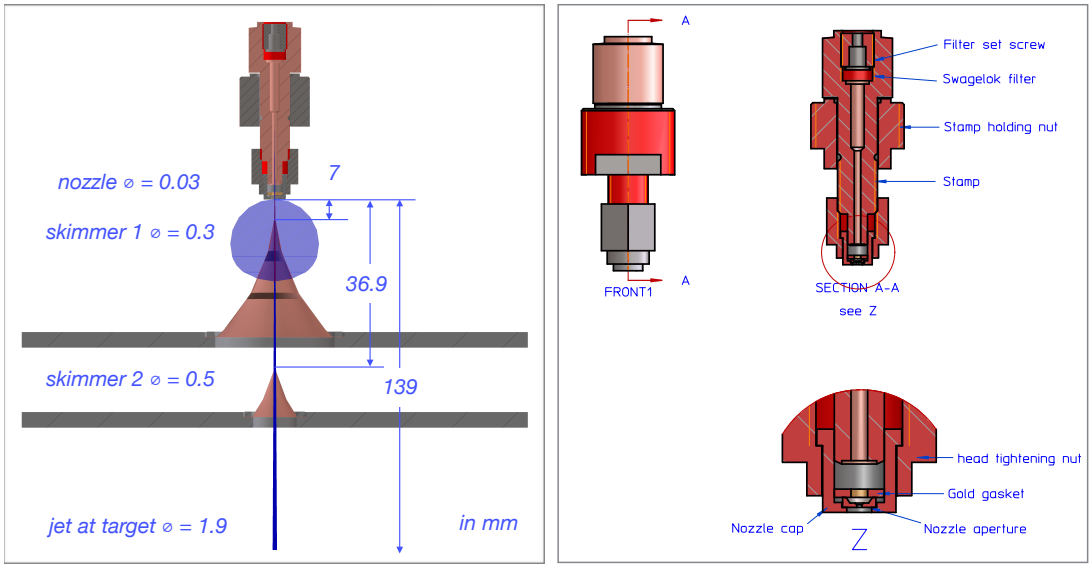

Figure 4.5: A schematic of the nozzle and skimmer assembly used to generate the supersonic gas jet in the MISTERS experimental endstation. The components are labeled within the figure. Figure adapted from [154].

The nozzle and two-stage expansion scheme used in the MISTERS endstation is depicted in Fig. 4.5. Target gas is injected into the source chamber via adiabatic free expansion through a 30 μm microscope aperture (Ted Pella Inc.) mounted to the end of the nozzle. A seal between the nozzle and gas line is formed using a solid gold gasket that is compressed onto a copper stamp. A filter (Swagelok) is installed in the gas line in order to prevent small particles from entering and obstructing the nozzle aperture. The nozzle is equipped with a heating element and cryogenic cooler, allowing low target temperatures to be achieved, or cluster formation to be enhanced or suppressed. The source chamber itself is pumped using a large magnetic bearing turbomolecular pump (Shimadzu), with a nominal pumping speed of 2000 l/s for N_2, allowing high jet driving pressures of up to a few bar. A 19 mm long conical skimmer (0.3 mm diameter, Beam Dynamics Inc.) is inserted into the zone of silence

of the supersonic expansion, where the relative position and distance between the nozzle and this skimmer can be adjusted using the 3-axis manipulator that the nozzle assembly is mounted to with a $\sim$ 40 cm long arm. At closer relative distances between the nozzle and skimmer, the jet density is higher, however, this compresses the zone of silence due to back-scattered gas particles from the skimmer surface. At larger relative distances between the nozzle and skimmer, the skimmer does not penetrate the zone of silence, which results in a jet that is not supersonic. Typical operating conditions are for relative nozzle-skimmer distances of 5–15 mm.

In order to reduce the divergence of the supersonic jet and minimize the flow of warm background gas into the interaction region, a second skimmer (0.5 mm diameter, Beam Dynamics Inc.) is placed downstream from the first stage. This second stage is independently pumped from the source stage, and due to the small diameter of the second skimmer aperture (which has low conductance), serves as a differential pumping stage between the source and target chambers, allowing higher vacuum conditions to be achieved at the experiment.

The diameter of the supersonic jet at the interaction region can be estimated from geometrical considerations and can be expressed as

$$d = \frac{d_{S2} l_X}{l_{S2}} \tag{4.3}$$

where d_{S2} is the second skimmer diameter, l_{S2} is the distance between the nozzle and the second skimmer, and l_X is the distance between the nozzle and the interaction region. The extent of the jet at the interaction region is roughly 1.9 mm.

The jet density at the interaction region, ρ, can estimated by measuring the rise in pressure in the jet dump stage, p_D, and if we assume the entire supersonic beam is deposited into the jet dump stage, the jet density can roughly be expressed as

$$\rho = \frac{4}{22.4\pi} \frac{N_A p_D L_D}{v^3 d^2} \tag{4.4}$$

where N_A is the Avagadro constant, L_D is the pumping speed in the jet dump stage, and v is the jet velocity. Typical jet densities range from $\sim 10^{10} - 10^{11}$ cm^{-3}.

To estimate the temperature of the supersonic jet, and thus find an estimate on the momentum spread of the gas target, we can apply the equipartition theorem (which states each degree of freedom of the system carries energy $\frac{1}{2}k_B T$) and treat the system as an ideal gas. Then for a target possessing n degrees of freedom, where the internal energy is converted into kinetic energy through adiabatic free expansion, the thermal temperature of the target after expansion, T_X, is related to the kinetic energy as

$$\frac{1}{2} m v^2 = \left(\frac{n+2}{2} \right) k_B (T_0 - T_X) \tag{4.5}$$

where m is the mass of the gas particles, v is the jet velocity, and T_0 is the initial temperature of the target gas. For $T_0 \gg T_X$, we can rewrite this expression as

$$T_X \simeq \left(\frac{n+2}{2}\right)\frac{T_0}{S^2} \tag{4.6}$$

where S is what is known as the speed ratio of the supersonic expansion, defined as the ratio between the jet velocity and the width of the velocity distribution

$$S = \frac{v}{\sqrt{2k_B T_X/m}} \tag{4.7}$$

where different measurements and calculations of these values are available in previously reported literature. An empirical equation for the speed ratio that lies within 10% accuracy for small molecules permits these speed ratios to be estimated as $S = 5.4(P_0 d)^{0.32}$, where P_0 and d are the nozzle pressure and diameter in Torr and cm, respectively.

The Full Width at Half Maximum for the thermal momentum distribution along the jet propagation direction can then be expressed as

$$\Delta p_{\parallel} = mv\left(\frac{2\sqrt{\ln 2}}{S}\right) \tag{4.8}$$

while the Full Width at Half Maximum for the thermal momentum distribution transverse to the jet propagation direction is given by

$$\Delta p_{\perp} = mv\left(\frac{d_{S2} + d_{nozzle}}{l_{S2}}\right) \tag{4.9}$$

where d_{nozzle} is the diameter of the nozzle aperture. The momentum uncertainty along the jet propagation direction is typically on the order of 1 a.u., while the momentum uncertainty transverse to the propagation direction is typically on the order of 0.1 a.u..

4.1.3 Vacuum System

The MISTERS vacuum chamber is itself designed for operation in ultrahigh vacuum (UHV) conditions. The chamber is composed of a special form of non-magnetic steel (316-LN ESR) that is heated to high temperatures to minimize hydrogen outgassing. The chamber was cleaned, handled and installed with careful attention in order to avoid contaminating in-vacuum surfaces. All components that are used inside the vacuum chamber are composed of materials with low outgassing rates (e.g. aluminium, copper, PEEK, Kapton). The flanges of the chamber use ConFlat knife edges that are sealed with copper gaskets, with the exception of a small number of viton o-rings. The chamber pressure without a chamber bake-out has been measured to reach 8×10^{-9} mbar, while after a bake-out temperature at 150° C an ultimate pressure of 5×10^{-11} mbar was measured with a hot filament ionization gauge (Leybold).

The various stages of the MISTERS chamber are pumped using a collection of different turbomolecular pumps (TMPs), in addition to a titanium sublimation pump (TSP) in the

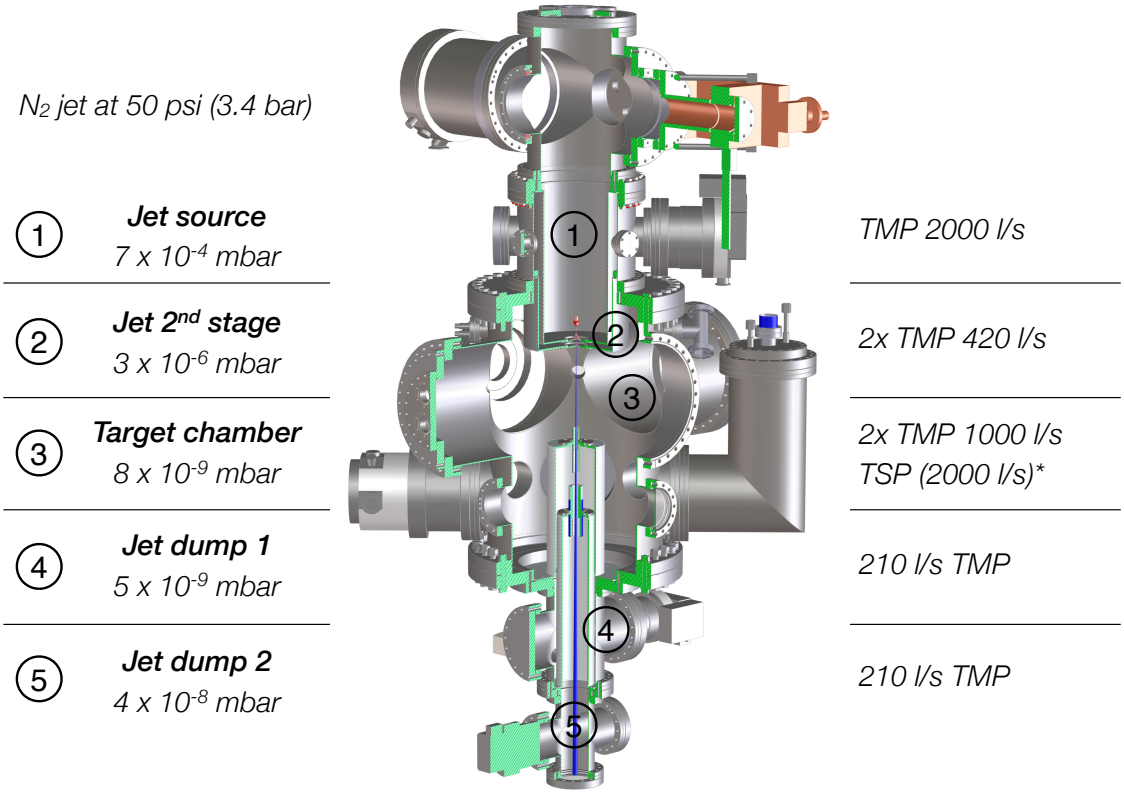

Figure 4.6: A rendering showing the cross section of the vacuum system. Typical system pressures are shown for the various stages at a driving pressure of 50 psi in a system that has not undergone bake-out. Baking the chamber helps eliminate water contamination, where pressures in the target chamber of 2×10^{-10} mbar can be reached and are limited by the aperture size of the second skimmer. Figure adapted from [154].

target chamber. A cross section of the different reservoirs of the MISTERS endstation can be seen in Fig. 4.6. A large scroll pump (Varian TriScroll 600) is used to pump the foreline of the TMPs connected to the source chamber, while the foreline of the second stage is pumped using a dry two-stage piston vacuum pump (Pfeiffer XtraDry). The vacuum compression ratio necessary to achieve pressures of 10^{-9} mbar in the target chamber requires the forelines of the TMPs in the target and jet dump stages to be connected to the inlet of a 80 l/s TMP. This small TMP in the foreline is itself backed by the dry two-stage piston vacuum pump. This oil-free piston pump can be operated in an interval mode, which helps extend the pump lifetime, while reducing vibrations. All stages of the MISTERS chamber can be connected via bypass lines, allowing the entire chamber to be vented or brought down to vacuum without creating pressure gradients that could damage the fragile skimmers.

4.2 Coincidence 3-D Momentum Imaging Spectrometer

The MISTERS endstation contains a charged particle momentum imaging spectrometer, capable of measuring the full 3-dimensional momentum vector of both photoelectrons and ions in coincidence. In this approach, the x and y hit positions and time-of-flight of the charged particles are measured on position- and time-sensitive detectors, which encode the different momentum components of the charged particle (p_x, p_y, p_z). Here, particles of opposite charge are accelerated towards detectors at opposite ends of the spectrometer using a low electric field, enabling electrons and ions produced in a single ionization event to be measured in coincidence on two separate detectors.

The static homogeneous electric field used to accelerate the charged particles is generated by applying a voltage to an aligned array of evenly spaced copper plates, that posses large round central cutouts. These copper plates are connected in series using ~ 300 kΩ resistors, which generates a smooth and constant potential gradient. A pair of Helmholtz coils possessing a diameter of roughly 2 m are coaxially placed such that the generated magnetic field coincides with the generated electric field. These Helmholtz coils are capable of producing a homogeneous magnetic field that lies parallel to the static electric field. This magnetic field confines electrons along the spectrometer time-of-flight axis, causing them to undergo cyclotron motion along the magnetic field lines as they propagate towards the electron detector, enabling full 4π solid angle collection of the photoelectrons to be achieved. The field strengths required to achieve full 4π solid angle collection depends on the kinetic energies of the charged particles involved, but generally lie within the range of 5–50 V/cm and 4–14 G.

4.2.1 Detectors

The charged particle detectors themselves are comprised of a micro-channel plate (MCP) stack in chevron, with a delay-line anode readout. The ion detector makes use of a two-layer anode (quadanode), while the electron detector uses a three-layer anode (hexanode). The MCP serves as a fast high-gain amplifier for the incident charged particle signal by converting the single particle into an electron avalanche, which then provides a sufficient signal for the delay-line detectors to pick up. An MCP and a depiction of the avalanche process is shown in Fig. 4.7(a). The microchannel plates are made from a highly resistive material, generally glass, which possess a hexagonal array of parallel micron sized channels evenly distributed spatially across the surface of the plate. These channels are typically around 10–20 μm in diameter. The plates themselves used for the electron and ion detector have a diameter of 80 mm and 120 mm, respectively, and are each around 1.5 mm thick.

When a charged particle is incident on the surface of the MCP and enters into a microchannel, the charged particle can collide with the wall, triggering an avalanche of secondary electrons. By applying a large potential (typically $\sim$800–1200 V) across the MCP stack, these avalanche electrons can be accelerated down the channel. Since the channels

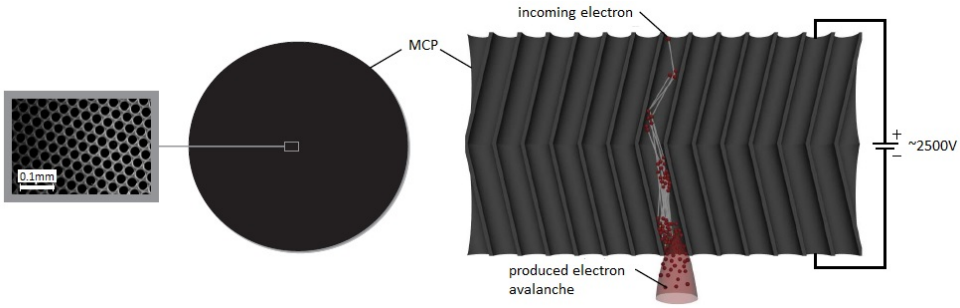

(a)

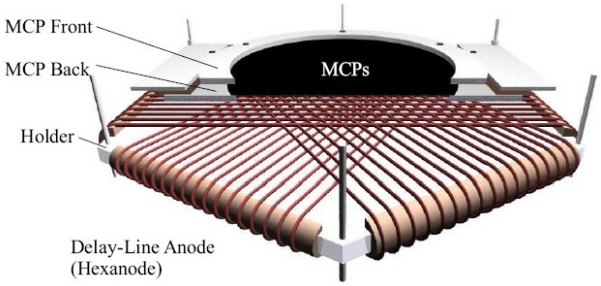

(b)

Figure 4.7: (a) A schematic depicting an MCP, with a magnified image of its microchannels, and its principle of operation, generating an electron avalanche from a single charged particle. (b) A diagram of the detector assembly, consisting of the MCP and delay-line anode (three-layer hexanode depicted). Figure from [66].

run at a slight angle ($\sim 8°$) relative to the normal vector of the surface, the cascade of electrons may undergo several collisions with the channel walls, generating more secondary electrons with each collision. Placing the MCP stack in chevron (such that the channels of the two plates form a V-shape) can result in a charge amplification of roughly 10^6. By using the time difference between the signal on the MCP and a laser timing reference signal, the time-of-flight of a charged particle can be retrieved.

Delay-line anode detectors are used to read out the amplified MCP signal. Each delay-line layer consists of a long helical wire pair that is densely wound around an insulating frame in a parallel configuration, with spacing of $\sim$0.5 mm. This forms a Lecher line that is capable of transporting high frequency signals with low noise. The helical wire pair consists of a collection wire, or signal wire, and a reference wire. The two wires are held at a potential difference of 20–50 V such that the collection wire picks up most of the charge emerging from

the MCP. The insulating frame is rectangular in the case of the two-layer quadanode and hexagonal in the case of the three-layer hexanode. When an electron avalanche created in the MCP hits the collection wire, a pair of signals travel to each end of the wire. Since external noise sources should be equally distributed across both the collection and reference wire, subtracting the reference wire signal from the collection wire signal attenuates any noise. The position of impact perpendicular to the wire winding direction is proportional to the difference in arrival time of the signal at either end of the wire. The conversion factor between the time difference and spatial position is defined as the ratio between the detector size to the maximum time difference of the layer.

Delay-line quadanodes make use of two delay-line layers that are rotated relative to each other by $\pi/2$, so that the parallel wire arrays run perpendicular between the two layers. This enables both the x and y hit positions to be read out, providing complete spatial information in the detector plane. Delay-line hexanodes make use of three delay-line layers, which are rotated relative to each other by $\pi/3$, providing an overdetermined position measurement, as one of the layers is redundant. This redundant layer improves the multihit capability of the detector, as multiple or missing signals can be reconstructed by using all the layers. The average position resolution across the detector is also improved using a post-processing algorithm that uses the redundancy to reconstruct the detector image. An example of a hexanode detector, together with an MCP and its ceramic ring holder, is shown in Fig. 4.7(b).

The time and position resolution of the detectors also depends on the electronics used for signal retrieval and timing, as well as fine tuning of hardware and experimental parameters. The various aspects of the hardware and electronics used in signal acquisition will be further discussed below.

4.2.2 Geometry

When the spectrometer was originally designed, various factors were taken into consideration when choosing its geometry. Typically in COLTRIMS experiments, the spectrometer geometry is adapted to the parameters that are specific to the measurement. The design used in MISTERS was required to be more flexible, such that it would perform in a range of different experiments. Additionally, the unique characteristics of the VUV photon beam introduced various challenges. Since the VUV fluence per pulse produced by HHG is very high, exceeding that produced by sychrotrons by orders of magnitude, this can lead to many ionization events within a single shot, which makes establishing coincidence challenging. Additionally, the repetition rate of the VUV pulses is 50 Hz, while synchrotrons provide pulses at repetitions rates in the MHz, which makes collecting data painfully slow. This forces experiments to be run at ionization rates in the range of 0.1–1 events per shot, orders of magnitude higher than the event rate of a synchrotron based measurement, where coincidence can be compromised. An additional challenge involves the VUV beam quality following propagation to the endstation. Since any VUV photons that hit the copper plates of the spectrometer will result in photoemission from that surface, the quality of the beam

mode must be good and any "halo" or diffuse and scattered photons around the primary mode must be eliminated.

An asymmetric spectrometer design was chosen, which can accommodate a range of photoionization and photodissociation experiments in atomic and molecular systems. The spectrometer is shown in Fig. 4.8, with specific dimensions labeled. The total length is ∼501 mm, while the distance from the interaction region to the electron detector is ∼304 mm, and the distance from the interaction region to the ion detector is ∼197 mm. The ∼304 mm long region is partitioned into two sections using a metal mesh, one ∼99 mm long and one ∼205 mm long. The electron side of the spectrometer forms the long side and the ion side forms the short side. Another metal mesh is placed at each end of the spectrometer just in front of the MCPs, which can be biased to form a short high field region. This acceleration region boosts charged particles before impact with the MCP, enabling efficient detection. The short ion side of the spectrometer is equipped with a 120 mm two-layer delay-line anode (quadanode) detector, while the long electron side is equipped with a 80 mm three-layer delay-line anode (hexanode) detector (both produced by RoentDek GmbH). The gap in the copper plates for coupling the VUV beam in and out of the spectrometer is ∼63 mm in the horizontal dimension and ∼40 mm in the vertical dimension, while the aligned copper plates themselves are spaced by ∼0.5 mm. A diagram of a spectrometer copper plate with a circular cutout is shown in Fig. 4.9(a), where the dimensions are labeled in inches. Fig. 4.9(b) shows a view of the assembled spectrometer along the time-of-flight axis, where the circular hole in the center acts as a conduit for the spectrometer detector wiring.

As mentioned above, in general operation, the short side of the spectrometer is used for collecting ions, while the long side is used for collecting the corresponding photoelectrons. The electrons traverse two stages before being imaged, a short acceleration region and a longer drift region, which greatly improves resolution. This is known as a Wiley-McLaren geometry [166], and reduces the momentum uncertainty associated with having a spatially extended target along the time-of-flight dimension. The present spectrometer design uses the standard 2:1 ratio of acceleration to drift region length. A hexanode detector is used on the electron side of the spectrometer, as it has good multi-hit capabilities, which can be necessary since the spread in electron time-of-flight is generally small, typically on the order of ∼10 ns.

Specific copper plates of the spectrometer are connected to high voltage DC power supplies (SRS PS300) using vacuum feedthroughs, which allows the spectrometer to be biased to generate a DC electric field. This allows a variety of different field strengths to be dialed in. The whole spectrometer and detector assembly is placed on a sleigh that can be slid into and out of the MISTERS endstation and into the target region along a track. The detectors and spectrometer are then connected to high voltage power supplies using SHV vacuum feedthroughs on the chamber walls and the two large flanges (ConFlat 300) that lie on either side of the spectrometer ends.

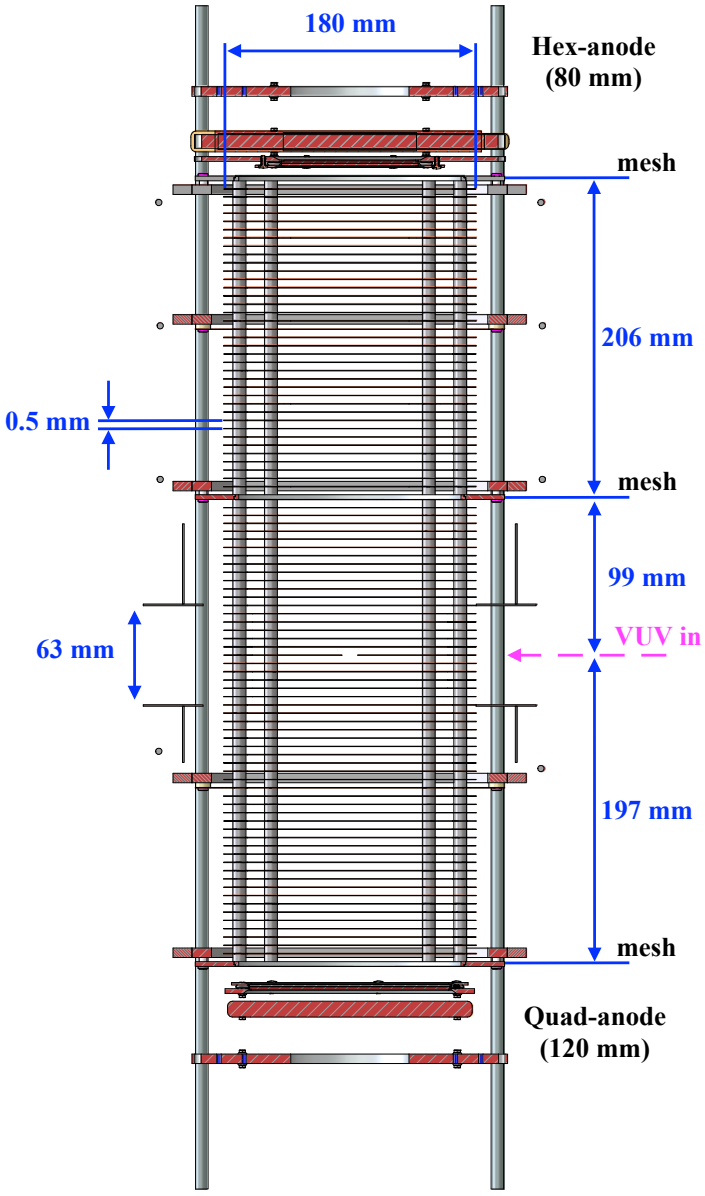

Figure 4.8: A schematic of the coincidence 3-D momentum imaging spectrometer housed in the MISTERS chamber. The copper plates of the spectrometer have gaps for coupling in both the VUV beam and the supersonic gas jet. The plates are extended at the gap for coupling the VUV beam in and out of the spectrometer, which aid in minimizing field distortion caused by the gap itself. Stainless steel shielding extends to either side of the extension plates, which helps reduce scattered light entering the spectrometer.

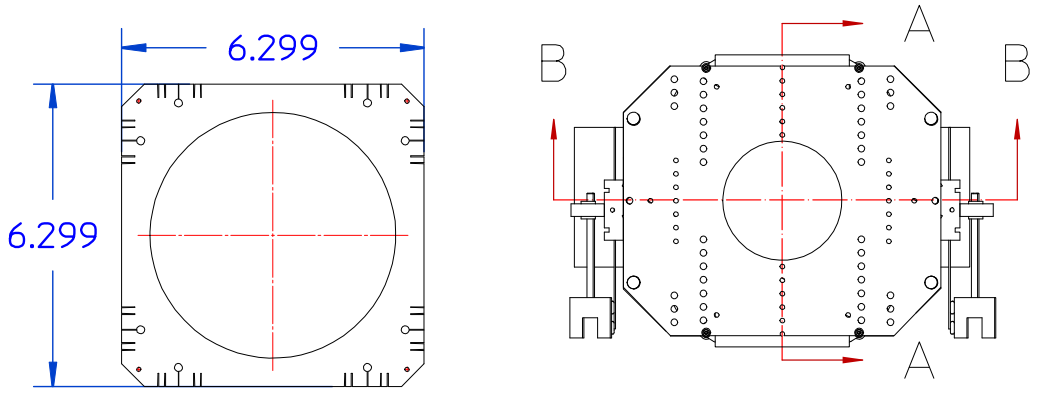

(a) (b)

Figure 4.9: (a) A front view of a copper spectrometer plate showing the circular cutout, with dimensions labeled in inches. (b) A front view of the assembled spectrometer, where the hole in the center serves as a conduit for the spectrometer detector wiring.

4.2.3 Signal Retrieval and Data Acquisition

In order to achieve the required gain for single particle detection, the MCP and delay-line detectors must be biased at high voltage. The generated signals on both the MCP and delay-line layers have an amplitude on the order of tens of mV, which then needs to be decoupled from the high voltage of the signal wires. This decoupling is performed using a home-built high-pass filter, composed of a capacitor (5 nF) combined with a potentiometer that is used to adjust the impedance mismatch between the connections. The decoupled signal is then amplified using a fast amplifer (RoentDek FAMP) to signal amplitudes of 0.6–1.2 V. In order to reduce the dependence of the signal timing on the pulse amplitude and convert the signal to a NIM standard, a constant fraction discriminator (CFD) is used.

The analogue time signals are then digitized and recorded on a data acquisition PC using a time-to-digital converter, or TDC (Cronologic GmbH). The data corresponding with each event are stored in list-mode file format (lmf). The raw data from each delay-line anode layer and the MCP is converted to time-of-flights and detector hit positions using commercial data acquisition software (COBOLD PC), which involves a complex resorting and reconstruction algorithm that can handle incomplete events via consistency considerations. If the count rate becomes too high, the CFD possesses a logic module that provides a “veto” and “gating” function. This function enables the timing outputs of the CFD to be switched on and off as a function of a voltage level on an input socket (labeled Veto) on the CFD. The veto voltage level is switched between a 0 V low and a -0.8 V high, at 50 Ohm input impedance. This allows events to be restricted to a certain time-of-flight range when a NIM level is present on the veto input, rejecting any unwanted events. A signal on a photodiode from the laser

serves as a timing reference signal and is used as a trigger in data acquisition, where the initial time of photoionization, t_0, is found by using the time-of-flight peak corresponding with scattered photons from the incoming VUV beam that hit the detector.

In order to reduce the number of stabilized power supplies needed to operate the spectrometer, adjustable resistor chains, or voltage dividers, were implemented across the spectrometer plates. By adding a high Ohm resistor in parallel to ground, called a load resistor, two power supplies can be connected at either end of the spectrometer across the resistor chain at the same polarity, while charge buildup is mitigated. It can be beneficial to hold the spectrometer at a negative potential, as this repels any electrons originating from outside the spectrometer. The spectrometer typically operates with a few hundred volts across it (from the electron detector mesh to the ion detector mesh), but varies depending on the required field strengths in the experiment.

The momentum resolution is determined by various factors, involving a convolution of the detector resolution, the electric and magnetic field, the finite temperature of the target, the location and spatial extent of the target, as well as the bandwidth of the VUV harmonics. Depending on the parameters of the particular experiment, the resolution will vary. A general rule of thumb for the expected energy resolution in an experiment is $E/\Delta E \sim 10$. The highest resolution is achieved along the time-of-flight axis of the spectrometer, corresponding with p_z. The increased resolution along p_z is a result of the geometry of the focal volume, which has smallest extent along the time-of-flight axis and is roughly 100 times smaller than the dimension extending along the Rayleigh length. Additionally, momentum uncertainty in the target is low along the time-of-flight axis, since the beam is skimmed in this dimension, while the momentum uncertainty is largest in the supersonic beam propagation direction.

4.2.4 VUV Flux Measurement

Because high harmonic generation is an intensity dependent extreme nonlinear up-conversion process, the VUV yield is very sensitive to any beam pointing, mode and energy instabilities. Since the VUV photons are generated in a cascaded harmonic generation process, i.e. first the NIR fundamental is frequency doubled in a nonlinear second harmonic generation process and then that second harmonic is used to drive high harmonic generation (harmonics generated from a harmonic, hence cascaded), this can result in large fluctuations in the VUV fluence, since two nonlinear processes are compounded that are both sensitive to changes in intensity. Further, the NIR fundamental is also subject to fluctuations (beam pointing, mode and energy) resulting from amplification in the multi-pass amplifier. The result is large shot-to-shot variations in VUV intensity, leading to a dynamic event rate. An instrument was designed in order to measure the relative intensity of the VUV beam on a shot-by-shot basis. This tool can be moved in order to record either the VUV flux entering or exiting the spectrometer, allowing it to be simultaneously operated with the coincidence momentum imaging spectrometer and permitting events to be tagged with a relative VUV intensity.

The device is composed of a rectangular copper plate ($\sim 5 \times 10$ cm) that is connected to a power supply and amplifier via electrical vacuum feedthroughs. The plate is mounted

to a rotational feedthrough adjacent to the Apollo iris. This allows the plate to be rotated into the incoming VUV beam, or rotated out to capture the diverging VUV beam after back-reflection out of the spectrometer. The work function for copper is 4.7 eV, hence all of the VUV harmonics will drive photoemission on the surface, while any NIR or 400 nm photons can not. The photoemission resulting from the VUV harmonics creates a small current between the copper plate and the power supply it is connected to. This signal is then amplified and transformed into a DC voltage between 0–10 V. Since the repetition rate of the laser system is 50 Hz, there is 20 ms between pulses, allowing the current to be read off shot-by-shot.

An analogue pulse height to time converter was built in-house (by Lothar Schmidt) that records to the TDC the VUV intensity for each event. This device compares the input signal from the copper plate with a pulse generated by a ramp generator, which delivers a standard NIM pulse (start pulse) at the beginning of the input pulse and a second pulse (stop pulse) when the amplitude matches that of the input pulse. The difference between the start and stop pulses is linearly dependent on the pulse height and therefore the VUV flux. This device can also be used for on-the-fly optimization of the VUV harmonics, where the DC voltage can be read off while different beam parameters and gas parameters are adjusted.

4.2.5 Data Analysis

In the data acquisition system, the TDC records the raw time signals off the detectors, relative to a trigger channel. This trigger channel is fed by a signal from a photodiode in the laser system, where the correct timing on each channel with respect to photoionization is determined by subtracting this trigger timing off each channel of the TDC. The time-of-flight and delay-line anode hit positions are reconstructed from these signals as described earlier.

Since the classical trajectories of charged particles in the electric and magnetic fields of the spectrometer are known from conventional electromagnetism, the photoelectron and ion momenta can be reconstructed from the hit position and time information of each event. For the ions, this assumes the correct mass assignment to the ionic species in question.

The charge to mass ratio $\sqrt{M/q}$ of the ions can be determined from the time-of-flight spectrum, since for a given electric field strength, the time-of-flight depends on the mass to charge ratio $\sqrt{M/q}$, allowing specific time-of-flights to be identified and assigned to specific ionic species. For a homogeneous electric field with magnitude E over a region l, the time-of-flight of an ion is given by

$$t = \sqrt{\frac{2l}{E}\frac{M}{q}} \tag{4.10}$$

for an ion of mass M and charge q. In order to account for the short boost region of high field just in front of the ion detector, this simple time-of-flight calculation is slightly modified to include the effect of the second small region of high acceleration field. Additional complications can arise from the back-focusing geometry, where the incoming VUV beam can

create electrons and ions in addition to the focusing beam, which results in charged particles being created at locations outside the interaction region and at a range of times. However, the small mm level offset between the incoming and focusing VUV beam results in different time-of-flights, enabling ionization of background gas in the chamber to be separated from ionization of the cold target.

The initial step in the post-processing of the recorded list-mode file data is performed using the LMF2Root software package. This program is written in C++ and has been extensively developed by Markus Schöffler, Till Jahnke, and Achim Czasch. After the list-mode file data are processed and transformed into detector hit position and time-of-flight data using LMF2Root, the rest of the calibration and analysis is performed using python and the various libraries present in the scientific python ecosystem. The equations used for transforming the hit positions and time-of-flights into momenta, as well as processes for selecting relevant events and calibrating the data, are well documented and additional details can be found in Refs. [40, 157, 66].

4.2.6 Handling Large Event Rates

As mentioned before, the VUV beam parameters that are produced via HHG are quite different from those at standard synchrotrons, which operate in the MHz at much lower fluences. As a result, the ion and electron event rates are much lower at synchrotrons, typically around one ionization event per 100–1000 pulses (far below the 1 event per shot limit that assure unambiguous coincidence), translating to a detector count rate on the order of 10,000 hits per second. This rate lies well within the operation limits of the detectors. However, the low repetition rate and high fluence of the harmonics pushes the detectors into less friendly and familiar territories.

Since synchrotrons typically produce 10^{13} photons per second at MHz repetition rates, this corresponds with roughly 10^7 photons per pulse. If a beamline monochromator is used to provide a narrow spectrum, this can reduce the flux by roughly two orders of magnitude, i.e. $\sim 10^5$ photons per pulse. The VUV harmonics are far brighter, delivering roughly 10^{10} photons per pulse, a factor of 1000 more photons per pulse than what is produced directly out of a typical VUV undulator. However, due to the low 50 Hz repetition rate of the laser system, the average flux is about one order of magnitude lower than what a synchrotron delivers. The large number of photons produced per pulse in HHG creates challenges for running the detectors successfully, since a large number of electrons and ions can be generated, which results in detector signals that saturate the amplifier. This arises due to their limited multi-hit capabilities, where issues emerge when a large number of charged particles impact the detector in a short window of time and/or near by one another. The result is a depletion of charge in the amplifier, where subsequent hits have a reduced baseline. This charge depletion can last for hundreds of microseconds, rendering the detector blind to any events that occur in this time window.

The multi-hit issue arising from high event rates is a more substantial problem for the electron detector, which picks up more signals resulting from scattered VUV photons in the

spectrometer. However, the ion detector is not impervious to these multi-hit issues and can also be saturated when the VUV fluence is too high, but this is not generally as much of an issue. Various attempts have been made at solving these problems, with no one specific approach completely resolving them.

Since the VUV photons can themselves cause detector saturation, it is important to both adjust the fluence to a suitable level, while also ensuring the beam mode is of good quality. If the fluence is too high, both the ion and electron detectors will saturate, while if it is too low, two-photon ionization can not be driven. The beam mode must also be reasonable and not possess a "halo" of scattered light co-propagating with the primary mode. The quality of the mode is controlled through optimization of the driving field mode, and careful alignment through the beamline to minimize clipping and diffraction. Additionally, a pair of collimators can be used to trim off any scattered photons surrounding the main beam. Accurate alignment of the VUV beam in and out of the spectrometer is also critical in ensuring that the detectors do not saturate. This involves hitting the center of the back-focusing mirror, and then carefully aligning the back-focusing mirror to jet and reflecting the beam cleanly out of the spectrometer. Here, care needs to be taken to ensure the beam does not clip any copper plates on its entrance and exit from the spectrometer, as this will generate pollution on the electron detector. After the VUV beam is dumped onto the copper plate used for reading out the VUV intensity, this plate can be carefully rotated using its feedthrough in order to minimize any back-reflected VUV photons re-entering the spectrometer.

The parameter with the largest effect on mitigating the problem of detector saturation comes from the electric and magnetic fields of the spectrometer. Once the beam parameters and alignment are optimized, the spectrometer fields can often be carefully chosen such that the high density problematic hits that do not correspond with the intended ionization are pushed out to later time-of-flights, where they can be gated out. This puts the relevant ionization events before the temporal depletion window on the detectors, making detector saturation a non-issue in terms of retrieving good ionization events in post-processing.

Chapter 5

Experimental Results

In this chapter, the first experimental measurements using the MISTERS endstation following two-photon absorption of the third harmonic of a 400 nm driving field are reported. A great deal of time was invested in understanding the relationship between measured signals on the detectors and the spectrometer and VUV field parameters. Arriving at fully optimized conditions was a genuine challenge, as the 50 Hz repetition rate is prohibitively low, largely impeding on-the-fly optimization. Further, since the dark count rate on the detectors can lie between 20-30 Hz, even running experiments at an average rate of one coincidence event per shot does not place the real signal far above the detector noise. This proved to be a character-building experience, since the ideal spectrometer and photon parameters can typically be optimized within a few minutes during synchrotron based experiments, where the photon pulse repetition rates lie in the MHz and the detector hit rates lie in the tens of kHz. In spite of these limitations, numerous successful experimental measurements were performed, demonstrating that these challenges can be overcome in the right conditions.

Once VUV harmonics were achieved, which was a multi-year challenge, it was a 6 month effort to get the first actual experiments running. MISTERS was pumped out in early January 2019, while the first data using the 400 nm driven harmonics was collected in June 2019. The spectrometer had been in a long slumber and had not be awakened since August 2016. The first measurement investigated the photoionization dynamics in non-resonant one-color two-photon ionization of neutral argon atoms, as per the suggestion of the postdoc Roger Y. Bello in the theory group of C. William McCurdy. Following the measurement on this atomic system, two more sets of experiments were performed on diatomic molecules. One measurement investigated the photoionization dynamics of non-resonant one-color two-photon ionization of neutral N_2, while the other measurement investigated the photodissociation dynamics of ion-pair formation following resonant one-color two-photon absorption in neutral O_2.

In the following sections, it is demonstrated that rich photoionization and photodissociation dynamics can be triggered in simple gas-phase systems by two-photon absorption of a VUV field, which can be probed in great detail using 3-D momentum imaging, allowing many-electron and non-adiabatic effects to be identified and characterized. We first start

with a discussion of the experiment in atomic argon, before turning to the the results of the measurements in O_2 and N_2. The raw photoelectron and photoion data will be presented in the first case of atomic argon, while the raw photoion data presented in the second case of dissociative ion-pair formation in molecular oxygen. Only the reconstructed momenta are presented in the final cases of bound two-photon single ionization of molecular nitrogen.

5.1 Argon

5.1.1 Angle-resolved non-resonant two-photon single ionization of argon using 9.3 eV photons produced via high harmonic generation

In this first section, an experimental study on the photoionization dynamics of non-resonant one-color two-photon single valence ionization of neutral argon atoms is presented. Using 9.3 eV photons produced via high harmonic generation and the MISTERS 3-D momentum imaging spectrometer, photoelectrons and ions produced from non-resonant two-photon ionization are detected in coincidence. Photoionization from the $3p$ orbital produces a photoelectron scattering wave function with p and f partial wave components, which interfere and result in a photoelectron angular distribution with peak amplitude perpendicular to the VUV polarization. The comparison between the present results and two previous sets of theoretical calculations indicates that electron-electron correlation contributes appreciably to the two-photon ionization dynamics [126, 113].

Background

The photoionization dynamics of multi-electron atomic and molecular systems are influenced by electron-electron correlation. Non-resonant two-photon ionization can probe such correlation effects in both the initial and final states of the target. A particularly sensitive observable is the photoelectron angular distribution (PAD), which can provide a detailed view of the underlying mechanisms involved in the photoionization process and its correlated nature, e.g. information on the role of continuum states and interchannel coupling [18, 169, 101, 14, 73, 150, 135, 70, 4, 146, 96, 83]. The PAD emerges from a coherent summation over a set of final continuum states. The sensitivity of the PAD to electron-electron correlation arises from its dependence on the amplitudes and phases of the different partial wave components of the coherent sum. These distinct angular momentum components can interfere to create nodes and antinodes in the PAD.

PADs are uniquely characterized by their energy-dependent anisotropy parameters, or β parameters. The number of β terms used to describe the PAD increases with the photon order. As such, a two-photon PAD can exhibit more anisotropy and structure than the corresponding one-photon PAD. Previous two-photon investigations of the anisotropy parameters in neon and argon have been realized using two-color two-photon above-threshold ionization

schemes [63, 114, 46], where ionization was performed with a VUV field in the presence of a strong NIR dressing field that generated photoelectron sidebands. This can make comparison with theory very challenging. Measurements that lie within the perturbative limit and target non-resonant bound-continuum transitions, driven by the second photon (rather than continuum-continuum transitions), are highly sensitive to electron-electron correlation and can be achieved in a one-color two-photon ionization scheme by exclusively using a VUV field with a photon energy in a non-resonant region below the ionization threshold. However, measuring a PAD from **n**on-resonant **o**ne-color **t**wo-**p**hoton **s**ingle **i**onization (NOTPSI) in an atomic gas requires sufficiently high VUV intensities to enable nonlinear processes. Since high intensity ultrashort VUV light sources are limited to a small number of free electron lasers (FELs) and tabletop high-order harmonic generation (HHG) systems, angle-resolved measurements on NOTPSI in rare gases are scarce.

Over the years, several studies have investigated one-color two-photon ionization in rare gases, first using HHG based light sources [112, 142], and later using VUV FELs [138, 110, 104]. PADs were measured in helium at several photon energies, across both the resonant and non-resonant regions, in Ref. [104]. Here, anisotropy parameters as well as amplitude ratios and phase differences of the partial wave components of the scattering wave function could be extracted, due to the simple nature of the target. By moving to more complex many-electron systems, more terms and higher angular momentum components contribute to the photoelectron scattering wave function, and many-electron effects become more significant. This increase in complexity represents a great challenge for experiment and theory alike.

Previous theoretical studies on angle-resolved two-photon ionization in helium have indicated that a single-active-electron picture appears to be a valid approach in describing the photoionization dynamics for photon energies below the ionization threshold (and even in the above threshold region) [18]. It is unlikely that this is true for more complex core targets. This compels angle-resolved measurements in more complicated systems, where many active and correlated electrons are required to describe the photoionization dynamics. To our knowledge, no angle-resolved measurements exist for complex multi-electron systems such as argon, were electron-electron correlation is expected to play a more significant role in the photoionization dynamics than in simple systems like helium. The aim of this experimental investigation is to reveal, for the first time, clear contributions from electron-electron correlation in the PADs emerging from NOTPSI of argon.

Despite the paucity of experimental data, the problem has not escaped theoretical treatment. Over a quarter of a century ago, the β parameters for one-color two-photon single ionization (including NOTPSI) were calculated for argon using a Hartree-Fock approach [126] providing uncorrelated and Coulomb correlated results, and a random phase approximation calculation [113], which neglected electron-electron correlation. The uncorrelated results of Ref. [126, 113] are somewhat ambiguous due to discrepancies between the calculations performed in the length and velocity gauge at various photon energies. The correlated results of Ref. [126] show better gauge invariance in both the resonant and non-resonant two-photon ionization regions and the computed β parameters suggest maximum photoelectron emission perpendicular to the ionizing field at 9.3 eV. However, to our knowledge, these calculations

have for decades remained unverified by any experimental measurement.

In this section, results on angle-resolved NOTPSI of argon from the $3p$ orbital using 3-D momentum imaging are presented, where the photoelectron and ion are measured in coincidence. Using a 400 nm driving field, we produce and select VUV photons with an energy of 9.3 eV via HHG, which are then used to perform NOTPSI. Interference between different angular momentum components of the photoelectron wave function results in a PAD exhibiting maximum intensity perpendicular to the ionizing VUV field. These experimental results are compared against previous calculations, which suggest that electron-electron correlation considerably influences the photoionization dynamics.

Experimental Parameters

The valence photoionization dynamics in neutral argon were investigated using the coincidence 3-D momentum imaging capabilities of the MISTERS endstation. Here the photoelectron and ion produced by non-resonant one-color two-photon ionization were collected with full 4π solid angle, and their 3-D momenta were measured in coincidence, on an event-by-event basis. The charged particles were guided by parallel DC electric and magnetic fields with values of 15.55 V/cm and 3.72 G, respectively, towards the position- and time-sensitive detectors at opposite ends of the spectrometer.

Here the laser system was configured to provide 12 mJ, 45 fs NIR pulses, which were frequency doubled using the 0.25 mm thick beta-barium borate (BBO) crystal, where the copropagating 800 nm NIR and 400 nm blue fields were then separated using the two dichroic mirrors. The reflected blue photons ($\sim$3.6 mJ, $\sim$50 fs) were then focused using the f = 6 m curved mirror into the 10 cm long gas cell containing 3 Torr of krypton to generate VUV odd harmonics via HHG. As described in Chapter 3, the resulting VUV frequency comb was then separated from the 400 nm fundamental by reflection from the three silicon mirrors near Brewster's angle for the 400 nm field, resulting in a suppression of the fundamental by a factor of $< 10^{-6}$. In this experiment, the 3$^{\text{rd}}$ harmonic (133 nm, 9.3 eV) was isolated by transmission through the 0.25 mm thick MgF_2 window, totally suppressing the 5^{th} harmonic and above. The femtosecond pulse duration of the 3$^{\text{rd}}$ harmonic was also maintained, while the residual 400 nm pulse was temporally separated from the 3$^{\text{rd}}$ harmonic pulse by $\sim$700 fs, due to the difference in the group velocity dispersion (GVD) of the window at ω_0 and $3\omega_0$ [2, 95] (see Chapter 3). After transmission through the window, the estimated pulse duration of the 3$^{\text{rd}}$ harmonic was $\sim$30 fs, based on its spectral bandwidth, its estimated attochirp, and the thickness and GVD of the MgF_2 window [141, 143] (again, see Chapter 3). The femtosecond 9.3 eV pulses were then back-focused using the f = 15 cm curved mirror into the MISTERS 3-D momentum imaging spectrometer using the protected aluminium mirror, the reflectance of which was measured to be 43% at 9.3 eV [89]. The pulse energy of the 3$^{\text{rd}}$ harmonic on target was approximately 10 nJ, which was measured using the previously described broadband VUV filters (Acton Optics FB130-B-1D.3) and a calibrated photodiode.

The beam of argon atoms was prepared from an adiabatic expansion through the MISTERS 0.03 mm nozzle, which was then collimated by the skimmer pair. This atomic jet

propagated orthogonally to the focusing VUV beam, where the two intersected in the interaction region (approximately 0.01 × 0.01 × 0.20 mm) of the spectrometer, resulting in a ionization rate of ∼0.3 events per VUV pulse.

Raw Data

In an offline analysis, the x- and y-hit position and Time-of-Flight of the measured charged particles are used to calculate the corresponding 3-D momentum vector (p_x, p_y, p_z). These momentum components are reconstructed using the equations of motion for a charged particle in the electric and magnetic fields of the spectrometer at the given spectrometer geometry. While there is no ambiguity about the photoelectron mass when reconstructing the momentum, the mass of the measured ions must determined by their Time-of-Flight, which encodes the mass-to-charge ratio. A detailed discussion of the momentum reconstruction and calibration can be found in various reviews, papers and theses [40, 157, 66].

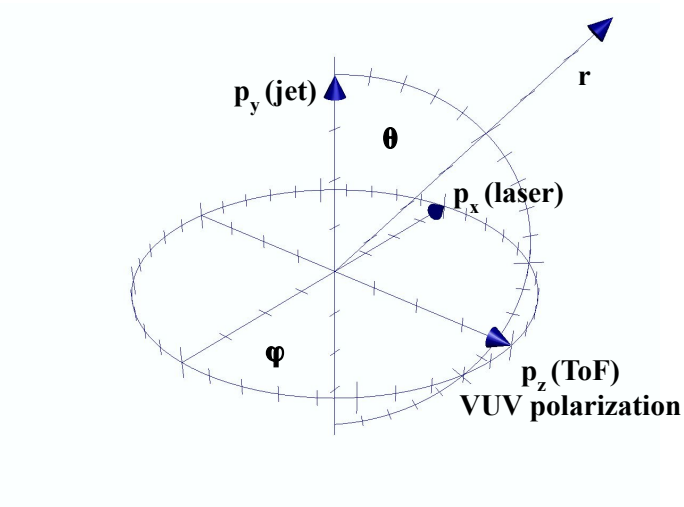

Figure 5.1: The cartoon indicating the laboratory frame coordinate system defined within the spectrometer. The x-axis corresponds with the laser beam propagation direction, the y-axis with the supersonic jet propagation direction, and the z-axis with the Time-of-Flight axis of the spectrometer, as well as the VUV polarization.

Before turning to the raw data or reconstructed momenta, we first define the coordinate system which is used throughout the analysis, shown in Fig. 5.1. Here, the laser beam enters the spectrometer perpendicular to the Time-of-Flight axis of the spectrometer (i.e. parallel to the spectrometer plates), which corresponds with the x-axis. The gas jet propagates perpendicularly to both the laser beam and the Time-of-Flight axis of the spectrometer, which corresponds with the y-axis. Finally, the z-axis coincides with the Time-of-Flight axis of the spectrometer. Photoelectrons and ions which are generated in the interaction region

formed by the laser focus and the jet fly along the z-axis towards detectors that lie parallel to the x-y plane. The VUV polarization is directed along the Time-of-Flight z-axis.

Fig. 5.2 shows the electron Time-of-Flight spectrum. The peak associated with photoelectrons emerging from two-photon ionization is centered near 55 ns. Pollution is observed in the Time-of-Flight spectrum as a secondary peak between 60-70 ns, which is sharper than the feature associated with ionization of the target. This pollution likely arises from electrons generated on the back-focusing mirror, which then creates an electron signal that competes with the true photoionization events. These electrons tend to fall near the edges of the detector, which can be seen in Fig. 5.2 as the events on the circle with a radius of 40 mm (where the pollution is higher near $x = \pm 20$ mm), while the real events show up as a ring with a radius of approximately 28 mm. Here the pollution is spatially localized to near the detector edges and slightly offset in Time-of-Flight, as seen in Fig. 5.2, enabling the real photoionization events to be separated from the pollution with relative ease. The ion Time-of-Flight spectrum is also shown in Fig. 5.2. Here we observe a single narrow peak centered near a 10460 ns Time-of-Flight, which corresponds with the argon cations originating from two-photon ionization.

Next we plot the photoelectron x- and y-hit position as a function of the Time-of-Flight, colloquially known as the electron x-fish and y-fish spectrum. These are shown in Fig. 5.3. In both plots, we observe the feature associated with photoelectrons emerging from two-photon ionization of the argon atoms, which manifests as the elliptical ring structure centered near a 55 ns Time-of-Flight. The pollution is seen at later Time-of-Flights centered near 64 ns, and is strongest near the detector edges ($y = 40$ mm, $x = -40$ mm). We also plot the electron hit radius, determined using the x- and y- hit positions, as a function of the Time-of-Flight, colloquially known as the electron wiggle spectrum, which is shown in Fig. 5.3. Here the photoelectron signal is seen as a bright arch, with most of the signal concentrated towards large hit radius, while less signal appears at low radius and shorter or longer Time-of-Flights. For photoelectrons emerging in the interaction region with constant energy, a shorter or longer Time-of-Flight is associated with emission along the Time-of-Flight axis, either towards or away from the detector. Since the Time-of-Flight axis coincides with the VUV polarization, the feature in the wiggle spectrum suggests that photoelectron emission is concentrated perpendicular to the polarization. This will be analyzed and discussed in detail below.

Reconstructed Momenta and Analysis

We now turn to the analysis of the charged particle momenta (p_x, p_y, p_z), which is reconstructed from the event hit positions and Time-of-Flight (x, y, ToF). The photoelectron momentum distributions are seen in Fig. 5.4, where two lab-frame momentum components are plotted against each other, p_x vs p_y, p_x vs p_z, and p_y vs p_z. These distirbutions show up as ring structures that show increased intensity at low longitudinal momentum, i.e. for values of p_z near zero. In Fig. 5.4 we also show the photoelectron-ion coincidences, which emerge as a diagonal feature with a slope of -1. Here we are plotting the photoelectron

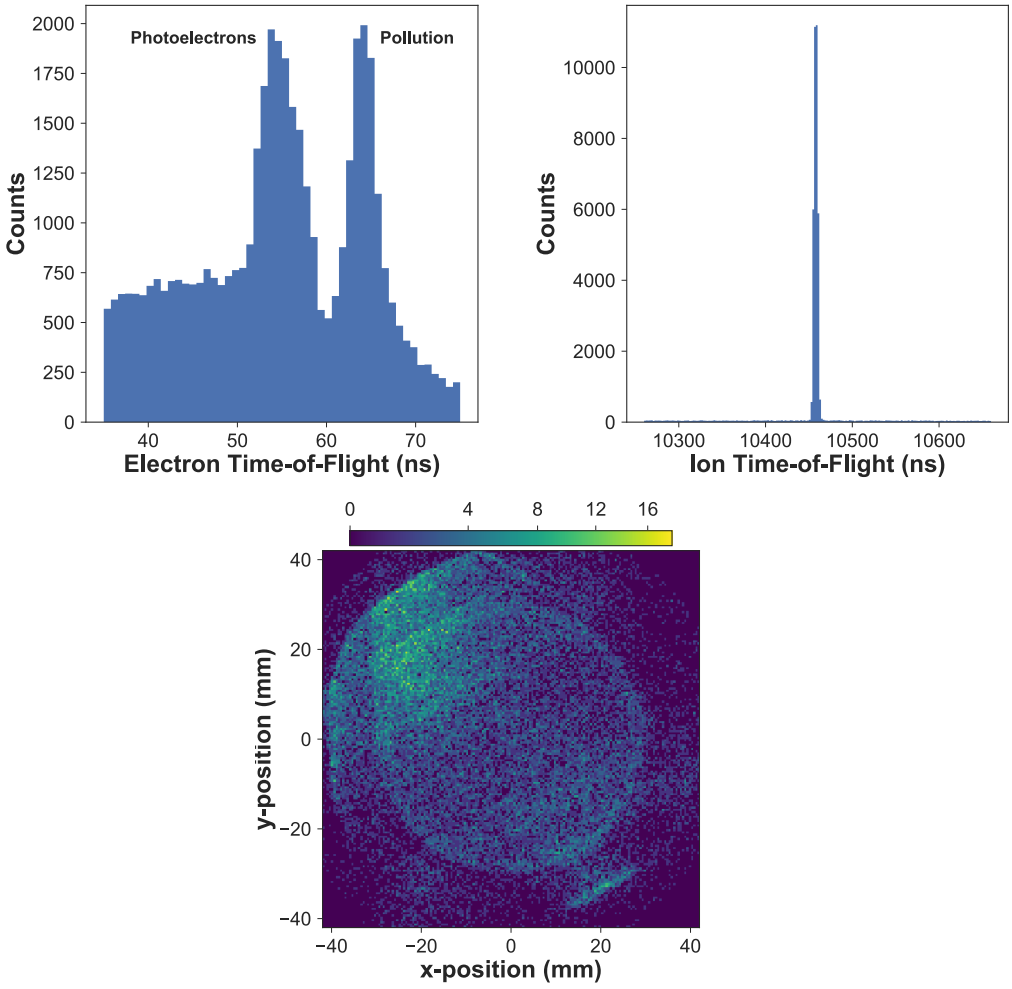

Figure 5.2: The photoelectron and photoion Time-of-Flight (in nanoseconds), and the photoelectron x- and y-hit positions on the electron detector.

momentum along the Time-of-Flight axis as a function of the ion momentum along that same axis. This figure shows the momentum conservation between the photoelectron and argon cation. As the electron carries away more momentum along the Time-of-Flight axis, the ion must correspondingly carries away the same amount of momentum in the opposite direction. By selecting the events that lie along this -1 diagonal, we are able to retrieve the real photoionization events (which must conserve momentum), while rejecting background events (which do not conserve momentum). Here lies the power of coincidence measurements, enabling momentum and energy conservation conditions to be enforced on the data, ensuring rare and real events are extracted with high fidelity, where high signal to noise is achieved. From the reconstructed photoelectron momenta, we can next calculate the kinetic

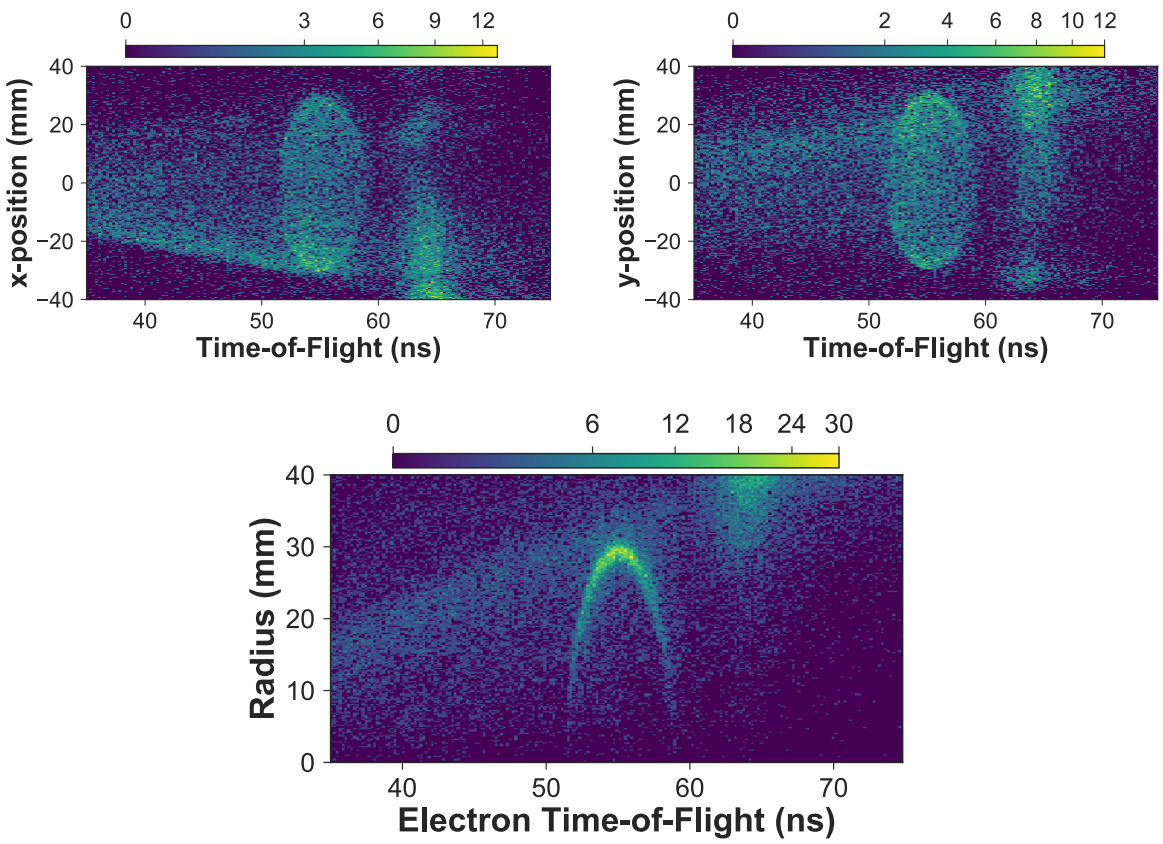

Figure 5.3: The photoelectron x- and y-hit positions as a function of the Time-of-Flight (also known as the electron x- and y-fish spectrum), and the photoelectron hit radius as a function of the Time-of-Flight (also known as the electron wiggle spectrum).

energy and angular distributions. Before doing so, we first provide some background on the electronic structure of argon and the nature of this photoionization problem.

The ground state electronic configuration of argon is $1s^2 2s^2 2p^6 3s^2 3p^6$ (^1S). Ionization from the $3p$ orbital results in the ground electronic state of the cation Ar^+, a ^2P state. From two-photon selection rules, the final states must have either ^1S or ^1D total symmetry, while the photoelectron wave function must be either a p- or an f-wave. It follows that we can express the allowed final states in the three forms listed below:

$$^1S: \ 3p^5 \ ^2P + \epsilon p \tag{5.1}$$

$$^1D: \ 3p^5 \ ^2P + \epsilon p \tag{5.2}$$

$$^1D: \ 3p^5 \ ^2P + \epsilon f \tag{5.3}$$

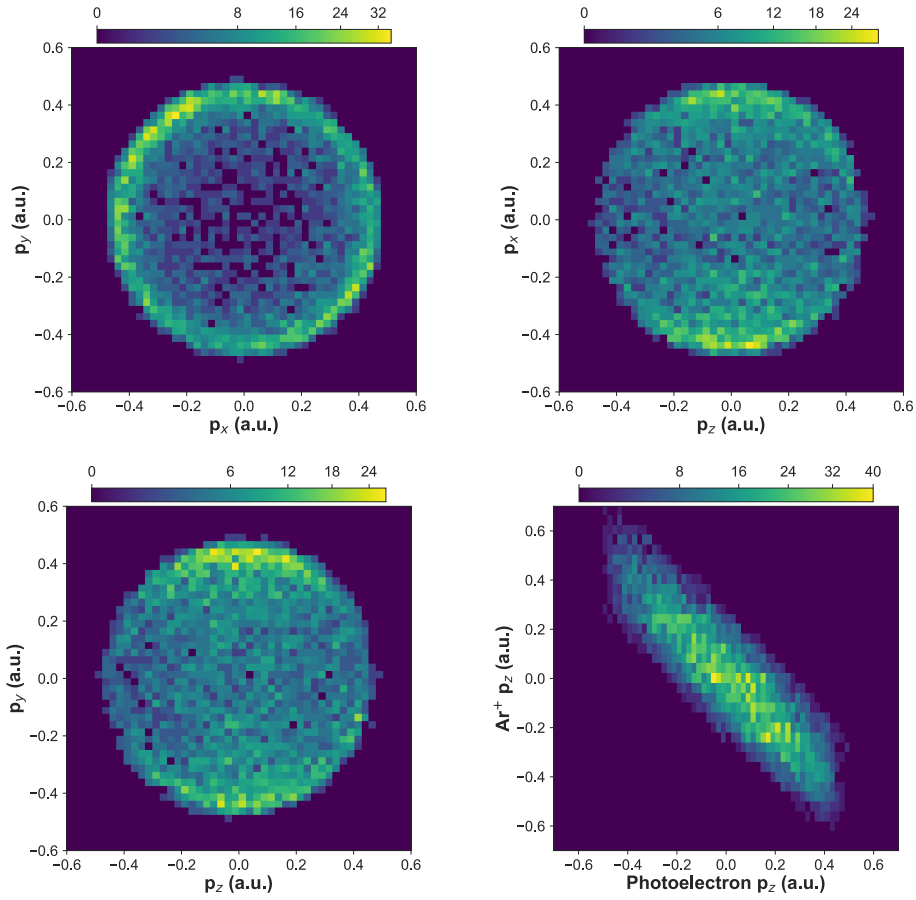

Figure 5.4: The 2-D photoelectron momentum distribution plotted in the lab-frame coordinate system, which manifest as ring features, and the photoelectron momentum along the z-axis (Time-of-Flight) as a function of the argon ion momentum along the same axis. The diagonal feature indicates the momentum conservation between the photoelectron-ion pair along the z-axis.

In (5.2) and (5.3) above, we see that the ^1D final state contains contributions from two different photoelectron angular momentum components, p- and f-waves. The coherent sum of these two partial waves can create an interference pattern in the PAD. Since the initial state has total magnetic quantum number $M = 0$, so too must the final states. Hence the m value of the photoelectron and ion wave functions must sum to 0. From this restriction, we see that only $m = 0, \pm 1$ values of the f-wave component can contribute, while all m values of the p-waves may contribute. These photoelectron states are paired to states of the core with the appropriate m value.

A diagram depicting the NOTPSI pathway in the present experiment is shown in Fig 5.5.

The grey box indicates the region containing the bound excited states of argon, beginning at 11.55 eV. The ionization potential of argon is 15.76 eV, while the two-photon energy is ∼18.6 eV, which results in an expected photoelectron kinetic energy of roughly 2.8 eV. Ionization of the ground state atoms via non-resonant two-photon absorption populates an ionic state and releases an electron into the continuum, with allowed final states listed in (5.1)-(5.3) above.

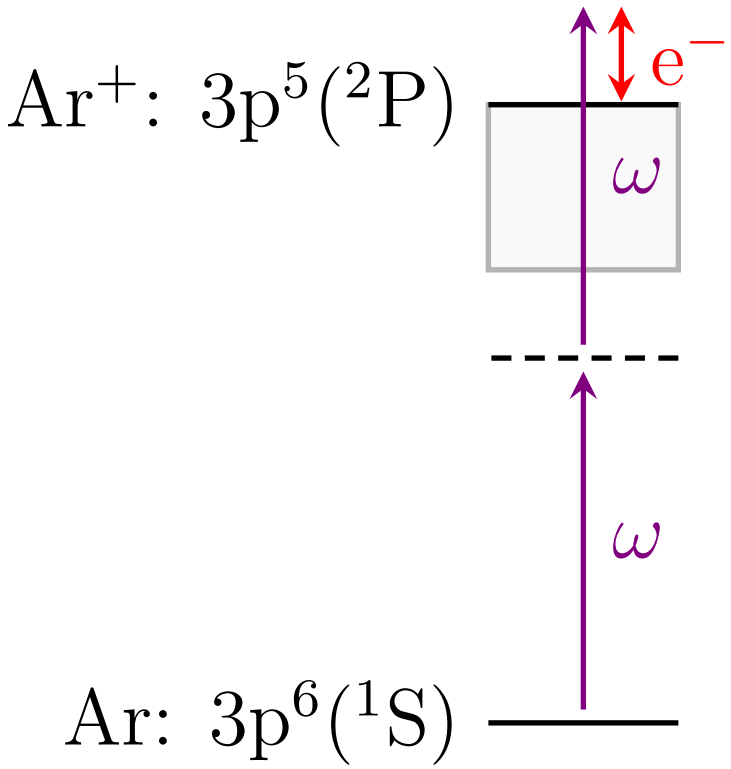

Figure 5.5: An energy level diagram depicting the NOTPSI pathway from the $3p$ orbital of Ar at 9.3 eV. The grey box indicates the region containing bound excited states, the first appearing at 11.55 eV. The ionization potential of Ar is 15.76 eV, hence the red double-arrow corresponds with a photoelectron kinetic energy of 2.84 eV.

The measured photoelectron kinetic energy spectrum is presented in Fig 5.6 (a). Here, we observe a single peak centered at 2.8 eV, with a full width at half maximum (FWHM) of ∼400 meV, indicative of the two-photon spectral bandwidth of the 3rd harmonic (convolved with the electron energy resolution of the spectrometer). The photoelectron momentum distribution transverse versus parallel to the VUV polarization vector is shown in Fig 5.6 (c), where we observe electron emission peaking towards high transverse momentum and low

longitudinal momentum. To gain more insight into the photoelectron emission pattern, we turn to the angle-differential photoionization cross section.

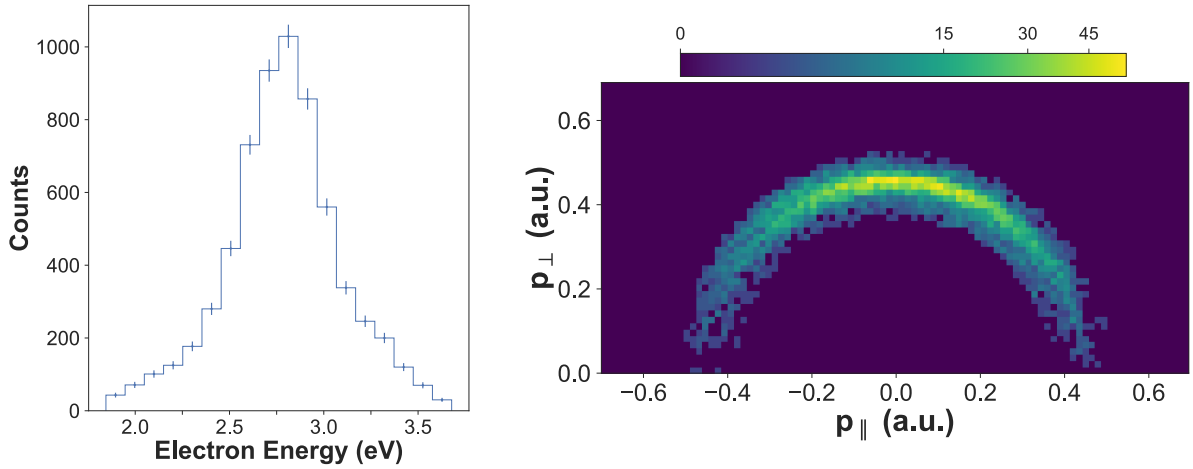

Figure 5.6: (a) The photoelectron energy spectrum and (b) momentum distribution parallel versus perpendicular to the VUV polarization.

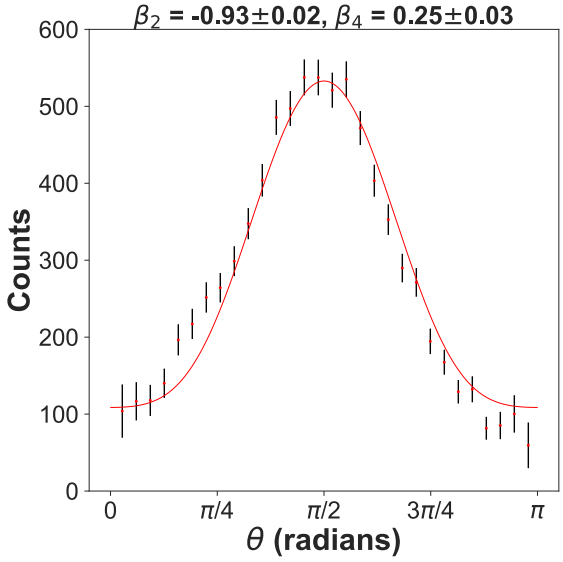

Figure 5.7: The angle-differential photoionization cross section for NOTPSI of Ar at 9.3 eV. The experimental data is fit using Equation 5.4, where the retrieved β parameters are displayed above the plot.

For two-photon ionization of a target atom by linearly polarized light, the angle-differential photoionization cross section is given by

$$\frac{d\sigma}{d\Omega} = \frac{\sigma_0}{4\pi}[1 + \beta_2 P_2(\cos\theta) + \beta_4 P_4(\cos\theta)] \tag{5.4}$$

where σ_0 is the total photoionization cross section, θ is the angle between the photoelectron momentum vector and the polarization vector of the light, β_2 and β_4 are the second and fourth order anisotropy parameters, and P_2 and P_4 are the second and fourth order Legendre polynomials in variable $\cos\theta$ [134]. The measured angle-differential photoionization amplitude is presented in Fig. 5.7. Equation 5.4 has been applied to fit the data (solid red line) using the projection method discussed in [97], where the error on the β parameters is determined via statistical bootstrapping [48]. The β parameters retrieved from the fit are β_2 = -0.93±0.02, β_4 = 0.25±0.03. Here the data is shown with a 6 degree bin size.

The PAD exhibits peak intensity at angles near $\pi/2$, corresponding with maximum photoelectron emission perpendicular to the VUV polarization. Intensity minima occur along the VUV polarization direction, near 0 and π. We attribute these features to the interference between the different p- and f-wave components of the photoelectron scattering wave function. These two angular momentum components destructively interfere along the polarization direction, yielding an angle-differential amplitude that peaks perpendicular to the field. This interference is analogous to the interference between the photoelectron s and d partial waves in photodetachment of I^- and O^- [105, 64, 31].

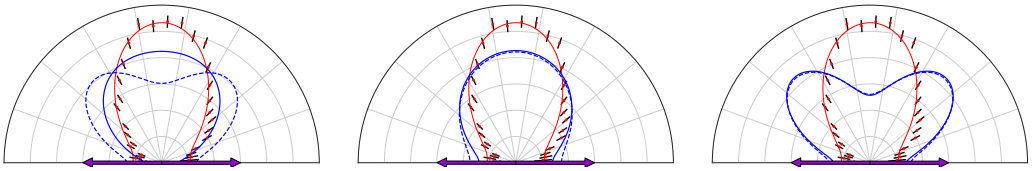

Figure 5.8: The photoelectron angular distribution for NOTPSI of Ar at 9.3 eV for the experimentally retrieved β parameters (solid red curve in (a), (b), and (c)) and those extracted from [126, 113]. The blue curves in (a) correspond with the uncorrelated HF calculation of [126], the blue curves in (b) correspond with the Coulomb correlated calculation of [126], and the blue curves in (c) correspond with the random phase approximation calculation of [113] (dashed: velocity gauge, solid: length gauge). The orientation of the VUV polarization is indicated by the horizontal double arrow.

We compare our retrieved β parameters with those extracted from Ref. [126] at a photon energy of 9.3 eV and Ref. [113] at a photon energy of 8.6 eV, presented in Table 5.1 and Fig. 5.8. In Ref. [126], the calculations were performed using a 2^{nd} order time-independent perturbation theory method, in both a Hartree-Fock (HF) approach and a Coulomb correlated HF approach. In the uncorrelated HF calculation, there is significant disagreement between the length and velocity gauges, while the Coulomb correlated HF approach exhibits

much better gauge invariance. We find that the Coulomb correlated HF calculations show good qualitative agreement with the present measurements (seen in Fig. 5.8 (b)), specifically in the direction of maximum photoelectron emission. There are, however, significant quantitative discrepancies in the magnitude of β_2 and the sign of β_4 (see Table 5.1). The uncorrelated HF calculations of Ref. [126], in either the length or velocity gauge, compare less favorably with the present measurements (seen in Fig. 5.8 (a)).

In Ref. [113], the two-photon ionization cross sections were calculated using a random phase approximation method with HF wave functions for the initial, intermediate, and target states, neglecting electron-electron correlation. There is reasonable agreement at this photon energy between the calculations in length and velocity gauge (seen in Fig. 5.8 (c)). They both resemble the uncorrelated results in the velocity gauge of Ref. [126] shown in Fig. 5.8 (a). However, there is poor qualitative and quantitative agreement between the uncorrelated theories and the measurement. Despite the quantitative disagreements, the correlated HF results of Ref. [126] suggest that electron-electron correlation is essential in the accurate description of the NOTPSI dynamics of argon.

	β_2	β_4
HF Length [126]	-0.62	-0.18
HF Velocity [126]	-0.13	-0.48
Correlated Length [126]	-0.54	-0.05
Correlated Velocity [126]	-0.48	-0.01
Random Phase Approx. Length [113]	0.03	-0.62
Random Phase Approx. Velocity [113]	0.04	-0.58
Experiment	-0.93	0.25

Table 5.1: The β parameters extracted from the calculations in [126] at a photon energy of 9.3 eV and in [113] at a photon energy of 8.6 eV, and those retrieved from the present measurement.

The discrepancies between the theory in Refs. [126, 113] and the present measurements may be attributed to an inadequate treatment of electron-electron correlation in the calculations. The level of correlation accounted for in the Coulomb correlated HF approach of Ref. [126] led to better gauge invariance and a PAD with greater similarity to the present measurements. This suggests that a higher level of electron-electron correlation must be included for a more accurate description of NOTPSI in argon.

Concluding Remarks

This section reported results on NOTPSI of argon using 3-D momentum imaging and an intense 9.3 eV femtosecond pulse. We find that the observed photoelectron emission pattern can be explained by the interference between the different p and f partial wave components

of the photoelectron scattering wave function, which add destructively along the polarization direction of the ionizing VUV field. Our measurements are compared against a previous set of calculations, which reveal that the photoionization dynamics are evidently influenced by electron-electron correlation effects. It appears that the level of electron-electron correlation accounted for in the Coulomb correlated HF calculations in Ref. [126] is not sufficient to reach complete agreement with the present results. Our measurements can serve as a benchmark for future ab initio theoretical treatments of NOTPSI dynamics in multi-electron systems. A particular challenge may be incorporating continuum-continuum coupling in the calculations, which is expected to be important in reproducing the PAD in non-resonant regions [16]. In addition to further development of theoretical methods, there is a clear need for follow-up experiments to investigate the photon energy dependence of electron-electron correlation effects by angle-resolved photoionization of multi-electron atoms and small molecules, using intense VUV, XUV, and soft X-rays, preferably at photon energies where calculated anisotropy parameters are gauge invariant, and correlated and uncorrelated results differ markedly.

5.2 Diatomic Oxygen

5.2.1 Distinguishing resonance symmetries with energy-resolved photoion angular distributions from ion-pair formation in O_2 following two-photon absorption of a 9.3 eV femtosecond pulse

In this second section, a combined experimental and theoretical study is presented on the photodissociation dynamics of ion-pair formation in O_2 following resonant two-photon absorption of a 9.3 eV femtosecond pulse, where the resulting O^+ ions are detected using 3-D momentum imaging enabled by MISTERS. Ion-pair formation states of $^3\Sigma_g^-$ and $^3\Pi_g$ symmetry are accessed through predissociation of optically dark continuum Rydberg states converging to the B $^2\Sigma_g^-$ ionic state, which are resonantly populated via a mixture of both parallel-parallel and parallel-perpendicular two-photon transitions. This mixture is evident in the angular distribution of the dissociation relative to the light polarization, and varies with the kinetic energy release (KER) of the fragmenting ion-pair. The KER-dependent photoion angular distribution reveals the underlying two-photon absorption dynamics involved in the ion-pair production mechanism and indicates the existence of two nearly degenerate continuum resonances possessing different symmetries, which can both decay by coupling to ion-pair states of the same total symmetry through internal conversion.

Background

Discrete electronic states lying above the first ionization threshold are energetically degenerate with states that are members of a continuous spectrum. Such discrete continuum states

were postulated in the early days of quantum mechanics by figures such as von Neumann and Wigner [118], and were later studied by Fano [56]. The configuration interaction between the discrete and continuous spectra causes such continuum-embedded discrete states to become quasi-bound and thus possess a finite lifetime. The coupling between the resonances and continuum creates a substantial challenge for theoretical descriptions of electronic structure, and on detailed experimental measurements to test those methods.

Many resonances with appreciable scattering amplitude may appear near-by one another energetically, so that the probability of interaction between the photoelectron and the core is highly dependent on the excitation energy. Neighboring continuum resonances may be interacting or non-interacting, depending on their relative positions and widths. If two adjacent resonances are broad, as in the case of shape resonances, they may overlap with each other. When such resonances possess different symmetries, yet combined with the core produce final states of the same total symmetry, the resonances can interfere and result in a rapid change in the electron emission pattern [90]. It is therefore of fundamental interest to identify and characterize neighboring continuum resonances, to better understand their properties, and to distinguish dynamics from quantum inference effects.

Electron-ion resonances in molecules often possess different decay mechanisms that compete, some involving ionization (e.g. autoionization) and others where all electrons remain bound (e.g. predissociation). These processes involve many-electron dynamics and are strongly mediated by electron-electron correlation. In certain instances, discrete continuum states may be predissociated by states that fragment to a cation-anion pair, rather than a neutral pair. When such resonances lie below the first dissociative ionization threshold, they are uniquely situated to be studied through the fragment ions emerging from the decay to the aforementioned ion-pair states. This offers advantages over photoelectron detection, because photoelectrons originate from various channels, such that photoelectrons emerging from autoionization compete with a stronger signal of photoelectrons emerging from direct ionization, leading to overlapping or unresolved photoelectron spectral features. In contrast, the ionic fragments emerge from the ion-pair formation channels, as dissociative photoionization is not energetically accessible (only bound photoionization, generating the parent cation, is possible). Thus any measured photofragment ions must originate from the decay of the resonances, and in this sense, studying the dissociaton of the ion-pair state probes the electron-ion resonances and their decay in the continuum in a clearer manner.

Coupling between ion-pair states and optically allowed continuum resonances has been studied in various molecular systems following photoabsorption and electron impact [35, 28, 111, 159, 123, 99, 65, 11, 49, 108, 172, 85, 87]. Optically forbidden continuum resonances, being more challenging to access, have remained largely unexamined both experimentally and theoretically. While they are not directly accessible by absorption of a single photon, optically dark resonances can be accessed directly by electron or ion impact excitation, and they are therefore relevant to the chemistry of planetary atmospheres and in technologies involving plasmas.

Such dark continuum states can be populated via two-photon absorption, which generally requires intense, ultrashort VUV pulses. If the bandwidth of the VUV excitation pulse is

broad enough to span more than one member of a resonance progression, cation-anion pairs can emerge as dissociation products from different resonances. If the symmetries of two adjacent continuum resonances are different, the excitation pathways leading to them will involve differing combinations of parallel and perpendicular transitions. The symmetry of the resonances and their mode of excitation can be determined through energy- and angle-resolved photofragment ion distributions. As the relative amount of parallel and perpendicular transitions vary with the excitation energy, the photoion angular distribution relative to the polarization of the ionizing field will correspondingly vary with the kinetic energy release (KER), encoding the composition of orientations contributing to the two-photon transition and thus the symmetries of the resonances.

In this section, energy- and angle-resolved measurements of ion-pair production in O_2 following resonant two-photon absorption are presented, where the O^+ ion is detected using 3-D momentum imaging. We use intense femtosecond 9.3 eV VUV pulses to populate ion-pair states of $^3\Sigma_g^-$ and $^3\Pi_g$ symmetry through excitation to optically dark, predissociated, continuum molecular Rydberg states. The variation in the KER-dependent photoion angular distribution maps the molecular orientations contributing to the two-photon transition, and indicates the presence of two narrowly separated continuum resonances of different symmetry that both couple to ion-pair states of the same total symmetry via internal conversion.

Experimental Parameters

The photodissociation dynamics of ion-pair formation in neutral O_2 molecules were investigated using the MISTERS momentum imaging spectrometer, where the cationic fragment produced by resonant two-photon absorption is collected with full 4π solid angle and its 3-D momentum measured on an event-by-event basis. In this measurement, the positive ions were guided by parallel DC electric and magnetic fields with values 12.26 V/cm and 4.55 G, respectively, towards the position- and time-sensitive ion detector (the 120 mm multi-channel plate (MCP) chevron stack with the two-layer quad delay-line anode readout). As has been described, the 3-D momentum of the ion is encoded into its hit position on the detector and its time-of-flight relative to the laser trigger. The time-of-flight distinguishes O^+ fragment ions from O_2^+ parent cations by their mass-to-charge ratio.

For this experiment, the Ti:sapphire near-infrared (NIR) laser system was made to produce 12 mJ, 45 fs pulses at a repetition rate of 50 Hz. These 800 nm pulses were then frequency doubled using the 0.25 mm thick beta-barium borate crystal, and the copropagating NIR and blue fields were then separated using the two dichroic mirrors. As before, the reflected 400 nm photons ($\sim$3.6 mJ, $\sim$50 fs) were used to generate femtosecond VUV pulses via high harmonic generation (HHG) of the fundamental laser light, using our 6 m focusing geometry and the 10 cm long gas cell containing 3 Torr of krypton. Again, the resulting VUV frequency comb was then separated from the 400 nm driving field by reflection from the three Si mirrors near Brewster's angle for the fundamental, suppressing the driving field by a factor of $< 10^{-6}$. For this measurement, the 3rd harmonic (133 nm, 9.3 eV) was selected via transmission through the previously described 0.30 mm thick MgF_2 VUV bandpass fil-

ter (Acton Optics FB130-B-1D.3), totally suppressing the 5th harmonic and above. The femtosecond pulse duration of the 3rd harmonic was also maintained, while temporally separating the residual fundamental pulse from the 3rd harmonic pulse by roughly 850 fs, due to the difference in the group velocity dispersion (GVD) of the window at ω_0 and $3\omega_0$ [2, 94] (see chapter 3). After transmission through the window, we estimated the pulse duration of the 3rd harmonic to be ∼35-40 fs, based on its spectral bandwidth, its estimated attochirp, and the thickness and GVD of the MgF_2 window [2, 141, 143, 94] (again, see chapter 3). The femtosecond 9.3 eV pulses are then back-focused using the f = 15 cm curved mirror into the MISTERS 3-D momentum imaging spectrometer using a protected Al mirror. The pulse energy of the 3rd harmonic on target is approximately 10 nJ, which was measured using a pair of bandpass VUV filters (same as above) and a calibrated photodiode.

The vibrationally cold beam of oxygen molecules was prepared via an adiabatic expansion through the MISTERS 0.03 mm nozzle, which was then collimated by the pair of skimmers. This molecular supersonic jet propagated perpendicular to the focusing VUV beam, where the two intersected in the interaction region of the spectrometer (∼0.01 × 0.01 × 0.20 mm), resulting in a measured ionization rate of approximately 20 Hz by two-photon absorption in the target oxygen molecules. No significant ionization processes due to gas impurities, higher photon energies, or 3-photon transitions were detected.

Theory

Theoretical calculations for this experiment were performed by Robert R. Lucchese at Lawrence Berkeley National Laboratory. Potential energy curves for the states of interest were computed using the MOLPRO program [164]. The one-electron basis set was aug-cc-pVTZ [44, 81]. Additional diffuse functions located at the bond midpoint were added to allow for an accurate representation of Rydberg orbitals [79] including diffuse s-type Gaussians with exponents 0.024624, 0.01125,0.005858, 0.003346, and 0.0020484, p-type Gaussians with exponents 0.01925, 0.009988, 0.005689, 0.003476, and 0.002242, and diffuse d-type Gaussians with exponents of 0.06054, 0.02745, 0.01420, 0.008077, 0.004927. A full valence state averaged complete active space self-consistent field (SA-CASSCF) was computed including the $^3\Sigma_g^-$ ground state of the O_2 molecule and two $^3\Sigma_u^-$, two $^3\Delta_u$, and two of $^3\Pi_u$ symmetry. The orbital space included three σ_g, two π_u, four σ_u, and one π_g orbital. Using these orbitals, internally contracted multireference configuration interaction (ic-MRCI) calculations were performed including single and double excitations from the SA-CASSCF wave function.

The calculated potential energy curves (PECs) for the electronic states relevant to the following discussion are shown in Fig 5.9 (a). The ion-pair PECs are adapted from Ref. [172]. The ion-pair states in the Franck-Condon region, where crossings with the Rydberg states occur, are located at energies above the ground state of the ion. Thus they are metastable and can only be computed using a stabilization type calculation, which can be quite challenging at such a high energy. This type of calculation is beyond the scope of this paper. The X $^3\Sigma_g^-$ ground state of O_2 has the valence electron configuration $(3\sigma_g)^2(1\pi_u)^4(1\pi_g)^2$,

while the two states with the dominant transition amplitudes (shown in Fig 5.9 (b)) are the B $^3\Sigma_u^-$ and E $^3\Sigma_u^-$ states. These states have dominant electron configurations $(3\sigma_g)^2(1\pi_u)^3(1\pi_g)^3$ and $(3\sigma_g)^2(1\pi_u)^4(1\pi_g)^1 3\mathrm{p}\pi_u$, respectively, with configuration interaction between the two [23, 162]. The electron configuration $(3\sigma_g)^1(1\pi_u)^4(1\pi_g)^2(3\sigma_u)^1$ also contributes to both states.

Given the two-photon excitation energy of 18.6 eV (± 0.15 eV), the relevant Rydberg series is that converging to the B $^2\Sigma_g^-$ ionic state, which has the valence electron configuration $(3\sigma_g)^1(1\pi_u)^4(1\pi_g)^2\mathrm{n}\alpha$, where n is the principal quantum number of the Rydberg state and α is the molecular orbital, e.g. σ_g and π_g. This Rydberg series is predissociated by ion-pair states of $^3\Sigma_g$ and $^3\Pi_g$ symmetry, which provide the continuum resonances a decay mechanism that competes with autoionization. These Rydberg states are of the opposite parity to those that have been previously studied in single-photon experiments and calculations, while the same is true for the ion-pair states that they couple to.

The intense VUV pulses in the present experiment are resonant with three electron configurations in O_2, therefore we consider two-photon excitation to occur in the following possible sequences. The first photon transition from the X $^3\Sigma_g^-$ to the B $^3\Sigma_u^-$ and E $^3\Sigma_u^-$ states involves a single electron excitation, either a $\pi_u \rightarrow \pi_g$, $\pi_g \rightarrow 3p\pi_u$, or $\sigma_g \rightarrow \sigma_u$ transition. Of the three electron configurations that result from these transitions, the first two do not provide a likely resonant pathway to the relevant Rydberg series, because a two-electron excitation is required to connect either of these intermediate state configurations to the relevant Rydberg series. Only the $(3\sigma_g)^1(1\pi_u)^4(1\pi_g)^2(3\sigma_u)^1$ configuration, resulting from the $\sigma_g \rightarrow \sigma_u$ transition, correlates with the electron configuration of the continuum resonances associated with the B $^2\Sigma_g^-$ state, in the sense that they connect through a single electron excitation. In this case, Rydberg states with the configurations $(3\sigma_g)^1(1\pi_u)^4(1\pi_g)^2 n\sigma_g$ and $(3\sigma_g)^1(1\pi_u)^4(1\pi_g)^2 n\pi_g$ can be populated via a parallel $\sigma_u \rightarrow \sigma_g$ or perpendicular $\sigma_u \rightarrow \pi_g$ transition, respectively.

From this process of deduction, we arrive at two distinct two-photon pathways that connect with the target continuum Rydberg states, namely:

$$(3\sigma_g)^2(1\pi_u)^4(1\pi_g)^2 \rightarrow (3\sigma_g)^{-1}3\sigma_u \rightarrow (3\sigma_g)^{-1}n\sigma_g \tag{5.5}$$

$$(3\sigma_g)^2(1\pi_u)^4(1\pi_g)^2 \rightarrow (3\sigma_g)^{-1}3\sigma_u \rightarrow (3\sigma_g)^{-1}n\pi_g \tag{5.6}$$

where pathway (1) is a parallel-parallel ($\|$-$\|$) transition, $\sigma_g \rightarrow \sigma_u \rightarrow \sigma_g$, and pathway (2) is a parallel-perpendicular ($\|$-$\perp$) transition, $\sigma_g \rightarrow \sigma_u \rightarrow \pi_g$. Since the intermediate state electron configuration contributes to both the B $^3\Sigma_u^-$ and E $^3\Sigma_u^-$ states and the excitation energy is in an avoided crossing region, the first transition creates a superposition of these two electronic states. The second photon then projects the excitation onto a continuum resonance of $(3\sigma_g)^{-1}\mathrm{n}\sigma_g$ or $(3\sigma_g)^{-1}\mathrm{n}\pi_g$ Rydberg character. Both Rydberg states can decay by autoionization, or through internal conversion to an ion-pair state with the same symmetry.

One-photon photoionization calculations were performed at a fixed geometry with $R_{\text{O-O}} = 1.19$ Å using the Schwinger variational method [148, 151]. The initial state for the excitation to the autoionizing Rydberg state was the B $^3\Sigma_u^-$ state, which at this geometry also has a significant Rydberg character. The autoionizing state was written as a close coupling

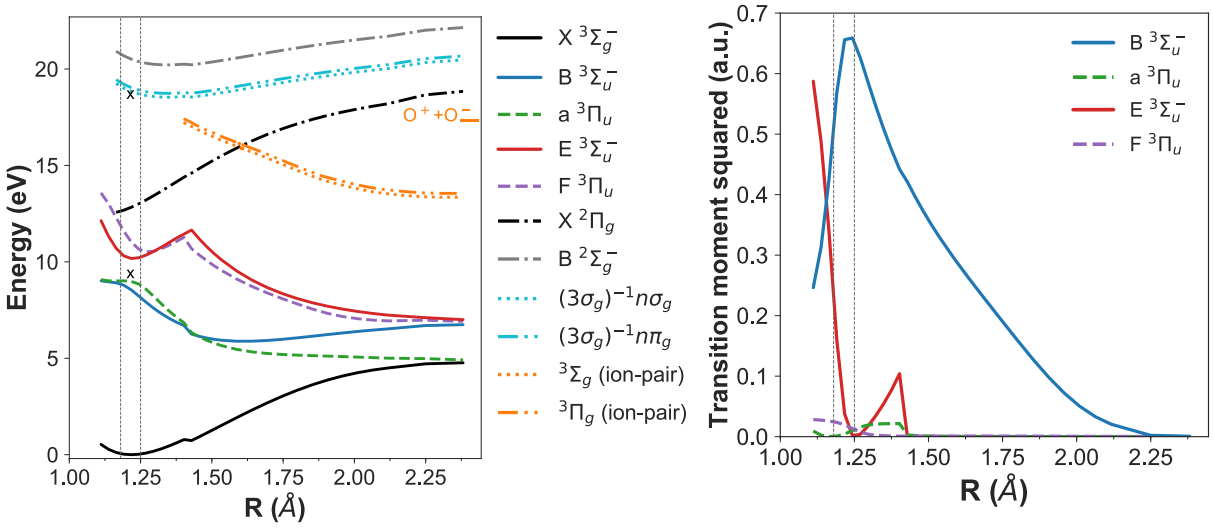

(a) (b)

Figure 5.9: (a) Potential energy curves for relevant states of molecular oxygen, with the one- and two-photon excitation energies indicated by the black x's. (b) The transition dipole moment squared for each of the excited states in the first excitation step. The FC region is indicated by the vertical dashed gray lines in (a) and (b). The dissociative limit for ion-pair production is indicated by the horizontal orange line at 17.3 eV on the right side of the figure in (a).

expansion of antisymmeterized products of continuum orbitals times a set of ion states, which included the X $^2\Pi_g$, a $^4\Pi_u$, A $^2\Pi_u$, b $^4\Sigma_g^-$ and B $^2\Sigma_g^-$ ion states. The ion states and the initial state were computed using the orbitals from the SA-CASSCF calculations disussed above. In each state a full valence configuration interaction calculation was performed using the orbitals from the SA-CASSCF calculations. The positions of these two autoionizing states in Fig. 5.9 (a), shown as the cyan PECs, stem from combining the quantum defect computed in the Schwinger calculation with the ion state energy of the MRCI calculation.

The cross sections of the two calculated resonances are shown in Fig 5.10. The Fano line shapes of these two autoionizing resonances are fit in accordance with the equation Fano proposed in 1961 for a resonance interacting with two or more continua [56],

$$\sigma(\omega) = A + B\left[\frac{(q+\epsilon(\omega))^2}{1+\epsilon(\omega)^2}\right] \tag{5.7}$$

where $\epsilon(\omega) = (\omega - \omega_0)/(\Gamma/2)$. The q parameter, width Γ, and position ω_0 for the Fano profile fits of the two resonances are displayed in Table 5.2. Note the different sign of q for each resonance, which is consistent with the fact that each resonance is a member of a different Rydberg series that belong to continua of different symmetries. Since $q^2 \gg 1$ for

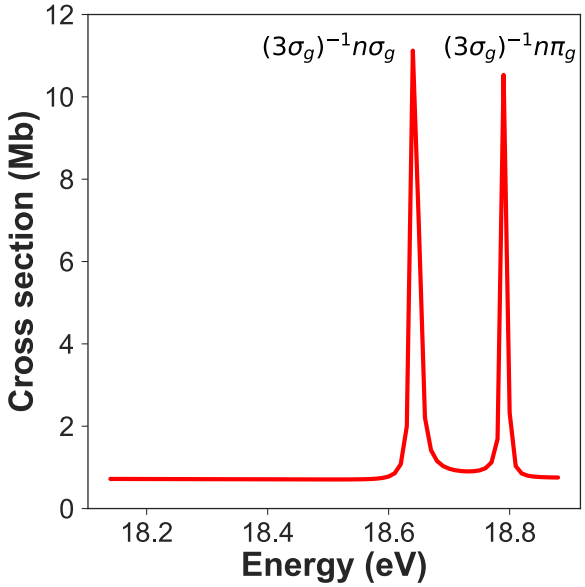

Figure 5.10: The calculated photoionization cross section in the region near the $(3\sigma_g)^{-1}n\sigma_g$ and $(3\sigma_g)^{-1}n\pi_g$ autoionizing resonances.

both resonances, we conclude that direct two-photon coupling is the primary mechanism for populating the two continuum resonances, rather than excitation to the continuum combined with coupling between the continuum and discrete resonances ("intensity borrowing") [131]. We estimate the lifetime of each resonance from its energy width Γ, using the time-energy uncertainty principle, finding lifetimes of 8 fs and 11 fs for the $(3\sigma_g)^{-1}n\sigma_g$ and $(3\sigma_g)^{-1}n\pi_g$ resonances, respectively.

Resonance	q	Γ (meV)	ω_0 (eV)
$(3\sigma_g)^{-1}n\sigma_g$	28.76	82	18.64
$(3\sigma_g)^{-1}n\pi_g$	-45.02	58	18.79

Table 5.2: The Fano line shape fit parameters q, Γ, and ω_0 for the two calculated resonances.

Raw Data

Fig. 5.11 shows the O^+ ion Time-of-Flight spectrum. Here we observe two peaks associated with O^+ ions emerging from dissociation of O_2 following two-photon absorption, where the total distribution is roughly symmetric about a Time-of-Flight of ~7300 ns. The peak at shorter Time-of-Flight emerges from dissociation events where the O^+ ion is directed towards

the ion detector, while the peak at later Time-of-Flight originates from fragmentation events where the O^+ ion is directed away from the ion detector. The ion detector x- and y-hit positions are shown in Fig. 5.11, where O^+ hits from ion-pair production show up as a roughly uniformly filled circle with a radius of approximately 20 mm.

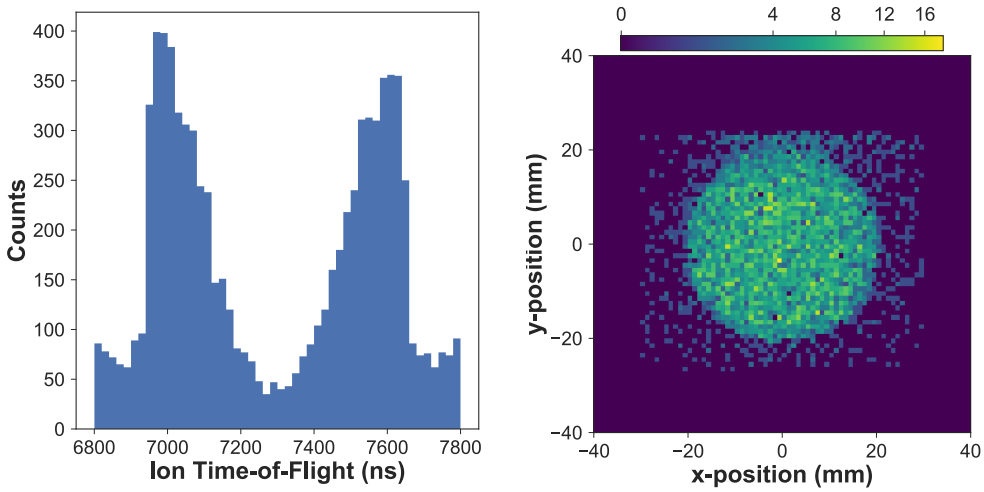

Figure 5.11: The O^+ photoion Time-of-Flight (in nanoseconds) and the x- and y-hit positions (in mm) on the ion detector.

Next we plot the photoion x- and y-hit position as a function of the Time-of-Flight, colloquially known as the ion x-fish and y-fish spectrum. These are shown in Fig. 5.12. In both plots, we observe the feature associated O^+ ions emerging from fragmentation of oxygen molecules upon two-photon absorption, which manifests as the ring structure centered near a 7300 ns Time-of-Flight. This ring feature is anisotropic, where most events lie towards shorter and longer Time-of-Flights. We also plot the O^+ ion hit radius, determined using the x- and y-hit positions, as a function of the Time-of-Flight, colloquially known as the ion wiggle spectrum. This spectrum is also shown in Fig. 5.12. Here the photoion signal is seen as a bright arch, with most of the hits concentrated towards the front and back of the arch structure, while less events appears at larger radii near the center of the arch.

The ring structures seen in the ion x- and y-fish spectra, and the arch feature seen in the ion wiggle spectrum, originate from charged photofragments born in the interaction region with a narrow kinetic energy that is received in the dissociation. The signal largely being concentrated towards shorter and longer Time-of-Flights indicates preferential dissociation along the Time-of-Flight axis, and much less fragmentation occurring perpendicular to this axis. The Time-of-Flight axis coincides with the VUV polarization, hence the features in the ion fish and wiggle spectrum suggest that O^+ emission is enhanced along to the polarization. This will be analyzed and discussed in detail below.

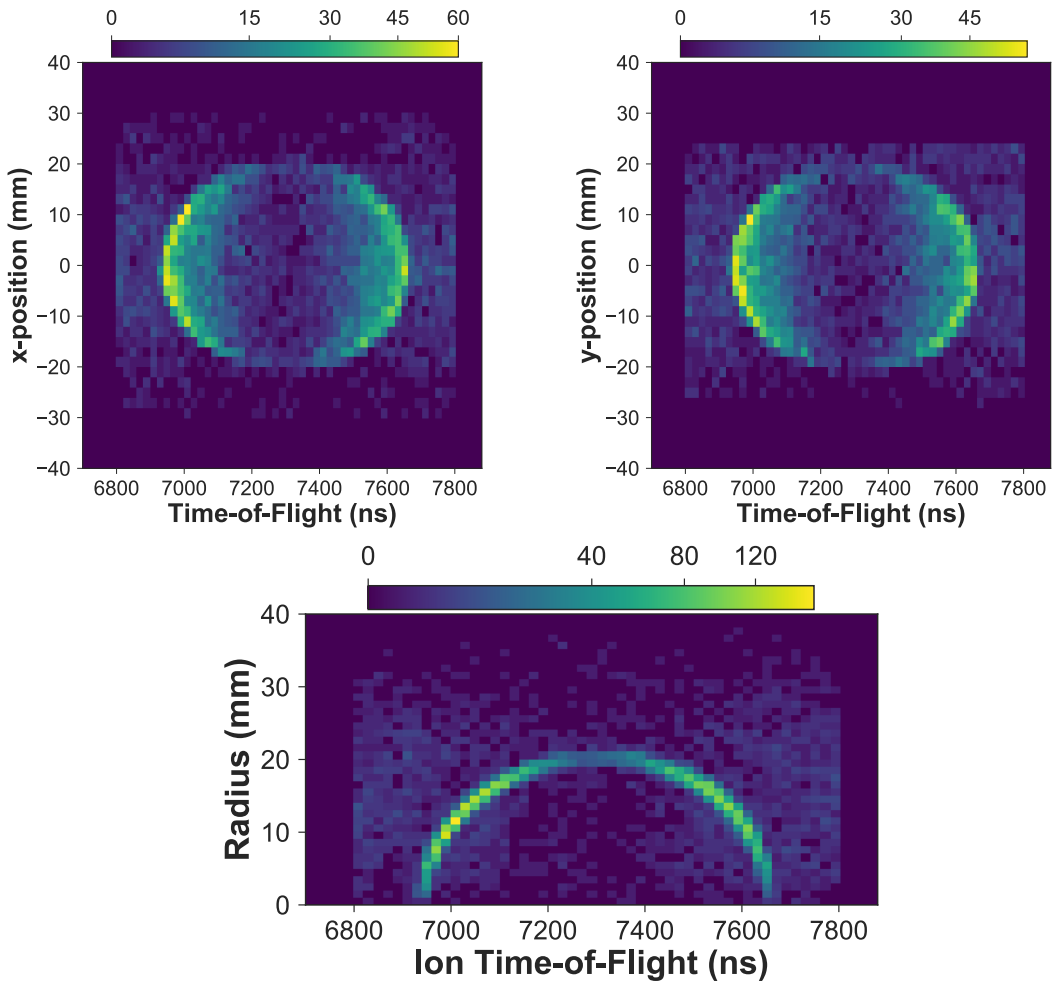

Figure 5.12: The O^+ photoion x- and y-hit positions as a function of the Time-of-Flight (also known as the ion x- and y-fish spectrum), and the O^+ hit radius as a function of the Time-of-Flight (also known as the ion wiggle spectrum).

Reconstructed Momenta and Analysis

We now turn to the analysis of the charged particle momenta (p_x, p_y, p_z), which are reconstructed from the event hit positions and Time-of-Flight (x, y, ToF). The O^+ photoion momentum distributions are seen in Fig. 5.13, where two lab-frame momentum components are plotted against one another, p_x vs p_y, p_x vs p_z, and p_y vs p_z. These distributions show up as ring structures that exhibit increased intensity at larger values along the z-axis. From the reconstructed O^+ photofragment ion momenta, we can next calculate the kinetic energy release of the dissociation and angular distributions. Before doing so, we first provide some

background on the neutral and continuum electronic structure of oxygen and the nature of the ion-pair creation mechanism.

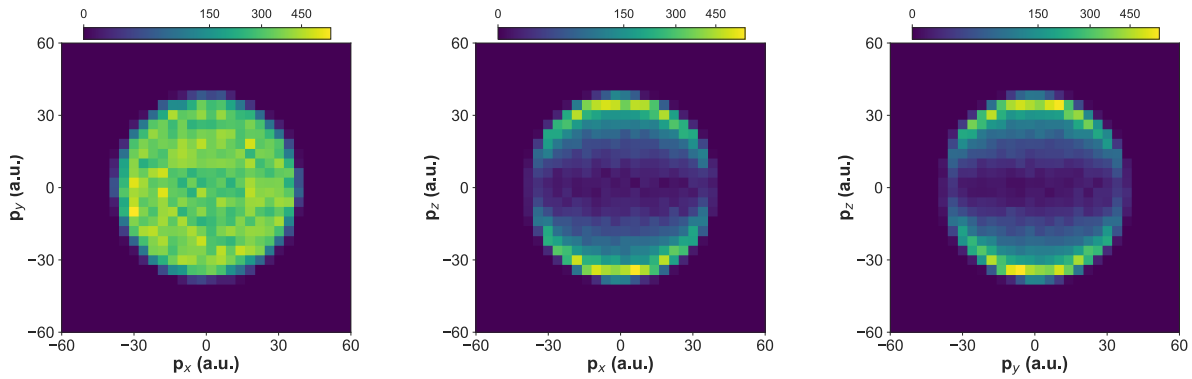

Figure 5.13: The 2-D O^+ photoion momentum distribution plotted in the lab-frame coordinates, which manifest as circular features.

The calculated 130 - 135 nm VUV photoabsorption partial cross sections of Ref. [12] for excitation to the B $^3\Sigma_u^-$ and E $^3\Sigma_u^-$ states are more than an order of magnitude larger than those of the a $^3\Pi_u$ and F $^3\Pi_u$ states at the equilibrium internuclear distance, which is consistent with our calculations shown in Fig 5.9 (b). Thus at these photon energies parallel dipole transitions are strongly favored over perpendicular transitions. Using a sufficiently intense VUV pulse, the B $^3\Sigma_u^-$ and E $^3\Sigma_u^-$ states can be resonantly populated, where a fraction of the excited population can then undergo a second transition driven within the same VUV pulse. In this way, two 9.3 eV photons can access parity-forbidden molecular Rydberg states converging to the B $^2\Sigma_g^-$ state of O_2^+. This second photon transition may be either parallel or perpendicular. These discrete continuum states are predissociated by ion-pair states [11, 123, 35, 65, 172, 85, 111], enabling the molecular orientation during photoabsorption to be captured and by extension the symmetries of the continuum resonances participating. Since this two-photon energy lies below the dissociative ionization threshold [17], any oxygen cations produced must originate from the decay of these continuum resonances into ion-pair channels.

The branching fractions for dissociative ion-pair production (O^+-O^-) versus bound two-photon ionization (O_2^+) is measured to be roughly 22% and 78%, respectively. The adiabatic dissociation limit of the ion-pair states is ∼17.3 eV [85], thus for an excitation energy of 18.6 eV we expect approximately 1.3 eV of KER. The measured KER of the dissociating ion-pair is presented in Fig. 5.14 (a). We observe a single peak centered near 1.26 eV, with a full width at half maximum (FWHM) of ∼150 meV, which is considerably smaller than the two-photon bandwidth (∼300 meV) of the excitation pulse. We attribute the narrow KER to a resonant two-photon excitation of a single vibrational level of either of two predissociated Rydberg states that are nearly degenerate in energy. The width of the

KER distribution corresponds with the widths and spacing of these two narrowly separated resonances, convoluted with the energy resolution of the ion detector, rather than the two-photon bandwidth of the excitation, as the ion-pair states are not directly accessed via a 2-photon transition. According to the reflection approximation, if the dissociative ion-pair states were excited directly, the width of the KER would correspond with the two-photon bandwidth, whereas the measured KER distribution is significantly narrower. Although two resonance peaks can not be resolved in the measured KER alone, we find that the two neighboring continuum states can be distinguished by their symmetry, where different regions of the KER distribution exhibit varying photoion angular distributions. The O^+ photoion momentum distribution transverse versus parallel to the VUV polarization vector is shown in Fig 5.14 (b). Here $p_\perp$ and $p_\parallel$ are the ion momentum components transverse and parallel to the VUV polarization, respectively. The photoion momentum distribution tends to exhibit high longitudinal momentum and low transverse momentum. To differentiate the two continuum resonances by their symmetries, we turn to the photoion angular distribution [170, 43].

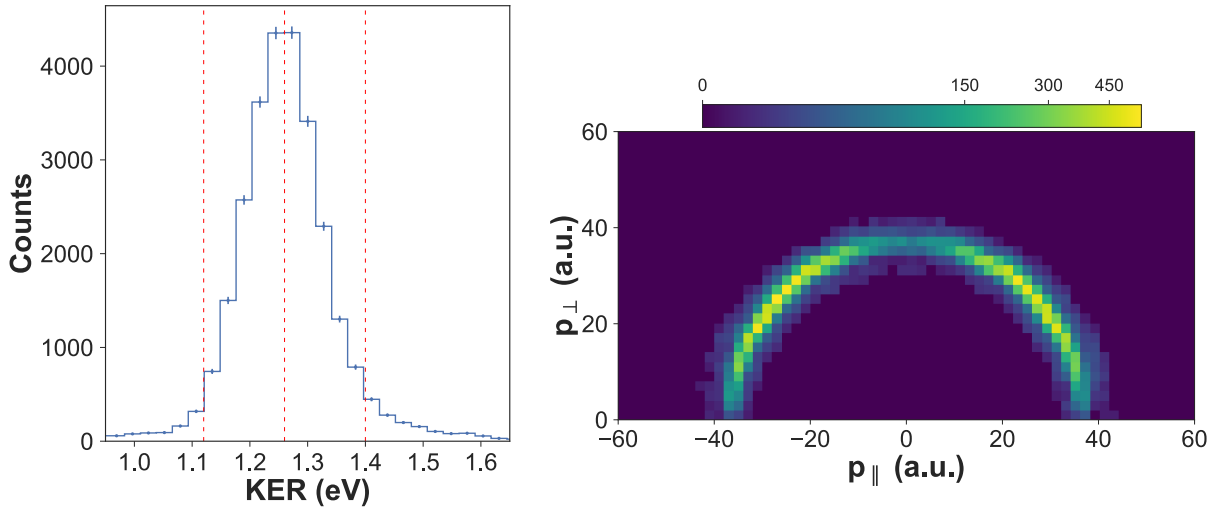

(a) (b)

Figure 5.14: (a) The ion-pair production KER and (b) O^+ momentum distribution parallel versus perpendicular to the VUV polarization. The red dashed vertical lines in (a) indicate two different regions of the KER distribution that are subsequently analyzed.

For two-photon processes, the energy-dependent photofragment angular distribution of a molecule dissociated by linearly polarized light is given by the parameterization:

$$\frac{d^2\sigma}{d\Omega dE} = \frac{\sigma_0(E)}{4\pi}[1 + \beta_2(E)P_2(\cos\theta) + \beta_4(E)P_4(\cos\theta)] \tag{5.8}$$

where σ_0 is the total cross section, θ is the angle between the photoion momentum vector and the polarization vector of the light, E is the kinetic energy release, β_2 and β_4 are the second and fourth order anisotropy parameters, and P_2 and P_4 are the second and fourth order Legendre polynomials in variable $\cos\theta$. The measured energy-integrated angle-differential photoion distribution is presented in Fig 5.15, where the data has been fit (solid red line) in accordance with equation 5.8, using the projection method discussed in [98], and the error on the β parameters determined via statistical bootstrapping [48]. The β parameters retrieved from the fit are β_2 = 1.25±0.01, β_4 = -0.50±0.02.

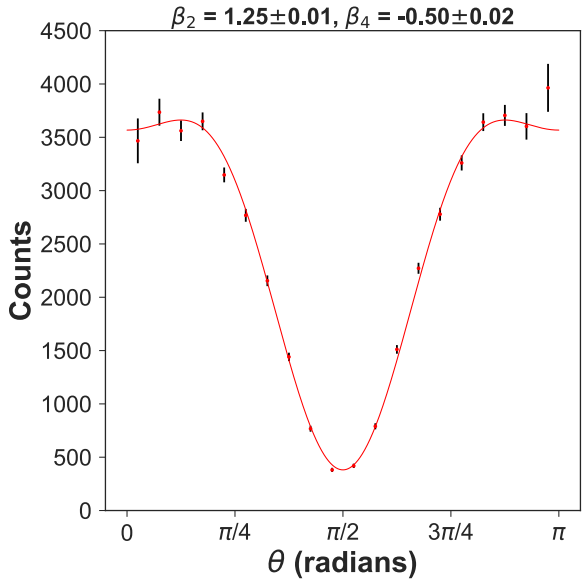

Figure 5.15: The energy-integrated O^+ photoion angular distribution from ion-pair formation in O_2 following resonant two-photon absorption at 9.3 eV. The data is fit using equation (1), where the retrieved β parameters are displayed above the plot.

The negative value of β_4 indicates that there is a ∥-⊥ two-photon transition that connects to the ion-pair formation states, since β_4 is positive for ∥-∥ and ⊥-⊥ transitions [38]. The varying contribution from the ∥-⊥ pathway can be probed by considering different regions of the KER distribution. This is because different regions of the KER distribution correspond with different two-photon excitation energies. As the excitation energy is varied, the scattering cross section for different symmetry autoionizing states can come in and out of resonance. This will lead to a corresponding variation in the β parameters. We divide the momentum distribution into two KER regions, indicated by the red vertical dashed lines in Fig 5.14 (a). These two slices are taken over the KER intervals 1.12 - 1.26 eV and 1.26 - 1.40 eV, where the centers of the two regions are separated by 0.14 eV in energy. The corresponding O^+ photofragment angular distributions for each KER slice and their β parameters are shown

in Fig 5.16.

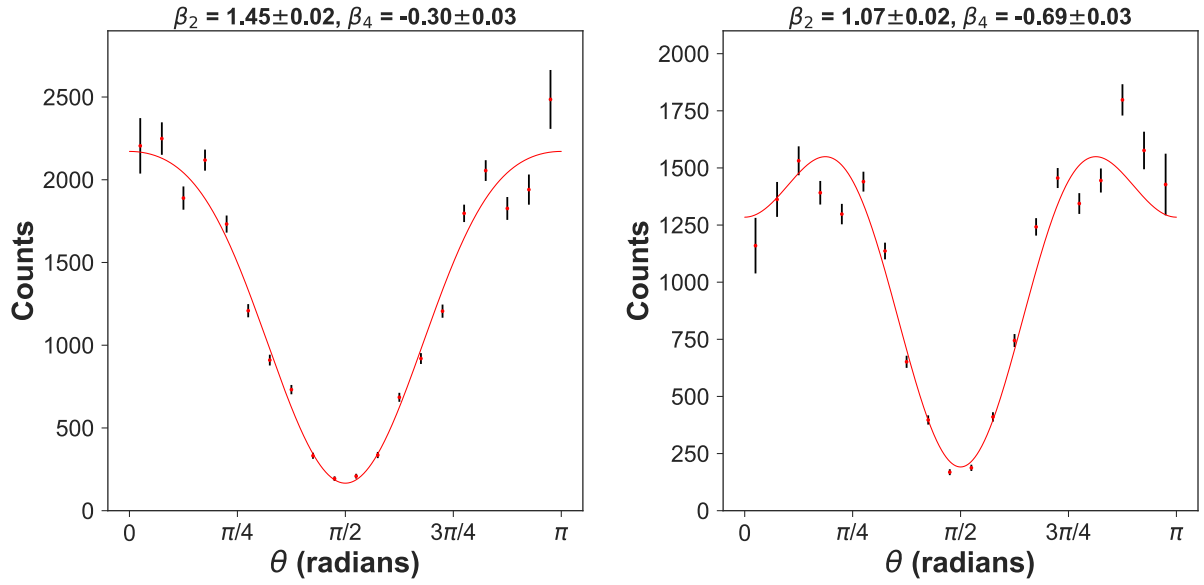

(a) (b)

Figure 5.16: The energy-resolved photoion angular distribution for the O^+ fragment produced from ion-pair formation in O_2 following resonant two-photon absorption at 9.3 eV for the low KER region in (a) and the high KER region in (b). These two KER regions are indicated in Fig 5.14 (a). The data is fit in accordance with equation (1), where the retrieved β parameters are shown above each plot.

The energy-resolved β parameters vary for the two KER slices, with β_2 = 1.45±0.02 and β_4 = -0.30±0.03 for the low KER region, and β_2 = 1.07±0.02 and β_4 = -0.69±0.03 for the high KER region. Here, as the KER increases, both β values decrease, meaning an increase in the relative amount of ∥-⊥ two-photon transitions. Since the high energy region of the KER distribution corresponds with higher excitation energies, the photoion angular distribution indicates the existence of two narrowly spaced continuum resonances possessing different symmetries, one of dominant $(3\sigma_g)^{-1}n\sigma_g$ character and the other with dominant $(3\sigma_g)^{-1}$nπ_g character lying slightly higher in energy. As the energy of the excitation increases, the scattering amplitude of the higher lying resonance increases while that of the lower lying resonance decreases and thus the amount of population decaying through this $(3\sigma_g)^{-1}n\pi_g$ resonance via the ∥-⊥ pathway increases and the population decaying through the $(3\sigma_g)^{-1}n\sigma_g$ resonance via the ∥-∥ pathway decreases. This is reflected by the energy-resolved photoion angular distributions, while the width of the KER distribution indicates these two resonances are nearly degenerate in energy, with a spacing of ∼100 meV. We point out that this analysis is predicated on the validity of the axial recoil approximation,

i.e. prompt dissociation before significant rotation of the molecule. Since the observed dissociation requires a non-adiabatic transition from an autoionizing state to an ion-pair state, this can potentially lead to a violation of this approximation, if the resonance lifetime is not short-lived and comparable to the rotational period of the molecule. However, we note that the lifetimes of the autoioning states are estimated to be much less than 100 fs. Furthermore, given the considerable anisotropy in the measured angular distributions, and significant changes in the anisotropy parameters across the narrow KER distribution, the non-adiabatic coupling apparently occurs on a timescale that is considerably faster than the rotational motion of the molecule, confirming the axial recoil approximation as valid.

Concluding Remarks

In the experiment reported in this second section, we used intense femtosecond 9.3 eV VUV pulses, resonant within the Schumann-Runge continuum, and the 3-D momentum imaging capabilities of the MISTERS endstation to study the decay of metastable, optically dark, continuum resonances in molecular oxygen, which are populated following two-photon absorption. These resonances are parity-forbidden in single-photon experiments, and to our knowledge, have not been studied before experimentally or theoretically. Since scattering through such resonances often weakly competes with the stronger direct ionization process, studying them in detail is challenging. Here, we overcame some of these challenges through the use of photofragment ion detection. A dipole allowed parallel transition to the B $^3\Sigma_u^-$ state is excited by a femtosecond VUV pulse. This valence states mixes with the E $^3\Sigma_u^-$ Rydberg state. A second VUV photon from within the same pulse populates continuum resonances lying below the dissociative ionization threshold, which can decay through to the ion-pair states, interrupting and competing with autoionization. The KER-dependent photoion angular distribution emerges from two optically dark, narrowly separated continuum resonances of different symmetry and reveals that these resonances are excited by $\parallel$-$\parallel$ and $\parallel$-$\perp$ two-photon transitions, where both decay by coupling to the ion-pair formation states of the same total symmetry via internal conversion. This work demonstrates that energy- and angle-resolved fragment ion momentum imaging can be highly sensitive to the symmetry of predissociating electronic states in the ionization continuum.

5.3 Diatomic Nitrogen

5.3.1 Energy- and angle-resolved non-resonant one-color two-photon ionization of N_2 using 9.3 eV femtosecond pulses

In this third and final section, an experimental and theoretical energy- and angle-resolved study on the photoionization dynamics of non-resonant one-color two-photon single valence ionization of neutral N_2 molecules is presented. Using 9.3 eV photons produced via high

harmonic generation and the MISTERS 3-D momentum imaging spectrometer, we detect the photoelectrons and ions produced from one-color two-photon ionization in coincidence. Photoionization of N_2 populates the X $^2\Sigma_g^+$, A $^2\Pi_u$, and B $^2\Sigma_u^+$ ionic states of N_2^+, where the photoelectron angular distributions associated with the X $^2\Sigma_g^+$ and A $^2\Pi_u$ states both vary with changes in photoelectron kinetic energy of only a few hundred meV. We attribute the rapid evolution in the photoelectron angular distributions to the excitation and decay of dipole-forbidden autoionizing resonances that belong to series of different symmetries, all of which are members of the Hopfield series, and compete with the direct two-photon single ionization.

Background

The photoionization continuum of molecular nitrogen posses both one- and two-electron resonances, i.e. shape resonances and autoionizing states, which can strongly influence the behavior of ejected photoelectrons. The observable that is most sensitive to these resonance effects is the energy-resolved photoelectron angular distribution (PAD). In the case of single photon ionization these resonance effects have been studied extensively both experimentally and theoretically [98, 150, 102, 103, 72, 130, 35, 28, 133, 125, 71, 84, 168, 129, 128]. However, due to its complexity, non-resonant two-photon ionization has received far less attention, while it provides the opportunity to observe the effect of discrete continuum states on the angular distributions of the photoelectrons and ions that are symmetry- and/or parity-forbidden in single photon excitation schemes [92]. Moreover, two-photon absorption resulting in single ionization is particularly sensitive to resonance and electron-electron correlation effects [91].

The presence of continuum-embedded discrete states can lead to interference effects, a paradigmatic example being the Fano resonance, where the scattering amplitudes of a resonant (discrete) and background (continuum) process interfere to give rise to the classic asymmetric line shape [56]. In photoionization, continuum states that decay via autoionization can provide an indirect channel to target states that can interfere with the direct ionization channel to those very same states [16, 47, 75, 137, 172]. This effect can be observed in a PAD [47, 121, 136], where the amplitudes and phases of the angular momentum components of the photoelectron scattering wave function from direct ionization interfere with those of the electron originating from autoionization.

The dipole oscillator strength of N_2 across most of the VUV photon energy range is quite weak, as the states that lie below $\sim$12 eV are dipole-forbidden transitions, because of either spin- or parity-conservation. Within the ionization continuum and below the B $^2\Sigma_u^+$ ionic state (situated at 18.74 eV in the Franck-Condon (FC) region) lies the Hopfield series of N_2 [68], a progression of narrow resonances emerging from continuum molecular Rydberg states converging to the B $^2\Sigma_u^+$ ionic state. Such quasi-bound states can decay through autoionization, where these two-electron resonances provide an indirect channel to the X $^2\Sigma_g^+$ and A $^2\Pi_u$ ionic states, along with the direct ionization channel to those very same

target states. By choosing a suitable photon energy, these autoionizing states can thus be populated and studied via non-resonant one-color two-photon ionization.

In this third section, experimental and theoretical results on energy- and angle-resolved Non-resonant One-color Two-Photon Single Ionization (NOTPSI) of molecular nitrogen using 3-D momentum imaging are presented, where the photoelectron and molecular cation are measured in coincidence. Using a 400 nm driving field, we produce and select VUV photons with an energy of 9.3 eV via High Harmonic Generation (HHG), which are then used to singly ionize the target via two-photon ionization. We observe that the energy-resolved PADs associated with the X $^2\Sigma_g^+$ and A $^2\Pi_u$ ionic states both vary appreciably with small changes in the photoelectron kinetic energy. We ascribe these effects to the excitation and decay of dipole-forbidden autoionizing resonances belonging to series possessing different total symmetries, which, in addition to the direct ionization channel, provide an indirect pathway to the target states.

Experimental Parameters

The valence photoionization dynamics in neutral N_2 were investigated again using the MISTERS experimental endstation, where the photoelectrons and cations produced by NOTPSI are collected with full 4π solid angle, and their 3-D momenta are measured in coincidence on an event-by-event basis. In this measurement, the charged particles were guided by parallel DC electric and magnetic fields with values of 11.34 V/cm and 4.0 G, respectively, towards the two position- and time-sensitive detectors at opposite ends of the 3-D momentum imaging spectrometer. As has been described, the electron and ion detectors are a three layer hex-anode with a 80 mm MCP stack and a two layer quad-anode with a 120 mm MCP stack, respectively, where a charge carrier's 3-D momentum is encoded into its hit position on the detector and its time-of-flight relative to the laser trigger.

For this experiment, near-infrared (NIR) laser pulses (12 mJ, 45 femtoseconds, 800 nm) from the 50 Hz Ti:sapphire laser system were frequency doubled using the 0.25 mm thick BBO crystal, and the copropagating NIR and blue fields were separated using the two dichroic mirrors. Once again, the reflected 400 nm photons ($\sim$3.6 mJ, $\sim$50 fs) were used to generate femtosecond VUV pulses via HHG in the loose f = 6 m focusing geometry, using the 10 cm long gas cell containing 2 Torr of krypton. As before, the resulting VUV frequency comb is then separated from the 400 nm driving field by reflection from three Si mirrors near Brewster's angle for the blue light. In this measurement, the 3$^{\text{rd}}$ harmonic (133 nm, 9.3 eV) was selected via transmission through the 0.25 mm thick MgF_2 window. This totally suppressed the 5$^{\text{th}}$ harmonic and above, maintained the femtosecond pulse duration of the 3$^{\text{rd}}$ harmonic, and separated the residual 400 nm pulses from the 3$^{\text{rd}}$ harmonic pulse temporally by roughly 700 fs (see chapter 3). After transmission through the window we estimate the pulse duration of the 3$^{\text{rd}}$ harmonic to be $\sim$30 fs. The femtosecond 9.3 eV pulses were then back-focused using the f = 15 cm curved mirror into the 3-D momentum imaging spectrometer using the protected Al mirror (43% reflectance at 9.3 eV, see [89]). The pulse

energy of the 3rd harmonic on target was approximately 10 nJ, and was measured in the same fashion as in the previous two sections.

A rotationally and vibrationally cold beam of nitrogen molecules (approximately 80 K) was prepared via an adiabatic expansion through the MISTERS 0.03 mm nozzle, which was then collimated by the pair of skimmers. Just as before, this molecular jet propagated perpendicular to the focused VUV beam, where the two intersected in the interaction region of the spectrometer ($\sim$0.01 $\times$ 0.01 $\times$ 0.20 mm), resulting in NOTPSI of the target molecules at an average rate of of $\sim$0.3 events per VUV pulse.

Theory

Theoretical calculations were performed by Roger Y. Bello, a postdoc in the group of C. William McCurdy. The potential energy curves of the neutral N_2 states relevant to this study were computed using the multi-reference configuration interaction (MRCI) capability of MOLPRO [165, 163], with single- and double excitations from an active space including four σ_g, four σ_u, two π_u and two π_g orbitals, with the $1\sigma_g$ and $1\sigma_u$ core orbitals always doubly occupied. These orbitals were optimized using a state averaged complete active space self-consistent field (CASSCF) calculation with one state of each symmetry, $^1\Sigma_g^+$, $^1\Pi_u$, $^1\Sigma_u^-$, and $^1\Delta_u$, included. The one-electron basis set was aug-cc-pVTZ [45, 82], augmented by four s, four p, and four d Rydberg diffuse functions [78] centered at the bond midpoint.

One-photon ionization cross sections and photoelectron β parameters were calculated at a fixed internuclear distance $R = 2.07$ a.u. using a multichannel configuration interaction method (MCCI) [149, 152]. The scattering state at a fixed energy is represented on a single-center expanded grid, with a partial wave expansion up to $l_{max} = 80$. The full N-electron scattering state was then written as a close-coupling expansion containing a sum of the products of $(N-1)$-electron ion state wave functions multiplied with one-electron photoelectron wave functions. The lowest eight ion states were included in the close-coupling expansion. The initial and ion states were computed performing a numerical CAS-CI using the orbitals from the CASSCF discussed above. We considered as the intermediate state for ionization the $b^1\Pi_u$ ($2\sigma_u \rightarrow 1\pi_g$) valence state shown in Fig. 5.17, which is the first dipole allowed excited state of N_2 lying at $\sim$13.5 eV above the ground state [25, 42]. The three lowest ionization thresholds of N_2 were found to be $\sim$15.6 eV, $\sim$17.1 eV and $\sim$18.8 eV corresponding to ionization into the $X^2\Sigma_g^+$, $A^2\Pi_u$, and $B^2\Sigma_u^+$ N_2^+ ionic states, respectively.

Two-photon single ionization β_2 and β_4 anisotropy parameters, have been calculated within the time-independent second order perturbation theory framework [39, 37, 120, 22, 6]. We have assumed a resonant transition to the $b^1\Pi_u$ excited state as the first photon absorption. The dipole couplings between the ground state and the intermediate state have been calculated using MOLPRO.

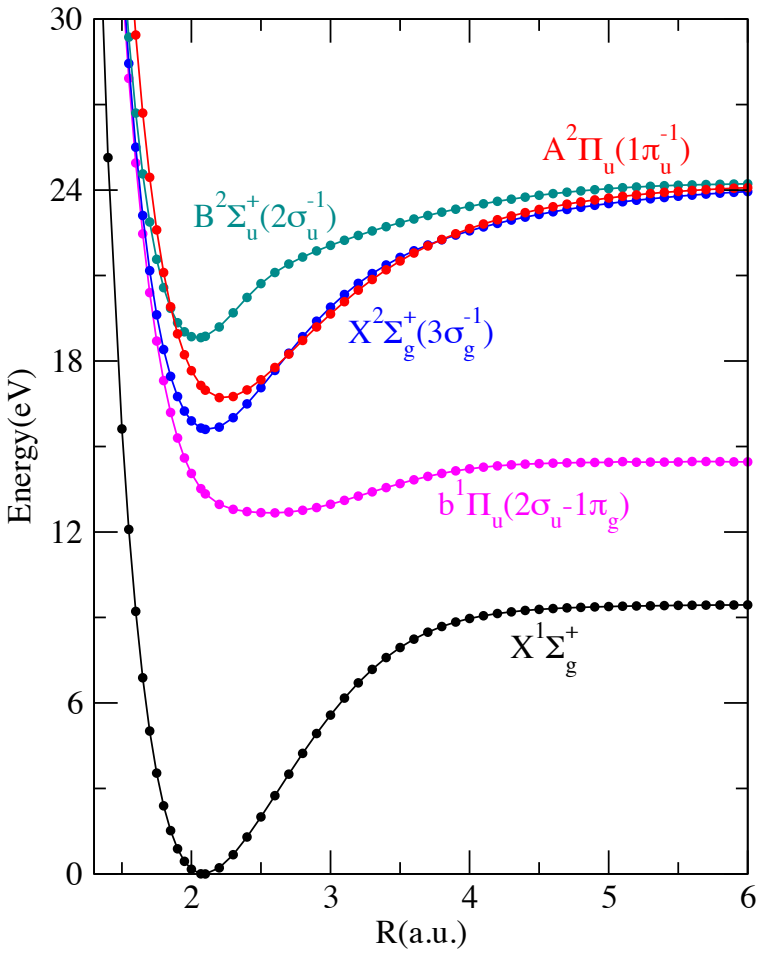

Figure 5.17: Relevant potential energy curves of N_2 and N_2^+. The figure shows the lowest $^1\Pi_u$ state of N_2 as well as the lowest three states of N_2^+.

Reconstructed Momenta and Analysis

The measured photoelectron energy spectrum is presented in Fig. 5.18(a), where we observe three peaks centered near 2.88 eV, 1.63 eV, and 0.15 eV, corresponding with the X $^2\Sigma_g^+$, A $^2\Pi_u$, and B $^2\Sigma_u^+$ ionic states of molecular nitrogen, respectively. The two-photon excitation energy and bandwidth is ∼18.6 eV and ∼300 meV, respectively. We point out that although our central two-photon energy lies below the ionization threshold of the B $^2\Sigma_u^+$ ionic state, the two-photon bandwidth of the excitation pulse enables its lowest vibrational level to be accessed. The X $^2\Sigma_g^+$ and A $^2\Pi_u$ state peaks are partitioned into two and three different photoelectron kinetic energy regions, respectively, for subsequent analysis. The horizontal black and red lines in Fig. 5.18(a) indicate the high and low energy regions, respectively,

while the horizontal blue line indicates a middle energy region that is considered in the case of the A $^2\Pi_u$ ionic state. The X $^2\Sigma_g^+$ state energy slices range from 2.50–2.85 eV and 2.85–3.20 eV, while the A $^2\Pi_u$ state slices span 1.18–1.64 eV, 1.41–1.83 ev, and 1.65–2.03 eV. These regions capture photoelectrons emerging from ionization events to different target state vibrational levels. The vertical green line segments in Fig. 5.18(a) indicate the energetic locations of the relevant vibrational levels of the X $^2\Sigma_g^+$ and A $^2\Pi_u$ ionic states and their corresponding FC factors [168]. In the X $^2\Sigma_g^+$ state, the high energy region roughly corresponds with photoionization to the ν=0 level of the target, and the low energy region captures photoionization to the $\nu = 1$ level. In the A $^2\Pi_u$ state, the high energy slice roughly corresponds with populating the $\nu = 0$, 1 vibrational levels of the target, the middle energy slice with the $\nu = 1$, 2, 3 levels, and the low energy slice with the $\nu = 2$, 3, 4 levels. Most of these slices sum over two or three vibrational levels, as the two-photon bandwidth, energy resolution, and statistics do not permit a fully vibrationally resolved measurement.

The photoelectron momentum distributions for the transverse and parallel momentum components with respect to the VUV polarization vector for the three ionic states are shown in Fig. 5.18(b). Here we see three arcs of differing photoelectron momentum, corresponding to each of the three populated molecular ionic states. To gain more insight into the photoelectron emission pattern for each of these three ionic states, we turn to the angle-differential photoionization cross section.

For two-photon ionization processes the energy-dependent angle-differential photoionization cross section of a target by linearly polarized light is given by

$$\frac{d^2\sigma}{d\Omega dE} = \frac{\sigma_0(E)}{4\pi}[1 + \beta_2(E)P_2(\cos\theta) + \beta_4(E)P_4(\cos\theta)], \tag{5.9}$$

where σ_0 is the total photoionization cross section, θ is the angle between the photoelectron momentum vector and the polarization vector of the light, E is the photoelectron kinetic energy, β_2 and β_4 are the second and fourth order anisotropy parameters, and P_2 and P_4 are the second and fourth order Legendre polynomials in variable $\cos\theta$. The measured energy-integrated angle-differential photoionization amplitude for each of the X $^2\Sigma_g^+$, A $^2\Pi_u$, and B $^2\Sigma_u^+$ ionic states are presented in Fig. 5.19(a), (b), and (c), respectively. The data has been fitted (solid red line) in accordance with equation (1), using the projection method discussed in [97], while the error on the β parameters was determined via statistical bootstrapping [48].

The PADs associated with the X $^2\Sigma_g^+$ and A $^2\Pi_u$ ionic states depicted in Fig. 5.19(a) and (b) both exhibit peak intensity along the VUV polarization, more dramatically in the case of the X $^2\Sigma_g^+$ state, whereas the A $^2\Pi_u$ state PAD is more isotropic. The PAD associated with the B $^2\Sigma_u^+$ state in Fig. 5.19(c) appears bimodal in shape with two photoelectron emission peaks roughly perpendicular to the VUV field, each slightly offset to opposite sides of $\pi/2$. The energy-integrated β parameters associated with these three ionic states can all be found in Table 5.3.

In Fig. 5.20 we show the energy-resolved PADs associated with the X $^2\Sigma_g^+$ ionic state, where we compare the low photoelectron energy portion with the high energy portion, indi-

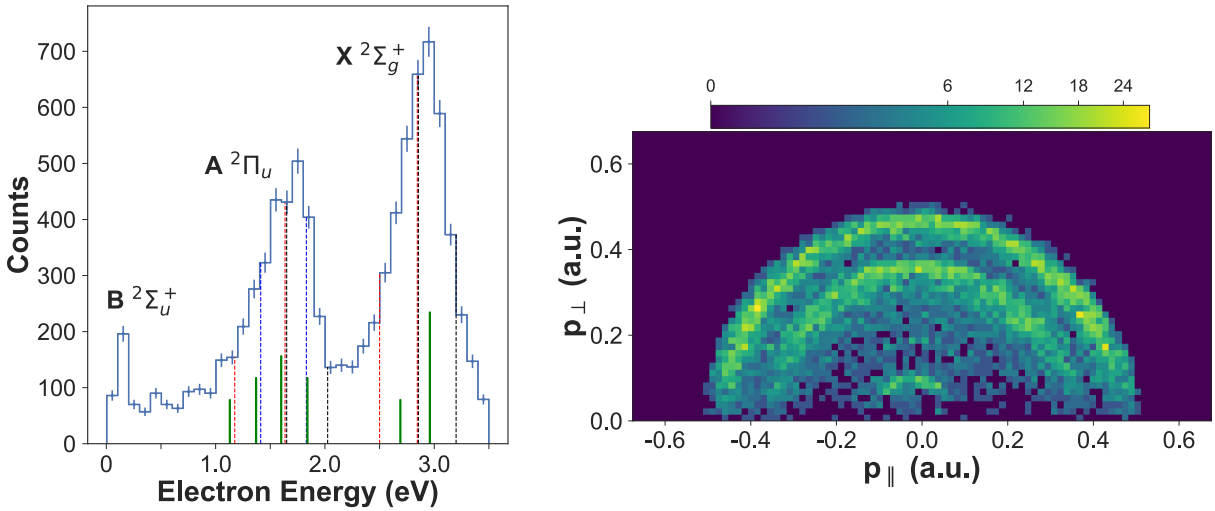

(a) (b)

Figure 5.18: (a) The measured photoelectron energy spectrum for NOTPSI of N_2. The colored horizontal lines indicate different energy regions of the X $^2\Sigma_g^+$ and A $^2\Pi_u$ states that are subsequently analyzed. The vertical green lines roughly indicate the location of the relevant vibrational levels of the two ionic states and their corresponding one-photon oscillator strengths. (b) Photoelectron momentum distribution parallel and perpendicular to the VUV polarization.

State	β_2	β_4
X $^2\Sigma_g^+$	0.91±0.04	0.32±0.06
A $^2\Pi_u$	0.30±0.04	0.05±0.06
B $^2\Sigma_u^+$	-0.38±0.11	-0.36±0.16

Table 5.3: The anisotropy (β) parameters retrieved from fitting the energy-integrated photoelectron angular distributions shown in Fig. 5.19 according to equation (1) for the X $^2\Sigma_g^+$, A $^2\Pi_u$, and B $^2\Sigma_u^+$ states of N_2^+.

cated by the red and black horizontal lines in Fig. 5.18(a). The energy-resolved β parameters for the X $^2\Sigma_g^+$ ionic state can be found in Table 5.4. We find that the PADs vary between the two regions, where β_2 undergoes a slight decrease in value, while β_4 increases by more than a factor of 2, as the photoelectron kinetic energy increases. Here, the high electron energy PAD in Fig. 5.20(b) exhibits a broader minimum perpendicular to the VUV polarization vector than the low energy PAD in Fig. 5.20(a).

In Fig. 5.21 we show the energy-resolved PADs associated with the A $^2\Pi_u$ ionic state,

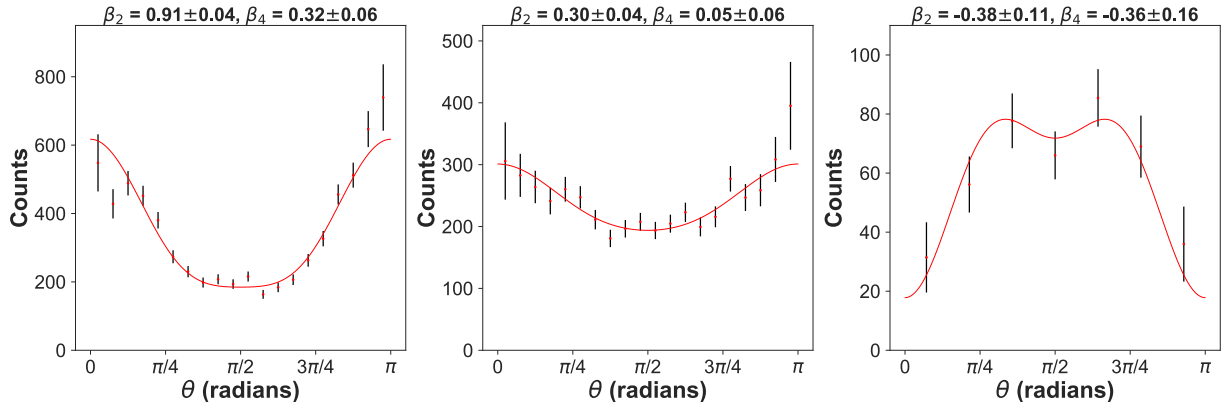

Figure 5.19: The energy-integrated photoelectron angle-differential photoionization cross section for NOTPSI of N_2 to the first three ionic states, (a) the X $^2\Sigma_g^+$ state, (b) the A $^2\Pi_u$ state, and (c) the B $^2\Sigma_u^+$ state. The data are fitted using equation (1), where the retrieved β parameters are displayed above each plot.

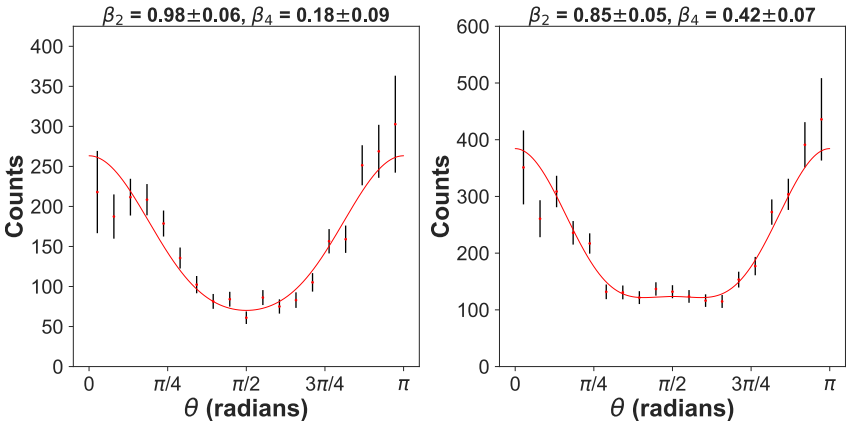

Figure 5.20: The energy-resolved photoelectron angle-differential photoionization cross sections of N_2 following NOTPSI. Depicted is the photoelectron angular distribution for the X $^2\Sigma_g^+$ ionic state for two different energy regions in the photoelectron spectrum, indicated in Fig. 5.18, with the low kinetic energy region shown in (a) and the high energy region in (b). The data are fitted using equation (1), where the retrieved β parameters are shown above each plot.

where we compare the low, middle and high energy regions, indicated by the red, blue and black horizontal lines in Fig. 5.18(a), respectively. The energy-resolved β parameters

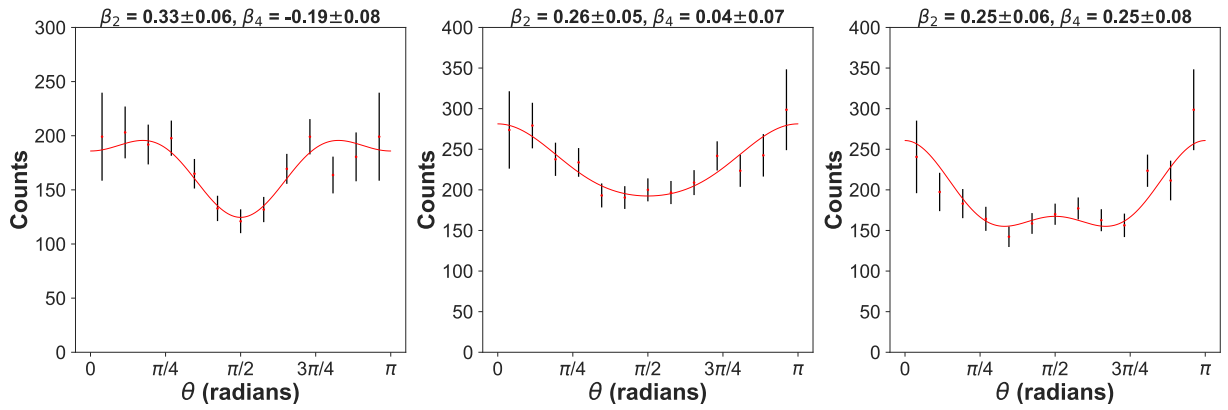

Figure 5.21: The energy-resolved photoelectron angle-differential photoionization cross sections of N_2 following NOTPSI. Depicted is the photoelectron angular distribution for the A $^2\Pi_u$ ionic state for three different energy regions in the photoelectron spectrum, indicated in Fig. 5.18, with the low kinetic energy region shown in (a), the middle energy region in (b), and the high energy region in (c). The data are fitted using equation (1), where the retrieved β parameters are shown above each plot.

State	Photoelectron Energy (eV)	β_2	β_4
X $^2\Sigma_g^+$	2.50–2.85	0.98±0.06	0.18±0.09
	2.85–3.20	0.85±0.05	0.42±0.07
A $^2\Pi_u$	1.18–1.64	0.33±0.06	-0.19±0.08
	1.41–1.83	0.26±0.05	0.04±0.07
	1.65–2.03	0.25±0.06	0.25±0.08

Table 5.4: The anisotropy (β) parameters retrieved from fitting the energy-resolved photoelectron angular distributions according to equation (1) for the X $^2\Sigma_g^+$ and A $^2\Pi_u$ ionic states of N_2, shown in Fig. 5.20 and Fig. 5.21.

associated with the A $^2\Pi_u$ ionic state can be found in Table 5.4. The PADs vary appreciably between the three slices, where β_2 slightly decreases in value, while β_4 increases in value dramatically and undergoes a sign change, as the photoelectron kinetic energy increases. The high energy PAD in Fig. 5.21(c) exhibits maxima parallel to the ionizing field and a smaller peak perpendicular to the field, while the low energy PAD in Fig. 5.21(a) shows a minimum perpendicular to the ionizing field and a smaller minimum parallel to the field. The middle energy PAD in Fig. 5.21(b) resembles the energy-integrated PAD of Fig. 5.19(b), exhibiting a shallow minimum perpendicular to the VUV polarization vector.

For both states, the variation in the retrieved β_2 asymmetry parameter is not particularly

significant, while the change in the β_4 parameter is more substantial. This is most striking in the A $^2\Pi_u$ state, where the value of β_4 changes sign, resulting in an appreciable variation in the PAD across the different photoelectron kinetic energy regions. Such a strong energy dependent variation in the PAD is unlikely to stem from the effect of the final vibrational level on the scattering wave function, as the two-photon bandwidth exceeds the spacing of the vibrational levels in the cationic states, where the two-photon bandwidth is ∼300 meV, while the level spacing in the A $^2\Pi_u$ ionic state is ∼230 meV [168]. Further, the different photoelectron energy regions considered here average over a family of adjacent vibrational levels, which should wash out the effect of the vibrational level on the photoelectron scattering wave function (i.e. our energy-resolved PADs integrate over numerous levels). Previous theoretical one-photon studies on the effect of the vibrational level of the target state of the photoelectron asymmetry parameter have indicated that the effect is negligible in the A $^2\Pi_u$ state [129], where we observe the strongest variation in the PAD. These effects are also unlikely to emerge from the shape resonance in the photoionization continuum of N_2 alone, as its peak is far higher in photoelectron kinetic energies (∼32 eV) than the kinetic energies of the electrons corresponding to the populated continuum states in the present work.

In order to better understand the experimental findings, in particular the rapid evolution in the measured PADs that are associated with the $A^2\Pi_u$ ionic state, we have performed one-photon single ionization calculations from a selected excited state of neutral N_2. We chose the $b^1\Pi_u$ state, which is the lowest dipole-allowed electronic state lying ∼13.5 eV above the N_2 ground-state. The total one-photon ionization cross sections from the N_2 ($b^1\Pi_u$) state along with the corresponding photoelectron β parameters for the $^1\Sigma_g^+$, $^1\Pi_g$, and $^1\Delta_g$ dipole-allowed total symmetries are shown in Figs. 5.23, 5.24, and 5.25, respectively. All these symmetries have to be taken into account, as our experiment probes randomly oriented molecules, and the two-photon energy lies below the dissociative ionization threshold, preventing the molecular orientation at the instant of photoionization from being determined without prealignment. The cross sections were calculated at a single fixed nuclear geometry over an energy range between 17.4 eV and 18.7 eV, where the $X^2\Sigma_g^+$ and $A^2\Pi_u$ ionic states are accessible (see Fig. 5.17).

The photoionization cross section in each symmetry exhibits a collection of structures that can be attributed to the Hopfield series of autoionizing states converging to the $B^2\Sigma_u^+$ state of the ion. The Hopfield series has been previously studied, theoretically and experimentally, in the one-photon ionization from the N_2 ground state leading to $^1\Sigma_u^+$ and $^1\Pi_u$ final symmetries. In contrast, the corresponding photoionization cross sections from an excited state of N_2 have not been reported theoretically to the best of our knowledge. These Rydberg states decay, via autoionization, to the $X^2\Sigma_g^+$ and $A^2\Pi_u$ ionic states, providing an alternative ionization path as depicted in Fig. 5.22. Two different series, np and nf, have been assigned in the cross sections using the Rydberg equation

$$E_n = (IP) - \frac{R}{(n-\delta)^2}, \tag{5.10}$$

where E_n represents the energy of the autoionizing state, R is the Rydberg constant,

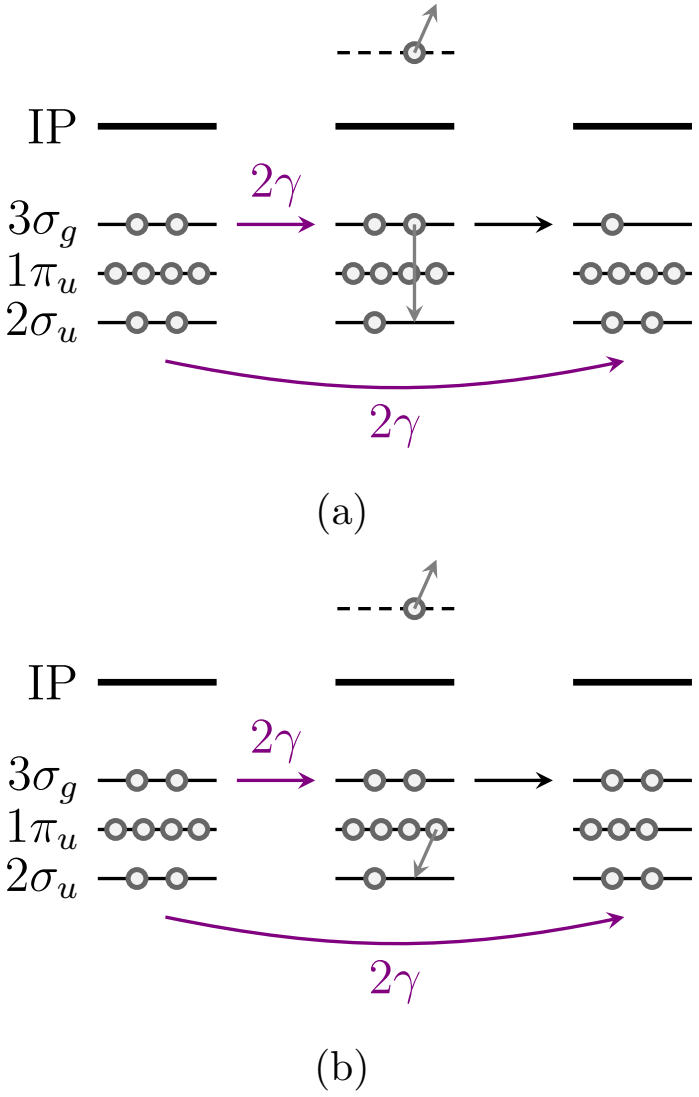

Figure 5.22: An energy level diagram depicting the direct and indirect two-photon single ionization pathways to the X $^2\Sigma_g^+$ ionic state of N_2 seen in (a), and the A $^2\Pi_u$ ionic state seen in (b). The intermediate state in both the indirect pathways is a continuum molecular Rydberg state converging to the B $^2\Sigma_u^+$ ionic state, which decays through autoionization.

n is the principal quantum number of the Rydberg electron, and δ is the quantum defect, which depends on the angular momentum l. For $l = 0$ a large quantum defect, i.e. $\delta \sim 1$, is expected while δ decreases rapidly as l increases such that nd and nf series ($l = 2, 3$) are characterized by $\delta \sim 0$.

While the np and nf series coexist in the $^1\Sigma_g^+$ and $^1\Pi_g$ symmetries, seen in the upper

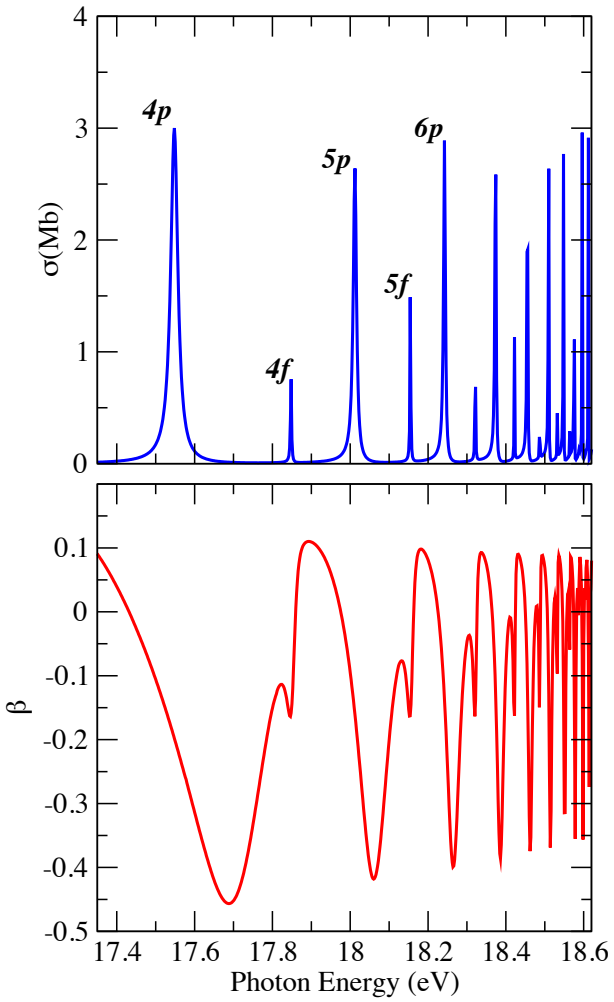

Figure 5.23: Upper panel: Total photoionization cross section from the N_2 ($b^1\Pi_u$) state between the second ($A^2\Pi_u$) and third ($B^2\Sigma_u^+$) ionization thresholds, while leaving the system in $^1\Sigma_g^+$ final symmetry. The nl labels indicate the $np\sigma_u$ and $nf(\delta_u$ or $\sigma_u)$ series of the autoionizing states converging to the N_2^+ ($B^2\Sigma_u^+$) cation state. Lower panel: Corresponding photoelectron asymmetry parameter for the one photon transition.

panel of Fig. 5.23 and 5.24, only the nf is visible in the $^1\Delta_g$ symmetry, seen in the upper panel of Fig. 5.25. The np series, σ_u or π_u, are characterized by a slightly different quantum defect, $\delta \sim 0.56$ or $\delta \sim 0.66$, respectively, appearing thus at different energy positions. In contrast, the nf series presents the same quantum defect number $\delta \sim -0.002$ in each final symmetry. The effect of the autoionizing states on the PADs is highly significant. The β parameter dramatically changes as the photon energy crosses their energy position, seen in the lower panels of Fig. 5.23, 5.24, and 5.25. In addition, both series of autoionizing states

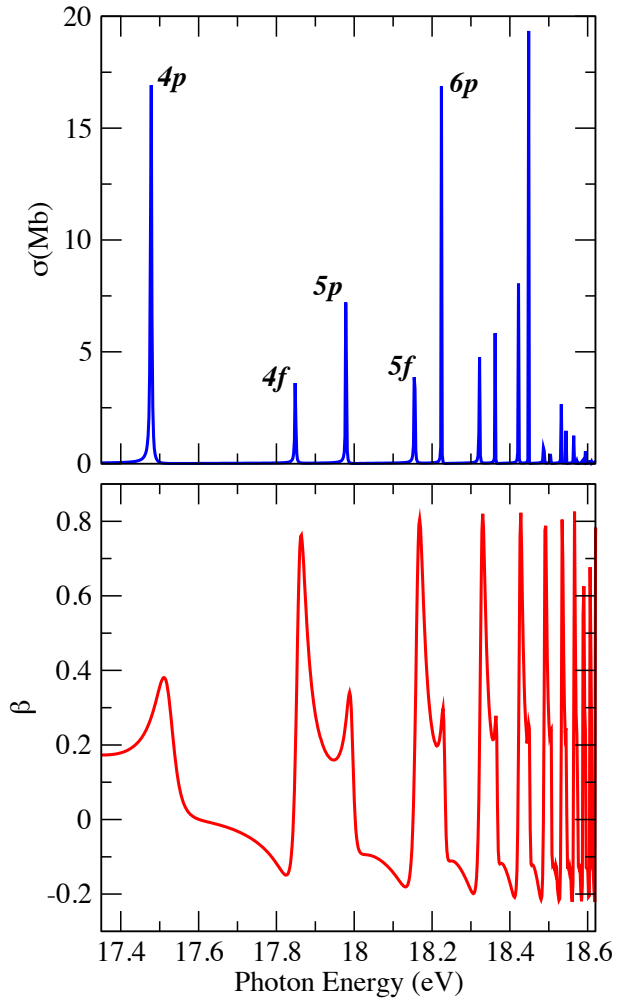

Figure 5.24: As in Fig. 5.23 but leaving the system in $^1\Pi_g$ final symmetry. The nl labels indicate the $np\pi_u$ and $nf(\phi_u$ or $\pi_u)$ series of the autoionizing states converging to the N_2^+ $(B^2\Sigma_u^+)$ cation state.

generate completely different values of the β parameter. For instance as observed in Fig. 5.24 the $5f$ autoionizing state gives rise to an asymmetry parameter of $\beta = 0.81$, while the $6p$ state is characterized by $\beta = 0.30$. Is important to mention that although the magnitudes of the cross sections and β parameters depend on the initial state, the positions of these same series of autoionizing states do not change when a different N_2 excited state is chosen as the initial state for the calculation.

An accurate calculation of the cross section for non-resonant two-photon single ionization of N_2 in lowest order perturbation theory would require a sum of single photon ionization amplitudes over a large number of ungerade intermediate electronic states, which is well

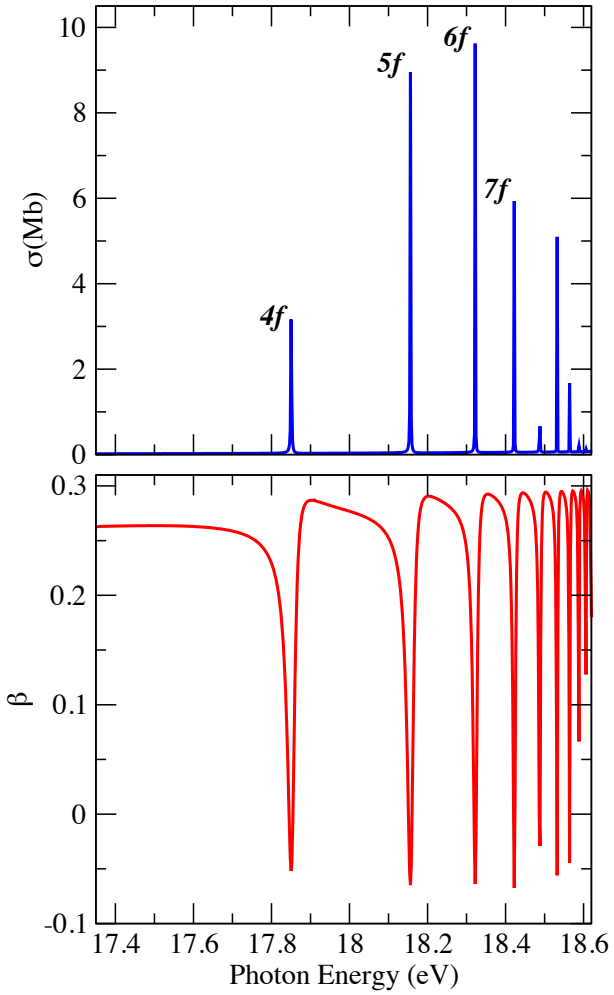

Figure 5.25: As in Fig. 5.23 but leaving the system in $^1\Delta_g$ final symmetry. The nl labels indicate the $nf(\delta_u$ or $\sigma_u)$ series of the autoionizing states converging to the N_2^+ ($B^2\Sigma_u^+$) cation state.

beyond the scope of the present study. To simplify the calculation, while providing further insight into the experimental observations, we have performed two-photon ionization calculations using the neutral $b^1\Pi_u$ state as the single intermediate state. Fig. 5.26 shows the calculated β_2 and β_4 parameters characterizing the two-photon ionization into the $A^2\Pi_u$ state of the ion. Both parameters exhibit strong variations as a function of the photon energy, as observed previously in Figs. 5.23, 5.24, and 5.25. This further underlines the effect of the autoionizing states on the PADs, as the autoionizing states appearing in each of the possible final symmetries are now taken into account. Considering the selected photoelectron kinetic energy intervals (see Fig. 5.18(a)), the np and nf Rydberg series contribute differently depending on the respective kinetic energy region, which results in completely different PADs

as depicted in panels (a) to (c) of Fig. 5.21. The finite bandwidth of the VUV pulses used in the present experiments produce photoelectrons from several final ion vibrational levels. It has also been shown in previous vibrationally-resolved single-channel calculations, which do not treat autoionization processes [129], that the influence of vibrational levels of the final state on the asymmetry parameter for the $A^2\Pi_u$ state are negligible. This prediction is consistent with the present calculations, stressing the major role of the continuum autoionizing states in NOTPSI of N_2, which manifests in a rapid variation in the anisoptropy parameters. Going beyond the scope of the present work, a quantitative comparison between the theoretical and experimental PADs would however require further calculations that take into account the non-resonant character of the first photon absorption step. This implies including dipole couplings between the ground state and several excited intermediate states as well as incorporating continuum-continuum dipole couplings.

Concluding Remarks

In this third section, energy- and angle-resolved experimental and theoretical results on the photoionization dynamics of N_2 were presented, analyzing ionic-state-selective photoelectron angular distribution following NOTPSI of neutral nitrogen molecules using coincidence 3-D momentum imaging and intense 9.3 eV femtosecond pulses produced via 400 nm driven HHG. Two-photon single ionization populates the first three ionic states of the molecular nitrogen cation, where we find that the PADs associated with the X $^2\Sigma_g^+$ and A $^2\Pi_u$ ionic states of N_2^+ both vary with minor changes in the photoelectron kinetic energy. We attribute this strong variation in the electron emission patterns on the photoelectron energy to the excitation and decay of dipole-forbidden autoionizing resonances of different total symmetry that belong to the Hopfield series. In addition to the direct ionization channel, these continuum-embedded discrete states provide an indirect pathway to the X $^2\Sigma_g^+$ and A $^2\Pi_u$ final states.

Despite our limited theoretical treatment, only invoking a single intermediate state and hence treating the two-photon ionization as resonant, our calculations provide insight into the non-resonant two-photon ionization dynamics, highlighting the important role of the dipole-forbidden autoionizing states on shaping the PADs and resulting β parameters. Further calculations involving a larger number of intermediate states lie beyond the scope of this work, however, the computed energies of the dipole-forbidden autoionizing states are insensitive to the intermediate state chosen, which suggests that such autoionizing resonances will remain important in the non-resonant regime.

The two competing pathways of autoionization and direct ionization can interfere for electrons ionized to the same final state. Experiments sensitive to such interference phenomena require the energy and angular momentum of detected autoionization electrons and photoelectrons (corresponding to indirect and direct pathways, respectively) to be identical. As the electron in the continuum can share angular momentum with the molecular axis in several ways, interference can only be observed for fixed-in-space molecular N_2^+ cations. As mentioned before, in the present work the target N_2 molecules were randomly orientated, and hence we could not isolate the small subset of events that would sensitively exhibit in-

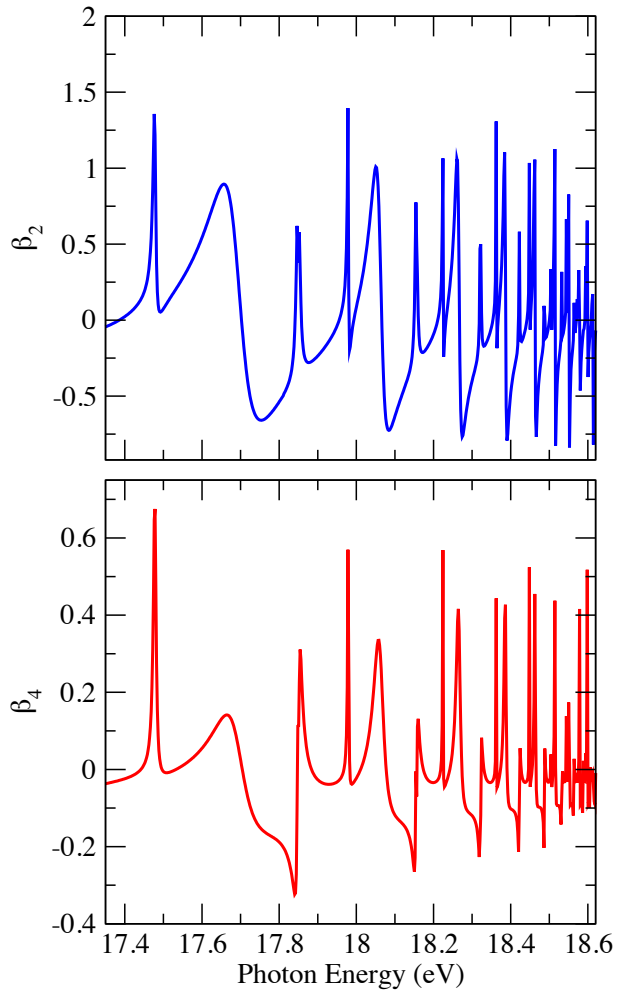

Figure 5.26: Two-photon photoelectron asymmetry parameters, β_2 (upper panel) and β_4 (lower panel), correlated to the $A^2\Pi_u$ state of the N_2^+ ion.

terference effects in the PADs. Future experiments could employ a multi-color interrogation scheme that enables prealigning the molecular axis via an additional laser pulse, which is able to impulsively align the neutral molecule with respect to the polarization vector of the intense VUV beam prior to ionization.

Chapter 6

Conclusion and Outlook

6.1 Summary

The work presented in this thesis demonstrates that the technique of HHG can be combined with coincidence 3-D momentum imaging in order to realize multi-modal measurements that carry high levels of information content and can reveal a detailed view on the correlated valence electron motion, as well a concerted electron-nuclear dynamics, in gas phase atomic and molecular systems. The VUV photons produced in the HHG process have energies that are capable of addressing and probing valence electrons in atoms and molecules, and ultrashort pulse durations that are necessary for driving two-photon absorption. The high-fluence VUV light source implemented in this thesis, as well as the VUV transport and spectral selection, illustrates that HHG can be used as an effective experimental tool for interrogating many-electron and coupled electron-nuclear dynamics. It is shown that by going to the second harmonic of the fundamental frequency of a Ti:sapphire laser system, a high intensity 9.3 eV light source can be achieved, allowing two-photon absorption to be efficiently driven resonantly and non-resonantly in the VUV. The coincidence 3-D momentum imaging spectrometer used in the experiments presented in this thesis was designed and optimized for the beam parameters of the HHG based VUV light source. This allowed highly differential energy- and angle-resolved coincidence measurements on photoelectrons and ions to be successfully conducted.

The first experiment presented in this thesis is a detailed investigation of the angle-resolved non-resonant one-color two-photon valence ionization dynamics of isolated argon atoms. This work reports the first measurements of the photoelectron angular distribution from non-resonant two-photon ionization of argon, revealing that the photoelectron angular distribution is strongly influenced by the interference between different orbital angular momentum components of the photoelectron scattering wave function. This interference pattern manifests as maximum emission intensity perpendicular to the ionizing VUV polarization. These results are compared with a previous set of theoretical calculations, that have been unverified for more than three decades, which indicates that electron-electron correlation

appreciably shapes the photoionization dynamics.

The second measurement presented is a thorough experimental and theoretical study of the energy- and angle-resolved resonant one-color two-photon absorption and dissociation dynamics of single O_2 molecules. This work reports the observation of two narrow and nearly degenerate autoionizing states of different symmetry that are both dipole-forbidden. These dipole-forbidden resonances can decay through internal conversion to ion-pair states of the same total symmetry, which competes with and interrupts autoionization. These measurements are compared against a set of calculations that indicate these two resonances are excited by parallel-parallel and parallel-perpendicular two-photon transitions and that the autoionizing states are directly populated, without intensity borrowing. The calculations also enable the electronic states participating in the two-photon transitions to be assigned and Fano line shapes of the involved resonances to be determined.

The final measurement presented in this thesis is a comprehensive experimental and theoretical investigation of the energy- and angle-resolved non-resonant one-color two-photon valence ionization dynamics of isolated nitrogen molecules. This study represents the first measurements of the photoelectron angular distribution from non-resonant two-photon valence ionization of N_2. Here it is found that the photoelectron angular distributions associated with the $X^2\Sigma_g^+$ and $A^2\Pi_u$ ionic states both vary significantly with small changes in photoelectron kinetic energy, specifically only a few hundred meV. The abrupt and swift variation in the photoelectron angular distributions is associated with the excitation and decay of dipole-forbidden autoionizing resonances belonging to series of different symmetries, all of which are members of the famous Hopfield series.

6.2 Outlook

6.2.1 Accessing The Molecular Frame

In the experiments on diatomic molecules presented in this thesis, since the two-photon energy of 18.6 eV lies below the dissociative ionization potential of both O_2 and N_2 (as well as most diatomic targets), it was not possible to both ionize the system and cleave a bond. It has been previously mentioned that dissociative ionization enables the orientation of the molecule at the instant of photoionization to be established, since the momentum of the recoiling ionic fragment can be used as a proxy for the molecular orientation, so long as the axial recoil approximation is valid. In essence, this means that the time-scales for fragmentation must be significantly less than the rotational period of the molecule, so that the internuclear axis at the moment of ionization and the recoiling fragment momentum vector coincide. With this information, molecular frame photoelectron angular distributions can then be recovered from the laboratory frame angular distributions by a suitable rotation of coordinates, which can be determined on an event-by-event basis. Since molecular frame photoelectron measurements carry far more information content than laboratory frame measurements (the form of the observable angular flux involves a summation over angular momentum components including

far more terms than the lab frame expression), these studies reveal rich and deep insight that can not be reached in more conventional laboratory frame measurements. Thus these types of measurements are highly desirable in order to accurately and completely characterize a many-particle quantum system and its dynamics, with such kinematically complete and highly differential molecular frame measurements approaching the fundamental limits imposed by quantum mechanics on the amount of information that can be extracted from the wave function of the system.

In the current experimental configuration, in order to gain access to the molecular frame, two methods are immediately apparent. In the first approach, molecular targets can be selected that have dissociative ionization potentials that lie below the two-photon energy of 18.6 eV. This typically involves going beyond diatomic molecules and towards larger polyatomic systems, which naturally have lower dissociative ionization potentials. Two promising targets are the linear molecule N_2O and the tetrahedral molecule CH_4. The ionization potential of N_2O is 12.9 eV, while the appearance energy of the NO^+ fragment is roughly 15.0 eV, the appearance energy of the N_2^+ fragment is roughly 17.3 eV, and the appearance energy of the O^+ fragment is roughly 15.3 eV. Meanwhile, the ionization potential of CH_4 is 12.6 eV, while the appearance energy of the CH_3^+ fragment is roughly 14.3 eV. In both of these molecular systems, a measurement on one of the recoiling ionic fragments in coincidence with an electron allows photoelectron angular distributions in the molecular frame to be determined. Such measurements exhibit great sensitivity to the many-electron and non-adiabatic dynamics involved in the photoionization and photodissociation mechanisms.

Since an increasingly complicated molecular target comes at the expense of greater complexity in interpretation of the measurement and data, a second approach involves going to higher order harmonics possessing higher photon energies, such that the dissociative ionization potential in simpler diatomic systems can be overcome. For example, the ionization potential of N_2 is 15.6 eV, while the appearance energy of the N^+ fragment is roughly 24.3 eV. As a second example, the ionization potential of O_2 is 12.1 eV, while the appearance energy of the O^+ fragment is roughly 18.7 eV. Since the photon energy of the third harmonic is roughly 9.3 eV and that of the fifth harmonic is roughly 15.5 eV, we see that using the third and fifth harmonic together results in a two-photon energy of 24.8 eV, while two photons of the fifth harmonic results in a two-photon energy of 31.0 eV. Both of these two-photon energies lie above the dissociative ionization potential of N_2 and O_2 and are thus capable of driving dissociative ionization and providing access to the molecular frame in these simpler diatomic systems. It is worth noting that although the fifth harmonic enables dissociative ionization in both N_2 and O_2, introducing this photon energy into an experiment results in single ionization of background gas in the MISTERS endstation along the beam propagation direction, as the fifth harmonic alone can photoionize many background species. This itself introduces challenges into performing successful measurements.

6.2.2 Higher Repetition Rates

Another important future prospect is the extension of the laser system towards higher repetition rates. This step would allow highly differential measurements with high statistics to be carried out in reasonable amounts of time. Since the current laser system only operates at 50 Hz and two-photon ionization is a non-linear process that is naturally difficult to drive efficiently, this makes accumulating decent statistics a significant challenge, as keeping the laser system and harmonics stable across many days is extremely difficult. This proved to be a primary limiting factor in the present experimental configuration, also inhibiting the ability to optimize the VUV beam and spectrometer parameters on-the-fly, resulting in experiments essentially "flying blind". Performing coincidence measurements that involve time-delay scans using the split-mirror interferometer is hence prohibitive, since collecting good statistics at a single delay can itself take days. Further, in the case of dissociative ionization, generating highly differential spectra, for example molecular frame photoelectron angular distributions with applied conditions, e.g. where the polarization vector of the ionizing field either lies parallel or perpendicular to the internuclear axis, requires data sets comprised of millions of coincidence events. Such large numbers are out of reach in the current 50 Hz set-up.

Higher repetition rate lasers are more naturally suited for coincidence measurements, since rare events are search for on a shot-to-shot basis, and increasing the repetition rate scales the coincidence event rate accordingly. Thus the strengths of coincidence 3-D momentum imaging are best harnessed at repetition rates between 10 kHz and 1 MHz. Fiber lasers operate at these repetition rates, and thus provide a viable path towards the highly differential measurements enabled by higher coincidence event rates. It has recently been demonstrated that femtosecond ytterbium-doped fiber lasers are capable of driving HHG, and can be used to create a high brightness milliwatt VUV source [30]. In the work presented in Ref. [30], the second, third, and fourth harmonic from a commercial femtosecond Yb-fiber laser (50 W, 166 kHz) producing 135 femtosecond pulses centered at 1030 nm was used to drive HHG. Here it was shown that the HHG efficiency was maximal using the third harmonic as a driver, producing $\sim$2 mW of average power at 18 eV using atomic argon as a generating medium. Implementing such a laser system in conjunction with the current coincidence 3-D momentum imaging spectrometer housed in the MISTERS endstation would result in an enormous increase in the data rate and the ability to greatly extend the scientific capabilities of the set-up. In particular, the coincidence event rate stands to increase by a factor of 3320 (assuming similar peak VUV intensities between the two systems). This means that experiments requiring a single day of data collection using the above fiber laser system would take over 9 years to conduct using the 50 Hz laser system used in this thesis. Here the benefits of an increased laser repetition rate becomes abundantly clear.

6.2.3 Reducing Background Electrons

An additional future possibility to improving the current experimental apparatus is to minimize the amount of electrons generated from metal surfaces inside the MISTERS chamber, which creates a background of hits on the electron detector that obfuscates real photoionization events. First, making improvements to the VUV mode quality can reduce the amount of scattered photons entering the spectrometer. Bringing a higher quality mode into the endstation results in higher quality data. This involves both improving the mode of the 400 nm driving field, which imprints its properties onto the VUV harmonics, as well as introducing more collimators and apertures into the beamline, which spatially confines the beam. Second and more importantly, minimizing the signal originating from electrons generated on the surface of the back-focusing mirror would greatly improve the data quality and reduce the amount of background electron counts. The current back-focusing mirror design enables a ring to be electrically biased in order to trap electrons generated on the mirror surface, as well as an outer shield that can be held at a voltage to minimize field distortion within the spectrometer. Slight improvements and modifications to the current design could be made in order to further mitigate this issue. For instance, the electrically biased ring used to trap electrons generated in photoemission from the mirror surface could be slightly extended along the beam propagation direction, such that it forms a slight hood around the mirror. This could possibly aid in capturing a larger number of electrons coming off of the mirror surface, however, the shield would also need to correspondingly extend out further into the spectrometer, potentially introducing greater fringe field effects that could be more problematic than in the current configuration.

Bibliography

[1] Selcuk Akturk et al. "Measuring spatial chirp in ultrashort pulses using single-shot Frequency-Resolved Optical Gating". In: *Optics Express* 11.1 (2003), pp. 68–78.

[2] T. K. Allison et al. "Separation of high order harmonics with fluoride windows". In: *Opt. Express* 17.11 (May 2009), pp. 8941–8946. DOI: 10.1364/OE.17.008941. URL: http://www.opticsexpress.org/abstract.cfm?URI=oe-17-11-8941.

[3] Thomas K. Allison. "Femtosecond Molecular Dynamics Studied with Vacuum Ultraviolet Pulse Pairs". PhD thesis. The University of California, Berkeley, 2010.

[4] Zikri Altun and Steven T. Manson. "Photoelectron angular distributions of ns subshells of open-shell atoms as indicators of interchannel coupling: Sc4*s* photoionization". In: *Phys. Rev. A* 61 (3 Feb. 2000), p. 030702. DOI: 10.1103/PhysRevA.61.030702. URL: https://link.aps.org/doi/10.1103/PhysRevA.61.030702.

[5] M. V. Ammosov, N. B. Delone, and V. P. Krainov. "Tunnel, ionization of complex atoms and atomic ions in a varying electromagnetic-field". In: *Zhurnal Eksperimentalnoi I Teoreticheskoi Fiziki* 91.6 (1986), pp. 2008–2013.

[6] David L. Andrews. "The theory of double-beam three-photon absorption". In: *The Journal of Chemical Physics* 77.6 (1982), pp. 2831–2835. DOI: 10.1063/1.444174. eprint: https://doi.org/10.1063/1.444174. URL: https://doi.org/10.1063/1.444174.

[7] Melanie T Asaki et al. "Generation of 11-fs pulses from a self-mode-locked Ti: sapphire laser". In: *Optics letters* 18.12 (1993), pp. 977–979.

[8] David E Aspnes and AA Studna. "Dielectric functions and optical parameters of si, ge, gap, gaas, gasb, inp, inas, and insb from 1.5 to 6.0 ev". In: *Physical review B* 27.2 (1983), p. 985.

[9] Peter W Atkins and Ronald S Friedman. *Molecular quantum mechanics*. Oxford university press, 2011.

[10] David Attwood and Anne Sakdinawat. *X-rays and extreme ultraviolet radiation: principles and applications*. Cambridge university press, 2017.

[11] Alexey V. Baklanov et al. "Direct mapping of recoil in the ion-pair dissociation of molecular oxygen by a femtosecond depletion method". In: *The Journal of Chemical Physics* 129.21 (2008), p. 214306. DOI: 10.1063/1.3026613. eprint: https://doi.org/10.1063/1.3026613. URL: https://doi.org/10.1063/1.3026613.

[12] N. Balakrishnan et al. "Time-dependent quantum mechanical study of photodissociation of molecular oxygen in the Schumann–Runge continuum". In: *The Journal of Chemical Physics* 112.3 (2000), pp. 1255–1259. DOI: 10.1063/1.480657. URL: https://doi.org/10.1063/1.480657.

[13] Philippe Balcou et al. "Generalized phase-matching conditions for high harmonics: The role of field-gradient forces". In: *Physical Review A* 55.4 (1997), p. 3204.

[14] Bryan Basden and Robert R. Lucchese. "Vibrationally resolved cross sections and asymmetry parameters for the photoionization of N_2 with coupling between the $(3\sigma_g)^{-1}$ and the $(2\sigma_u)^{-1}$ channels". In: *Phys. Rev. A* 37 (1 Jan. 1988), pp. 89–97. DOI: 10.1103/PhysRevA.37.89. URL: https://link.aps.org/doi/10.1103/PhysRevA.37.89.

[15] D Bauer and P Mulser. "Exact field ionization rates in the barrier-suppression regime from numerical time-dependent Schrödinger-equation calculations". In: *Physical Review A* 59.1 (1999), p. 569.

[16] Roger Y. Bello. private communication. Mar. 26, 2020.

[17] R.G.C. Blyth, I. Powis, and C.J. Danby. "Competing pre-dissociations of O_2^+ ($B^2\Sigma_g^-$)". In: *Chemical Physics Letters* 84.2 (1981), pp. 272–275. ISSN: 0009-2614. DOI: https://doi.org/10.1016/0009-2614(81)80343-0. URL: http://www.sciencedirect.com/science/article/pii/0009261481803430.

[18] Diego I. R. Boll et al. "Angularly resolved two-photon above-threshold ionization of helium". In: *Phys. Rev. A* 99 (2 Feb. 2019), p. 023416. DOI: 10.1103/PhysRevA.99.023416. URL: https://link.aps.org/doi/10.1103/PhysRevA.99.023416.

[19] Max Born and Robert Oppenheimer. "Zur quantentheorie der molekeln". In: *Annalen der physik* 389.20 (1927), pp. 457–484.

[20] A Börzsönyi et al. "Dispersion measurement of inert gases and gas mixtures at 800 nm". In: *Applied optics* 47.27 (2008), pp. 4856–4863.

[21] Robert W Boyd. *Nonlinear optics*. Academic press, 2019.

[22] R.G. Bray and R.M. Hochstrasser. "Two-photon absorption by rotating diatomic molecules". In: *Molecular Physics* 31.4 (1976), pp. 1199–1211. DOI: 10.1080/00268977600100931. eprint: https://doi.org/10.1080/00268977600100931. URL: https://doi.org/10.1080/00268977600100931.

[23] Robert J. Buenker, Sigrid D. Peyerimhoff, and Miljenko Perić. "AB initio vibrational analysis of the Schumann—Runge bands and the neighboring absorption region of molecular oxygen". In: *Chemical Physics Letters* 42.2 (1976), pp. 383–389. ISSN: 0009-2614. DOI: https://doi.org/10.1016/0009-2614(76)80391-0. URL: http://www.sciencedirect.com/science/article/pii/0009261476803910.

[24] Elio G. Champenois. "Resolving Non-Adiabatic Dynamics in Small Molecules with Few-Femtosecond Sensitivity". PhD thesis. The University of California, Berkeley, 2017.

[25] W.F. Chan et al. "Absolute optical oscillator strengths for discrete and continuum photoabsorption of molecular nitrogen (11–200 eV)". In: *Chemical Physics* 170.1 (1993), pp. 81–97. ISSN: 0301-0104. DOI: https://doi.org/10.1016/0301-0104(93)80095-Q. URL: http://www.sciencedirect.com/science/article/pii/030101049380095Q.

[26] David W Chandler and Paul L Houston. "Two-dimensional imaging of state-selected photodissociation products detected by multiphoton ionization". In: *The Journal of chemical physics* 87.2 (1987), pp. 1445–1447.

[27] Michael Chini, Kun Zhao, and Zenghu Chang. "The generation, characterization and applications of broadband isolated attosecond pulses". In: *Nature Photonics* 8.3 (2014), pp. 178–186.

[28] WA Chupka, PM Dehmer, and WT Jivery. "High resolution photoionization study of ion-pair formation in H2, HD, and D2". In: *The Journal of Chemical Physics* 63.9 (1975), pp. 3929–3944.

[29] Douglas Clark. *Thermal Conductivity of Helium*. Tech. rep. Fermi National Accelerator Lab.(FNAL), Batavia, IL (United States), 1992.

[30] A Comby et al. "Cascaded harmonic generation from a fiber laser: a milliwatt XUV source". In: *Optics express* 27.15 (2019), pp. 20383–20396.

[31] J. Cooper and R. N. Zare. "Angular Distribution of Photoelectrons". In: *The Journal of Chemical Physics* 48.2 (1968), pp. 942–943. DOI: 10.1063/1.1668742. eprint: https://doi.org/10.1063/1.1668742. URL: https://doi.org/10.1063/1.1668742.

[32] Paul B Corkum. "Plasma perspective on strong field multiphoton ionization". In: *Physical review letters* 71.13 (1993), p. 1994.

[33] Carlos E Crespo-Hernández et al. "Ultrafast excited-state dynamics in nucleic acids". In: *Chemical reviews* 104.4 (2004), pp. 1977–2020.

[34] Joseph L Dehmer. "Shape resonances in molecular fields". In: ACS Publications, 1984.

[35] P. M. Dehmer and W. A. Chupka. "High resolution study of photoionization processes in O2". In: *The Journal of Chemical Physics* 62.11 (1975), pp. 4525–4534. DOI: 10.1063/1.430359. eprint: https://doi.org/10.1063/1.430359. URL: https://doi.org/10.1063/1.430359.

[36] P. Dietrich et al. "High-harmonic generation and correlated two-electron multiphoton ionization with elliptically polarized light". In: *Phys. Rev. A* 50 (5 Nov. 1994), R3585–R3588. DOI: 10.1103/PhysRevA.50.R3585. URL: https://link.aps.org/doi/10.1103/PhysRevA.50.R3585.

[37] R.N. Dixon, J.M. Bayley, and M.N.R. Ashfold. "The rotational structure of three-photon resonances of polyatomic molecules". In: *Chemical Physics* 84.1 (1984), pp. 21–34. ISSN: 0301-0104. DOI: https://doi.org/10.1016/0301-0104(84)80003-8. URL: http://www.sciencedirect.com/science/article/pii/0301010484800038.

[38] Richard N Dixon. "Recoil anisotropy following multiphoton dissociation via near-resonant intermediate states". In: *The Journal of chemical physics* 122.19 (2005), p. 194302.

[39] Richard N. Dixon. "Recoil anisotropy following multiphoton dissociation via near-resonant intermediate states". In: *The Journal of Chemical Physics* 122.19 (2005), p. 194302. DOI: 10.1063/1.1896951. eprint: https://doi.org/10.1063/1.1896951. URL: https://doi.org/10.1063/1.1896951.

[40] R. Dörner et al. "Cold Target Recoil Ion Momentum Spectroscopy: a 'momentum microscope' to view atomic collision dynamics". In: *Physics Reports* 330.2-3 (June 2000), pp. 95–192. ISSN: 0370-1573. DOI: doi:DOI:10.1016/S0370-1573(99)00109-X. URL: http://www.sciencedirect.com/science/article/B6TVP-401HH57-1/2/587a27ccbfe492bcbe5b72191579ddbd.

[41] R Dörner et al. "Electron-electron interaction in projectile ionization investigated by high resolution recoil ion momentum spectroscopy". In: *Physical Review Letters* 72.20 (1994), p. 3166.

[42] Kurt Dressler. "The lowest valence and Rydberg states in the dipole-allowed absorption spectrum of nitrogen. A survey of their interactions". In: *Canadian Journal of Physics* 47.5 (1969), pp. 547–561. DOI: 10.1139/p69-072. eprint: https://doi.org/10.1139/p69-072. URL: https://doi.org/10.1139/p69-072.

[43] Gordon H. Dunn. "Anisotropies in Angular Distributions of Molecular Dissociation Products". In: *Physical Review Letters* 8.2 (Jan. 1962), pp. 62–64. DOI: 10.1103/PhysRevLett.8.62. URL: https://link.aps.org/doi/10.1103/PhysRevLett.8.62 (visited on 03/27/2020).

[44] Jr. Dunning Thom H. "Gaussian basis sets for use in correlated molecular calculations. I. The atoms boron through neon and hydrogen". In: *Journal of Chemical Physics* 90.2 (1989), pp. 1007–1023.

[45] Thom H. Dunning. "Gaussian basis sets for use in correlated molecular calculations. I. The atoms boron through neon and hydrogen". In: *The Journal of Chemical Physics* 90.2 (1989), pp. 1007–1023. DOI: 10.1063/1.456153. eprint: https://doi.org/10.1063/1.456153. URL: https://doi.org/10.1063/1.456153.

[46] Stefan Düsterer et al. "Two-color XUV+ NIR femtosecond photoionization of neon in the near-threshold region". In: *New Journal of Physics* 21.6 (2019), p. 063034.

[47] Martin Eckstein et al. "Direct Imaging of Transient Fano Resonances in N_2 Using Time-, Energy-, and Angular-Resolved Photoelectron Spectroscopy". In: *Phys. Rev. Lett.* 116 (16 Apr. 2016), p. 163003. DOI: 10.1103/PhysRevLett.116.163003. URL: https://link.aps.org/doi/10.1103/PhysRevLett.116.163003.

[48] Bradley Efron. "Bootstrap methods: another look at the jackknife". In: *Breakthroughs in statistics*. Springer, 1992, pp. 569–593.

[49] C. Elkharrat et al. "Ion Pair Formation in Multiphoton Excitation of NO2 Using Linearly and Circularly Polarized Femtosecond Light Pulses: Kinetic Energy Distribution and Fragment Recoil Anisotropy". In: *The Journal of Physical Chemistry A* 114.36 (2010). PMID: 20704179, pp. 9902–9918. DOI: 10.1021/jp103672h. eprint: https://doi.org/10.1021/jp103672h. URL: https://doi.org/10.1021/jp103672h.

[50] André TJB Eppink and David H Parker. "Velocity map imaging of ions and electrons using electrostatic lenses: Application in photoelectron and photofragment ion imaging of molecular oxygen". In: *Review of Scientific Instruments* 68.9 (1997), pp. 3477–3484.

[51] eSourceOptics. *VUV-UV Optical Material Properties*. eSource Optics / PMB 126 / 1225 Providence Rd. / Whitinsville, MA 01588. URL: https://www.esourceoptics.com/vuv_material_properties.html.

[52] Edilson L Falcao-Filho et al. "Scaling of high-order harmonic efficiencies with visible wavelength drivers: A route to efficient extreme ultraviolet sources". In: *Applied Physics Letters* 97.6 (2010), p. 061107.

[53] Edilson L Falcao-Filho et al. "Scaling of high-order harmonic efficiencies with visible wavelength drivers: A route to efficient extreme ultraviolet sources". In: *Applied Physics Letters* 97.6 (2010), p. 061107.

[54] Edilson L Falcão-Filho et al. "Analytic scaling analysis of high harmonic generation conversion efficiency". In: *Optics Express* 17.13 (2009), pp. 11217–11229.

[55] RW Falcone and J Bokor. "Dichroic beam splitter for extreme-ultraviolet and visible radiation". In: *Optics Letters* 8.1 (1983), pp. 21–23.

[56] Ugo Fano. "Effects of configuration interaction on intensities and phase shifts". In: *Physical Review* 124.6 (1961), p. 1866.

[57] M Ferray et al. "Multiple-harmonic conversion of 1064 nm radiation in rare gases". In: *Journal of Physics B: Atomic, Molecular and Optical Physics* 21.3 (1988), p. L31.

[58] P. A. Franken et al. "Generation of Optical Harmonics". In: *Phys. Rev. Lett.* 7 (4 Aug. 1961), pp. 118–119. DOI: 10.1103/PhysRevLett.7.118. URL: https://link.aps.org/doi/10.1103/PhysRevLett.7.118.

[59] Mette B Gaarde and Kenneth J Schafer. "Quantum path distributions for high-order harmonics in rare gas atoms". In: *Physical Review A* 65.3 (2002), p. 031406.

[60] Thomas Gaumnitz et al. "Streaking of 43-attosecond soft-X-ray pulses generated by a passively CEP-stable mid-infrared driver". In: *Optics express* 25.22 (2017), pp. 27506–27518.

[61] TE Glover, AH Chin, and RW Schoenlein. "High-order harmonic pulse broadening in an ionizing medium". In: *Physical Review A* 63.2 (2001), p. 023403.

[62] Maria Göppert-Mayer. "Über elementarakte mit zwei quantensprüngen". In: *Annalen der Physik* 401.3 (1931), pp. 273–294.

[63] Louis H Haber, Benjamin Doughty, and Stephen R Leone. "Photoelectron angular distributions and cross section ratios of two-color two-photon above threshold ionization of argon". In: *The Journal of Physical Chemistry A* 113.47 (2009), pp. 13152–13158.

[64] J. L. Hall and M. W. Siegel. "Angular Dependence of the Laser Photodetachment of the Negative Ions of Carbon, Oxygen, and Hydrogen". In: *The Journal of Chemical Physics* 48.2 (1968), pp. 943–945. DOI: 10.1063/1.1668743. eprint: https://doi.org/10.1063/1.1668743. URL: https://doi.org/10.1063/1.1668743.

[65] Yusong Hao, Chang Zhou, and Yuxiang Mo. "Velocity Map Imaging Study of the O2 Ion-Pair Production at 17.499 eV: Simultaneous Parallel and Perpendicular Transitions". In: *The Journal of Physical Chemistry A* 109.26 (2005). PMID: 16833917, pp. 5832–5835. DOI: 10.1021/jp0519262. eprint: https://doi.org/10.1021/jp0519262. URL: https://doi.org/10.1021/jp0519262.

[66] Saijoscha Heck. "Photoelectrons in Molecular Fields: An Investigation of Shape Resonances and Electron Retroaction using Coincident 3D Momentum Imaging Technique". PhD thesis. Max Planck Institut fur Kernphysik, Heidelberg, 2017.

[67] Burton L Henke, Eric M Gullikson, and John C Davis. "X-ray interactions: photoabsorption, scattering, transmission and reflection E= 50-30,000 eV, Z= 1-92". In: *Atomic data and nuclear data tables* 54.2 (1993). URL: https://henke.lbl.gov/optical_constants/.

[68] John J. Hopfield. "Absorption and Emission Spectra in the Region $\lambda 600 - 1100$". In: *Phys. Rev.* 35 (9 May 1930), pp. 1133–1134. DOI: 10.1103/PhysRev.35.1133. URL: https://link.aps.org/doi/10.1103/PhysRev.35.1133.

[69] James A Hostetter et al. "Semiclassical approaches to below-threshold harmonics". In: *Physical Review A* 82.2 (2010), p. 023401.

[70] R G Houlgate et al. "Angular distribution and photoionization cross section measurements on the 3p and 3s subshells of argon". In: *Journal of Physics B: Atomic and Molecular Physics* 7.17 (Dec. 1974), pp. L470–L473. DOI: 10.1088/0022-3700/7/17/003. URL: https://doi.org/10.1088%2F0022-3700%2F7%2F17%2F003.

[71] K. P. Huber, G. Stark, and K. Ito. "Rotational structure in the Hopfield series of N2". In: *The Journal of Chemical Physics* 98.6 (1993), pp. 4471–4477. DOI: 10.1063/1.465006. eprint: https://doi.org/10.1063/1.465006. URL: https://doi.org/10.1063/1.465006.

[72] Markus Ilchen et al. "Photoelectron angular distribution studies of the outer valence states of N2". In: *Journal of Physics B: Atomic, Molecular and Optical Physics* 45.22 (Nov. 2012), p. 225102. DOI: 10.1088/0953-4075/45/22/225102. URL: https://doi.org/10.1088%2F0953-4075%2F45%2F22%2F225102.

[73] J. Jose, R. R. Lucchese, and T. N. Rescigno. "Interchannel coupling effects in the valence photoionization of SF6". In: *The Journal of Chemical Physics* 140.20 (2014), p. 204305. DOI: 10.1063/1.4876576. eprint: https://doi.org/10.1063/1.4876576. URL: https://doi.org/10.1063/1.4876576.

[74] W. Kaiser and C. G. B. Garrett. "Two-Photon Excitation in CaF_2: Eu^{2+}". In: *Phys. Rev. Lett.* 7 (6 Sept. 1961), pp. 229–231. DOI: 10.1103/PhysRevLett.7.229. URL: https://link.aps.org/doi/10.1103/PhysRevLett.7.229.

[75] A. Kaldun et al. "Observing the ultrafast buildup of a Fano resonance in the time domain". In: *Science* 354.6313 (2016), pp. 738–741. ISSN: 0036-8075. DOI: 10.1126/science.aah6972. eprint: https://science.sciencemag.org/content/354/6313/738.full.pdf. URL: https://science.sciencemag.org/content/354/6313/738.

[76] Hyuk Kang et al. "Intrinsic lifetimes of the excited state of DNA and RNA bases". In: *Journal of the American Chemical Society* 124.44 (2002), pp. 12958–12959.

[77] Franz X Kärtner, Erich P Ippen, and Steven T Cundiff. "Femtosecond laser development". In: *Femtosecond Optical Frequency Comb: Principle, Operation, and Applications*. Springer, 2005, pp. 54–77.

[78] K Kaufmann, W Baumeister, and M Jungen. "Universal Gaussian basis sets for an optimum representation of Rydberg and continuum wavefunctions". In: *Journal of Physics B: Atomic, Molecular and Optical Physics* 22.14 (July 1989), pp. 2223–2240. DOI: 10.1088/0953-4075/22/14/007. URL: https://doi.org/10.1088%2F0953-4075%2F22%2F14%2F007.

[79] Karl Kaufmann, Werner Baumeister, and Martin Jungen. "Universal Gaussian basis sets for an optimum representation of Rydberg and continuum wavefunctions". In: *Journal of Physics B: Atomic, Molecular and Optical Physics* 22 (1989), pp. 2223–2240.

[80] LV Keldysh et al. "Ionization in the field of a strong electromagnetic wave". In: *Sov. Phys. JETP* 20.5 (1965), pp. 1307–1314.

[81] Rick A. Kendall, Jr. Dunning Thom H., and Robert J. Harrison. "Electron affinities of the first-row atoms revisited. Systematic basis sets and wave functions". In: *Journal of Chemical Physics* 96.9 (1992), pp. 6796–6806.

[82] Rick A. Kendall, Thom H. Dunning, and Robert J. Harrison. "Electron affinities of the first-row atoms revisited. Systematic basis sets and wave functions". In: *The Journal of Chemical Physics* 96.9 (1992), pp. 6796–6806. DOI: 10.1063/1.462569. eprint: https://doi.org/10.1063/1.462569. URL: https://doi.org/10.1063/1.462569.

[83] David J. Kennedy and Steven Trent Manson. "Photoionization of the Noble Gases: Cross Sections and Angular Distributions". In: *Phys. Rev. A* 5 (1 Jan. 1972), pp. 227–247. DOI: 10.1103/PhysRevA.5.227. URL: https://link.aps.org/doi/10.1103/PhysRevA.5.227.

[84] Markus Klinker et al. "Electron correlation in the ionization continuum of molecules: Photoionization of N2 in the vicinity of the Hopfield series of autoionizing states". In: *The journal of physical chemistry letters* 9.4 (2018), pp. 756–762.

[85] Morris Krauss and David Neumann. "Ion-pair states of O2". In: *The Journal of Chemical Physics* 63.12 (1975), pp. 5073–5076. DOI: 10.1063/1.431312. eprint: https://doi.org/10.1063/1.431312. URL: https://doi.org/10.1063/1.431312.

[86] Ferenc Krausz and Misha Ivanov. "Attosecond physics". In: *Reviews of Modern Physics* 81.1 (2009), p. 163.

[87] AH Kung et al. "Rydberg spectroscopy of H 2 via stepwise resonant two-photon ion-pair (H+ + H-) production". In: *Physical review letters* 56.4 (1986), p. 328.

[88] Lev D Landau. "Zur theorie der energieubertragung ii". In: *Z. Sowjetunion* 2 (1932), pp. 46–51.

[89] K. A. Larsen et al. "VUV and XUV reflectance of optically coated mirrors for selection of high harmonics". In: *Opt. Express* 24.16 (Aug. 2016), pp. 18209–18216. DOI: 10.1364/OE.24.018209. URL: http://www.opticsexpress.org/abstract.cfm?URI=oe-24-16-18209.

[90] KA Larsen et al. "Resonance signatures in the body-frame valence photoionization of CF 4". In: *Physical Chemistry Chemical Physics* 20.32 (2018), pp. 21075–21084.

[91] Kirk A Larsen, Daniel S Slaughter, and Thorsten Weber. "Angle-resolved nonresonant two-photon single ionization of argon using 9.3-eV photons produced via high-order harmonic generation". In: *Physical Review A* 101.6 (2020), p. 061402.

[92] Kirk A Larsen et al. "Distinguishing resonance symmetries with energy-resolved photoion angular distributions from ion-pair formation in O2 following two-photon absorption of a 9.3 eV femtosecond pulse". In: *The Journal of Chemical Physics* 153.2 (2020), p. 021103.

[93] Maciej Lewenstein et al. "Theory of high-harmonic generation by low-frequency laser fields". In: *Physical Review A* 49.3 (1994), p. 2117.

[94] H. H. Li. "Refractive index of alkaline earth halides and its wavelength and temperature derivatives". In: *Journal of Physical and Chemical Reference Data* 9.1 (1980), pp. 161–290. DOI: 10.1063/1.555616. eprint: https://doi.org/10.1063/1.555616. URL: https://doi.org/10.1063/1.555616.

[95] HH Li. "Refractive index of alkaline earth halides and its wavelength and temperature derivatives". In: *Journal of Physical and Chemical Reference Data* 9.1 (1980), pp. 161–290.

[96] C. D. Lin. "Channel interaction and threshold behavior of photoionization". In: *Phys. Rev. A* 9 (1 Jan. 1974), pp. 171–180. DOI: 10.1103/PhysRevA.9.171. URL: https://link.aps.org/doi/10.1103/PhysRevA.9.171.

[97] X-J Liu et al. "Molecular-frame photoelectron and electron-frame photoion angular distributions and their interrelation". In: *Journal of Physics B: Atomic, Molecular and Optical Physics* 40.3 (Jan. 2007), pp. 485–496. DOI: 10.1088/0953-4075/40/3/004. URL: https://doi.org/10.1088%2F0953-4075%2F40%2F3%2F004.

[98] X-J Liu et al. "Molecular-frame photoelectron and electron-frame photoion angular distributions and their interrelation". In: *Journal of Physics B: Atomic, Molecular and Optical Physics* 40.3 (Jan. 2007), pp. 485–496. DOI: 10.1088/0953-4075/40/3/004. URL: https://doi.org/10.1088%2F0953-4075%2F40%2F3%2F004.

[99] R. Locht and J. Momigny. "Mass spectrometric study of ion-pair processes in diatomic molecules: H2, CO, NO and O2". In: *International Journal of Mass Spectrometry and Ion Physics* 7.2 (1971), pp. 121–144. ISSN: 0020-7381. DOI: https://doi.org/10.1016/0020-7381(71)80033-5. URL: http://www.sciencedirect.com/science/article/pii/0020738171800335.

[100] Per-Olov Löwdin. "Quantum Theory of Many-Particle Systems. III. Extension of the Hartree-Fock Scheme to Include Degenerate Systems and Correlation Effects". In: *Phys. Rev.* 97 (6 Mar. 1955), pp. 1509–1520. DOI: 10.1103/PhysRev.97.1509. URL: https://link.aps.org/doi/10.1103/PhysRev.97.1509.

[101] Robert R. Lucchese. "Effects of interchannel coupling on the photoionization cross sections of carbon dioxide". In: *The Journal of Chemical Physics* 92.7 (1990), pp. 4203–4211. DOI: 10.1063/1.457778. eprint: https://doi.org/10.1063/1.457778. URL: https://doi.org/10.1063/1.457778.

[102] Robert R. Lucchese, Georges Raseev, and Vincent McKoy. "Studies of differential and total photoionization cross sections of molecular nitrogen". In: *Phys. Rev. A* 25 (5 May 1982), pp. 2572–2587. DOI: 10.1103/PhysRevA.25.2572. URL: https://link.aps.org/doi/10.1103/PhysRevA.25.2572.

[103] Robert R. Lucchese and Robert W. Zurales. "Comparison of the random-phase approximation with the multichannel frozen-core Hartree-Fock approximation for the photoionization of N_2". In: *Phys. Rev. A* 44 (1 July 1991), pp. 291–303. DOI: 10.1103/PhysRevA.44.291. URL: https://link.aps.org/doi/10.1103/PhysRevA.44.291.

[104] R Ma et al. "Photoelectron angular distributions for the two-photon ionization of helium by ultrashort extreme ultraviolet free-electron laser pulses". In: *Journal of Physics B: Atomic, Molecular and Optical Physics* 46.16 (2013), p. 164018.

[105] Richard Mabbs et al. "Photoelectron imaging: an experimental window into electronic structure". In: *Chem. Soc. Rev.* 38 (8 2009), pp. 2169–2177. DOI: 10.1039/B815748K. URL: http://dx.doi.org/10.1039/B815748K.

[106] P Maine et al. "Generation of ultrahigh peak power pulses by chirped pulse amplification". In: *IEEE Journal of Quantum electronics* 24.2 (1988), pp. 398–403.

[107] C Marceau et al. "Wavelength scaling of high harmonic generation for 267 nm, 400 nm and 800 nm driving laser pulses". In: *Journal of Physics Communications* 1.1 (2017), p. 015009.

[108] S. Marggi Poullain et al. "The role of Rydberg states in photoionization of NO2 and (NO+, O-) ion pair formation induced by one VUV photon". In: *The Journal of Chemical Physics* 139.4 (2013), p. 044311. DOI: 10.1063/1.4811713. eprint: https://doi.org/10.1063/1.4811713. URL: https://doi.org/10.1063/1.4811713.

[109] A McPherson et al. "Studies of multiphoton production of vacuum-ultraviolet radiation in the rare gases". In: *JOSA B* 4.4 (1987), pp. 595–601.

[110] M. Meyer et al. "Two-Photon Excitation and Relaxation of the $3d-4d$ Resonance in Atomic Kr". In: *Phys. Rev. Lett.* 104 (21 May 2010), p. 213001. DOI: 10.1103/PhysRevLett.104.213001. URL: https://link.aps.org/doi/10.1103/PhysRevLett.104.213001.

[111] Koichiro Mitsuke, Hiroaki Yoshida, and Hideo Hattori. "Positive ion — negative ion coincidence spectroscopy of O2 and H2 using synchrotron radiation". In: *Zeitschrift für Physik D* 27 (Sept. 1993), pp. 267–273. DOI: 10.1007/BF01436543.

[112] Naoki Miyamoto et al. "Observation of Two-Photon Above-Threshold Ionization of Rare Gases by xuv Harmonic Photons". In: *Phys. Rev. Lett.* 93 (8 Aug. 2004), p. 083903. DOI: 10.1103/PhysRevLett.93.083903. URL: https://link.aps.org/doi/10.1103/PhysRevLett.93.083903.

[113] R Moccia, N K Rahman, and A Rizzo. "Two-photon ionisation cross section calculations of noble gases: results for Ne and Ar". In: *Journal of Physics B: Atomic and Molecular Physics* 16.15 (Aug. 1983), pp. 2737–2751. DOI: 10.1088/0022-3700/16/15/016. URL: https://doi.org/10.1088%2F0022-3700%2F16%2F15%2F016.

[114] S. Mondal et al. "Pulse-delay effects in the angular distribution of near-threshold EUV + IR two-photon ionization of Ne". In: *Phys. Rev. A* 89 (1 Jan. 2014), p. 013415. DOI: 10.1103/PhysRevA.89.013415. URL: https://link.aps.org/doi/10.1103/PhysRevA.89.013415.

[115] Uwe Morgner et al. "Sub-two-cycle pulses from a Kerr-lens mode-locked Ti: sapphire laser". In: *Optics letters* 24.6 (1999), pp. 411–413.

[116] Robert Moshammer et al. "Low-energy electrons and their dynamical correlation with recoil ions for single ionization of helium by fast, heavy-ion impact". In: *Physical review letters* 73.25 (1994), p. 3371.

[117] Peter F Moulton. "Spectroscopic and laser characteristics of Ti: Al 2 O 3". In: *JOSA B* 3.1 (1986), pp. 125–133.

[118] John von Neumann and Eugene P Wigner. "Über merkwürdige diskrete Eigenwerte". In: *The Collected Works of Eugene Paul Wigner*. Springer, 1993, pp. 291–293.

[119] ETJ Nibbering et al. "Determination of the inertial contribution to the nonlinear refractive index of air, N 2, and O 2 by use of unfocused high-intensity femtosecond laser pulses". In: *JOSA B* 14.3 (1997), pp. 650–660.

[120] George C. Nieman. "Vibronic intensities and rotational line strength factors for the three-photon absorption spectrum of ammonia". In: *The Journal of Chemical Physics* 75.2 (1981), pp. 584–595. DOI: 10.1063/1.442074. eprint: https://doi.org/10.1063/1.442074. URL: https://doi.org/10.1063/1.442074.

[121] P O'Keeffe et al. "Vibrationally resolved photoionization of N2 near threshold". In: *The Journal of chemical physics* 136.10 (2012), p. 104307.

[122] Patrick O'shea et al. "Highly simplified device for ultrashort-pulse measurement". In: *Optics letters* 26.12 (2001), pp. 932–934.

[123] H. Oertel, H. Schenk, and H. Baumgärtel. "Ion pair formation from photon irradiation of O2, NO and CO in 17–30 eV". In: *Chemical Physics* 46.3 (1980), pp. 251–262. ISSN: 0301-0104. DOI: https://doi.org/10.1016/0301-0104(80)85201-3. URL: http://www.sciencedirect.com/science/article/pii/0301010480852013.

[124] Abe Offner. *Unit power imaging catoptric anastigmat*. US Patent 3,748,015. July 1973.

[125] M. Ogawa and Y. Tanaka. "RYDBERG ABSORPTION SERIES OF N2". In: *Canadian Journal of Physics* 40.11 (1962), pp. 1593–1607. DOI: 10.1139/p62-165. eprint: https://doi.org/10.1139/p62-165. URL: https://doi.org/10.1139/p62-165.

[126] Cheng Pan and Anthony F. Starace. "Angular distribution of electrons following two-photon ionization of the Ar atom and two-photon detachment of the F^- ion". In: *Phys. Rev. A* 44 (1 July 1991), pp. 324–329. DOI: 10.1103/PhysRevA.44.324. URL: https://link.aps.org/doi/10.1103/PhysRevA.44.324.

[127] HR Philipp and EA Taft. "Optical constants of silicon in the region 1 to 10 eV". In: *Physical Review* 120.1 (1960), p. 37.

[128] Etienne Plésiat, Piero Decleva, and Fernando Martın. "Vibrational branching ratios in the photoelectron spectra of N 2 and CO: Interference and diffraction effects". In: *Physical Chemistry Chemical Physics* 14.31 (2012), pp. 10853–10871.

[129] Etienne Plésiat, Pietro Decleva, and Fernando Martın. "Vibrationally resolved photoelectron angular distributions from randomly oriented and fixed-in-space N2 and CO molecules". In: *Journal of Physics B: Atomic, Molecular and Optical Physics* 45.19 (2012), p. 194008.

[130] E. W. Plummer et al. "Partial photoionization cross sections of N_2 and CO using synchrotron radiation". In: *Phys. Rev. A* 15 (6 June 1977), pp. 2339–2355. DOI: 10.1103/PhysRevA.15.2339. URL: https://link.aps.org/doi/10.1103/PhysRevA.15.2339.

[131] Alexander Plunkett et al. "Ultrafast Rydberg-state dissociation in oxygen: Identifying the role of multielectron excitations". In: *Physical Review A* 99.6 (2019), p. 063403.

[132] Tenio Popmintchev et al. "Bright coherent ultrahigh harmonics in the keV x-ray regime from mid-infrared femtosecond lasers". In: *science* 336.6086 (2012), pp. 1287–1291.

[133] M Raoult et al. "Ab initio approach to the multichannel quantum defect calculation of the electronic autoionisation in the Hopfield series of N2". In: *Journal of Physics B: Atomic and Molecular Physics* 16.24 (Dec. 1983), pp. 4601–4617. DOI: 10.1088/0022-3700/16/24/016. URL: https://doi.org/10.1088%2F0022-3700%2F16%2F24%2F016.

[134] Katharine L Reid. "Photoelectron angular distributions". In: *Annual review of physical chemistry* 54.1 (2003), pp. 397–424.

[135] T. N. Rescigno, B. H. Lengsfield, and A. E. Orel. "Interchannel coupling and ground state correlation effects in the photoionization of CO". In: *The Journal of Chemical Physics* 99.7 (1993), pp. 5097–5103. DOI: 10.1063/1.466010. eprint: https://doi.org/10.1063/1.466010. URL: https://doi.org/10.1063/1.466010.

[136] I. Sanchez and F. Martin. "Resonant effects in photoionization of H2 and D2". In: *The Journal of Chemical Physics* 107.20 (1997), pp. 8391–8396. DOI: 10.1063/1.475039. eprint: https://doi.org/10.1063/1.475039. URL: https://doi.org/10.1063/1.475039.

[137] Giuseppe Sansone et al. "Electron localization following attosecond molecular photoionization". In: *Nature* 465.7299 (2010), pp. 763–766.

[138] Takahiro Sato et al. "Determination of the absolute two-photon ionization cross section of He by an XUV free electron laser". In: *Journal of Physics B: Atomic, Molecular and Optical Physics* 44.16 (2011), p. 161001.

[139] KJ Schafer et al. "Above threshold ionization beyond the high harmonic cutoff". In: *Physical review letters* 70.11 (1993), p. 1599.

[140] RW Schoenlein et al. "The first step in vision: femtosecond isomerization of rhodopsin". In: *Science* 254.5030 (1991), pp. 412–415.

[141] Taro Sekikawa et al. "Measurement of the Intensity-Dependent Atomic Dipole Phase of a High Harmonic by Frequency-Resolved Optical Gating". In: *Phys. Rev. Lett.* 88 (19 Apr. 2002), p. 193902. DOI: 10.1103/PhysRevLett.88.193902. URL: https://link.aps.org/doi/10.1103/PhysRevLett.88.193902.

[142] Taro Sekikawa et al. "Nonlinear optics in the extreme ultraviolet". In: *Nature* 432.7017 (2004), pp. 605–608.

[143] Taro Sekikawa et al. "Pulse Compression of a High-Order Harmonic by Compensating the Atomic Dipole Phase". In: *Phys. Rev. Lett.* 83 (13 Sept. 1999), pp. 2564–2567. DOI: 10.1103/PhysRevLett.83.2564. URL: https://link.aps.org/doi/10.1103/PhysRevLett.83.2564.

[144] Vladimir Shiltsev. "Particle beams behind physics discoveries". In: *Phys. Today* 73.FERMILAB-PUB-20-105-AD-APC (2020).

[145] J. C. Slater. "The Theory of Complex Spectra". In: *Phys. Rev.* 34 (10 Nov. 1929), pp. 1293–1322. DOI: 10.1103/PhysRev.34.1293. URL: https://link.aps.org/doi/10.1103/PhysRev.34.1293.

[146] S. H. Southworth et al. "Channel coupling and shape resonance effects in the photoelectron angular distributions of the $3\sigma_g^{-1}$ and $2\sigma_u^{-1}$ channels of N_2". In: *Phys. Rev. A* 33 (2 Feb. 1986), pp. 1020–1023. DOI: 10.1103/PhysRevA.33.1020. URL: https://link.aps.org/doi/10.1103/PhysRevA.33.1020.

[147] David E Spence, P Np Kean, and Wilson Sibbett. "60-fsec pulse generation from a self-mode-locked Ti: sapphire laser". In: *Optics letters* 16.1 (1991), pp. 42–44.

[148] R. E. Stratmann and Robert R. Lucchese. "A graphical unitary group approach to study multiplet specific multichannel electron correlation effects in the photoionization of O2". In: *Journal of Chemical Physics* 102.21 (1995), pp. 8493–8505. DOI: 10.1063/1.468841.

[149] R. E. Stratmann and Robert R. Lucchese. "A graphical unitary group approach to study multiplet specific multichannel electron correlation effects in the photoionization of O2". In: *The Journal of Chemical Physics* 102.21 (1995), pp. 8493–8505. DOI: 10.1063/1.468841. eprint: https://doi.org/10.1063/1.468841. URL: https://doi.org/10.1063/1.468841.

[150] R. E. Stratmann and Robert R. Lucchese. "Resonances and the effects of interchannel coupling in the photoionization of CS2". In: *The Journal of Chemical Physics* 97.9 (1992), pp. 6384–6395. DOI: 10.1063/1.463699. eprint: https://doi.org/10.1063/1.463699. URL: https://doi.org/10.1063/1.463699.

[151] R. E. Stratmann, Robert W. Zurales, and Robert R. Lucchese. "Multiplet-specific multichannel electron-correlation effects in the photoionization of NO". In: *Journal of Chemical Physics* 104.22 (1996), pp. 8989–9000. DOI: 10.1063/1.471632.

[152] R. E. Stratmann, Robert W. Zurales, and Robert R. Lucchese. "Multiplet-specific multichannel electron-correlation effects in the photoionization of NO". In: *The Journal of Chemical Physics* 104.22 (1996), pp. 8989–9000. DOI: 10.1063/1.471632. eprint: https://doi.org/10.1063/1.471632. URL: https://doi.org/10.1063/1.471632.

[153] Donna Strickland and Gerard Mourou. "Compression of amplified chirped optical pulses". In: *Optics Communications* 56.3 (1985), pp. 219–221.

[154] Felix P. Sturm. "Time Resolved 3D Momentum Imaging Spectroscopy with VUV-XUV Pulse Pairs". PhD thesis. Goethe-Universitat Frankfurt am Main, 2016.

[155] Alan Sullivan. "Propagation of High-Intensity Ultrashort Laser Pulses in Plasmas." In: (1993).

[156] Dirk H Sutter et al. "Semiconductor saturable-absorber mirror–assisted Kerr-lens mode-locked Ti: sapphire laser producing pulses in the two-cycle regime". In: *Optics letters* 24.9 (1999), pp. 631–633.

[157] Joachim Ullrich et al. "Recoil-ion and electron momentum spectroscopy: reaction-microscopes". In: *Reports on Progress in Physics* 66.9 (2003), p. 1463.

[158] Susanne Ullrich et al. "Electronic relaxation dynamics in DNA and RNA bases studied by time-resolved photoelectron spectroscopy". In: *Physical Chemistry Chemical Physics* 6.10 (2004), pp. 2796–2801.

[159] R. J. Van Brunt and L. J. Kieffer. "Electron energy dependence of the energy and angular distributions of O- from dissociative ion pair formation in O2". In: *The Journal of Chemical Physics* 60.8 (1974), pp. 3057–3063. DOI: 10.1063/1.1681490. eprint: https://doi.org/10.1063/1.1681490. URL: https://doi.org/10.1063/1.1681490.

[160] Markus W Walser et al. "High harmonic generation beyond the electric dipole approximation". In: *Physical Review Letters* 85.24 (2000), p. 5082.

[161] He Wang et al. "Bright high-repetition-rate source of narrowband extreme-ultraviolet harmonics beyond 22 eV". In: *Nature communications* 6.1 (2015), pp. 1–7.

[162] J. Wang et al. "Effects of the close approach of potential curves in photoabsorption by diatomic molecules—II. Temperature dependence of the O2 cross section in the region 130–160 nm". In: *Journal of Quantitative Spectroscopy and Radiative Transfer* 38.1 (1987), pp. 19–27. ISSN: 0022-4073. DOI: https://doi.org/10.1016/0022-4073(87)90106-3. URL: http://www.sciencedirect.com/science/article/pii/0022407387901063.

[163] H.-J. Werner et al. *MOLPRO, version 2015.1, a package of ab initio programs*. 2015.

[164] H.-J. Werner et al. "Molpro: a general-purpose quantum chemistry program package". In: *WIREs Comput. Mol. Sci.* 2 (2012), pp. 242–253. DOI: 10.1002/wcms.82.

[165] Hans-Joachim Werner et al. "Molpro: a general-purpose quantum chemistry program package". In: *WIREs Computational Molecular Science* 2.2 (2012), pp. 242–253. DOI: 10.1002/wcms.82. eprint: https://onlinelibrary.wiley.com/doi/pdf/10.1002/wcms.82. URL: https://onlinelibrary.wiley.com/doi/abs/10.1002/wcms.82.

[166] WC Wiley and Ii H McLaren. "Time-of-flight mass spectrometer with improved resolution". In: *Review of scientific instruments* 26.12 (1955), pp. 1150–1157.

[167] Wei-Hao Xiong et al. "Mechanisms of below-threshold harmonic generation in atoms". In: *Physical review letters* 112.23 (2014), p. 233001.

[168] Andrew J Yencha, Kate Ellis, and George C King. "High-resolution threshold photoelectron and photoion spectroscopy of molecular nitrogen in the 15.0–52.7 eV photon energy range". In: *Journal of Electron Spectroscopy and Related Phenomena* 195 (2014), pp. 160–173.

[169] F. L. Yip et al. "Fully Differential Single-Photon Double Ionization of Neon and Argon". In: *Phys. Rev. Lett.* 110 (17 Apr. 2013), p. 173001. DOI: 10.1103/PhysRevLett.110.173001. URL: https://link.aps.org/doi/10.1103/PhysRevLett.110.173001.

[170] R.N. Zare and D.R. Herschbach. "Doppler line shape of atomic fluorescence excited by molecular photodissociation". In: *Proceedings of the IEEE* 51.1 (Jan. 1963), pp. 173–182. ISSN: 1558-2256. DOI: 10.1109/PROC.1963.1676.

[171] Clarence Zener. "Non-adiabatic crossing of energy levels". In: *Proceedings of the Royal Society of London. Series A, Containing Papers of a Mathematical and Physical Character* 137.833 (1932), pp. 696–702.

[172] Chang Zhou and Yuxiang Mo. "Ion-pair dissociation dynamics of O2 in the range 17.2–17.5 eV studied by XUV laser and velocity map imaging method". In: *The Journal of Chemical Physics* 139.8 (2013), p. 084314. DOI: 10.1063/1.4819079. eprint: https://doi.org/10.1063/1.4819079. URL: https://doi.org/10.1063/1.4819079.